MODELING AND CONTROL OF THREE-DOF ROBOTIC BULLDOZING

MODELING AND CONTROL

OF

THREE-DOF ROBOTIC BULLDOZING

BY

SCOTT GRAHAM OLSEN, B.Sc., B.Sc.M.E., M.Sc.

A Thesis
Submitted to the School of Graduate Studies
in Partial Fulfillment of the Requirements
for the Degree
Doctorate of Philosophy

McMaster University

DOCTORATE OF PHILOSOPHY (2012) MCMASTER UNIVERSITY

(Mechanical Engineering) Hamilton, Ontario

TITLE: Modeling and Control of Three-DOF Robotic Bulldozing

AUTHOR: Scott Graham Olsen, B.Sc. (Dalhousie University), B.Sc.M.E. (University of New Brunswick), M.Sc. (University of Calgary)

SUPERVISOR: Dr. Gary M. Bone

NUMBER OF PAGES: xxx, 199

To my parents, Sigrid and Ted, exemplars of hard work and perseverance, for their boundless love and encouragement over these many years of my journey through academia.

To my wife, Camille, and our adopted dependents, Mittens and Bojangles, for their unwavering love, support and trust that this would all work out eventually. This would have been impossible without them. Chou, this belongs to you.

Abstract

There is an increasing interest in automated mobile equipment in the construction, agriculture and mining industries to improve productivity, efficiency and operator safety. In general, these machines belong to a class of mobile vehicles with a tool for manipulating its environment to accomplish a repetitive task. Forces and motions are inherently coupled between the tool (*e.g.* bucket or blade) and the means of vehicle propulsion (*e.g.* wheels or tracks). Furthermore, they are often operated within uncertain and unstructured environments. A particularly challenging case involves the use of a bulldozer for the removal of excavated material. Modeling and control of mobile robots that interact forcibly with their environment, such as robotic excavation machinery, is a challenging problem that has not been adequately addressed in prior research. This thesis investigates the low-level modeling and control of a 3-DOF robotic bulldozing operation.

Motivated by a bulldozing process in an underground mining application, a theoretical nonlinear hybrid dynamic model was developed. The model includes discrete operation modes contained within a hybrid dynamic model framework. The dynamics of the individual modes are represented by a set of linear and nonlinear differential equations. An instrumented scaled-down bulldozer and environment were developed to emulate the full scale operation. Model parameter estimation and validation was completed using experimental data from this system. The model was refined based on a global sensitivity analysis. The refined model was found to be suitable for simulation and design of robotic bulldozing control laws.

Optimal blade position control laws were designed based on the hybrid dynamic model to maximize the predicted material removal rate of the bulldozing process. A stability analysis of the underlying deterministic closed-loop process dynamics was performed using Lyapunov's second method. Monte Carlo simulation was used for further performance and stability analysis of the closed-loop process dynamics including stochastic state disturbances and input constraints. Results of the Monte Carlo simulation were also used for tuning the blade position control laws. Experiments were conducted with the scaled-down robotic bulldozing system. The control laws were implemented with various tuning values. As a comparison, a rule-based blade control algorithm was also designed and implemented. The experimental results with the optimal control laws demonstrated a 33% increase in the average material removal rate compared to the rule-based controller.

Acknowledgements

I wish to express my deepest gratitude to my supervisor Dr. Gary Bone for taking a chance on me and this research project. I shall remain eternally grateful for his advice, guidance and support.

I also wish to thank the members of my supervisory committee, Dr. Christopher Swartz and Dr. Stephen Veldhuis, for their time and consideration in reviewing my work.

Furthermore, I wish to convey my sincere thanks to those who were involved at an earlier stage. The support and opportunities provided for several years by Dr. Robert Hall are very much appreciated. The discussions with Dr. Laeeque Daneshmend initiated invaluable insights into robotics, mining and academia in general. The support, technical expertise and consideration by Pat Murphy, Jason Hineman, Mary Owen, Ron Butter and everyone at Sandvik are truly appreciated. I am indeed grateful for the exceptional opportunities that were made possible.

I must extend my appreciation to my graduate student colleagues Matt, Darren, Mike and William, for their willingness to tolerate my esoteric parables and for just being there when I needed them the most.

The funding from the Natural Sciences and Engineering Research Council is acknowledged and greatly appreciated.

Table of Contents

List of Figures

List of Tables

Nomenclature

a	Analysis of variance number of treatments
$C_{da1:4,\Gamma}$	Parameters of the d_a dynamic equations per mode Γ
$C_{H1:3,\Gamma}$	Measured disturbance model coefficients for mode Γ
$C_{vb1:4,\Gamma}$	Parameters of the v_b dynamic equations per mode Γ
$C_{zc1:4}$, $C_{zb1:6}$	Parameters of the z_c and z_b equations
$C_{\phi 1:3,\Gamma}$	Parameters of the ϕ dynamic equations per mode Γ
D, $D_{i_1 i_2 \ldots i_s}$	Total variance and partial variances in the Sobol global sensitivity analysis
d_a	Depth of material accumulation on the blade
$d_{a,k}$	Discrete-time measured material accumulation
$d_{a,k}^{meas}$	Unfiltered material accumulation measurement
$\hat{d}_{a,k+1}$	One-step ahead prediction of d_a
$d_{a,k+1,\Gamma}^{cl}$, $d_{a,ss,\Gamma}$	Closed-loop and steady state material accumulation for mode Γ
$d_{a,max}$	Maximum material accumulation
$\bar{d}_{a,pass}$, $\bar{d}_{a,pass,\Gamma}$	Mean d_a over one pass and over one pass per mode Γ of control experiment results
$\bar{d}_{a,run}$	Mean d_a over a stochastic simulation run
$\bar{d}_{a,set}$	Mean $\bar{d}_{a,run}$ over a set of simulation runs

$d_{a,ss,\Gamma,stall}$	Closed-loop stall steady state material accumulation for mode Γ
$d_{a,thres}$	Threshold of d_a for the rule-based control algorithm
$\bar{d}_{a,trial}$	Mean d_a over all trials of control experiments
$d_{a,\Gamma,stall}$	Open-loop stall material accumulation
$e_{sum,xfit,\Gamma}$	Sum of the squared error between the measured state value and the predicted state value
$e_{x,\Gamma}^{EKF}$	Prediction error of between the EKF filtered measurement values
$e_{x,\Gamma}^{unfilt}$	Prediction error between the unfiltered measurement values
$\bar{e}_{x,\Gamma}^{unfilt}$	Mean prediction error from unfiltered measurements
$\mathbf{f}$	Function predicting the one step-ahead system state dynamics
$F_{actuator}$	Force transmitted through the blade positioning actuator
F_{arm}	Force transmitted through the blade arm
$f_{ctrl,\Gamma}$	Mode dependent blade control algorithm
F_{env}	Combined interaction forces between the blade and the environment
F_{k-1}^{EKF}	State transition matrix of the extended Kalman filter
$F_{traction}$	Traction force between the tracks and the ground
$f_{xfit}(\cdot)$	Function for which the parameters are estimated
$\mathbf{h}$	System output function

h_a	Averaged height of the material profile at location x_a
h_b	Average height of the material profile at location x_b
h_c	Average height of the material profile at location x_c
H_k^{EKF}	Observation matrix of the extended Kalman filter
h_{local}	Local mound height
$h_{local,max}$	Maximum allowable local mound height
h_{meas}	Measured material profile height
h_{peak}	Maximum height of the material profile peak at the local mound
h_r	Average ridge profile height at location x_b
$h_{r,l}$, $h_{r,r}$	Average heights of the left and right material ridge profiles
h_{thres1}, h_{thres2}	Average heights of a single layer and several layers of stones
$h_{\delta r}$	Difference between the average material ridge height and the average profile height along the blade
$H_{\Gamma,cl,stall}$	Closed-loop stall measured disturbance for mode Γ
$H_{\Gamma,k}$	Discrete-time combined measured disturbance term
$H_{\Gamma,min}$, $\bar{H}_\Gamma$, $H_{\Gamma,max}$	Minimum, mean and maximum measured disturbance term
J_Γ	Optimal control cost function for mode Γ
K_k^{EKF}	Extended Kalman filter gain
K_{rb}	Maximum blade constraint parameter
L_Γ	Lagrangian of the cost function for mode Γ

MS_E Analysis of variance mean squares

N Analysis of variance number of observations

N_p^{val} Number of prediction steps ahead used for model validation

N_s^{fit} Number of samples in the fitting data set

$N_{s,\Gamma,total}^{fit}$ Number of samples in the segmented fitting data set per mode Γ

$N_{seg,\Gamma}^{val}$ Number of mode segments within the validation data

$N_{s,\Gamma,seg}^{val}$ Number of samples within a particular mode segment of the validation data

$N_{s,\Gamma,total}^{val}$ Number of mode-segmented samples in the validation data set

N_r Duration of each stochastic simulation run

N_θ Number of parameters in the Sobol global sensitivity analysis

$n_{6,avoid}$ Number of passes where mode 6 did not become active

$n_{6,stuck}$ Number of passes that the robot became stuck after mode 6 activation

p Number of bulldozing passes completed

$P_{k|k-1}^{EKF}$, $P_{k|k}^{EKF}$ Predicted and updated estimate covariance of the extended Kalman filter

Q^{EKF} Process noise or disturbance covariance matrix of the extended Kalman filter

$\hat{Q}_{k+1}$ One-step ahead predicted material removal rate

$\bar{Q}_{pass}, \bar{Q}_{pass,\Gamma}$	Mean Q over one pass and over one pass per mode Γ of control experiment results
$\bar{Q}_{run}$	Mean material removal rate over a stochastic simulation run
$\bar{Q}_{set}$	Mean $\bar{Q}_{run}$ over the set of simulation runs
$Q_{ss,\Gamma}$	Deterministic steady state material removal rate
$\bar{Q}_{trial}$	Mean Q over all trials of control experiments
R^{EKF}	Measurement disturbance covariance matrix of the extended Kalman filter
$r^{cl}_{b,stall,\Gamma,min}$	Worst case closed-loop stall blade position reference
r_b	Blade position reference input
$r^{*}_{b,k,\Gamma}$	Optimal blade position reference input for mode Γ
$\overline{\lvert r_{b,run}\rvert}$	Mean absolute value of the blade position reference over a stochastic simulation run
$\overline{\lvert r_b\rvert}_{set}$	Mean $\overline{\lvert r_{b,run}\rvert}$ over the set of simulation runs
$\overline{\lvert r_b\rvert}_{pass}, \overline{\lvert r_b\rvert}_{pass,\Gamma}$	Mean r_b over one pass and over one pass per mode Γ of control experiment results
$r_{b,min}$, $r_{b,max}$	Minimum and maximum blade position constraints
$\overline{\lvert r_b\rvert}_{trial}$	Mean r_b over all trials of control experiments
$r_{b,\Gamma,stall}$	Open-loop stall blade position reference

$r_{b,\Gamma,stall,min}$	Worst case blade position stall condition
R_Γ	Optimal control law gain for mode Γ
$R_{\Gamma,cl,stall}$	Closed-loop stall control law gain for mode Γ
$S_{i_1 i_2 \ldots i_s}$	Sobol sensitivity indices
$\bar{S}_i^T$	Average total effect sensitivity index of the i^{th} parameter over a simulated trajectory
S_j^T	Total effect sensitivity index of the j^{th} parameter
S_k^{EKF}	Innovation covariance of the extended Kalman filter
SS_E	Analysis of variance sum of squares due to error
SS_{Total}	Analysis of variance total sum of squares
$SS_{Treatments}$	Analysis of variance sum of squares due to treatments
T_α	Analysis of variance comparison between means test statistic
T_{drive}	Torque generated by the track drive motors
T_s	Discrete-time sampling period
$t_{set,da}$, $t_{set,v}$	Deterministic closed loop material accumulation and robot velocity settling times
T1, T2	Delay-off timers of the switching controller algorithm
$\boldsymbol{u}_k$	Discrete-time input vector
u_t	Track control input
v_b	Blade velocity in the X-direction

$v_{b,k}$	Discrete-time measured blade velocity in the X-direction
$v_{b,k}^{meas}$	Unfiltered robot velocity measurement
$\hat{v}_{b,k+1}$	One-step ahead prediction of v_b
$v_{b,k+1,\Gamma}^{cl}$, $v_{b,ss,\Gamma}$	Closed-loop and steady state robot velocity for mode Γ
$v_{b,max}$	Maximum robot velocity
$\bar{v}_{b,pass}$, $\bar{v}_{b,pass,\Gamma}$	Mean v_b over one pass and over one pass per mode Γ of control experiment results
$\bar{v}_{b,run}$	Mean v_b over a stochastic simulation run
$\bar{v}_{b,trial}$	Mean v_b over all trials of control experiments
$\bar{v}_{b,set}$	Mean $\bar{v}_{b,run}$ over a set of simulation runs
$v_{b,thres}$	Thresholds of v_b for the rule-based control algorithm
v_{dozing}	Forward velocity of the bulldozer
$\boldsymbol{v}_k$	Zero mean multivariate Gaussian measurement noise vector
$V(\mathbf{x})$	Lyapunov function
w_b	Robot blade width
$w_{C.I.}$	Analysis of variance aggregate comparison interval
$\hat{w}_{d,k}$, $\hat{w}_{v,k}$, $\hat{w}_{\phi,k}$	Expected values of the stochastic disturbances in the d_a, v_b and ϕ Dynamics
$\boldsymbol{w}_k$	Zero mean multivariate Gaussian process noise or disturbance vector

x_a	Environment X coordinate a distance δ_a ahead of the blade
x_b	Environment X coordinate of the robot blade
x_c	Environment X coordinate of the robot centre
x_{edge}	X-coordinate where the removal space begins
$\mathbf{x}_{eq}$	State equilibrium vector
x^{fit}, x^{other}	State variable to be fit and other variables in the function $f_{xfit}(\cdot)$
$\boldsymbol{x}_k$	Discrete-time state vector
$\hat{\boldsymbol{x}}_{k\|k-1}^{EKF}$, $\hat{\boldsymbol{x}}_{k\|k}^{EKF}$	Predicted and updated state vector estimate from the extended Kalman filter
x_{meas}, x_{pred}	Measured and predicted states
$\bar{x}_{meas,\Gamma,seg}$	Mean state measurement within a mode segment of the validation data
x_{meas}^{EKF}	State measurement filtered with the extended Kalman filter
x_{pred}^{EKF}	State prediction from the extended Kalman filtered measurements
x_{meas}^{unfilt}	Unfiltered state measurement
x_{pred}^{unfilt}	State prediction from unfiltered measurement
$\tilde{\boldsymbol{y}}_k^{EKF}$	Innovation residual of the extended Kalman filter
z_c, z_b	Elevations of the robot centre and the robot blade
z_{est}	Estimated elevation variable
$\boldsymbol{z}_k$	Discrete-time output vector

$\alpha_{V,\Gamma}$	Lyapunov function parameter for mode Γ
Γ	Operation mode number
δ_a	Maximum effective length of material accumulated by the blade
δ_m	Stochastic Lyapunov worst case stability bound in the m^{th} mean
Δr_b	Blade position change increment of the rule-based control algorithm
Δt_6	Duration of mode 6 activation
ε_m	Stochastic Lyapunov stability bound in the m^{th} mean
ζ_k	Discrete-time measured blade position
ζ	Blade position
$\eta_{wx,\Gamma}$	Residual state disturbance Gaussian distribution
$\boldsymbol{\theta}_{\mathbf{z}}$, $\boldsymbol{\theta}_{\mathbf{x}}$	Parameter vector for the estimation optimization problem of the elevation equations and state equations
λ_1, λ_2	Lagrange multipliers
$\boldsymbol{\Sigma}$	Set of mode transition conditions
$\sigma^2_{v,xy,\Gamma}$	State measurement noise covariance
$\sigma^2_{w,x,\Gamma}$	State process disturbance variance
$\sigma_{\eta,wx,\Gamma}$	Residual state disturbance variance
τ_b, τ_d	Time constant and delay time for the blade position control

ϕ	Robot pitch angle
ϕ_k	Discrete-time measured robot pitch
ϕ_k^{meas}	Unfiltered robot pitch measurement
$\%fit_{x,\Gamma,seg}$	Relative model fit calculated per mode segment
$\%fit_{x,\Gamma}$	Relative model fit calculated per mode

Chapter 1

Introduction

1.1 Introduction to Research Topic

A major unaddressed challenge with mobile robots is the control of vehicles interacting forcibly with their environment, such as robotic tractors, bulldozers, loaders and snow plows. Forces and motions are inherently coupled between the tool (*e.g.* bucket or blade) and the means of vehicle propulsion (*e.g.* wheels or tracks). Furthermore, they are often operated within uncertain and unstructured environments. There is a growing industrial interest in the development of robotic mobile machinery to improve productivity, efficiency and safety. With reduced dependence on operator skill and a lower operator work load, full or partial automation (*e.g.* teleoperation) will contribute to more consistent, higher quality results and improved machine utilization.

Fig. 1.1 Teleoperated bulldozer used in underground mining.

A particularly challenging case involves the use of a bulldozer for the removal of fragmented rock in an underground mining application, such as the operation shown in Fig. 1.1. The resistance faced by the machine from the environment may vary significantly depending on the physical properties of the media (*e.g.* density and hardness) and the distribution of particle sizes and shapes.

1.2 General Description of a Bulldozing Process

A bulldozer consists of a main body driven by two motorized tracks. A blade for pushing material is joined to the machine by two arms. The blade is raised/lowered by a position controlled actuator. During the bulldozing process, the torque generated by each track drive motor is translated into a shear force between the track and the surface it is in contact with. A complex combination of the geometry and physical properties of the material below the tracks, and of the tracks themselves, determines the maximum torque that can be transferred before traction loss, or track slip, occurs, which was studied in Wong (2001). The amount of slip depends on the profile and area of the tracks; bulldozer weight and its distribution; static and dynamic friction functions; and the strength of the underlying material. The effective environment force on the blade is a combination of friction forces on the blade and the resistance of the material being pushed. The force is transmitted from the blade, through the blade arms and the main body, into the tracks. Lowering the blade tends to increase the environment force and vice-versa. For constant track motor hydraulic pressure (or voltage if the motor is electric) the forward velocity of the blade will decrease when the blade is lowered due to the increased force and resulting increased traction loss. In additional to increased resistance due to friction, lowering the

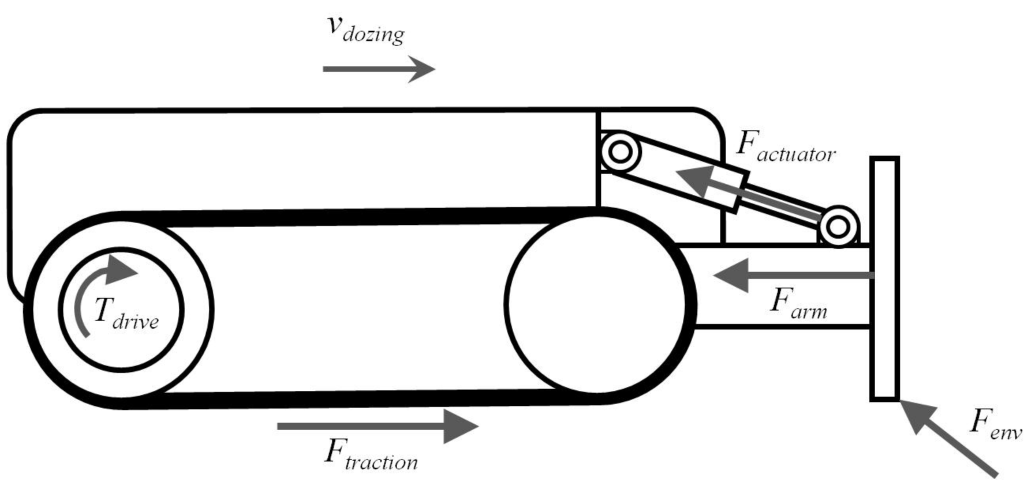

Fig. 1.2 Simplified machine and interaction forces.

blade tends to lift the front end of the chassis upward, thus reducing the contact pressure between the tracks and the ground, leading to reduced traction force. The decrease is nonlinear since the rate of material accumulation is proportional to the velocity, and the friction functions are nonlinear. The relevant simplified machine and interaction forces are illustrated in Fig. 1.2, where v_{dozing} is the forward velocity of the bulldozer, T_{drive} is the torque generated by the track drive motors, $F_{traction}$ is the traction force between the tracks and the ground, F_{env} is the combined interaction forces between the blade and the environment, F_{arm} is the force transmitted through the blade arm and $F_{actuator}$ is the force transmitted through the blade positioning actuator.

Machine operators tend to develop an intuitive understanding of how to most effectively accomplish their task. Operators do not explicitly consider the complex interaction forces between the vehicle and its environment to successfully maneuver the machine throughout the execution of the task. For instance, a general excavation material removal clearance task, other than grading, requires the operator to maneuver the vehicle forward while maintaining the bulldozer blade in a desired fixed position to accumulate as much material on the blade as possible. Upon observing the occurrence of significant traction loss or forward motion ceasing entirely, the blade will be raised by the operator until the machine regains traction and sufficient forward velocity is achieved.

1.3 Bulldozing Process in Underground Mining

A specific underground mining ore extraction operation involving a low-profile bulldozer was studied as part of a preliminary investigation toward further modeling and control development. The task of the bulldozer is to push excavation material from an operation space into a separate removal space where a different machine carries the material away. The first step in the overall ore extraction process is blasting of the face with explosives. The blast is designed to throw as much material as possible into a removal space known as the gully area. The resulting blasted material that fills the panel is a very coarse mix of ore and waste rock with an uneven distribution of sizes and shapes. A bulldozer then removes the excavation material from the very restricted space of the panel to the gully. The gully is a larger, more open space where an LHD (load-haul-dump) vehicle collects the material for transport to a conveyor hopper. This process is illustrated in Figure 1.3. The panel dimensions typically measure 4 meters wide, 21 meters along the face and as little as 1 meter high from the floor to the roof, the details of which were provided by Murphy (2005). This underground mining operation, including the bulldozing process, was observed directly onsite at the Lonmin Karee 1B mine in South Africa.

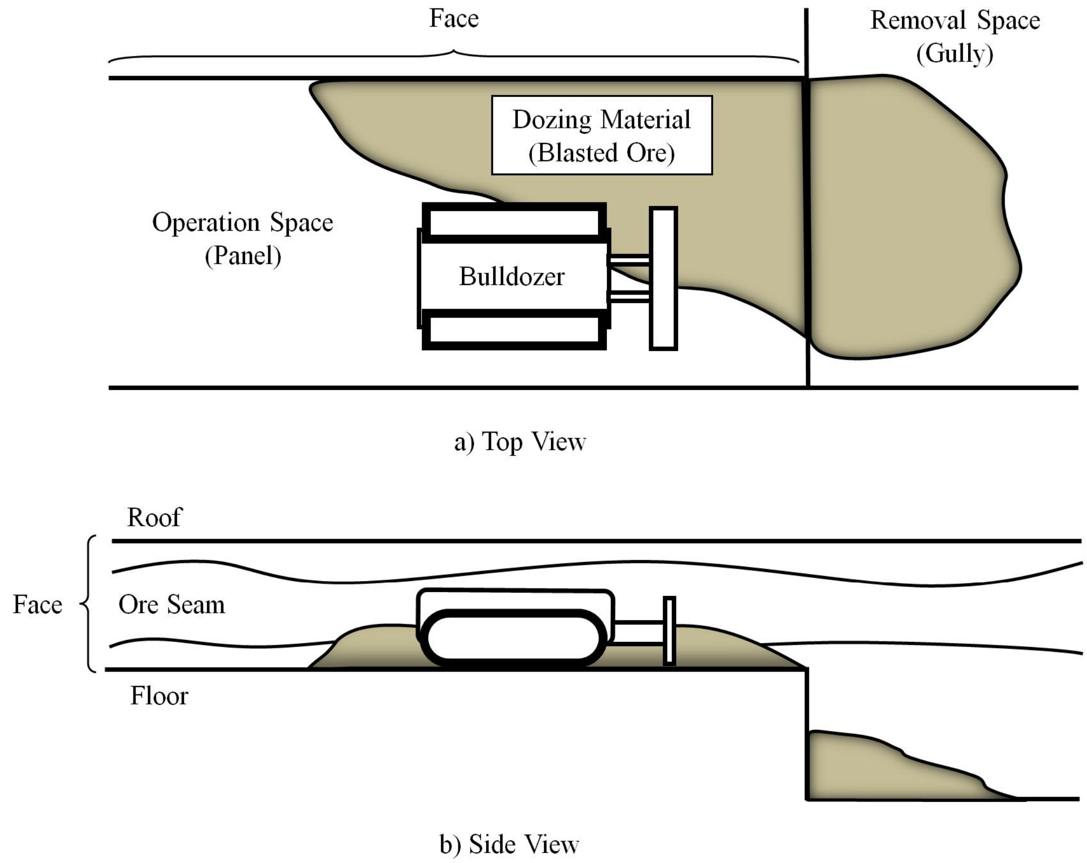

Fig. 1.3 Underground mining ore extraction operation.

An extra low profile (XLP) bulldozer was recently developed by Sandvik Mining and Construction specifically for the underground mining panel clearance operation. The initial concept design commenced in 2004 and a fully operational prototype, shown in Figure 1.4, entered service at the Lonmin Karee 1B mine in 2005. Following completion of extensive design improvements, full production of the XLP bulldozer began in 2006.

The machine was designed for remote radio control operation with a hand held controller. Each track is driven by a variable hydraulic motor. The blade is driven by two hydraulic cylinders. The hydraulic actuators are controlled via electro-mechanical servo-valves. The base machine dimensions are 850mm (h) x 1600 mm (w) x 2750 mm (l) and the weight is 5700 kg. The maximum speed is 4 km/hr. Further technical details on the design of the machine and mining application may be found in Olsen *et al.* (2006) and Olsen *et al.* (2008a).

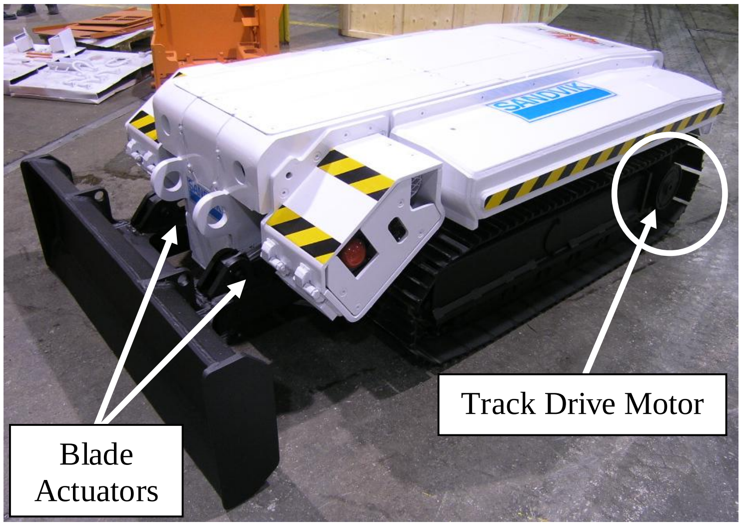

Fig. 1.4 Sandvik prototype extra low profile bulldozer.

1.4 Preliminary Investigations

Preliminary analysis of the bulldozing process and some experimental work was completed with the first pre-production prototype version of the Sandvik XLP bulldozer. The machine was developed into an experimental testbed with an onboard data acquisition and control computer and various sensors. For protection, the computer hardware and regulated variable DC source (used to power some sensors) were housed in a foam-lined hard plastic box that was mounted to the rear of the machine. The computer and DC source were powered by a portable AC power supply. To allow interaction with the computer, a flat screen monitor, key board and mouse were set up on the right side of the machine. A picture of the externally mounted computer hardware and power supply is shown in Fig. 1.5a. Encoders were used to measure rotational velocity of each track drive motor. Each encoder was mounted externally to the frame of the machine such that a rubber follower wheel, fixed to the shaft of the encoder, made contact and rotates with the outer casing of the track drive motor, as shown in Fig. 1.5b. A compliant spring mechanism ensured that there is sufficient pressure between the wheel and motor to eliminate slipping between the two. For protection, an outer steel casing is mounted over each encoder (not shown in the picture). Pressure transducers were used to measure the pressure across each motor, across the blade cylinders and across the hydraulic drive pump. A cable-extension position transducer was used to measure the extension of the blade cylinders.

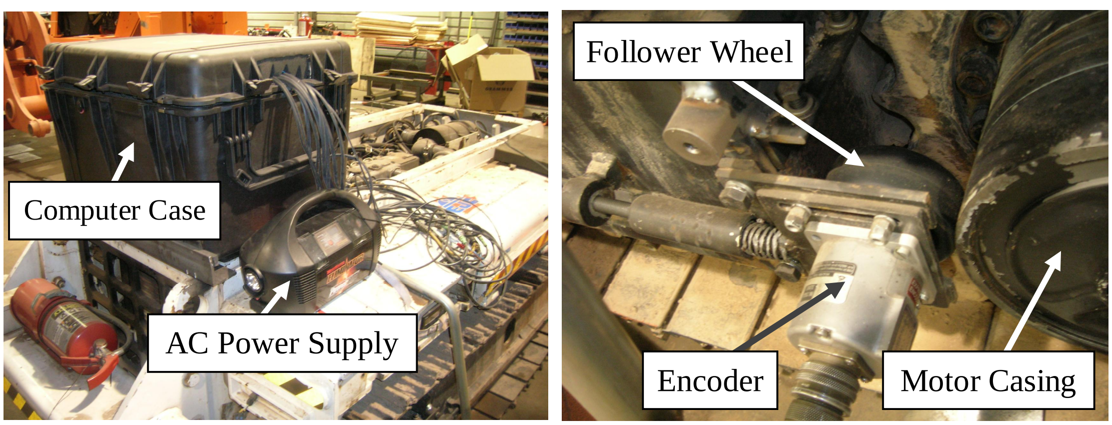

a) b)

Fig. 1.5 Instrumentation on the Sandvik prototype XLP bulldozer.

Proportional integral (PI) feedback control of the actuators was implemented for each track motor and proportional (P) control was implemented for the blade arm cylinders to maintain desired set points (*e.g.* track speed and blade arm position).

Experimental results involving the instrumentation and control of the full-scale machine actuators may be found in Olsen *et al.* (2008b).

Preliminary experimental testing was conducted within a special purpose test area onsite at the plant in Burlington, Ontario. Operating the machine under a range of operating conditions provided valuable experience in understanding the bulldozing process. A preliminary comprehensive task analysis of the bulldozing process revealed that it can be decomposed into distinct operation modes. Furthermore, different control requirements are necessary for different modes of operation, as discussed in Olsen *et al.* (2008b).

This machine was intended to serve as the experimental system on which the work in this thesis was to be developed. However, experiments were difficult to set up, expensive and weather dependent. For these reasons, plus hardware failures and high cost of repairs, experimental work with this machine proved prohibitive and had to be discontinued. Thus, an alternative reduced-scale experimental system was designed and built.

1.5 Research Objectives

The overall goal of this thesis was to develop a novel approach to autonomous bulldozing operations. Specific research objectives are summarized as follows:

- Design and build a reduced-scale robotic bulldozer and experimental environment for further investigation and validation of models and control algorithms.

- Development of a comprehensive dynamic model of a robotic bulldozing process with respect to the machine and its working environment.
- Experimental validation of the theoretical model framework and system identification of the robotic bulldozing process model.
- Formulate an optimal control approach to optimize the execution of the robotic bulldozing operation by maximizing the material removal rate.
- Experimental validation of the robotic bulldozing control design.

1.6 Thesis Organization

Proceeding from this introductory chapter, the remainder of this thesis is organized as follows: The literature on automation and control of bulldozing and related excavation operations is reviewed in Chapter 2. A novel hybrid dynamic model of the robotic bulldozing operation is proposed in Chapter 3. The experimental reduced-scale robotic bulldozing system is described in Chapter 4. Experimental methodology and results of system identification including model parameter estimation, model validation and a sensitivity analysis are presented in Chapter 5. Design of an extended Kalman filter and modeling of the state disturbances are presented in Chapter 6. The development of a model-based control approach is described in Chapter 7. In Chapter 8 an analysis of stability and performance of the deterministic open loop and closed loop dynamics is presented, followed by an analysis of stability and performance of the stochastic closed loop dynamics in Chapter 9. The experimental methodology and results of control implementation are presented in Chapter 10. Conclusions and recommendations for future work are discussed in Chapter 11.

Chapter 2

Literature Review

2.1 Introduction

This chapter presents a review of the literature on automation and control of bulldozers and related work involving similar excavation and service machinery. The greatest challenge facing autonomous bulldozing and excavation is the nature of the machine-environment interactions that occur during the operation. The resistance faced by the machine as it attempts to penetrate and displace the excavation material may vary significantly depending on the physical properties of the media (*e.g.* density and hardness) and the distribution of particle sizes and shapes. Therefore, it is very difficult, if not impossible, to predetermine the exact nature of the machine-environment interactions prior to execution of the operation. This can cause significant difficulties with respect to control. Since simple motion or trajectory control is insufficient, most methods developed to control machines for earthmoving tasks involve both force and position feedback.

The literature on bulldozer automation is very sparse. The main area of focus has been on blade position control for grading soil. Typical assumptions include uniform soil conditions and constant vehicle speed. These control system implementations tend to be ad-hoc schemes for operator assist applications that lack a systematic approach with respect to optimality and robustness in task execution.

Other related work includes the control of excavation machines used for digging tasks. Unlike bulldozing, which involves pushing material forwards, digging involves scooping, lifting and carrying material. The machine is typically modeled as a multiple-link robotic manipulator mounted on a static base with control design involving position and/or force feedback. Several significant investigations involve modeling and control of excavation tasks using a small tool carried by a robotic manipulator and a scaled-down experimental environment.

A few papers have presented high-level artificial intelligence approaches for coordinating multiple autonomous robots for complex excavation operations. This work involves using artificial intelligence methods for higher-level coordination of multiple robotic excavation machines, including bulldozers, for remote site preparation tasks. Strategic objectives are achieved through emergent multi-robot coordination.

Finally, there is some significant related work involving modeling and control of other service machinery that is characterized by machine-environment interactions.

2.2 Bulldozer Automation and Control

An operator assist feature was proposed for a remotely operated underwater bulldozer in Ohtsubo and Ward (1975). A nonlinear control system for the blade cylinders based on a simplified mass-spring-damper system model was developed to maintain blade position control during a soil cutting task. Although it was not actually implemented, a simulation is presented to show the feasibility of the system.

A simple control system to control the blade position based solely on the pressure in the hydraulic cylinders is demonstrated in Ito (1991). The controller is designed to maintain a constant blade position while remaining below a certain pressure setpoint. When the pressure in the cylinders reaches a desired setpoint the blade is moved upward until the pressure drops below it, then position control is resumed. Although results are presented to show successful implementation, there is no description of how to choose suitable pressure setpoints.

A fuzzy logic operator assist control system was developed in Terano *et al.* (1992) where the fuzzy rules are based on expert operator control actions. Two different types of operations were considered: ‘flattening’ the earth horizontally or with a constant slope and maintaining constant load on the blade to avoid track slip.

An experimental investigation is described in Qinsen and Shuren (1994) to estimate bulldozer blade forces as a function of known soil parameters during a soil cutting process. Experiments involved moving a scaled-down blade at a fixed position on rails at a fixed constant velocity. The soil used for experiments was carefully prepared and compacted with known uniform properties.

Various patents exist that deal with similar bulldozer blade position control schemes for operator assist soil grading applications. Yamamoto (2001) describes a method for maintaining a desired blade position by correcting actual position based on an estimation of the amount of material loaded on the cutting edge. Nakagami *et al.* (1998) describes a cutting edge position detector to be used to maintain a preset target cutting edge position. An integrated automatic blade lift and tilt control system is described in Koch (2005) for soil grading to maintain blade position with respect to a three-dimensional computerized site plan. Machine position and orientation are determined with either a laser system or global positioning system.

Other patents involve methods to detect track slip and control the tractive effort. For example, a 'running slip' detector is described in Nakagami (1997) to detect track slip based on vehicle acceleration. The track slip can then be reduced by lifting the blade. The patent described in Matsushita (1996) is concerned with detecting 'actual tractive force' so that tractive effort can be controlled 'gradually' to reach a target setting.

2.3 Excavator Automation and Control

2.3.1 Full-Scale Excavator Automation and Control Investigations

A technique proposed by Bullock and Oppenheim (1992) involves using strain gauges to measure the resistive forces encountered by the excavator bucket. Force feedback measurements are processed at a higher level to alter the low level trajectory changes in a supervisory control scheme.

An impedance control approach was proposed in Bernold (1993) that utilizes force and position feedback. In the case of robotic excavation, the robot was considered an impedance that translates motion into force, and the soil as an admittance, reacting with a change in position or motion. A similar impedance control approach was proposed in Ha *et al.* (2000). Having developed kinematic and dynamic models for the excavator, a sliding mode impedance controller was implemented on a retrofitted mini-excavator.

In Vaha and Skibniewski (1993) a dynamic model was developed for the excavator and used in conjunction with a model for the soil. Further details of the backhoe excavator dynamic model were derived in Koivo *et al.* (1996). The model includes the relationship between the forces generated by the hydraulic cylinders to the pose of the bucket. The forces acting on the bucket due to interaction with the soil while digging are also taken into account.

A position-based impedance controller was developed in Salcudean *et al.* (1997) for an excavator backhoe. This approach models the bucket as a position source with the contact force measured through cylinder pressure sensors used to modify the trajectory.

A rules-based control approach was developed in Bradley and Seward (1998) to automate an excavator specifically for trench digging. The digging task is decomposed into three separate phases consisting of penetrate, drag and empty. In addition to the ability to follow a predetermined path, there are rules to enable the robot to cope with a variety of conditions that emerge while digging.

A full-scale robotic excavation and autonomous truck loading system is described in Stentz *et al.* (1999). The system utilizes two scanning laser range-finders to recognize and localize the truck, measure the soil face and detect obstacles. Onboard software was used to make decisions regarding digging and dumping operations. The digging operation is described as being executed by a force based closed loop control scheme.

Marshall *et al.* (2008) describes experiments and analysis of an excavation process for fragmented rock in a mining environment involving a wheeled load-haul-dump (LHD) machine. The experimental analysis focused on characterizing the forces experienced by the bucket through measurements of the hydraulic actuator cylinder pressures. The design of an actuator force-feedback admittance controller is discussed but not implemented.

2.3.2 Reduced-Scale Excavator Automation and Control Investigations

In Shi *et al.* (1996) the bucket motion of a front loading excavator machine was simulated using a PUMA 560 robot arm. A fuzzy-logic based control strategy was developed by emulating the actions of skilled human operators. Experiments were performed within a simulated rock excavation environment.

A theoretical model was developed in Takahashi *et al.* (1999) to predict the resistive forces on the bucket of an excavator known as a load-haul-dump machine during the scooping phase of operation. The predicted forces agreed well with those obtained using a scaled rock pile environment.

A method is presented in Althoefer *et al.* (2009) for identifying the unknown parameters required for real-time prediction of interaction forces between an excavator tool and the soil using a hybrid dynamic soil model. A Mitsubishi RV-M1 robotic manipulator was used to push a flat metal tool through the soil. Force measurements were obtained using a six-axis ATI Mini40 force/torque sensor. Their experimental results demonstrated good correlation between the estimated and measured forces.

2.4 Coordination of Multiple Excavation Robots

An algorithm is developed in Parker and Zhang (2006) for site preparation based on the concept of "blind bulldozing" which models the collective nest building behaviour of ants. The goal of clearing a specified circular area is achieved as the result of the interactions between individual robots exhibiting simple reactive behaviours. The performance of the algorithm is verified with experiments involving small instrumented "toy" bulldozers.

In Thangavelautham (2009) an “artificial neural tissue” (ANT) control architecture is used to coordinate multiple robots for autonomous excavation and clearing tasks. Simple behaviours are defined for multiple robots with different tool implements (*e.g.* bulldozer blade, front loader scoop or bucket wheel). The higher-level control architecture determines the best implements and behaviours to achieve a specified global excavation goal. Simulation and experiments with small specially designed robots show the effectiveness of the control architecture.

2.5 Other Service Machinery Modeling and Control

An analytical model was developed in Bevly (2002) for the yaw dynamics of a farm tractor for the purposes of improved automatic steering control. A system identification approach was presented to estimate the model parameters of a large farm tractor. Experimental results showed that the lateral control was improved with the new model and controller. This work was extended in Gartley (2008) with online identification of the yaw dynamics for adaptive steering control. Their experimental results demonstrated that the adaptive controller achieved good performance regardless of the load on the implement. Since their focus was on steering control, they did not explicitly model the machine-environment interaction dynamics.

Le *et al.* (1997) develop a method for real-time estimation of soil parameters from trajectory data of a tracked vehicle using an extended Kalman filter. Results are given for simulated motion of an experimental tracked vehicle maneuvering over different types of soil.

2.6 Conclusions

The low-level modeling and control of the bulldozing process, *i.e.* the interaction between the bulldozer and its environment, has not been addressed in the existing literature. The remainder of this thesis addresses these deficiencies with the development of a novel hybrid dynamic model of a robotic bulldozing process and system identification methodology which provides the framework for the development of a novel approach to autonomous control of the robotic bulldozing operation.

Chapter 3

Hybrid Dynamic Model Development

3.1 Introduction

This chapter focuses on the development of a novel hybrid dynamic modeling framework of a constrained robotic bulldozing operation for the purposes of system identification, simulation and control design.

The complete bulldozing process involves the position and orientation of the machine (*i.e.* 6 degrees-of-freedom (DOF)), the position of the blade, the material accumulation on the blade, the 3-dimensional environment (*i.e.* a volume of material distributed on a hard floor), and their interaction dynamics. In this thesis, the process is kinematically constrained such that the machine motions are reduced to the three DOF that characterize the primary low-level dynamic behavior of a typical bulldozing process, specifically the X, Z and pitch DOF. Similarly, the variation in the environment is reduced to mainly the X and Z dimensions. The material to be pushed consists of fragmented rock or stones.

Careful observations of the full scale bulldozing process have revealed that it consists of discrete operation modes. It is characterized by the behavior within each mode, defined by continuous dynamics, and mode transitions that are discrete events, and therefore belongs to the class of hybrid dynamic systems. Several hybrid dynamic system modeling frameworks have been developed. The framework used here is similar to the "controlled general hybrid dynamical system" presented in Branicky *et al.* (1998).

3.2 Dynamic Equations

A novel set of hybrid nonlinear dynamic system equations have been developed that model the low-level bulldozing process. Ten discrete operation modes have been defined. The model structure is the same for all modes, only the parameters change. Fig. 3.1 illustrates the state variables and the auxiliary variables. The set of system equations are as follows:

$$\dot{d}_a = v_b \cdot \left(C_{da1,\Gamma} \cdot d_a + C_{da2,\Gamma} \cdot h_a + C_{da3,\Gamma} \cdot h_b + C_{da4,\Gamma} \cdot h_{\delta r} + C_{da5,\Gamma} \cdot \zeta \right) \tag{3.1}$$

$$\dot{x}_b = v_b \tag{3.2}$$

$$\dot{v}_b = \frac{1}{C_{vb1,\Gamma}} \left(C_{vb2,\Gamma} \cdot u_t - v_b \right) + C_{vb3,\Gamma} \cdot d_a + f\left(\zeta\right) \cdot C_{vb4,\Gamma} \cdot \zeta \tag{3.3}$$

$$\dot{\zeta} = \frac{1}{\tau_b} \left(r_b \left(t - \tau_d \right) - \zeta \right) \tag{3.4}$$

$$\dot{\phi} = v_b \cdot \left(C_{\phi 1,\Gamma} \cdot d_a + C_{\phi 2,\Gamma} \cdot \zeta + C_{\phi 3,\Gamma} \cdot h_c + C_{\phi 4,\Gamma} \cdot h_b \right) \tag{3.5}$$

$$z_c = C_{zc1} \cdot h_c + C_{zc2} \cdot d_a \tag{3.6}$$

$$z_b = C_{zb1} \cdot z_c + C_{zb2} \cdot \sin\left(\phi\right) + C_{zb3} \cdot d_a + C_{zb4} \cdot \zeta \tag{3.7}$$

$$f\left(\zeta\right) = \begin{cases} 1 & \text{if } \zeta < 0 \\ 0 & \text{otherwise} \end{cases} \quad \text{and} \tag{3.8}$$

$$h_{\delta r} = h_r - h_b \tag{3.9}$$

subject to the conditions:

$$r_{b,min} \le r_b \le r_{b,max} \tag{3.10}$$

$$\begin{bmatrix} h_a & h_b & h_c & h_{r,l} & h_{r,r} & z_b & z_c \end{bmatrix} \ge \mathbf{0} \tag{3.11}$$

$$d_a > \zeta \text{ and} \tag{3.12}$$

$$v_b \geq 0 \ \forall \ \Gamma \neq 9 \tag{3.13}$$

where Γ is the operation mode number. The system inputs are: r_b, the blade position reference input; and u_t, the track control input. The minimum and maximum constraints on r_b are $r_{b,min}$ and $r_{b,max}$, respectively. The system states are: d_a, the depth of material accumulation on the blade; x_b, the environment X coordinate of the blade; v_b, the blade velocity in the X-direction; ζ, the blade position; τ_b and τ_d, the time constant and delay time for the blade position control, respectively; ϕ, the robot pitch angle; z_c, the elevation of the robot centre (see point $\mathbf{P_c}$ in Fig. 3.1); and z_b, the elevation of the robot blade (see point $\mathbf{P_b}$ in Fig. 3.1).

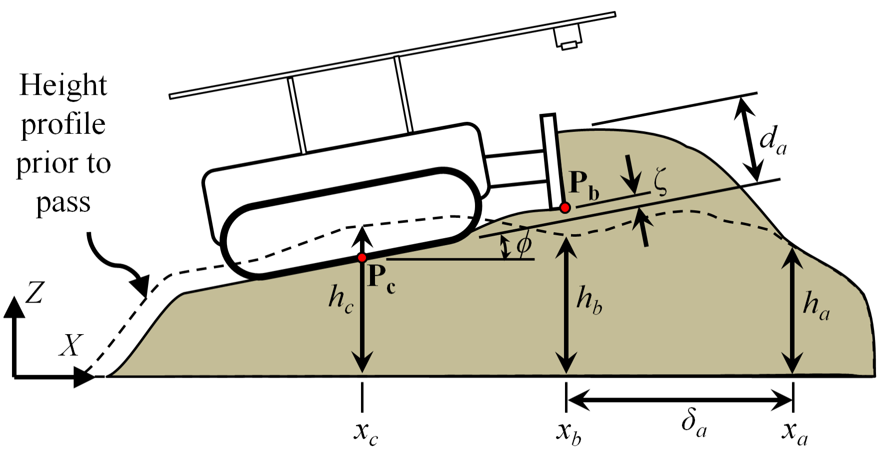

Fig. 3.1 Illustration of the state variables d_a, x_b, z_b, z_c, ϕ and ζ; and auxiliary variables h_a, h_b and h_c (note that $\mathbf{P_b}=[x_b \ z_b]^T$ and $\mathbf{P_c}=[x_c \ z_c]^T$).

The auxiliary variables are: h_b, the height of the material profile prior to the current pass at location x_b, averaged over the robot width; $h_{r,l}$ and $h_{r,r}$, the heights of the material ridge profiles on the left and right sides of the robot, respectively, prior to the current pass at location x_b and are used to calculate the average ridge profile height $h_r = ½(h_{r,l} + h_{r,r})$; h_a the averaged height of the material profile prior to the current pass at location $x_a = x_b + \delta_a$, where δ_a is the maximum effective length of material accumulated by the blade (*i.e.* the wave front of the accumulated material whereby the underlying material profile remains undisturbed past x_a); and $h_{\delta r}$, defined as the difference between the average height of the material ridges that form along the left and right sides of the blade minus the average profile height along the blade.

Note that the parameters $C_{vb1:4,\Gamma}$, $C_{da1:4,\Gamma}$ and $C_{\phi 1:3,\Gamma}$ are dependent on the mode; whereas $C_{zc1:4}$ and $C_{zb1:6}$ are elevation equation parameters that are independent of the mode. The estimation of these parameters will be discussed in Chapter 5.

Some of the terms in the dynamic equations warrant further explanation. As Eq. (3.13) states, for all modes except Γ=9, the robot will be stationary or driving forwards, therefore $v_b \geq 0$. Equations (3.1) and (3.5) assume that the rates of change of the accumulation and pitch angle are proportional to v_b. This agrees with the geometry and kinematics of the process, based on the assumption that the friction of the material is sufficient to prevent robot or material motion when v_b=0. Multiplying by v_b in Eq. (3.1) and Eq. (3.5) captures this dynamic behavior such that the rates of change of d_a and ϕ diminish to zero as v_b decreases to zero. With Eq. (3.1), from the process physics $C_{da1,\Gamma} <0$, so the term $v_b \cdot C_{da1,\Gamma} \cdot d_a$ will be nonpositive, and will tend to limit the growth of d_a. The terms $v_b \cdot C_{da3,\Gamma} \cdot h_b$, $v_b \cdot C_{da2,\Gamma} \cdot h_a$ and $v_b \cdot C_{da4} \cdot h_{\delta r}$ represent the influences of the material directly below the blade, δ_a ahead of the blade, and along the sides of the blade, respectively. In Eq. (3.3), the parameters C_{vb1} and C_{vb2} represent the robot velocity time constant and steady state gain, respectively. Note that the effects of track slip on the robot velocity are implicitly included in Eq. (3.3). The terms $C_{vb3,\Gamma} \cdot d_a$ and $C_{vb4,\Gamma} \cdot \zeta$ represent the influences of the resistances due to the material accumulated on the blade, and due to the blade position, respectively. In Eq. (3.5), the combined term $C_{\phi 3} \cdot h_c + C_{\phi 4} \cdot h_b$ represents the effect of the gradient of the material profile beneath the robot on the pitch. In Eq. (6), the term $C_{zb3} \cdot \sin(\phi)$ represents the change in elevation due to the robot pivoting about point $\mathbf{P_c}$. In Eqns. (3.5) - (3.7), the terms $C_{\phi 1} \cdot d_a$, $C_{zc2} \cdot d_a$ and $C_{zb3} \cdot d_a$, respectively, model the changes in the underlying material profile due to material accumulation on the blade.

3.3 Operation Modes and Transitions

The set of discrete operation modes is defined as follows (note that mode transitions do not necessarily occur sequentially throughout the bulldozing process even though the enumeration of the mode numbers may suggest this):

- ***At Start***, Γ=0, $[v_b\ d_a\ \zeta\ \phi\ z_c\ z_b] = \mathbf{0} \wedge u_t = 0 \wedge r_b = 0 \wedge p = 0$: The robot is at rest in front of the leading edge of the material pile. The blade is positioned at a height of 0 mm (*i.e.* just touching the floor surface). All state variables are zero and control inputs are set to zero. This mode is shown in Fig. 3.2a.
- ***Approach***, Γ=1, $v_b \geq 0 \wedge x_b < x_{edge} \wedge u_t = u_{t,nom}$: The track control input is activated and the robot drives forward. This mode is shown in Fig. 3.2b.
- ***Engage***, Γ=2, $d_a > 0 \wedge z_b < h_{thres1} \wedge x_b < x_{edge}$: The robot blade makes contact with the leading edge of the material pile and the robot continues to drive forward into the

material pile. Material accumulates on the blade as it is being pushed. The robot tracks remain in contact with the floor surface (*i.e.* there is no increase in robot elevation). This mode is shown in Fig. 3.2c. If, due to material flowing around the left and right sides of the blade as it travels through the material, the robot tracks begin to drive up onto the material pile (*i.e.* robot elevation increases) the robot will transition to another mode.

- ***Leveling***, Γ=3, $z_b \geq h_{thres2} \wedge x_b < (x_{edge} - \delta_a) \wedge r_b = f_{ctrl,3}$: If the pile of underlying material is sufficiently supportive and high (*i.e.* several layers of stones), the robot climbs up onto the top of the pile. The material underneath the tracks is relatively loose, decreasing traction, and the blade can penetrate down into the pile of material as it pushes, increasing the amount of material being pushed. This mode is shown in Fig. 3.2d.
- ***Pushing***, Γ=4, $z_b \geq h_{thres1} \wedge z_b < h_{thres2} \wedge h_a \geq h_{thres2} \wedge x_b < (x_{edge} - \delta_a) \wedge r_b = f_{ctrl,4}$: The pile of material in the environment is at a negligible height (*i.e.* only a sparse layer of stones) at the blade location, but a significant height of material is located ahead of the blade, increasing the rate of material accumulation of the blade and the resistance felt by the robot. The blade cannot penetrate down into the stones so further blade downward movement has no effect on accumulation. However, it will increase the resistance against the robot due to friction. This mode is shown in Fig. 3.2e.
- ***Scraping***, Γ=5, $z_b < h_{thres2} \wedge h_a < h_{thres2} \wedge x_b < (x_{edge} - \delta_a) \wedge r_b = f_{ctrl,5}$: This mode is similar to mode 4, except that no significant height of material is located ahead of the blade. This mode is shown in Fig. 3.2f.

- ***Disengage***, Γ=6, $d_a < 0 \wedge x_b < (x_{edge} - \delta_a)$: This mode may occur if the blade is raised above its zero position (*i.e.* $\zeta > 0$) while an amount of material is being pushed forward. If the material flows beneath the blade to form a small mound in front of the robot tracks then the robot will drive up onto this local mound and its blade will become disengaged with the underlying material. This mode is shown in Fig. 3.2g.
- ***Near Edge***, Γ=7, $x_b \geq (x_{b,edge} - \delta_a) \wedge x_b < x_{edge} \wedge r_b = f_{ctrl,7}$: When the blade is within the previously defined distance δ_a from the forward edge of the environment, material accumulation on the blade will drop off rapidly into the *removal space* that is significantly below grade. The environment force due to material resistance will decrease. This mode is shown in Fig. 3.2h.
- ***Blade At Edge***, Γ=8, $x_b = x_{b,edge} \wedge u_t = 0 \wedge p = p + 1$: When the robot blade has reached the edge of the environment, the track input is deactivated and the robot decelerates to a stop.
- ***Reverse***, Γ=9, $u_t = -u_{t,nom} \wedge r_b = r_{b,max}$: The track input is set to drive the robot in reverse to return to the start location. The blade position is set to its maximum height in order to avoid dragging material backwards.

Where: p is the number of passes completed, h_{thres1} is the average height of a single layer of stones; h_{thres2} is the height of several layers of stones; and x_{edge} is the forward boundary of the environment where the removal space begins.

Note that a blade control algorithm is initiated in modes 2 - 7 (denoted as $f_{ctrl,\Gamma}$) to accomplish the desired bulldozing process objective (*e.g.* minimizing the time required to complete the bulldozing process). For the other modes, the blade is servoed to the specified fixed position. The mode transition diagram is given in Fig. 3.3.

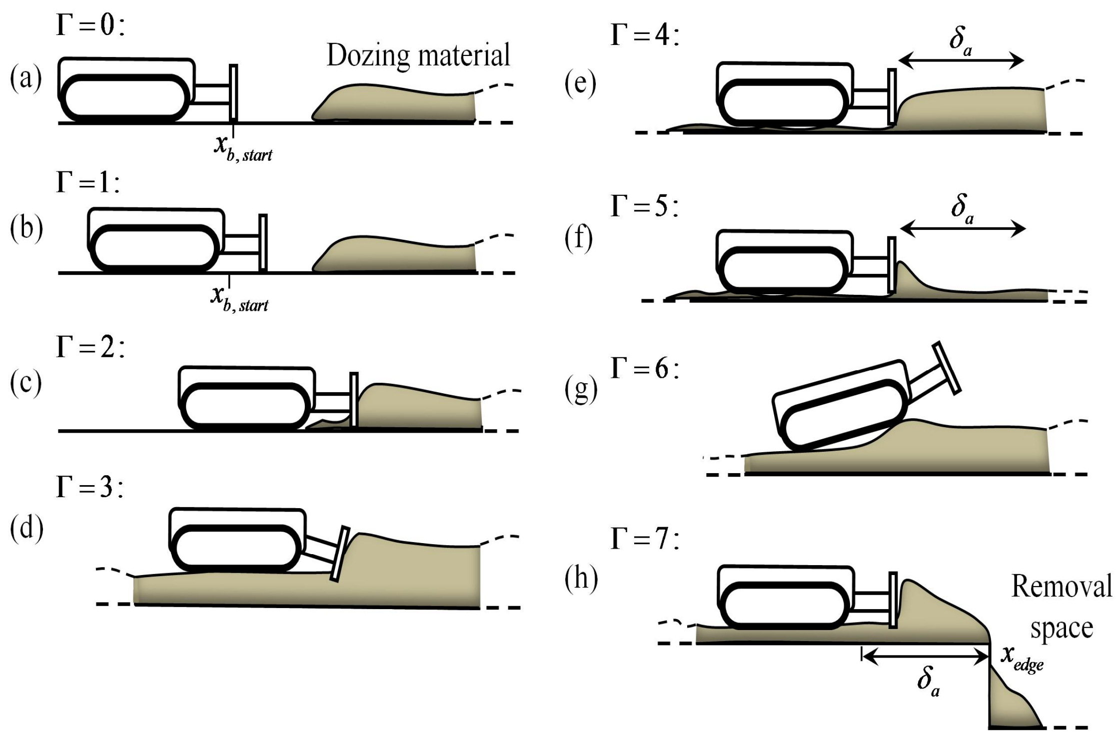

Fig. 3.2 Illustration of the discrete operating modes.

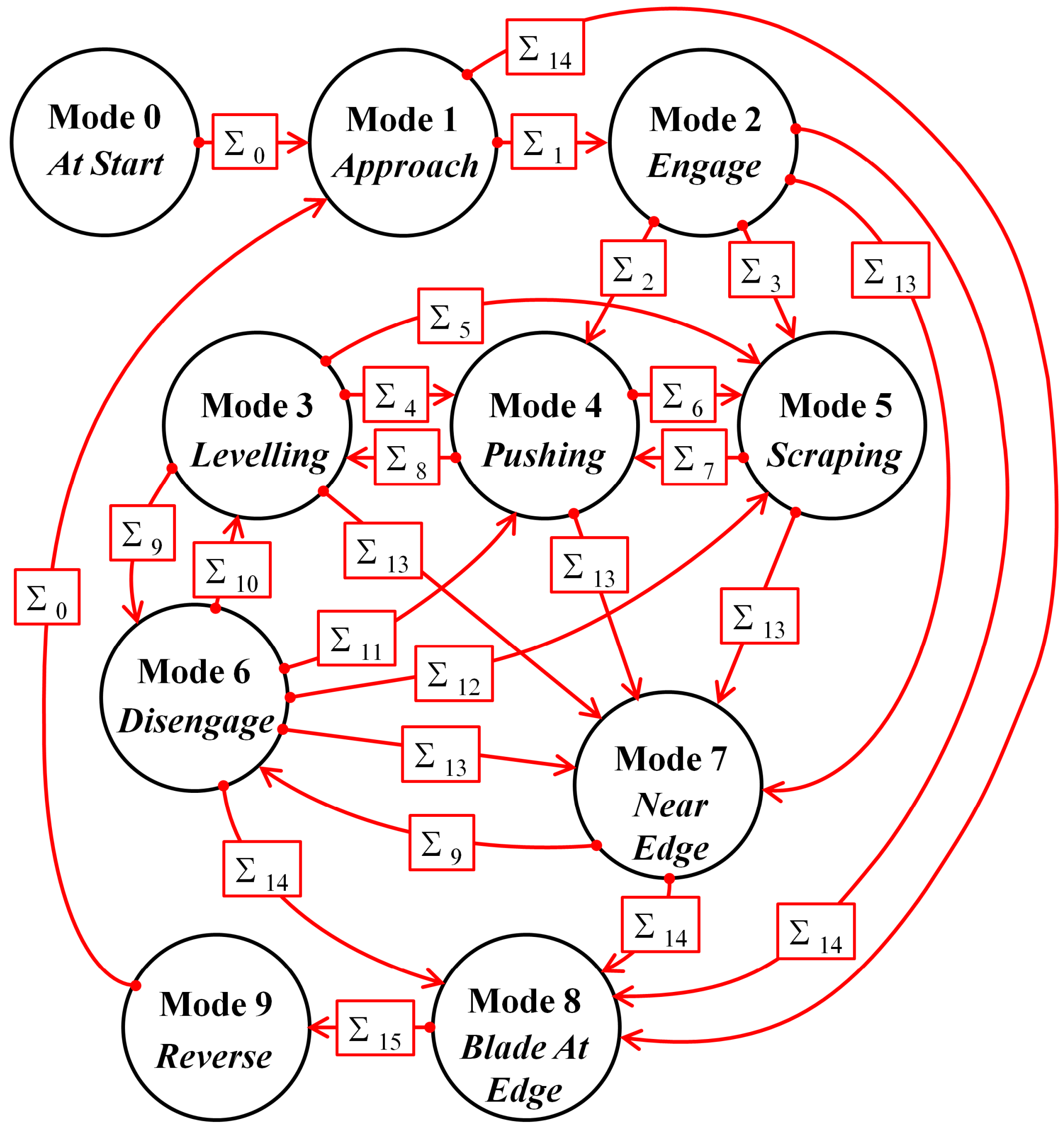

Fig. 3.3 Mode transition diagram.

The set of mode transition conditions, **Σ**, is defined as follows:

$$\Sigma_0 : x_b \leq x_{b,start}$$

$$\Sigma_1 : d_a > 0 \wedge x_b < \left(x_{edge} - \delta_a\right)$$

$$\Sigma_2 : z_b \geq h_{thres1} \wedge h_a \geq h_{thres2} \wedge x_b < \left(x_{edge} - \delta_a\right)$$

$$\Sigma_3 : z_b \geq h_{thres1} \wedge h_a < h_{thres2} \wedge x_b < \left(x_{edge} - \delta_a\right)$$

$$\Sigma_4 : z_b < h_{thres2} \wedge h_a \geq h_{thres2} \wedge d_a \geq 0 \wedge x_b < \left(x_{edge} - \delta_a\right)$$

$$\Sigma_5 : z_b < h_{thres2} \wedge h_a < h_{thres2} \wedge d_a \geq 0 \wedge x_b < \left(x_{edge} - \delta_a\right)$$

$$\Sigma_6 : z_b < h_{thres2} \wedge h_a < h_{thres2} \wedge x_b < \left(x_{edge} - \delta_a\right)$$

$$\Sigma_7 : h_a \geq h_{thres2} \wedge x_b < \left(x_{edge} - \delta_a\right)$$

$$\Sigma_8 : z_b \geq h_{thres2} \wedge x_b < \left(x_{edge} - \delta_a\right)$$

$$\Sigma_9 : d_a < 0$$

$$\Sigma_{10} : d_a \geq 0 \wedge z_b \geq h_{thres2} \wedge x_b < \left(x_{edge} - \delta_a\right)$$

$$\Sigma_{11} : d_a \geq 0 \wedge z_b < h_{thres2} \wedge h_a \geq h_{thres2} \wedge x_b < \left(x_{edge} - \delta_a\right)$$

$$\Sigma_{12} : d_a \geq 0 \wedge z_b < h_{thres2} \wedge h_a < h_{thres2} \wedge x_b < \left(x_{edge} - \delta_a\right)$$

$$\Sigma_{13} : d_a \geq 0 \wedge x_b \geq \left(x_{edge} - \delta_a\right)$$

$$\Sigma_{14} : x_b \geq x_{edge}$$

$$\Sigma_{15} : \dot{x}_b = 0 \wedge p < N_{passes}$$

3.4 Discrete-time Dynamic Prediction Model

For model parameter estimation and control design, the one-step-ahead prediction discrete-time formulations of the d_a, v_b and ϕ differential equations were used. The discrete-time model also allows d_a, v_b and ϕ stochastic disturbances to be included in a straightforward manner. The dynamic Eqns. (3.1), (3.3) and (3.5) were discretized using

Euler's method. The discrete-time equations predicting one-step ahead from the k^{th} sample are then as follows:

$$\hat{d}_{a,k+1} = d_{a,k} + T_s \cdot \left(C_{da1,\Gamma} \cdot d_{a,k} + C_{da2,\Gamma} \cdot h_{a,k} + C_{da3,\Gamma} \cdot h_{b,k} + C_{da4,\Gamma} \cdot h_{\delta r,k} + C_{da5,\Gamma} \cdot \zeta_k \right) \cdot v_{b,k} + \hat{w}_{d,k} \quad (3.14)$$

$$\hat{v}_{b,k+1} = \left(1 - \frac{T_s}{C_{vb1,\Gamma}} \right) \cdot v_{b,k} + T_s \cdot \left(\frac{C_{vb2}}{C_{vb1}} \cdot u_{t,nom} - C_{vb3,\Gamma} \cdot d_{a,k} + C_{vb4,\Gamma} \cdot \zeta_k \right) + \hat{w}_{v,k} \text{ and} \quad (3.15)$$

$$\hat{\phi}_{k+1} = T_s \cdot \left(C_{\phi 1,\Gamma} \cdot d_{a,k} + C_{\phi 2,\Gamma} \cdot \zeta_k + C_{\phi 3,\Gamma} \cdot h_{c,k} + C_{\phi 4,\Gamma} \cdot h_{b,k} \right) \cdot v_{b,k} + \hat{w}_{\phi,k} \quad (3.16)$$

where T_s is the sampling period. $d_{a,k}$ is the measured material accumulation, $v_{b,k}$ is the measured blade velocity in the X-direction, ϕ_k is measured robot pitch, ζ_k is the blade position, $\hat{w}_{d,k}$ is the expected value of the material accumulation disturbance, $\hat{w}_{v,k}$ is the expected value of the robot velocity disturbance, $\hat{w}_{\phi,k}$ is the expected value of the robot pitch disturbance.

Regarding the remaining dynamic equations, Eq. (3.2) simply represents an intermediate state variable which was not used explicitly, thus it was not included in the set of discrete-time equations. With subsequent system identification in Chapter 5 and control design in Chapter 7, discretization of Eq. (3.4) will be addressed

3.5 Conclusions

The development of a nonlinear hybrid dynamic model of robotic bulldozing was presented. The model consists of a set of nine equations (three of which are nonlinear differential equations), 10 discrete operation modes and 16 mode transition conditions. The next chapter describes the experimental reduced-scale robotic bulldozing system that was used for system identification involving model parameter estimation, validation and sensitivity analysis.

Chapter 4

Experimental System

4.1 Introduction

This chapter describes a novel reduced-scale integrated experimental system developed for experimental validation of the theoretical hybrid dynamics, system identification and control implementation.

Due to the many impracticalities involved in full scale experiments (*e.g.* machine cost, setup time, safety, etc.), an integrated experimental system has been developed including an instrumented scaled-down robot bulldozer, a 0.5 m wide by 2 m long environment containing loose material for the robot to push, a vision-based robot localization system, and a vision-based laser scanning system for measuring the height profile of the loose material before and after each dozing pass. The bulldozer and its environment have been designed empirically to emulate the behavior of the full scale process.

The emulated bulldozing task objective was to maximize the material removal rate (MRR) with dynamic blade position control. This entails design of the bulldozer and environment such that the optimal MRR cannot be obtained by simply fixing the blade position at any point. Furthermore, the emulated bulldozer and environment were designed to constrain the process to the three DOF that characterize the primary low-level dynamic behavior. An aspect of the reduced-scale system which was very difficult to emulate is the effect of the robot weight with respect to the properties of the underlying material. The weight of the full scale machine influences traction properties and may cause significant compression of the underlying material. The weight of the reduced-scale bulldozer has less influence on traction and is insufficient to compress the underlying material.

A diagram of the overall experimental environment is shown in Fig. 4.1 and photographs are given in Fig. 4.2 and Fig. 4.3. All of the hardware is interfaced to a PC-based data acquisition and control system. The dozing material is composed of loose stones with an average size of 5 mm within a range of 4 mm to 10 mm.

The experimental setup included two computers, denoted PC1 and PC2, that were linked via serial communication with a 115200 Baud rate. PC1 executed the real-time robot control loop, reading sensor measurements and sending actuator control signals. PC1 also executed the laser mounted stepper motor control loop to synchronize the laser scanning camera with the movement of the laser stripe. The code executed on PC1 was implemented in C language with National Instruments LabWindows. PC2 interfaced with the two cameras and executed the image processing. For robot localization, PC2 calculated the robot heading and X-Y coordinates in units of mm. For material profile scanning, PC2 calculated the material profile height in units of mm. The code executed on PC2 was implemented in C language with Microsoft Visual Studio.

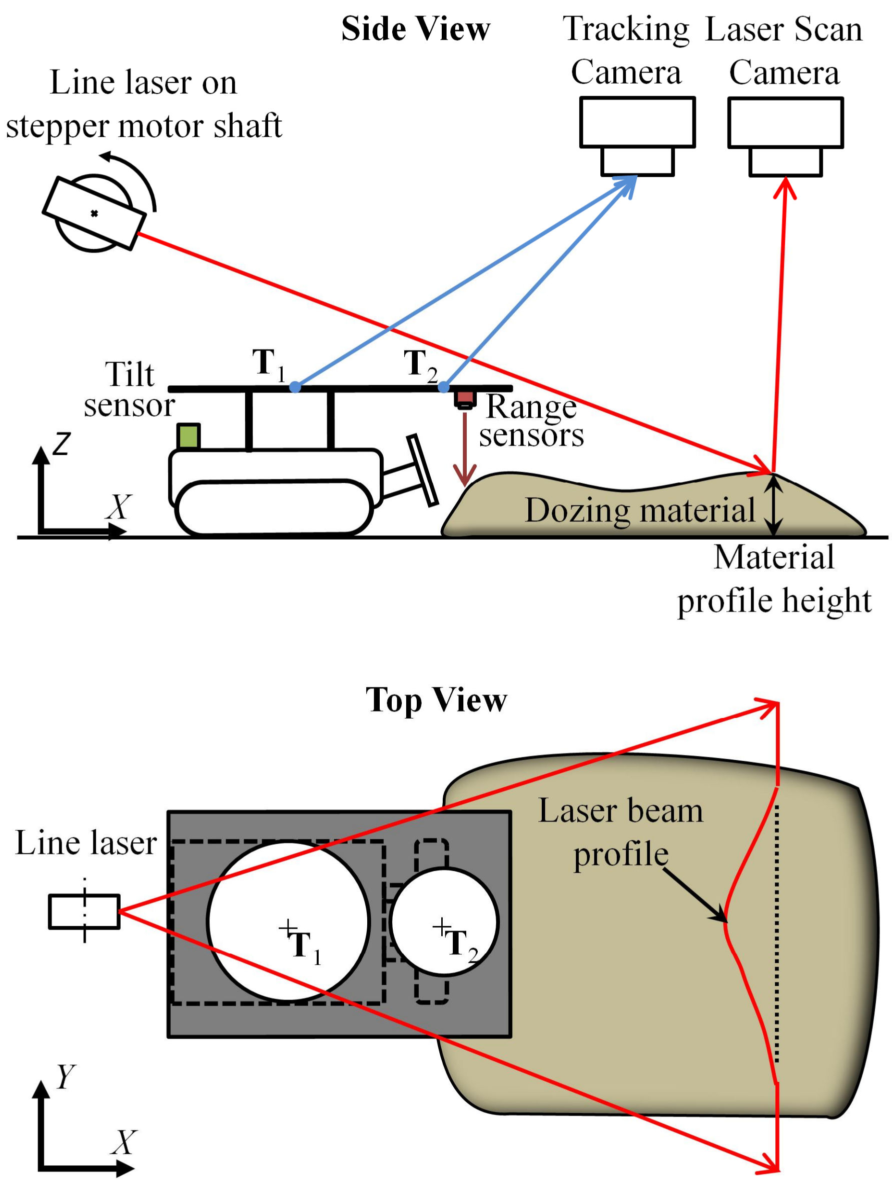

Fig. 4.1 Diagram of the experimental robot and environment.

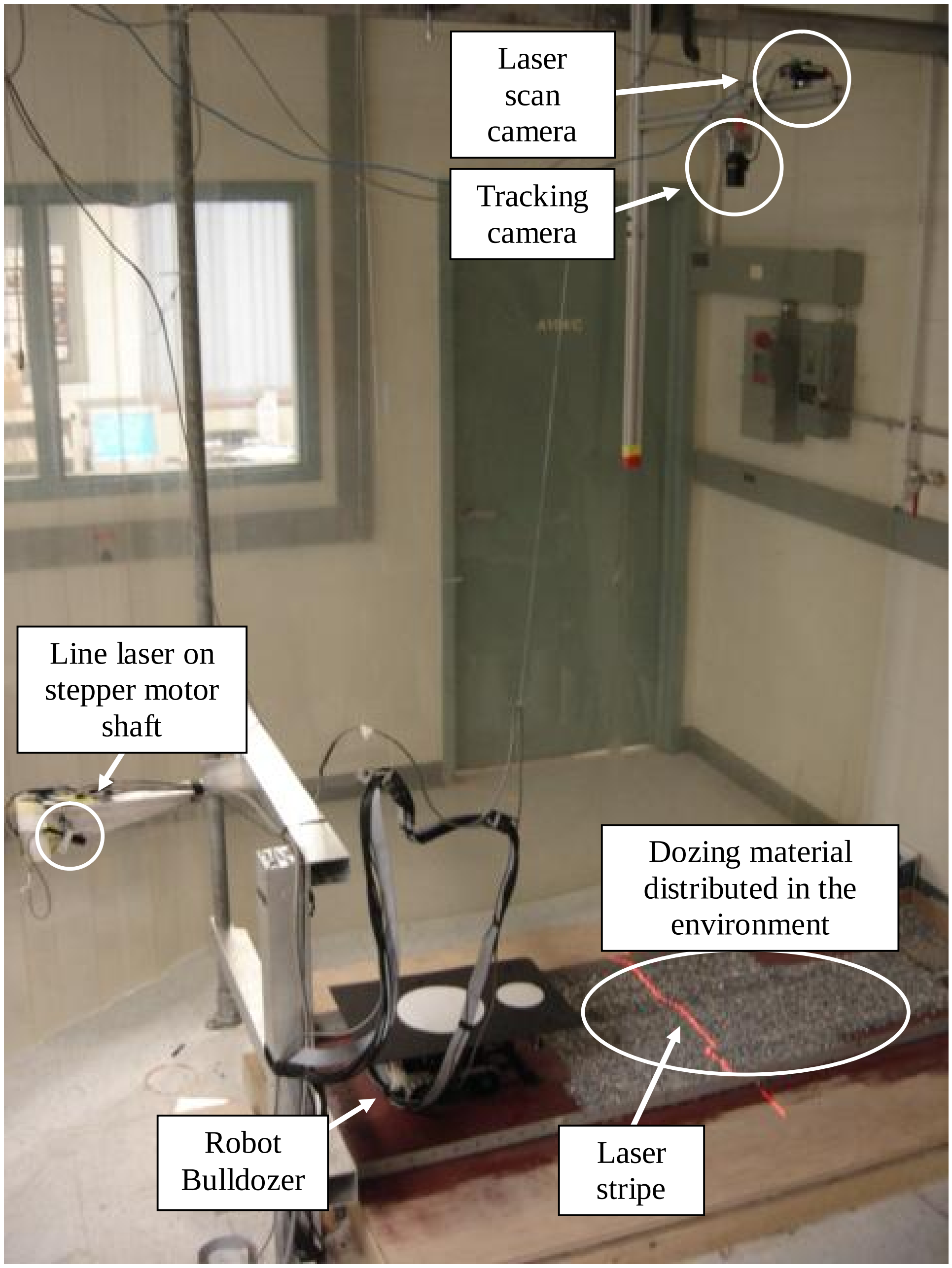

Fig. 4.2 Photograph of the robot and experimental environment.

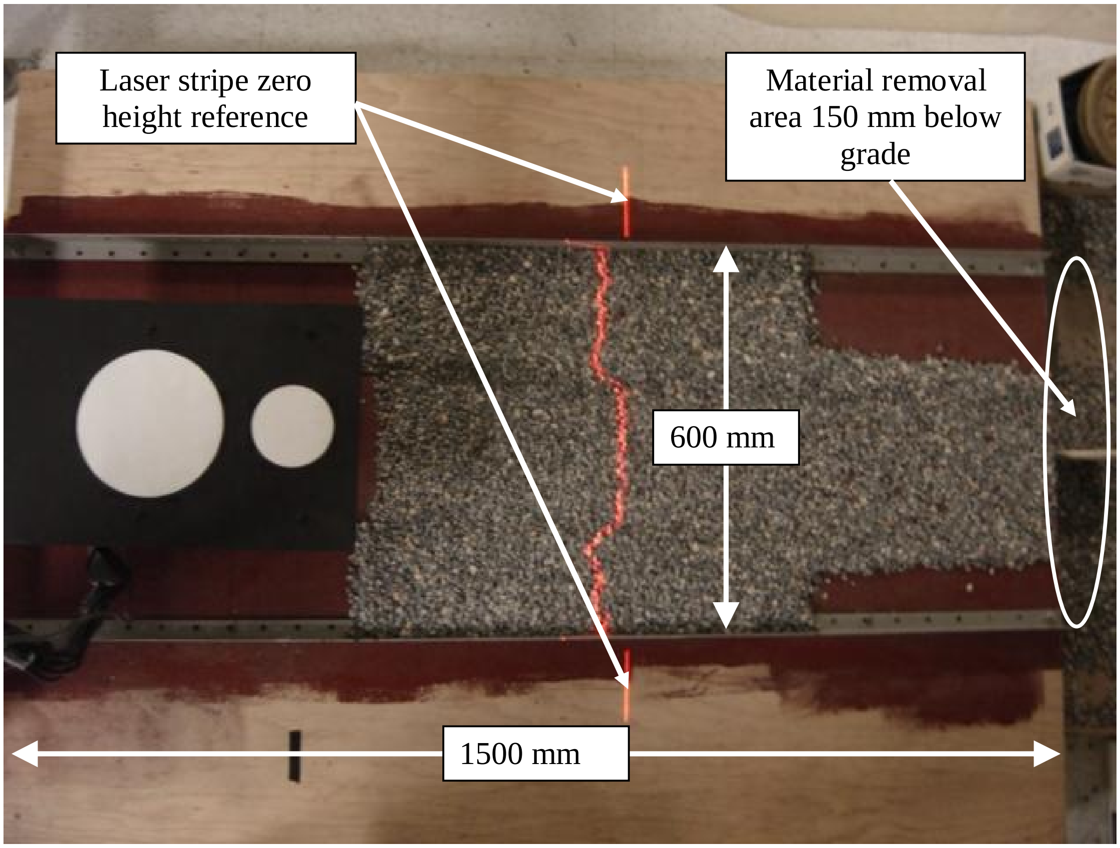

Fig. 4.3 Top view photograph of the experimental environment.

4.2 Reduced-Scale Instrumented Robot Bulldozer

The instrumented robot is shown in Fig. 4.4. Each robot track is driven by a DC gearmotor. The blade actuator mechanism is composed of a leadscrew driven by a DC motor with an integrated encoder providing feedback for closed-loop position control at a 1 kHz sampling rate. A simple sliding-mode algorithm is used for the position control. The blade motor encoder measurement is calibrated to measure the blade position, ζ, in units of mm. A line of five range sensors (Baumer FADK 14I4470/S14) is located above and slightly ahead of the blade edge to measure the height of material accumulated on the blade as material is being pushed. The range sensor measurements are calibrated to measure the height of material beneath them with respect to the plane of the tracks. The calibrated outputs are averaged to measure d_a in units of mm. For this robotic bulldozer the maximum height of material accumulation on the blade is $d_{a,max}$ = 55 mm. A tilt sensor (Crossbow CXTA02) measures the pitch angle, ϕ, in units of degrees. A differential steering proportional-integral (PI) heading controller is used to maintain forward motion along a straight path with a constant heading. In response to heading error, the controller decreases the input to one track and increases the input to the other track by the same amount until the heading error diminishes to zero. The maximum velocity of this robotic bulldozer is $v_{b,max}$ = 92 mm/s.

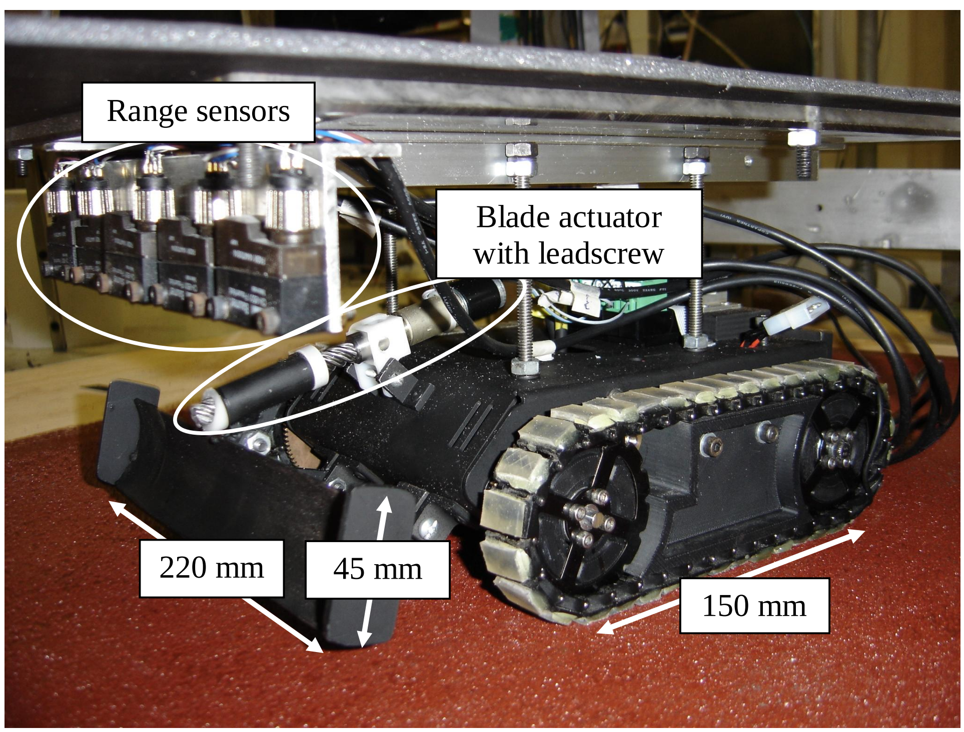

Fig. 4.4 Instrumented reduced-scale robot bulldozer.

4.3 Robot Localization System

The vision-based robot localization system tracks two target circles, of different sizes, fixed to the top of the robot. A large circle is positioned above the centre of the robot chassis and a small circle is positioned above the blade edge. The circles are detected in an image of the environment taken by the 1st overhead camera (see Fig. 4.2). The position coordinates of the circle centers are used to calculate the position and heading angle of the robot. The measured positions are used to calculate x_a, x_b and x_c. The robot velocity, v_b, is estimated by backwards differencing the position data in units of mm/s. The sampling rate is 16 Hz.

4.4 Material Profile Laser Scanning System

The laser scanning system consists of a line laser, stepper motor and 2nd overhead camera. The system estimates the height of the profile of material from the reflected laser light using the triangulation method to give h_a, h_b, h_c, $h_{r,l}$ and $h_{r,r}$ in units of mm. The beam is advanced along the X-direction of the environment by a stepper motor that is synchronized with the camera. An example of material profile data from a scan is shown in Fig. 4.5

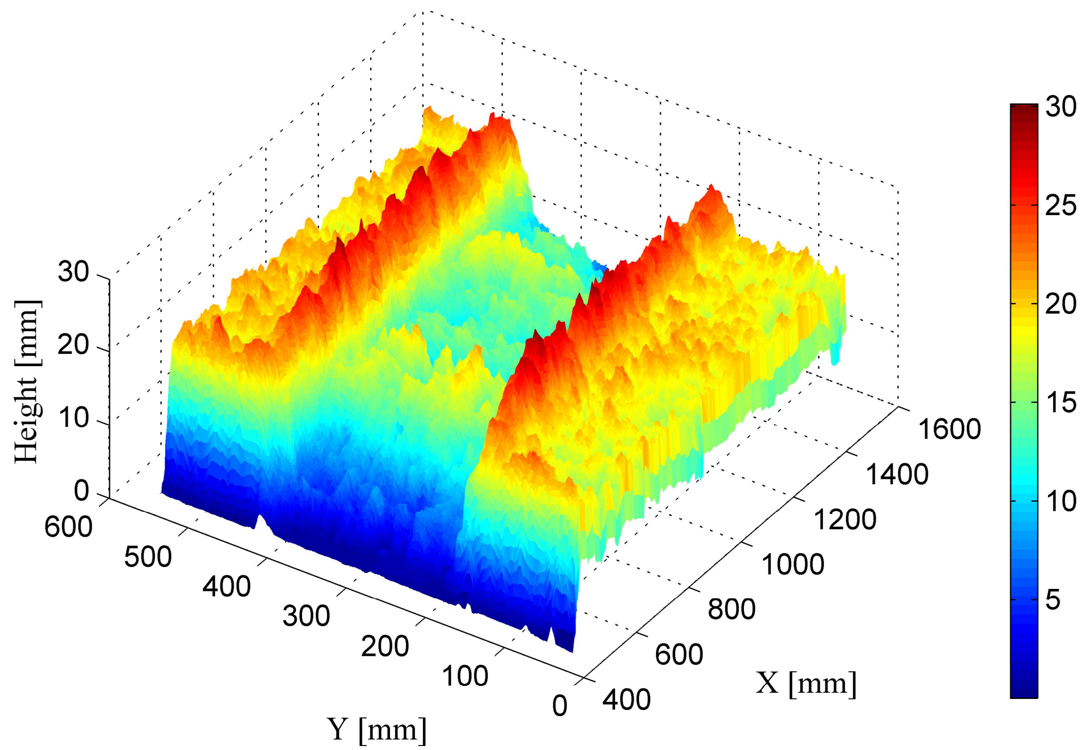

Fig. 4.5 Example result of a material profile scan.

4.5 Conclusions

An instrumented reduced-scale robotic bulldozer system and environment were developed for experimental investigation of process modeling and autonomous control. Further details of the experimental robotic bulldozing system may be found in Appendix A. The next chapter describes the experimental methodology and results of system identification involving model parameter estimation, validation and sensitivity analysis.

Chapter 5

System Identification

5.1 Introduction

This chapter presents an experimental system identification methodology which includes an iterative procedure of model parameter estimation based on a sensitivity analysis to refine and validate the model proposed in Chapter 3. The robotic bulldozing system described in Chapter 4 was used to gather the data.

5.2 Experiments

A series of multiple pass experiments were performed to obtain the data needed for model fitting and validation. Recall from Chapter 3 that a completed pass is defined as the robot beginning in mode 0, transitioning through a series of modes and ending in mode 8. Since open-loop control was unable to reliably maintain blade contact with the material without the robot becoming stuck during a pass (*i.e.* the robot velocity decreases to zero and stays indefinitely), a closed-loop control algorithm had to be created. This algorithm attempts to simultaneously maintain forward motion of the robot while keeping material on its blade. It employs a form of switching control whereby the blade position is increased incrementally by an amount Δr_b when the robot speed falls below a specified threshold, $v_{b,thres}$, and the blade position is decreased incrementally by an amount Δr_b when the material accumulation on the blade falls below a specified threshold, $d_{a,thres}$. A time delay is introduced after blade control is initiated. Delay-off timers T1 and T2 with different delay periods are used depending on the direction of blade motion. These time delays are introduced after blade control is initiated to provide the hysteresis needed to avoid excessive aggressive blade motion due to measurement noise. The rule-based blade control algorithm is defined in Table 5.1.

Table 5.1 Rule-based blade control algorithm.

WHILE $x_b < x_{edge}$
    IF $\left(d_a < d_{a,thresh}\right) \wedge \left(v_b \geq v_{b,thres}\right) \wedge \left(\neg \mathrm{T1}\right)$
        $r_b = r_b - \Delta r_b$
        ENABLE T1
    ENDIF
    IF $\left(v_b < v_{b,thres}\right) \wedge \left(\neg \mathrm{T2}\right)$
        $r_b = r_b + \Delta r_b$
        ENABLE T2
    ENDIF
ENDWHILE

Delay-off periods of 0.1 s and 0.5 s were found experimentally to be suitable for T1 and T2, respectively. The manually tuned rule-based controller parameters were: $d_{a,thres}$ = 35 mm, $v_{b,thres}$ = 50 mm/s and Δr_b = 1 mm. All of the experiments were performed using this control algorithm with a control sampling rate of 16 Hz. The d_a , v_b and ϕ signal measurements were digitally filtered online with a 2^{nd} order Butterworth low-pass filter with a 1 Hz cutoff.

The initial material coverage conditions were intended to make modes 1 - 5 and 7 active over multiple bulldozing passes. This was done since models of modes 2 - 5 and 7 are necessary for development of model-based control. The importance of modeling mode 1 is explained in Section 5.3. Note that multiple passes are realistic for full scale bulldozing, and produce greater process variation than possible with a single pass, as will be shown later in this section. Another factor in the design of the initial coverage was to inhibit any tendency of the robot to roll and to limit pitch to less than $\pm 10^{o}$. Thus the initial distribution was flat and level laterally (*i.e.* constant height along the Y-direction), and restricted in height so that relatively steep slopes did not develop. Indeed, if the pitch is large enough the bulldozer could possibly slide backwards which would violate Eq. (3.13).

Each set of multiple passes will be termed a *trial*. The trials consisted of initially setting up the material in a structured pile. Simple pile structures were used so that the initial conditions of each trial could be made consistent. The robot blade location, x_b, was located 0.2 m away from the leading edge of the pile, x_p, at the start of each pass. Two versions of initial material pile structure were used: (a) uniform nominal height of 20 mm and length of 1.1 m, covering to the edge of the environment; and (b) uniform nominal height of 20 mm and length of 0.7 m, with no material covering the remaining 0.4 m of the environment. The second version was used to introduce greater variation in the overall process to induce a wider range of dynamic behavior. For each initial pile structure, the robot performed multiple passes through the material to complete each trial. Before and after each pass the material height profile was measured with the laser scanning system. Even if the initial height profile was relatively flat, each bulldozing pass produces significant height variations due to the nondeterministic nature of the process. An example of the average material profile height along the robot path prior to the first bulldozing pass, after two passes and after four passes is shown in Fig. 5.1. The graphs show that while the initial height profile stays close to 20 mm, after two passes it varies from 3 to 26 mm. After four passes the lack of material remaining on the floor caused a reduction in the height variation.

The experimental data sets include eight trials of four passes with the *initial full*

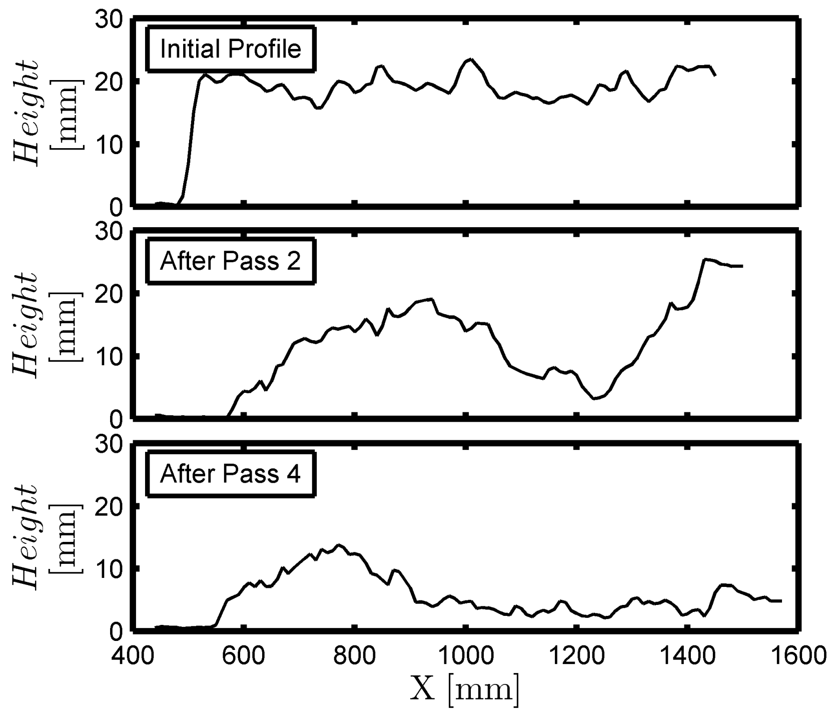

Fig. 5.1 Example of the average material profile height along the robot path after zero, two and four passes.

coverage condition (material pile structure (a)) and eight trials of four passes with the *initial partial coverage condition* (material pile structure (b)). Different modes and sequences of modes became active in each pass due to the natural variation of the process. Each trial was stopped after four passes since the remaining material was insufficient to excite the dynamics of the chosen modes.

The experimental data was divided into two sets. One was used for model fitting and the other for model validation. The model fitting data was composed of six trials with the initial full coverage condition and six trials with the initial partial coverage condition. The model validation data was composed of two trials with the initial full coverage condition and two trials with the initial partial coverage condition.

5.3 Model Fitting and Validation

5.3.1 Mode Transition Parameter Determination

The set of mode transitions, $\mathbf{\Sigma}$, requires knowledge of h_{thres1}, h_{thres2} and δ_a. The value of h_{thres1} should be determined by measuring the average height of a single layer of stones (or other fragmented material). A value of h_{thres1} = 5 mm was found for the experimental environment using the laser scanning system. Due to friction between the stones and the floor and the irregular contact interfaces between the stones, the robot blade cannot penetrate a single uniform layer of stones. The value of h_{thres2} should be determined by measuring the average minimum height of several layers of stones, layered such that the robot blade can penetrate downward into at least two layers of stones above the single base layer of stones in contact with the floor. A value of h_{thres2} = 10 mm was measured for the experimental environment. The value of δ_a should be determined using the following procedure. The robot is driven forwards on top of a flat pile of stones of approximate height equal to h_{thres2} with the robot blade at a nominal downward position of $r_b = -\, h_{thres1}$ so that it can penetrate the stones and accumulate material on the blade. Once it is observed that the material accumulation on the blade, d_a, has reached its steady state maximum height the robot should be stopped. The value of δ_a is then found by measuring the distance from the edge of the robot blade to the furthest edge of the mound of material pushed ahead. A value of δ_a = 150 mm was found for our experimental environment.

5.3.2 Elevation Model Parameter Estimation

Before fitting a complete dynamic model of the bulldozing process, it is necessary to estimate the elevations of the robot [z_b z_c] throughout each pass since they are not directly measured. The estimated elevations will be used to identify the mode transitions in Section 5.3.3. The elevation estimation equations can also be used as an on-line observer to determine the mode transitions required for implementation of model-based control.

The robot elevations were estimated from the measurements of d_a, x_b, ϕ, ζ, h_b and h_c. Assuming negligible disturbance of the underlying material profile after the blade has passed, the elevations z_b and z_c are approximately equal to the profile heights measured in the post-pass laser scan at locations x_b and x_c (*i.e.* the material profile along the path of the robot after a pass is an approximate measure of the robot elevation at each location during the pass).

The parameters for each elevation estimation equation are determined by minimizing the sum of the squared errors between the measured profile height and the predicted elevation value over the entire experimental data set. A global sampling-based search algorithm is used to solve the least squared error optimization problem. Details of the search algorithm are described in Perttunen *et al.* (1993). The Matlab code used to implement this search algorithm can be found at Finkel (2004). The parameter estimation optimization problem for each of Eqs. (3.6) and (3.7) is:

$$\boldsymbol{\theta}_z = \arg\min e_{sum,z}\left(\boldsymbol{\theta}_z\right) \tag{5.1}$$

$$\text{subject to } e_{sum,z} = \sum_{i=1}^{N_s^{fit}} \left(z_{est}\left(i\right) - h_{meas}\left(i\right)\right)^2 \tag{5.2}$$

where $\boldsymbol{\theta}_\mathbf{z}$ is the parameter vector, z_{est} is the elevation variable, h_{meas} is the corresponding post-pass measured height, and N_s^{fit} is the number of points in the fitting data set. For Eq. (3.6): $\boldsymbol{\theta}_\mathbf{z}$ = [C_{zc1} C_{zc2}] and $z_{est} = z_c$. For Eq. (3.7): $\boldsymbol{\theta}_\mathbf{z}$ = [C_{zb1} C_{zb3} C_{zb4} C_{zb5}] and $z_{est} = z_b$. Assuming the robot pivots about its centre point, the parameter C_{zb2} represents the distance from the robot centre to the edge of the blade when the blade is in the zero position (*i.e.* from $\mathbf{P_c}$ to $\mathbf{P_b}$ in Fig. 3.1) so it was fixed to the measured value of 177 mm. The root-mean-square errors (RMSE) of the estimated elevations are 2.0 mm and 5.3 mm for z_c, and z_b, respectively. An example of the estimated z_b is shown in Fig. 5.2. The elevation estimation equation parameters are tabulated in Table 5.2.

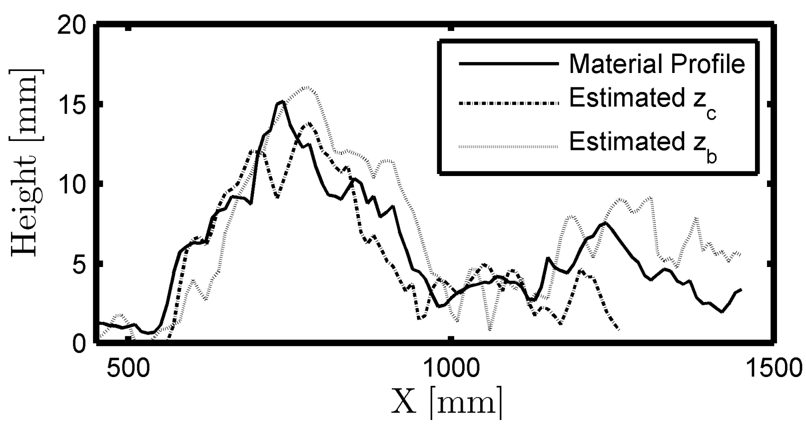

Fig. 5.2 Example of robot elevation estimation.

Table 5.2 Elevation estimation equation parameters.

Parameter					
C_{zc1} [mm/mm]	C_{zc2} [mm/mm]	C_{zb1} [mm/mm]	C_{zb2} [mm]	C_{zb3} [mm/mm]	C_{zb4} [mm/mm]
0.96	-0.11	0.32	177	0.062	-0.37

5.3.3 Hybrid Dynamic Model Parameter Estimation

The experimental fitting data was categorized into segments based on the mode transition criteria (*i.e.* $\mathbf{\Sigma}$ from Chapter 3) so the mode-dependent parameters of the dynamic equations could be estimated. Using this segmented set of experimental fitting data, the parameters of the remaining discretized state equations (*i.e.* Eqs. (3.14), (3.15) and (3.16)) were determined for each mode by minimizing the sum of the squared error between the measured state value and the predicted state value. A one-step-ahead prediction was used with each equation. The same global search algorithm and Matlab code as the previous section was used to solve the least squared error optimization problem.

The parameter estimation optimization problem for each mode segment of the data set is:

$$\boldsymbol{\theta}_x = \arg\min e_{sum,xfit,\Gamma}\left(\boldsymbol{\theta}_x\right) \tag{5.3}$$

$$\text{subject to } e_{sum,xfit,\Gamma} = \sum_{i=1}^{N_{s,\Gamma,total}^{fit}-1}\left(x_{pred}^{fit}\left(i+1\right)-x_{meas}^{fit}\left(i+1\right)\right)^2 \tag{5.4}$$

$$x_{pred}^{fit}\left(i+1\right) = f_{xfit}\left(x_{meas}^{fit}\left(i\right), x_{meas}^{other}\left(i\right)\right) \tag{5.5}$$

where $\boldsymbol{\theta}_{\mathbf{x}}$ is the parameter vector (*e.g.* to fit Eq. (3.14) to mode 5 data, $\boldsymbol{\theta}_{\mathbf{x}}=[C_{da1,5}\ C_{da2,5}\ C_{da3,5}\ C_{da4,5}\ C_{da5,5}]$), i is the sample number, x^{fit} is the state variable to be fit with function $f_{xfit}(\cdot)$, x^{other} are the other state variables in the equation, and $N^{fit}_{s,\Gamma,total}$ is the number of points in the segmented fitting data set per mode Γ. Measurement values are denoted x_{meas} and predicted values are denoted x_{pred}. The parameters of modes 1 - 5 and 7 were estimated. The total number of samples per mode within the model fitting data set and the model validation data set are given in Table 5.3.

Table 5.3 Total number of samples per mode within the experimental data set.

	Mode Number, Γ					
	1	2	3	4	5	7
Samples, model fitting set	3150	1533	2774	1255	2075	1465
Samples, model validation set	1625	712	1097	645	1244	693

Note that some of the parameters required special treatment. In mode 1, the robot is simply driving forward on the flat clean floor surface so the only significant parameters of all the dynamic equations are $C_{vb1,1}$ and $C_{vb2,1}$ which represent the robot velocity time constant and steady state gain. All other parameters were set to zero in mode 1. For the remaining modes the parameters C_{vb1} and C_{vb2} were fixed to equal $C_{vb1,1}$ and $C_{vb2,1}$. In modes 2, 4 and 5 the robot blade position is constrained by the hard floor surface, thus for any $\zeta \leq 0$ material will accumulate on the blade. Therefore, for these modes parameter C_{da5} was set to zero. In mode 7, the height of material ahead, h_a, is undefined since the removal space is significantly below grade so parameter $C_{da2,7}$ was set to zero.

A total of 52 parameters were estimated. The total elapsed time to estimate the model parameters was 403 seconds running on an Intel T7100 1.80 GHz processor with 2 GB RAM. Note that since τ_d and τ_r are much smaller than the sampling period of $\frac{1}{16}$ s they were not included.

5.3.4 Dynamic Model Validation

The model was validated with the data from the four trials of the validation data (*i.e.* 16 passes). The mode transitions were determined as in model fitting. The relative model fit was calculated for each state and mode as follows:

$$\%fit_{x,\Gamma,seg} = 100 \cdot \left(1 - \frac{\sqrt{\sum_{i=1}^{N_{s,\Gamma,seg}^{val} - N_p^{val}} \left(x_{pred}\left(i + N_p^{val}\right) - x_{meas}\left(i + N_p^{val}\right)\right)^2}}{\sqrt{\sum_{i=1}^{N_{s,\Gamma,seg}^{val} - N_p^{val}} \left(x_{meas}\left(i + N_p^{val}\right) - \bar{x}_{meas,\Gamma,seg}\right)^2}} \right) \text{ and} \tag{5.6}$$

$$\%fit_{x,\Gamma} = \frac{\sum_{j=1}^{N_{seg,\Gamma}^{val}} N_{s,\Gamma,j}^{val} \cdot \%fit_{x,\Gamma,j}}{N_{s,\Gamma,total}^{val}} \tag{5.7}$$

where x_{pred} is the N_p^{val}-steps-ahead predicted state, x_{meas} is the state measurement, $N_{s,\Gamma,total}^{val}$ is the total number of mode-segmented samples in the validation data, $N_{s,\Gamma,seg}^{val}$ is the total number of samples within a particular mode segment of the validation data, $\bar{x}_{meas,\Gamma,seg}$ is the mean of the state measurements within a particular mode segment of the validation data, and $N_{seg,\Gamma}^{val}$ is the number of mode segments within the validation data.

The relative fit was calculated with the validation set for each of the mode dynamics. The relative fit averaged over modes 2 - 5 and 7 is listed in Table 5.4. After the system identification procedure generated a set of estimated parameters a global sensitivity analysis was used to refine the model. In addition to the parameters known to be zero, the sensitivity analysis showed that other parameters contributed negligibly to the dynamics. These parameters were removed and the system identification procedure was repeated. The validation and sensitivity analysis was also repeated to confirm that these parameters could be removed without significantly affecting the model fit. The sensitivity analysis is described in the next section.

Table 5.4 Model validation relative fit over different prediction horizons for modes 2-5 and 7.

Mode, Γ	State	Relative Fit (%)		
		$N_{p,val} = 1$	$N_{p,val} = 2$	$N_{p,val} = 3$
2	d_a	85.1	70.3	56.1
	v_b	73.0	49.9	31.0
	ϕ	86.5	75.1	66.0
3	d_a	90.3	81.2	72.7
	v_b	76.6	57.5	42.9
	ϕ	80.3	63.8	51.2
4	d_a	92.4	85.5	79.4
	v_b	76.2	56.1	40.3
	ϕ	65.3	36.3	15.0
5	d_a	88.9	78.6	69.3
	v_b	74.6	53.5	37.2
	ϕ	71.1	46.8	28.5
7	d_a	77.0	58.5	43.3
	v_b	73.0	50.5	33.3
	ϕ	63.2	32.7	10.5
Average	d_a	86.8	74.8	64.2
	v_b	74.7	53.5	37.0
	ϕ	73.3	50.9	34.2

5.4 Sensitivity Analysis

In general, global sensitivity analysis (GSA) methods evaluate the effect of a parameter while all other parameters are varied simultaneously. A sensitivity index is a number that gives quantitative information about the relative sensitivity of the model to the selected parameters. The Sobol GSA method is a variance-based sensitivity analysis approach presented in Sobol (2001). This method is based on the decomposition of the variance of the model output function $f(\boldsymbol{\theta}) = f(\theta_1, \theta_2, \ldots, \theta_{N_\theta})$ with parameter vector $\boldsymbol{\theta}$ into summands of variances in combinations of input parameters in increasing dimensionality as follows:

$$f(\boldsymbol{\theta}) = f_0 + \sum_{i=1}^{N_\theta} f_i(\theta_i) + \sum_{i=1}^{N_\theta} \sum_{j=i+1}^{N_\theta} f_{ij}(\theta_j, \theta_k) + \cdots + f_{12\ldots N_\theta}(\theta_1, \theta_2, \ldots, \theta_{N_\theta}) \tag{5.8}$$

Where $\boldsymbol{\theta}$ is the parameter set and N_θ is the number of parameters.

For any subset of parameters $\theta_{i_1}, \theta_{i_2}, \ldots, \theta_{i_s}$ with indices $1 \le i_1 < \ldots < i_s \le N_\theta$, the total variance, D, is defined as:

$$D = \sum_{s=1}^{N_\theta} \sum_{i_1 < \ldots < i_s}^{N_\theta} D_{i_1 \ldots i_s} \tag{5.9}$$

Where the partial variances, $D_{i_1 i_2 \ldots i_s}$, are:

$$D_{i_1 i_2 \ldots i_s} = \int_0^1 f_{i_1 i_2 \ldots i_s}^2 (\theta_{i_1}, \theta_{i_2}, \ldots, \theta_{i_s}) \mathrm{d}\theta_{i_1}, \mathrm{d}\theta_{i_2}, \ldots, \mathrm{d}\theta_{i_s} \tag{5.10}$$

The Sobol sensitivity indices, $S_{i_1 i_2 \ldots i_s}$, are calculated by:

$$S_{i_1 i_2 \ldots i_s} = \frac{D_{i_1 i_2 \ldots i_s}}{D} \tag{5.11}$$

Where $S_{i_1 i_2 \ldots i_s}$ gives the fraction of the total variance which is apportioned to the individual model parameters or combination of them. For example, $S_i = D_i / D$ quantifies the contribution of the parameter θ_i to the output variance. It can be shown that all $S_{i_1 i_2 \ldots i_s}$ are nonnegative and add up to one as follows:

$$\sum S_{i_1,i_2,\ldots,i_s} = \sum_{i=1}^{N_\theta} S_j + \sum \sum_{1 \le i < j \le N_\theta} S_{ij} + S_{1,2,\ldots,N_\theta} = 1 \tag{5.12}$$

An extension of the Sobol sensitivity indices proposed by Homma and Saltelli (1996) is the total effect sensitivity index to measure the mutual interactions of parameters. The total effect index with respect to parameter θ_j is defined as:

$$S_j^T = 1 - \sum_{i_k \ne j} S_{i_1,i_2,\ldots,i_s} \tag{5.13}$$

Where the summation is taken over all the different groups of indices that do not include *j*. The total effect sensitivity index quantifies the overall effects of a parameter, in combination with other parameters on the model output.

An extension for a time-varying function $f(\mathbf{x},t)$, involves computing the sensitivity indices at each measurement or sample time point, then calculating the average of all of the $S_i^T(t)$ over the simulated trajectory for each parameter as follows:

$$\overline{S}_i^T = \frac{1}{N_t} \sum_{k=1}^{N_t} S_{ij}(t_k) \tag{5.14}$$

Where N_t is the number of samples in the simulated trajectory.

The Sobol GSA method was used to confirm the significance of the parameters in the dynamic model. The Matlab toolbox used to calculate the Sobol sensitivity indices is described in Rodriguez (2010).

The sensitivity analysis was completed for the d_a, v_b and ϕ state dynamic equations. For each state equation a set of mean total effect sensitivity indices, $\bar{S}^{T}_{\theta_{i,\Gamma}}$, were calculated for parameter $\theta_{i,\Gamma}$ and mode Γ over a simulated trajectory of the dynamics with sample time increments equal to the experimental sample period T_s = 0.0625 s. The parameter C_{vb2} was not included in the sensitivity analysis because it is a fundamental property of the robot velocity dynamics (*i.e.* the steady state gain) with negligible uncertainty. Each mode was simulated with its corresponding set of equation parameters independent of the other modes (*i.e.* no switching between modes throughout a simulated trajectory). Each simulated trajectory terminated at 14 seconds. Piece-wise constant values for the blade position input and auxiliary variables, r_b, h_b, h_a and h_r, were changed at times t_{rb}, t_{hb}, t_{ha} and t_{hr}, respectively. The simulated trajectory blade position inputs and auxiliary variables for each mode are tabulated in Table 5.5. The same initial conditions d_a = 0 mm, v_b = 92 mm/s and ϕ = 0 degrees were used for the simulation of all mode trajectories.

Table 5.5a Simulated trajectory blade position inputs and auxiliary variables for mode 2.

Mode, Γ	t_{rb} (s)	r_b (mm)	t_{ha} (s)	h_a (mm)	t_{hb} (s)	h_b (mm)	t_{hr} (s)	h_r (mm)
2	0	0	0	10	0	0	0	5
	2	-5	3	5	1	5	1	6
	4	5	4	15	3	15	2	30
	6	-10	5	5	5	10	4	11
	8	0	9	15	7	5	5	15
	10	-15	10	5	9	15	7	20
	12	10	12	10	11	10	10	11

Table 5.5b Continuation of the simulated trajectory blade position inputs and auxiliary variables for mode 3.

Mode, Γ	t_{rb} (s)	r_b (mm)	t_{ha} (s)	h_a (mm)	t_{hb} (s)	h_b (mm)	t_{hr} (s)	h_r (mm)
3	0	0	0	15	0	10	0	15
	2	-5	3	10	1	15	1	16
	4	5	4	20	3	10	2	25
	6	-10	5	10	5	15	4	16
	8	0	9	20	7	20	5	30
	10	-15	10	15	9	10	7	15
	12	10	12	10	11	15	10	11

Table 5.5c Continuation of the simulated trajectory blade position inputs and auxiliary variables for mode 4.

Mode, Γ	t_{rb} (s)	r_b (mm)	t_{ha} (s)	h_a (mm)	t_{hb} (s)	h_b (mm)	t_{hr} (s)	h_r (mm)
4	0	0	0	20	0	5	0	15
	2	-5	3	15	1	7	1	8
	4	5	4	25	3	5	2	30
	6	-10	5	10	5	10	4	25
	8	0	9	25	7	25	5	10
	10	-15	10	15	9	15	7	6
	12	10	12	10	11	10	10	25

Table 5.5d Continuation of the simulated trajectory blade position inputs and auxiliary variables for mode 5.

Mode, Γ	t_{rb} (s)	r_b (mm)	t_{ha} (s)	h_a (mm)	t_{hb} (s)	h_b (mm)	t_{hr} (s)	h_r (mm)
5	0	0	0	5	0	55	0	15
	2	-5	3	10	1	7	1	22
	4	5	4	7	3	10	2	35
	6	-10	5	10	5	7	4	17
	8	0	9	5	7	10	5	15
	10	-15	10	5	9	5	7	5
	12	10	12	10	11	7	10	12

Table 5.5e Continuation of the simulated trajectory blade position inputs and auxiliary variables for mode 7.

Mode, Γ	t_{rb} (s)	r_b (mm)	t_{ha} (s)	h_a (mm)	t_{hb} (s)	h_b (mm)	t_{hr} (s)	h_r (mm)
7	0	0	0	0	0	10	0	15
	2	-5	3	0	1	5	1	6
	4	5	4	0	3	10	2	25
	6	-10	5	0	5	15	4	16
	8	0	9	0	7	20	5	30
	10	-15	10	0	9	5	7	10
	12	10	12	0	11	15	10	16

After the first iteration of system identification, if the sensitivity of a parameter was less than 0.01 and the estimated value of that parameter was small relative to those of the other modes, that parameter was set to zero in the second iteration of system identification.

The parameters found after the second iteration of system identification are tabulated in Table 5.6. The results of the sensitivity analysis after the second iteration of system identification are tabulated in Table 5.7.

Table 5.6a Hybrid dynamic model estimated parameters of the d_a and v_b dynamic equations for modes 2-5 and 7.

	Parameter								
Mode, Γ	C_{da1} (mm^{-1}) x10^{-3}	C_{da2} (mm^{-1}) x10^{-3}	C_{da3} (mm^{-1}) x10^{-3}	C_{da4} (mm^{-1}) x10^{-3}	C_{da5} (mm^{-1})	C_{vb1} (s)	C_{vb2} (mm·s^{-1})	C_{vb3} (s^{-2})	C_{vb4} (s^{-2})
2	-4.2	8.9	5.7	-6.8	*	0.92	2.3	-1.4	5.6
3	**	5.1	-7.5	**	-0.013	0.92	2.3	-1.1	1.7
4	-5.4	**	1.6	12	*	0.92	2.3	-1.8	2.6
5	-1.9	5.1	3.1	2.1	*	0.92	2.3	-1.0	3.6
7	**	*	-17.6	3.2	**	0.92	2.3	-0.9	4.0

* Removed based on known system conditions

** Removed based on sensitivity analysis

Table 5.6b Continuation of the hybrid dynamic model estimated parameters of the ϕ dynamic equation for modes 2-5 and 7.

Mode, Γ	Parameter $C_{\phi 1}$ (°/mm) x10^{-4}	$C_{\phi 2}$ (°/mm) x10^{-4}	$C_{\phi 3}$ (°/mm) x10^{-4}	$C_{\phi 4}$ (°/mm) x10^{-4}
2	**	-41	18	**
3	3.1	18	-9.0	2.7
4	4.5	-7.6	5.3	14
5	2.4	-6.1	-9.4	-2.0
7	1.4	2.3	3.4	4.4

* Removed based on known system conditions

** Removed based on sensitivity analysis

Table 5.7a Sensitivity analysis results for the estimated parameters of the d_a and v_b dynamic equations for modes 2-5 and 7.

Mode, Γ	Sensitivity Index S_{Cda1}	S_{Cda2}	S_{Cda3}	S_{Cda4}	S_{Cda5}	S_{Cvb1}	S_{Cvb3}	S_{Cvb4}
2	0.14	0.49	0.17	0.2	N/A	0.47	0.15	0.38
3	< 0.01	0.32	0.54	< 0.01	0.13	0.41	0.22	0.37
4	0.52	< 0.01	0.12	0.36	N/A	0.54	0.3	0.16
5	0.38	0.3	0.12	0.2	N/A	0.52	0.34	0.14
7	< 0.01	N/A	0.93	0.07	< 0.01	0.23	0.57	0.2

Table 5.7b Continuation of the Sensitivity analysis results for the estimated parameters of the ϕ dynamic equation for modes 2-5 and 7.

Mode, Γ	Sensitivity Index			
	$S_{C\phi 1}$	$S_{C\phi 2}$	$S_{C\phi 3}$	$S_{C\phi 4}$
2	< 0.01	0.07	0.93	< 0.01
3	0.03	0.17	0.7	0.1
4	0.51	0.03	0.06	0.4
5	0.11	0.12	0.29	0.48
7	0.5	0.01	0.2	0.29

From the first iteration of system identification and subsequent sensitivity analysis, the parameters $C_{da1,3}$, $C_{da2,4}$, $C_{da4,3}$, $C_{da5,7}$ were determined to provide negligible contribution to the material accumulation dynamics. Also, the parameters $C_{\phi 1,2}$, $C_{\phi 4,2}$ were shown to provide negligible contribution to the robot pitch dynamics. The model validation relative fit calculated for the second iteration refined model was nearly identical to the fit of the first iteration model (less than 1% change in the relative fit values), confirming the validity of removing the selected parameters.

A simulation of the deterministic d_a, v_b and ϕ dynamics with the refined set of parameters and the full set of parameters is shown in Fig. 5.3 for different modes, different values of r_b and material profile heights, where $h_{r,l} = h_{r,r} = h_r$. These simulation results confirm the expected dynamic behavior discussed in Chapter 3. The simulation results also further reinforce the validity of the refined model.

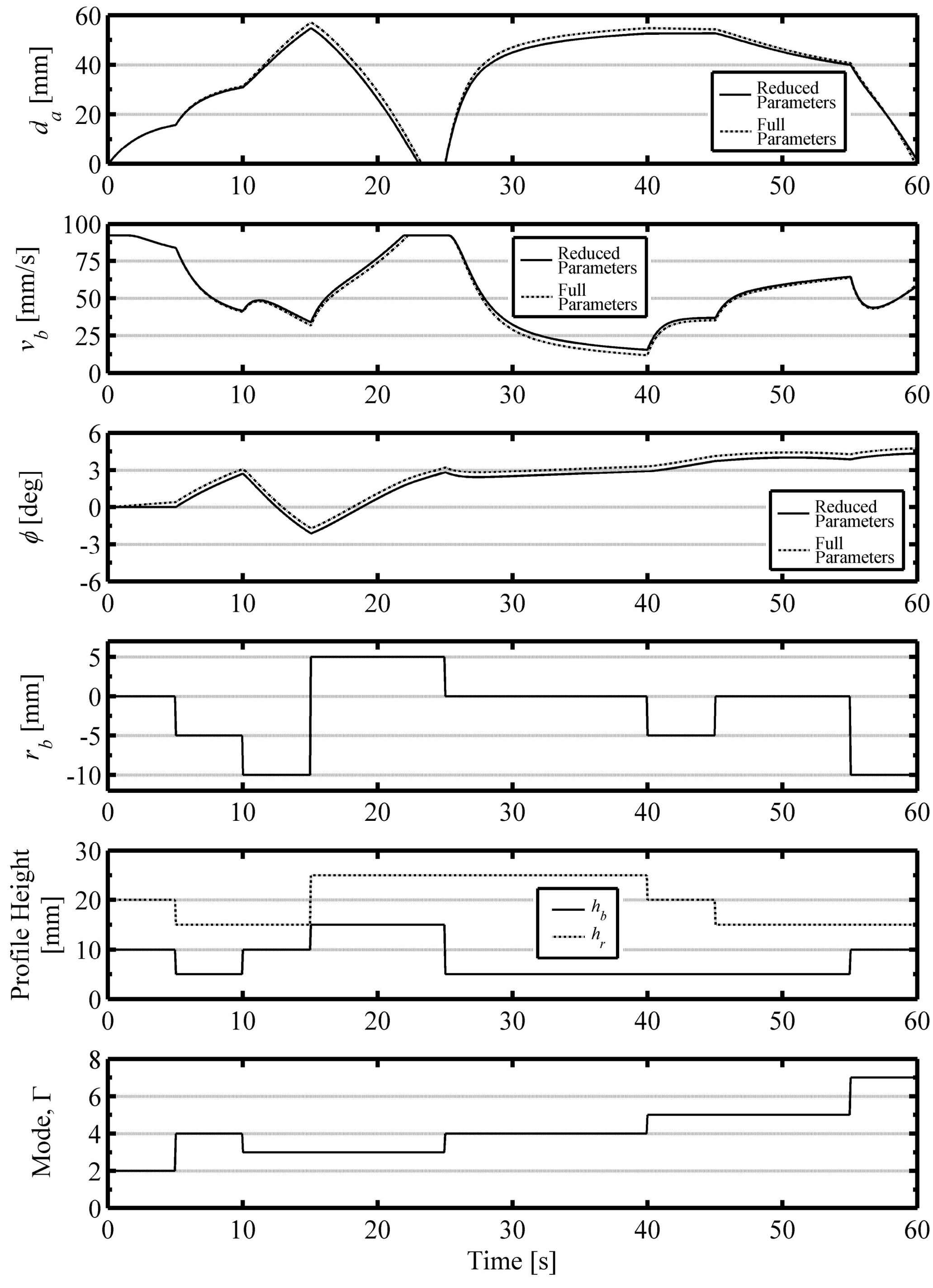

Fig. 5.3 Simulation of state dynamics with refined and full sets of estimated parameters.

Some observations of the more interesting aspects of the state dynamics will now be presented, beginning with mode 4. This mode is characterized by a significant amount of material located δ_a ahead of the robot (*i.e.* $h_a > h_{thres2}$). The material ahead acts to support the material accumulated on the blade causing a more rapid increase in d_a. This is reflected by $|C_{da1,4}|$ being greater than both $|C_{da1,2}|$ and $|C_{da1,5}|$. However, the material ahead does not directly influence the accumulation dynamics, as indicated by the insignificance of $C_{da2,4}$. This suggests that the rate of accumulation is not affected when the depth of material ahead exceeds h_{thres2}. In modes 3 and 7, the positive values of parameters $C_{\phi2,3}$ and $C_{\phi2,7}$ implies that within these modes, the robot effectively follows the blade as it penetrates down into the depth of the material below. For the other modes, since the blade is constrained by the hard floor surface, making ζ negative will tend to lift the front end of the robot, increasing its pitch and resulting in negative $C_{\phi2,\Gamma}$ values.

The measured and $N_p^{val} = 3$ predicted values of d_a, v_b, ϕ and z_b from one of the 16 validation passes are shown in Fig. 5.4. This example was selected to show a range of active modes throughout a pass, and also demonstrates the quality of the predictions when a longer prediction horizon is used. Note that the one-step-ahead and two-step-ahead predictions (*i.e.* $N_p^{val} = 1$ and $N_p^{val} = 2$) are not shown since they are not visually discernible from the measured values. The plots in Fig. 5.4 also confirm the general trends of the process dynamics discussed in Chapter 3. For example, a decrease in r_b causes a decrease in v_b and an increase in d_a, and vice-versa. It is also apparent that v_b responds more rapidly than d_a to a change in r_b.

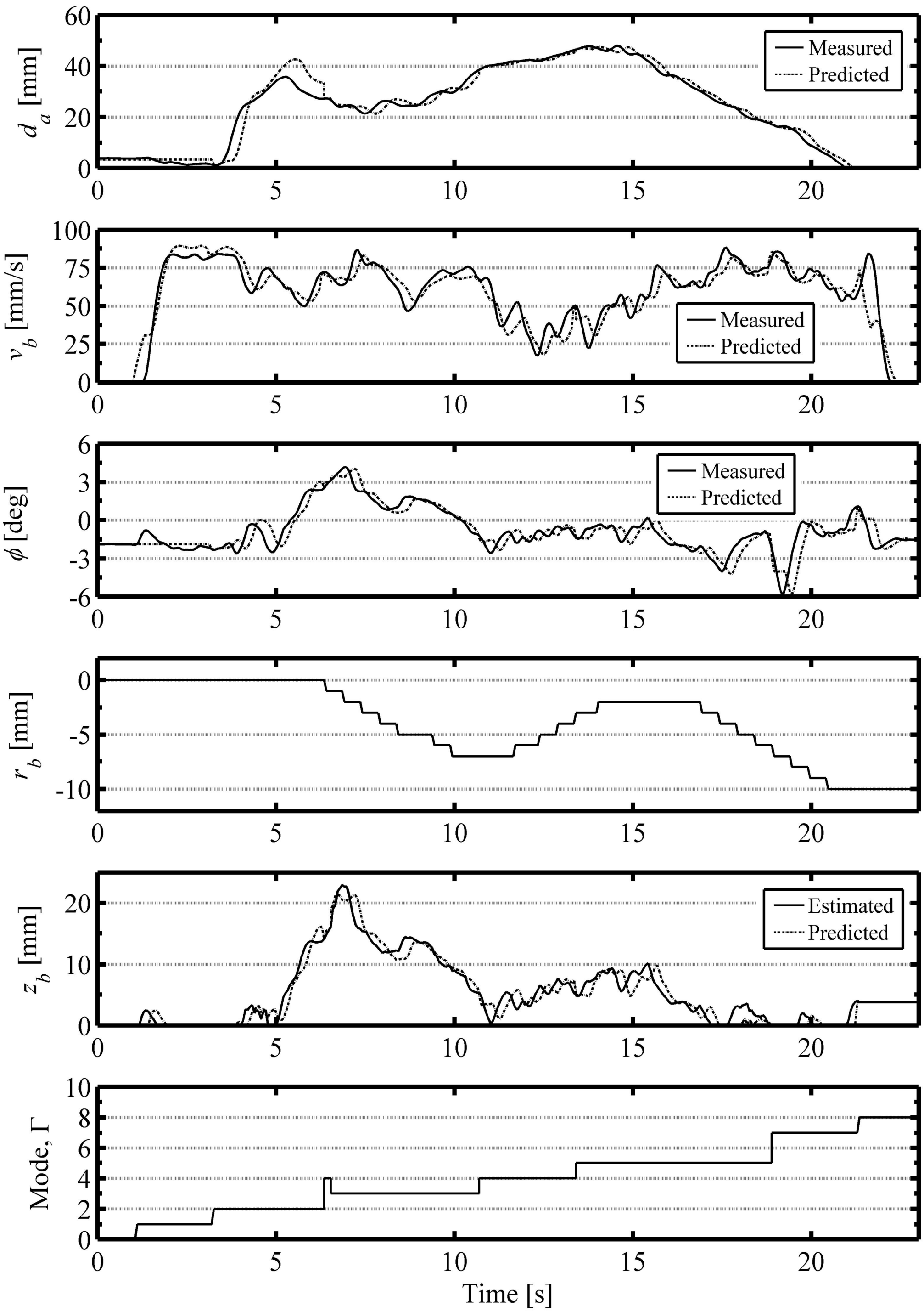

Fig. 5.4 Measured and predicted states for a 3-step ahead prediction horizon, r_b and Γ for one pass of the validation data set.

5.5 Conclusions

A series of system identification experiments were performed with a rule-based blade control algorithm implemented. The parameters of the dynamic equations were estimated using one-step-ahead predictions for operation modes 1-5 and 7. A global sensitivity analysis was performed to determine the relative contribution of each parameter and refine the model. The refined model was validated using a separate data set. The next chapter will present the design of an extended Kalman filter based on the identified state dynamic equations; and the statistics of the state process disturbances.

Chapter 6

Extended Kalman Filter Design

6.1 Introduction

This chapter presents the design of an extended Kalman filter (EKF) using the d_a, v_b and ϕ dynamic equations to reduce the errors in the state estimates relative to the system states due to the combination of process noise or disturbance and measurement noise. The one-step prediction error variance was used in the EKF measurement noise covariance matrix. The values of the EKF process noise covariance matrix were tuned manually. The smoothing behaviour of the Kalman filter was then compared to the performance of the 2nd order 1 Hz Butterworth lowpass filter used in Chapter 5.

6.2 Extended Kalman Filter Design

The purpose of the EKF is to obtain estimates of system states defined by nonlinear dynamics based on measurements Simon (2006). For a discrete nonlinear system of the form:

$$\boldsymbol{x}_k = \mathbf{f}\left(\boldsymbol{x}_{k-1}, \boldsymbol{u}_{k-1}\right) + \boldsymbol{w}_{k-1} \text{ and} \tag{6.1}$$

$$\boldsymbol{z}_k = \mathbf{h}\left(\boldsymbol{x}_k\right) + \boldsymbol{v}_k \tag{6.2}$$

Where, $\boldsymbol{x}_k$ is the state vector, $\boldsymbol{u}_k$ is the input vector, $\boldsymbol{w}_k$ is the zero mean multivariate Gaussian process noise or disturbance vector, $\boldsymbol{z}_k$ is the output vector, $\boldsymbol{v}_k$ is the zero mean multivariate Gaussian measurement noise vector, **f** is the function predicting the one step-ahead system state dynamics and **h** is the system output function.

The recursive EKF equations at the k^{th} sample take the form:

$$\hat{\boldsymbol{x}}_{k|k-1}^{EKF} = \mathbf{f}\left(\hat{\boldsymbol{x}}_{k-1|k-1}^{EKF}, \boldsymbol{u}_{k-1}\right) \tag{6.3}$$

$$P_{k|k-1}^{EKF} = F_{k|k-1}^{EKF} P_{k-1|k-1}^{EKF} \left(F_{k|k-1}^{EKF}\right)^T + Q^{EKF} \tag{6.4}$$

$$\tilde{\boldsymbol{y}}_k^{EKF} = \mathbf{z}_k - \mathbf{h}\left(\hat{\boldsymbol{x}}_{k|k-1}^{EKF}\right) \tag{6.5}$$

$$S_k^{EKF} = H_k^{EKF} P_{k|k}^{EKF} \left(H_k^{EKF}\right)^T + R^{EKF} \tag{6.6}$$

$$K_k^{EKF} = P_{k|k-1}^{EKF} \left(H_k^{EKF}\right)^T \left(S_k^{EKF}\right)^{-1} \tag{6.7}$$

$$\hat{\boldsymbol{x}}_{k|k}^{EKF} = \hat{\boldsymbol{x}}_{k|k-1}^{EKF} + K_k^{EKF} \tilde{\boldsymbol{y}}_k^{EKF} \tag{6.8}$$

$$P_{k|k}^{EKF} = \left(I - K_k^{EKF} H_k^{EKF}\right) P_{k|k-1}^{EKF} \tag{6.9}$$

$$F_{k-1}^{EKF} = \left.\frac{\partial \mathbf{f}}{\partial \boldsymbol{x}}\right|_{\hat{\boldsymbol{x}}_{k-1|k-1}^{EKF}, \boldsymbol{u}_{k-1}} \quad \text{and} \tag{6.10}$$

$$H_k^{EKF} = \left.\frac{\partial \mathbf{h}}{\partial \boldsymbol{x}}\right|_{\hat{\boldsymbol{x}}_{k|k-1}^{EKF}} \tag{6.11}$$

where, $\hat{\boldsymbol{x}}_{k|k-1}^{EKF}$ is the predicted state vector estimate from the extended Kalman filter, $P_{k|k-1}^{EKF}$ is the predicted estimate covariance, Q^{EKF} is the process noise or disturbance covariance matrix, R^{EKF} is the measurement disturbance covariance matrix, K_k^{EKF} is the Kalman filter gain, $\tilde{\boldsymbol{y}}_k^{EKF}$ is the innovation residual, S_k^{EKF} is the innovation covariance, $\hat{\boldsymbol{x}}_{k|k}^{EKF}$ is the updated state estimate, $P_{k|k}^{EKF}$ is the updated estimate covariance, F_{k-1}^{EKF} is the state transition matrix, H_k^{EKF} is the observation matrix. The EKF is implemented by performing the following procedure at each sample k

1. Compute the state partial derivative matrix F_{k-1}^{EKF} using Eq. (6.10)
2. Perform the time update of the state estimate, $\hat{\boldsymbol{x}}_{k|k-1}^{EKF}$, using Eq. (6.3) and estimation-error covariance $P_{k|k-1}^{EKF}$ using Eq. (6.4).
3. Compute the observation partial derivative matrix, H_k^{EKF}, using Eq. (6.11).
4. Compute the Kalman filter gain, K_k^{EKF}, using Eq. (6.7)
5. Perform the measurement update of the state estimate, $\hat{\boldsymbol{x}}_{k|k}^{EKF}$, using Eqs. (6.5) and (6.8) and estimation-error covariance, $P_{k|k}^{EKF}$, using Eq. (6.9).

For the robotic bulldozing process, using the discrete-time d_a, v_b and ϕ system equations, Eqs. (3.14)-(3.16), the predicted EKF state estimation vector takes the form:

$$\hat{\boldsymbol{x}}_{k|k-1}^{EKF} = \begin{bmatrix} \hat{d}_{a,k|k-1}^{EKF} \\ \hat{v}_{b,k|k-1}^{EKF} \\ \hat{\phi}_{k|k-1}^{EKF} \end{bmatrix} = \begin{bmatrix} \hat{d}_{a,k-1|k-1}^{EKF} + T_s \cdot \left(C_{da1,\Gamma} \cdot \hat{d}_{a,k-1|k-1}^{EKF} + C_{da2,\Gamma} \cdot h_{a,k-1} + C_{da3,\Gamma} \cdot h_{b,k-1} + C_{da4,\Gamma} \cdot h_{\delta r,k-1} - C_{d_a 5,\Gamma} \cdot \zeta_{k-1} \right) \cdot \hat{v}_{b,k-1|k-1}^{EKF} \\ \left(1 - \frac{T_s}{C_{vb1,\Gamma}} \right) \cdot \hat{v}_{b,k-1|k-1}^{EKF} + T_s \cdot \left(\frac{C_{vb2,\Gamma}}{C_{vb1,\Gamma}} \cdot u_{t,k-1} - C_{vb3,\Gamma} \cdot \hat{d}_{a,k-1|k-1}^{EKF} + C_{vb4,\Gamma} \cdot \zeta_{k-1} \right) \\ \hat{\phi}_{k-1|k-1}^{EKF} + T_s \cdot \left(C_{\phi 1,\Gamma} \cdot \hat{d}_{a,k-1|k-1}^{EKF} + C_{\phi 2,\Gamma} \cdot u_{b,k-1} + C_{\phi 3,\Gamma} \cdot h_{c,k-1} + C_{\phi 4,\Gamma} \cdot h_{b,k-1} \right) \cdot \hat{v}_{b,k-1|k-1}^{EKF} \end{bmatrix} \tag{6.12}$$

The resulting updated EKF state estimate takes the form:

$$\hat{\boldsymbol{x}}_{k|k}^{EKF} = \begin{bmatrix} \hat{d}_{a,k|k-1}^{EKF} \\ \hat{v}_{b,k|k-1}^{EKF} \\ \hat{\phi}_{k|k-1}^{EKF} \end{bmatrix} + K_k^{EKF} \tilde{\boldsymbol{y}}_k^{EKF} \tag{6.13}$$

with the innovation residual taking the form:

$$\tilde{\boldsymbol{y}}_k^{EKF} = \boldsymbol{z}_k - \hat{\boldsymbol{x}}_{k|k-1}^{EKF} \quad \text{(6.14}$$

and the EKF output vector is:

$$\boldsymbol{z}_k = \begin{bmatrix} d_{a,k}^{meas} \\ v_{b,k}^{meas} \\ \phi_k^{meas} \end{bmatrix} \tag{6.15}$$

where $d_{a,k}^{meas}$, $v_{b,k}^{meas}$ and ϕ_k^{meas} are the unfiltered state measurements.

Taking the partial derivatives of the state prediction equations, the corresponding EKF state transition matrix is:

$$F_{k-1}^{EKF} = \begin{bmatrix} 1+T_s \cdot C_{da1,\Gamma} \cdot \hat{v}_{b,k-1|k-1}^{EKF} & T_s \cdot \left(C_{da1,\Gamma} \cdot \hat{d}_{a,k-1|k-1}^{EKF} + C_{da2,\Gamma} \cdot h_{a,k-1} + C_{da3,\Gamma} \cdot h_{b,k-1} + C_{da4,\Gamma} \cdot h_{\delta r,k-1} - C_{da5,\Gamma} \cdot \zeta_{k-1} \right) & 0 \\ -T_s \cdot C_{vb3,\Gamma} & \left(1 - \frac{T_s}{C_{vb1,\Gamma}} \right) & 0 \\ T_s \cdot C_{\phi 1,\Gamma} \cdot \hat{v}_{b,k-1|k-1}^{EKF} & T_s \cdot \left(C_{\phi 1,\Gamma} \cdot \hat{d}_{a,k-1|k-1}^{EKF} + C_{\phi 2,\Gamma} \cdot \zeta_{k-1} + C_{\phi 3,\Gamma} \cdot h_{c,k-1} + C_{\phi 4,\Gamma} \cdot h_{b,k-1} \right) & 1 \end{bmatrix} \tag{6.16}$$

and the EKF observation matrix is:

$$H_k^{EKF} = \begin{bmatrix} 1 & 0 & 0 \\ 0 & 1 & 0 \\ 0 & 0 & 1 \end{bmatrix} \tag{6.17}$$

Assuming independent process noise or disturbance characteristics between states, the mode-dependent process noise or disturbance covariance matrix is defined as:

$$Q_\Gamma^{EKF} = \begin{bmatrix} \sigma_{w,da,\Gamma}^2 & 0 & 0 \\ 0 & \sigma_{w,vb,\Gamma}^2 & 0 \\ 0 & 0 & \sigma_{w,\phi,\Gamma}^2 \end{bmatrix} \tag{6.18}$$

The mode-dependent measurement noise covariance matrix is defined as:

$$R_\Gamma^{EKF} = \begin{bmatrix} \sigma_{v,da,\Gamma}^2 & \sigma_{v,davb,\Gamma}^2 & \sigma_{v,da\phi,\Gamma}^2 \\ \sigma_{v,vbda,\Gamma}^2 & \sigma_{v,vb,\Gamma}^2 & \sigma_{v,vb\phi,\Gamma}^2 \\ \sigma_{v,\phi da,\Gamma}^2 & \sigma_{v,\phi vb,\Gamma}^2 & \sigma_{v,\phi,\Gamma}^2 \end{bmatrix} \tag{6.19}$$

The measurement noise covariances of the state dynamics for each mode were determined using the one-step prediction errors of the unfiltered mode-segmented set of experimental fitting data. The measurement noise covariances $\sigma^2_{v,xy,\Gamma}$ were calculated for the states x and y and mode Γ as follows:

$$\sigma^2_{v,xy,\Gamma} = \frac{1}{\left(N^{fit}_{s,\Gamma,total}-1\right)-1} \sum_{i=1}^{N^{fit}_{s,\Gamma,total}-1} \left(e_{x,\Gamma}\left(i+1\right)-\overline{e}_{x,\Gamma}\right)\left(e_{y,\Gamma}\left(i+1\right)-\overline{e}_{y,\Gamma}\right) \tag{6.20}$$

$$e^{unfilt}_{x,\Gamma}\left(i+1\right) = x^{unfilt}_{pred}\left(i+1\right) - x^{unfilt}_{meas}\left(i+1\right) \text{ and} \tag{6.2`}$$

$$\overline{e}^{unfilt}_{x,\Gamma} = \frac{1}{\left(N^{fit}_{s,\Gamma,total}-1\right)} \sum_{i=1}^{N^{fit}_{s,\Gamma,total}-1} e_{x,\Gamma}\left(i+1\right) \tag{6.22}$$

where, i is the sample number; $N^{fit}_{s,\Gamma,total}$ is the number of points in the segmented fitting data set per mode Γ; $e^{unfilt}_{x,\Gamma}$ is the prediction error of state x between the unfiltered measurement values, denoted x^{unfilt}_{meas}, and the values predicted from the unfiltered measurements, denoted x^{unfilt}_{pred}; and $\overline{e}^{unfilt}_{x,\Gamma}$ is the mean prediction error of state x from unfiltered measurements. It was assumed that these prediction errors were predominantly due to the measurement noise. The measurement disturbance covariances of the d_a, v_b and ϕ state dynamics are tabulated in Table 6.1.

Table 6.1 Measurement disturbance covariances of the d_a , v_b and ϕ state dynamics for each mode.

Mode, Γ	Measurement disturbance covariance								
	$\sigma^2_{v,da,\Gamma}$	$\sigma^2_{v,davb,\Gamma}$	$\sigma^2_{v,da\phi,\Gamma}$	$\sigma^2_{v,vbda,\Gamma}$	$\sigma^2_{v,vb,\Gamma}$	$\sigma^2_{v,vb\phi,\Gamma}$	$\sigma^2_{v,\phi da,\Gamma}$	$\sigma^2_{v,\phi vb,\Gamma}$	$\sigma^2_{v,\phi,\Gamma}$
1	1.3	0.43	0.019	0.44	71	1.9	0.019	1.91	0.92
2	3.1	1.4	-1.1	1.4	378	12	-1.1	12	12
3	1.7	-0.91	-0.48	-0.91	241	4.9	-0.47	4.9	4.1
4	0.91	-0.50	-0.71	-0.50	354	6.1	-0.71	6.1	6.7
5	2.2	-0.67	-1.1	-0.67	509	9.3	-1.1	9.3	11
7	2.4	-2.0	-0.59	-2.0	444	5.8	-0.59	5.8	10

The values of the mode-dependent process noise or disturbance variances, $\sigma^2_{w,da,\Gamma}$, $\sigma^2_{w,vb,\Gamma}$ and $\sigma^2_{w,\phi,\Gamma}$ were selected manually and are tabulated in Table 6.2.

Table 6.2 Process noise or disturbance variances of the d_a , v_b and ϕ state dynamics for each mode.

Mode, Γ	Process noise or disturbance variance		
	$\sigma^2_{w,da,\Gamma}$	$\sigma^2_{w,vb,\Gamma}$	$\sigma^2_{w,\phi,\Gamma}$
1	0.2	10	0.05
2	0.2	50	0.3
3	0.1	50	0.5
4	0.1	50	0.5
5	0.1	50	0.5
7	0.2	60	0.2

An example of the d_a , v_b and ϕ state measurements filtered with the EKF and a 2nd order 1 Hz Butterworth low-pass filter is shown in Fig. 6.1. In terms of smoothing behaviour, the performance of the EKF is similar to the performance of the low-pass filter. The main advantages of the EKF are that less delay is introduced in the filtered signal, and the design is based on parameters that are more physically quantifiable (*i.e.* variance of the prediction error).

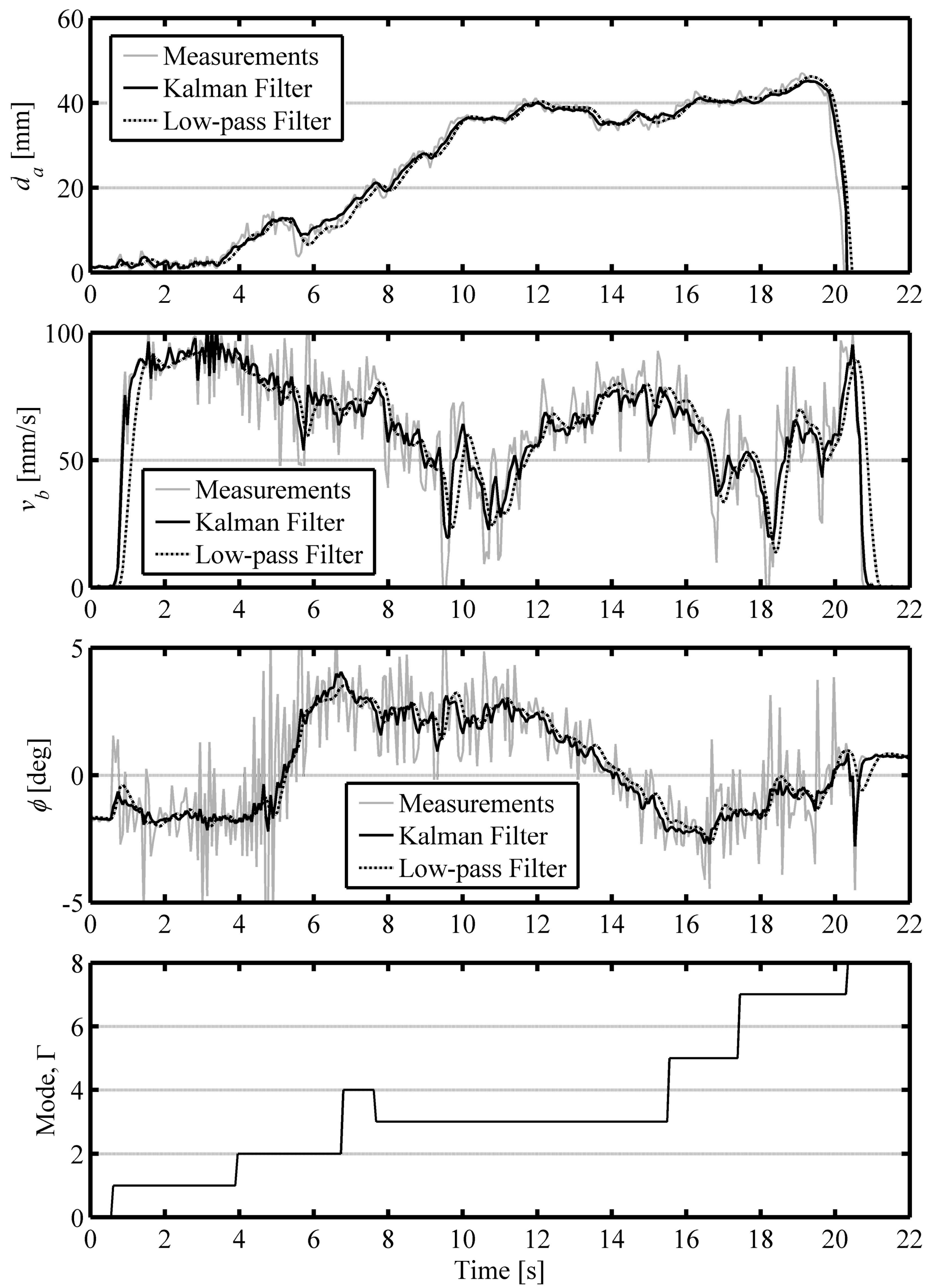

Fig. 6.1 Example of the d_a, v_b and ϕ state measurements filtered with the EKF and a 2^{nd} order 1 Hz Butterworth low-pass filter.

6.3 Residual Disturbance Model

The residual disturbances of the EKF filtered state measurements were modeled as zero mean Gaussian stochastic processes. The disturbances were determined using the one-step ahead prediction error from the EKF filtered mode-segmented data sets, similar to the previous section. The residual disturbance model for each state x and mode Γ takes the form

$$\hat{w}_{x,\Gamma}\left(i\right) = e_{x,\Gamma}^{EKF}\left(i\right) = \eta_{wx,\Gamma} \tag{6.23}$$

where $e_{x,\Gamma}^{EKF}\left(i\right) = x_{pred}^{EKF}\left(i\right) - x_{meas}^{EKF}\left(i\right)$, for samples i = 2, 3, … , $N_{s,\Gamma,total}^{fit}$; $\eta_{wx,\Gamma}$ is a Gaussian distribution with standard deviations $\sigma_{\eta,wx,\Gamma}$; $N_{s,\Gamma,total}^{fit}$ is the number of points in the segmented fitting data set per mode Γ; $e_{x,\Gamma}^{EKF}$ is the prediction error of state x between the EKF filtered measurement values, denoted x_{meas}^{EKF}, and the values predicted from the EKF filtered measurements, denoted x_{pred}^{EKF}. The residual disturbance standard deviations of the EKF filtered d_a , v_b and ϕ state dynamics are tabulated in Table 6.3.

Table 6.3 Residual disturbance standard deviations of the EKF filtered d_a, v_b and ϕ state dynamics for each mode.

Mode, Γ	State	$\sigma_{\eta,wx,\Gamma}$
1	d_a	0.42
	v_b	2.82
	ϕ	0.36
2	d_a	0.37
	v_b	3.1
	ϕ	0.36
3	d_a	0.39
	v_b	3.6
	ϕ	0.36
4	d_a	0.35
	v_b	3.9
	ϕ	0.37
5	d_a	0.37
	v_b	3.5
	ϕ	0.34
7	d_a	0.38
	v_b	3.6
	ϕ	0.33

6.4 Conclusions

An extended Kalman filter (EKF) was designed using the d_a , v_b and ϕ dynamic equations. The smoothing behaviour of the EKF is similar to the performance of the 2nd order 1 Hz Butterworth lowpass filter used in Chapter 5. The main advantage of the Kalman filter is that less delay is introduced in the signal and tuning is more flexible with more meaningful parameters. The EKF was implemented within the experimental data acquisition and control system for subsequent experimental investigations. The residual disturbances were modeled as zero mean Gaussian distributions. The residual disturbance models are used in Chapter 9 for a simulation analysis of the stochastic dynamics.

The next chapter presents the development of a control method for the robotic bulldozing operation based on the hybrid dynamic model presented in Chapters 3 and 5.

Chapter 7

Control Design

7.1 Introduction

This chapter describes the development of a control method for the robotic bulldozing operation based on the hybrid dynamic model presented in Chapter 3. To address the overall bulldozing task objective of maximizing the material removal rate, different control laws were designed for the unique dynamics of each mode. Thus as the mode transitions are identified throughout task execution, the mode-specific blade control law is activated. Since the material removal rate primarily depends on d_a and v_b, only those states are controlled. The EKF estimates of d_a and v_b given by Eq. (6.13) are employed by the controller.

7.2 Optimal Blade Control Design for Modes Γ = 2-5 and 7

Optimal blade position control laws were designed for modes Γ = 2-5 and 7 that perform the majority of the material removal. The control objective is focused on enhancing productivity by maximizing the material removal rate.

7.2.1 Condensed Discrete-time Prediction Model

The discrete-time one-step ahead prediction formulations of the d_a and v_b equations from Chapter 3 were used. The equations Eq. (3.14) and Eq. (3.15) are reformulated here in a condensed form. For brevity, the underlying material profile auxiliary variables were combined into the measured disturbance term:

$$H_{\Gamma,k} = T_s \cdot \left(C_{da2,\Gamma} \cdot h_{a,k} + C_{da3,\Gamma} \cdot h_{b,k} + C_{da4,\Gamma} \cdot h_{\delta r,k} \right) \tag{7.1}$$

where T_s is the sampling period. The discrete-time equations predicting one-step ahead from the k^{th} sample are then as follows:

$$\hat{d}_{a,k+1} = d_{a,k} + C_{11,\Gamma} \cdot v_{b,k} \cdot d_{a,k} + C_{12,\Gamma} \cdot v_{b,k} \cdot r_{b,k} + v_{b,k} \cdot H_{\Gamma,k} + \hat{w}_{d,\Gamma,k} \text{ and} \tag{7.2}$$

$$\hat{v}_{b,k+1} = C_{tr} + C_{21,\Gamma} \cdot d_{a,k} + C_{22,\Gamma} \cdot v_{b,k} + C_{23,\Gamma} \cdot r_{b,k} + \hat{w}_{v,\Gamma,k} \tag{7.3}$$

where $d_{a,k}$ is material accumulation EKF filtered measurement, $v_{b,k}$ is the EKF filtered robot blade velocity in the X-direction, $r_{b,k}$ is the calculated blade reference position, $\hat{w}_{d,k}$ is the expected value of the material accumulation EKF filtered residual process noise or disturbance, $\hat{w}_{v,k}$ is the expected value of the EKF filtered robot velocity residual process noise or disturbance, $C_{11,\Gamma} = T_s \cdot C_{da1,\Gamma}$, $C_{12,\Gamma} = T_s \cdot C_{da5,\Gamma}$, $C_{tr} = \frac{T_s \cdot C_{vb2}}{C_{vb1}} \cdot u_t$, $C_{21,\Gamma} = -T_s \cdot C_{vb3,\Gamma}$, $C_{22,\Gamma} = 1 - \frac{T_s}{C_{vb1,\Gamma}}$ and $C_{23,\Gamma} = T_s \cdot C_{vb4,\Gamma}$. Note that since $\tau_d \ll T_s$ and $\tau_r \ll T_s$, it was assumed that $\zeta_k \approx r_{b,k}$ in order to simplify the equations. In Chapter 6, it was determined experimentally that the EKF filtered material accumulation and robot velocity residual disturbances can be effectively modeled as zero mean Gaussian noise so their expected values in Eq. (7.2) and (7.3) equal zero, *i.e.* $\hat{w}_{d,k} = \hat{w}_{v,k} = 0$.

7.2.2 Optimal Blade Control Laws

Optimal control refers to the solution of an optimization problem for the control input that drives the system along a trajectory that minimizes or maximizes a performance index. When the optimal control solution includes model-based predictions of the system dynamics and control inputs into the future it is known as model predictive control (MPC), with an overview provided in Qin and Bagwell (2000). MPC was chosen for this research since it is a systematic optimal control approach that exploits a process model. While significant progress has been made with MPC, when applied to nonlinear processes like bulldozing the solutions typically employ numerical optimization that is too computationally demanding for real-time control of mechanical systems, as discussed in Grune and Pannek (2001). A further problem with applying both conventional MPC and feedback control to optimize bulldozing is that optimal desired values of the process states cannot be computed since they depend on future values of $H_{\Gamma,k}$ that are unpredictable. These values are unpredictable because the coefficients in Eq. (7.1) depend on unpredictable future Γ values; plus h_a, h_b and $h_{\delta r}$ depend on the future values of x_a, x_b and Γ. The unpredictability is due to the stochastic nature of the interaction between the machine and the material.

An important aspect of MPC design is the length of the prediction horizon. While in general a long prediction horizon will produce a result that is closer to the global optimum, a short prediction horizon is preferable in this application for three reasons. First, it has been determined experimentally that predictions of d_a and v_b farther than one-step-ahead are highly inaccurate due to the stochastic disturbances. Second, the longer the prediction horizon the greater the amount of computation that must be performed in real-time. Third, the difficulty of stability analysis grows as the horizon is increased.

For the reasons provided above, a one-step-ahead analytical MPC approach was developed for designing optimal control laws for the bulldozing process. This approach solves for a blade position control law that minimizes a one-step-ahead cost function formulated from the prediction equations Eq. (7.2) and Eq. (7.3). An obvious choice for the cost function is the negative of the one-step-ahead predicted approximate material removal rate given by:

$$\hat{Q}_{k+1} = -\hat{d}_{a,k+1} \cdot \hat{v}_{b,k+1} \cdot w_b \tag{7.4}$$

where w_b is the blade width. However, this choice is undesirable since it does not include the blade position reference so it will tend to produce an overly aggressive control law; plus w_b is constant and therefore redundant. More suitable cost functions will now be introduced.

Due to inherent differences in the dynamics of certain operation modes, two different cost functions are proposed, one for mode 3 and one for modes 2, 4, 5 and 7. The fundamental difference in dynamics is reflected in the dynamic equations by the parameter C_{da5}, as determined in Chapter 4. This parameter is present in the mode 3 dynamics signifying that the rate of material accumulation is partially dependent on blade position. This parameter is not present in the other controlled modes due to the constraint of the hard floor surface, thus the material accumulation in these modes is independent of blade position. The cost function proposed for mode 3 is:

$$\mathrm{J}_3 = -\hat{d}_{a,k+1} \cdot \hat{v}_{b,k+1} + \mathrm{R}_3 \cdot r_{b,k}^2 \tag{7.5}$$

where R_3 is a positive controller tuning parameter. The purpose of the first term in this equation is to maximize the predicted material removal rate, while the second term is included to allow the aggressiveness of the control to be tuned. The optimal control law that minimizes J_3 is found by substituting Eq. (7.2) and Eq. (7.3) into Eq. (7.5) for $\hat{d}_{a,k+1}$ and $\hat{v}_{b,k+1}$, respectively, taking its derivative with respect to $r_{b,k}$, setting it equal to zero and solving as follows:

$$\frac{d\,\mathrm{J}_3}{dr_{b,k}} = 2\cdot a_3 \cdot r_{b,k}^{*} + b_3 = 0 \qquad \text{and} \tag{7.6}$$

$$r_{b,k,3}^{*} = \frac{-b_3}{2\cdot a_3} \tag{7.7}$$

with

$$a_3 = -C_{12,3}\cdot C_{23,3}\cdot v_{b,k} + \mathrm{R}_3 \qquad \text{and}$$

$$b_3 = -C_{12,3}\cdot v_{b,k}\cdot\left(C_{tr} + C_{21,3}\cdot d_{a,k} + C_{22,3}\cdot v_{b,k}\right) - C_{23,3}\cdot\left(d_{a,k} + C_{11,3}\cdot d_{a,k}\cdot v_{b,k} + H_{3,k}\cdot v_{b,k}\right)$$

where $r_{b,k,3}^{*}$ is the optimal blade position reference input for mode 3.

The material accumulation model of modes 2, 4, 5 and 7 is characterized as being independent of blade position (*i.e.* model parameter $C_{12,\Gamma} = 0$). Therefore, a more appropriate objective for modes 2, 4, 5 and 7 is to maintain contact between the blade and the floor (*i.e.* minimizing r_b) while the robot travels forward as fast as possible (*i.e.* maximizing v_b). The cost function that accomplishes this objective is:

$$\mathrm{J}_\Gamma = \hat{v}_{b,k+1}\cdot r_{b,k} + \mathrm{R}_\Gamma \cdot r_{b,k}^2 \tag{7.8}$$

where R_Γ is a positive controller tuning parameter. Following the same procedure as above, optimal blade control law for Γ = 2, 4, 5 and 7 is:

$$r^*_{b,k,\Gamma} = \frac{-b_\Gamma}{2 \cdot a_\Gamma} \tag{7.9}$$

with

$$a_\Gamma = C_{23,\Gamma} + \mathrm{R}_\Gamma \qquad \text{and}$$

$$b_\Gamma = C_{tr} + C_{21,\Gamma} \cdot d_{a,k} + C_{22,\Gamma} \cdot v_{b,k}$$

where $r^*_{b,k,\Gamma}$ is the optimal blade position reference input for mode Γ.

7.2.3 Optimality Conditions

These optimal control laws must satisfy certain optimality conditions, as in Boyd and Vandenberghe (2004). These include the first-order optimality conditions (or Karush-Kuhn-Tucker (KKT) conditions) with respect to the constraints, $r_{b,min} \le r_{b,k} \le r_{b,max}$ and the second-order optimality condition. The KKT conditions are formulated with respect to the Lagrangian of the cost function and the blade position constraints as follows:

$$L_\Gamma\left(r_{b,k}, \lambda\right) = \mathrm{J}_\Gamma(r_{b,k}) + \lambda_1\left(r_{b,\max} - r_{b,k}\right) + \lambda_2\left(-r_{b,\min} + r_{b,k}\right) \tag{7.10}$$

where λ_1, λ_2 are Lagrange multipliers. The two different cost functions, Eq. (7.5) and Eq. (7.8), take the same general form $\mathrm{J}_\Gamma(r_{b,k}) = a_\Gamma \cdot r^2_{b,k} + b_\Gamma \cdot r_{b,k} + c_\Gamma$. From the Lagrangian in Eq. (7.10), the following conditions must be satisfied to ensure optimality:

$$\nabla_{r_{b,k}} L_\Gamma\left(r_{b,k}, \lambda\right) = 2 \cdot a_\Gamma \cdot r_{b,k} + b_\Gamma - \lambda_1 + \lambda_2 = 0 \tag{7.11}$$

$$r_{b,k} \le r_{b,max} \tag{7.12}$$

$$-r_{b,k} \le -r_{b,min} \tag{7.13}$$

$$\lambda_1\left(r_{b,max}-r_{b,k}\right)=0 \tag{7.14}$$

$$\lambda_2\left(-r_{b,min}+r_{b,k}\right)=0 \quad \text{and} \tag{7.15}$$

$$\lambda_1,\lambda_2 \geq 0 \tag{7.16}$$

If a constraint is not active, its associated Lagrange multiplier is zero. Thus, the solution to determining the optimal value of $r_{b,k}$ is reduced to checking the follow cases:

if $\lambda_1 = 0 \wedge \lambda_2 = 0$, $r_{b,k} = r^*_{b,k,\Gamma} = \dfrac{-b_\Gamma}{2 \cdot a_\Gamma}$

if $\lambda_1 = 0 \wedge \lambda_3 = 0$, $r_{b,k} = r_{b,min}$

if $\lambda_2 = 0 \wedge \lambda_3 = 0$, $r_{b,k} = r_{b,max}$

The second order optimality condition stipulates that, if a constraint is not active, a local minimum exists if the cost function is convex. This condition is satisfied when the second derivative of J_Γ with respect to $r_{b,k}$ is positive as follows:

$$\frac{d^2 J_\Gamma(r_{b,k})}{dr_{b,k}^2} = 2 \cdot a_\Gamma > 0 \tag{7.17}$$

Since the parameter a_Γ is a positive constant for all modes Γ = 2-5 and 7, a local minimum always exists.

7.3 Avoidance and Recovery Control for Mode Γ = 6

The d_a and v_b dynamics of mode $\Gamma = 6$ are fundamentally different from the other modes. Consequently, they could not be modeled within the same analytical structure of the system equations. Therefore, the mode 6 dynamics and blade control approach were investigated experimentally. This mode is undesirable since it indicates that the robot has lost contact with the underlying material, resulting in no bulldozing work being accomplished. The conditions that cause the robot to transition into mode 6 were investigated experimentally with the objective of developing an approach to reducing the possibility of this transition (*i.e.* mode 6 avoidance). It was found that mode 6 avoidance can be accomplished with an appropriate state dependent blade position constraint imposed in modes Γ = 2-5 and 7. The results of this investigation formed the basis for the development of a blade control law for mode 6 to expedite a transition into a desirable mode (*i.e.* mode 6 recovery).

7.3.1 State Dependent Blade Constraint for Mode Γ = 6 Avoidance

Recall from Chapter 3, mode $\Gamma = 6$ is defined by the condition $d_a < 0$, *i.e.* a 'negative' accumulation of material on the blade. A transition to mode 6 tends to result when the blade is raised above its zero position, *i.e.* $\zeta > 0$, while a significant amount of accumulated material, *i.e.* $d_a > 0$, is being pushed. When the blade is raised above its zero position a small local mound of material is created in the underlying material profile. Once the robot tracks reach the location of the small local mound, after traveling a distance approximately equal to the length of the blade arm, the robot will begin to ascend the local mound. If the relative height of the local mound, h_{local}, is sufficiently large the elevation of the robot will cause the blade to lose contact with the underlying material profile, and the d_a measurement will become negative. The conditions of ζ and d_a prior to transitioning to mode 6 are illustrated in Fig. 7.1. The relationship between h_{local} and d_a during mode 6 is illustrated in Fig. 7.2.

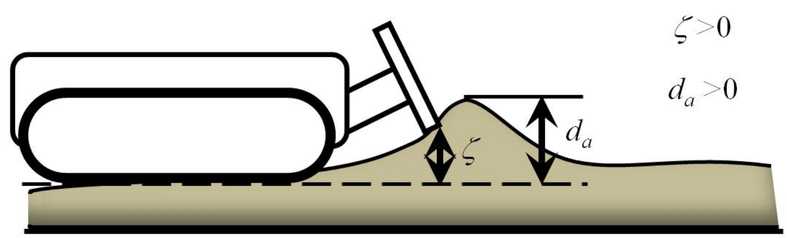

Fig. 7.1 Conditions of ζ and d_a prior to transition to mode 6.

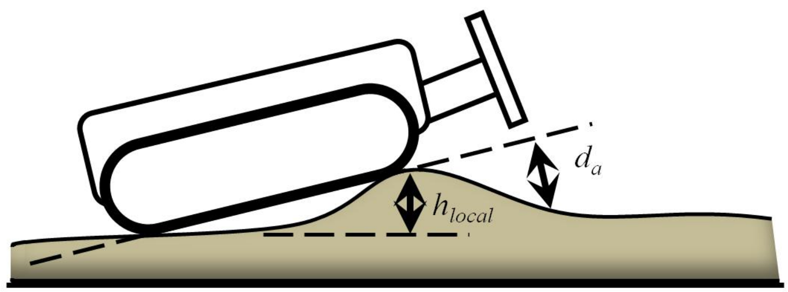

Fig. 7.2 Relationship between h_{local} and d_a during mode 6.

A very conservative approach to avoid a transition to mode 6 is to constrain the blade to remain below its zero position, *i.e.* $r_b < 0$. However, this will result in a significant reduction in overall bulldozing performance. Since the height of h_{local} is determined by the blade position another approach is to constrain the blade position reference input proportionately relative to the height of material accumulation as follows:

$$r_b < K_{rb} \cdot d_a \tag{7.18}$$

where K_{rb} is a positive constant. This blade position constraint will not necessarily avoid a transition to mode 6, however, it will be much less likely to occur. Furthermore, if a transition to mode 6 does occur this blade constraint will allow faster recovery from it.

A series of two-pass experimental trials were performed to investigate the conditions that tend to result in a transition to mode 6. Similar to the experiments discussed in Chapter 5, material was initially set up in a structured pile with a uniform nominal height of 20 mm and length of 1.1 m, covering to the edge of the environment. The robot blade location, x_b, was located 150 mm away from the leading edge of the pile at the start of each pass (*i.e.* mode 0). The robot was driven forward with the blade at its zero position (*i.e.* mode 1). After the robot blade reached the leading edge of the material pile (*i.e.* mode 2) and transitioned to mode 3 or mode 4 the blade position reference was set to a constant downward position equal to the average height of one layer of stones, $r_b = -h_{thres1} = -5$ mm. When the material accumulated on the blade reached a threshold value of 80% of its maximum, *i.e.* $d_a = 0.8 \cdot d_{a,\max} = 0.8 \cdot 55$ mm, the blade control $r_b = K_{rb} \cdot d_a$ was initiated until a transition to mode 6 occurred. When a transition to mode 6 occurred, the blade position was set to zero. When a transition out of mode 6 occurred, the blade position was again set to $r_b = -h_{thres1}$ to cause another transition to mode 6. Different values of K_{rb} were selected for each set of experimental trials. This cycle was repeated until the robot reached near the far edge of the task space (*i.e.* mode 7) and stopped (*i.e.* mode 8). After a bulldozing pass with the initial material coverage was completed, an additional pass was attempted with the subsequent material profile. This constituted one experimental trial. Five sets of two-pass experimental trials were completed for K_{rb} values of 1, 0.5 and 0.25. The mode 6 activation algorithm is summarized in Table 7.1, where the intermediate variable S_{rb} is used to latch the blade position control.

Table 7.1 Mode 6 activation algorithm.

INITIALIZE $\Gamma = 0$
ACTIVATE $\Gamma = 1$
$S_{rb} = 0$
WHILE $\Gamma > 2 \wedge \Gamma \neq 7$
    IF $\Gamma \neq 6$
        IF $S_{rb} = 0$
            $r_b = -h_{thres1}$
        ELSEIF $S_{rb} = 0 \wedge d_a > 0.8 \cdot d_{a,max}$
            $S_{rb} = 1$
        ELSEIF $S_{rb} = 0$
            $r_b = K_{rb} d_a$
        ENDIF
    ELSEIF $\Gamma = 6$
        $r_b = 0$
        $S_{rb} = 0$
    ENDIF
ENDWHILE

The effect of the mode 6 activation algorithm is to instantly create a significantly large local mound of material which the robot will subsequently climb. As the robot ascends the local mound the blade is elevated above the underlying material to such an extent that it can no longer remain in contact, thus no work can be accomplished.

Measures used to quantify the experimental results of the mode 6 activation investigation include: h_{peak}, the maximum height of the underlying material profile peak at the local mound that caused the transition into mode 6; $\left|d_a\right|_{\max}$, the maximum 'negative accumulation' during mode 6; and Δt_6, the duration of mode 6 activation.

An example of the experimental results of two passes with the mode 6 activation algorithm using K_{rb} = 1 are shown in Fig. 7.3 and Fig. 7.4. This example shows very large and very steep peaks created which result in long durations of mode 6 active with very deep ‘negative accumulation’ (*i.e.* large magnitude $d_a < 0$) indicating large relative elevation of the robot blade with respect to the underlying material profile. In addition to causing poor performance during a bulldozing pass, the steep local mounds cause severe problems during subsequent passes. The robot is likely to become stuck in the underlying material profile trough between local mounds, as indicated in Fig. 7.4 and illustrated in Fig. 7.5. Altogether, this is highly undesirable for bulldozing performance.

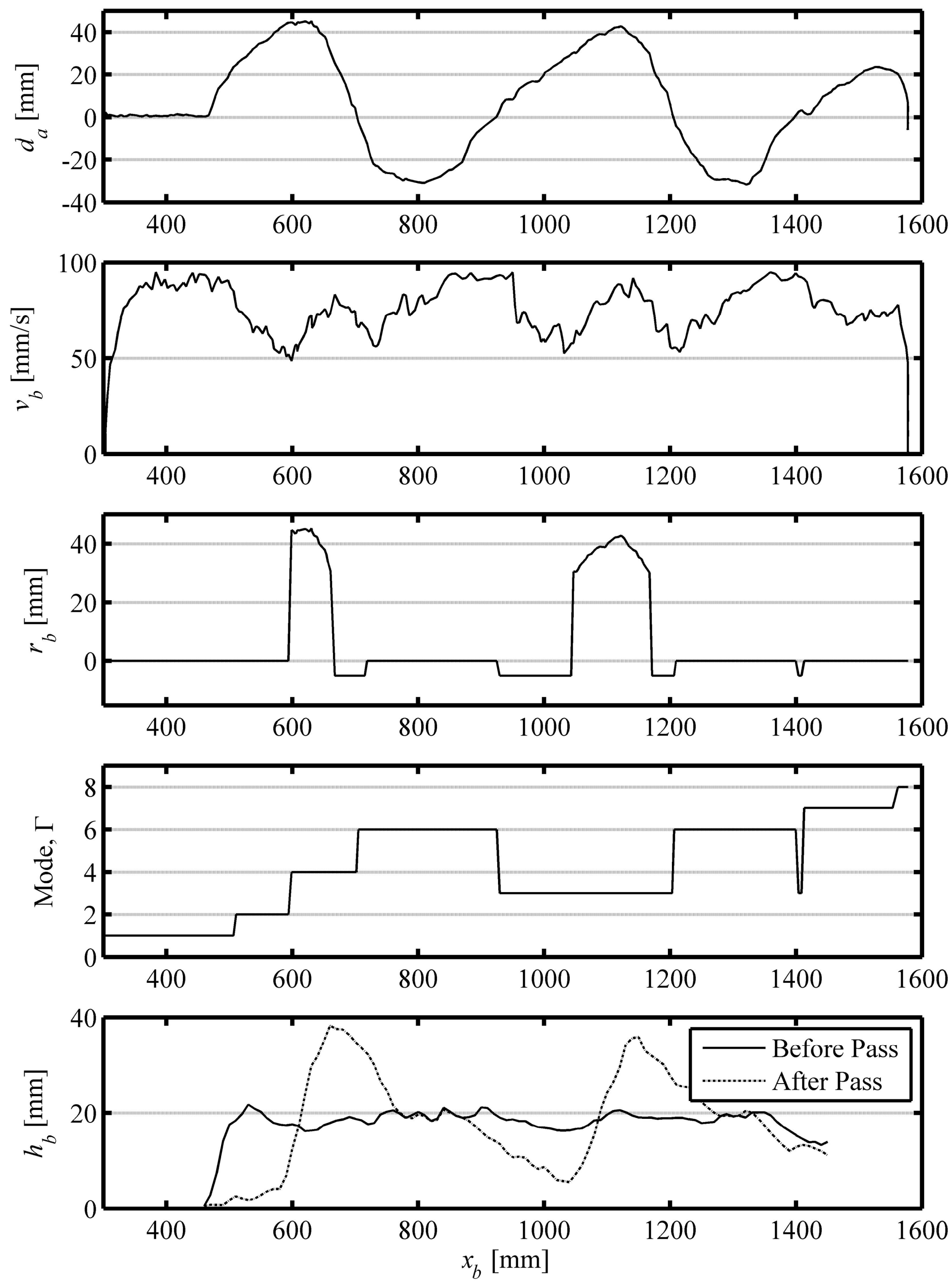

Fig. 7.3 Example of mode 6 activation experimental results using K_{rb} = 1, pass 1.

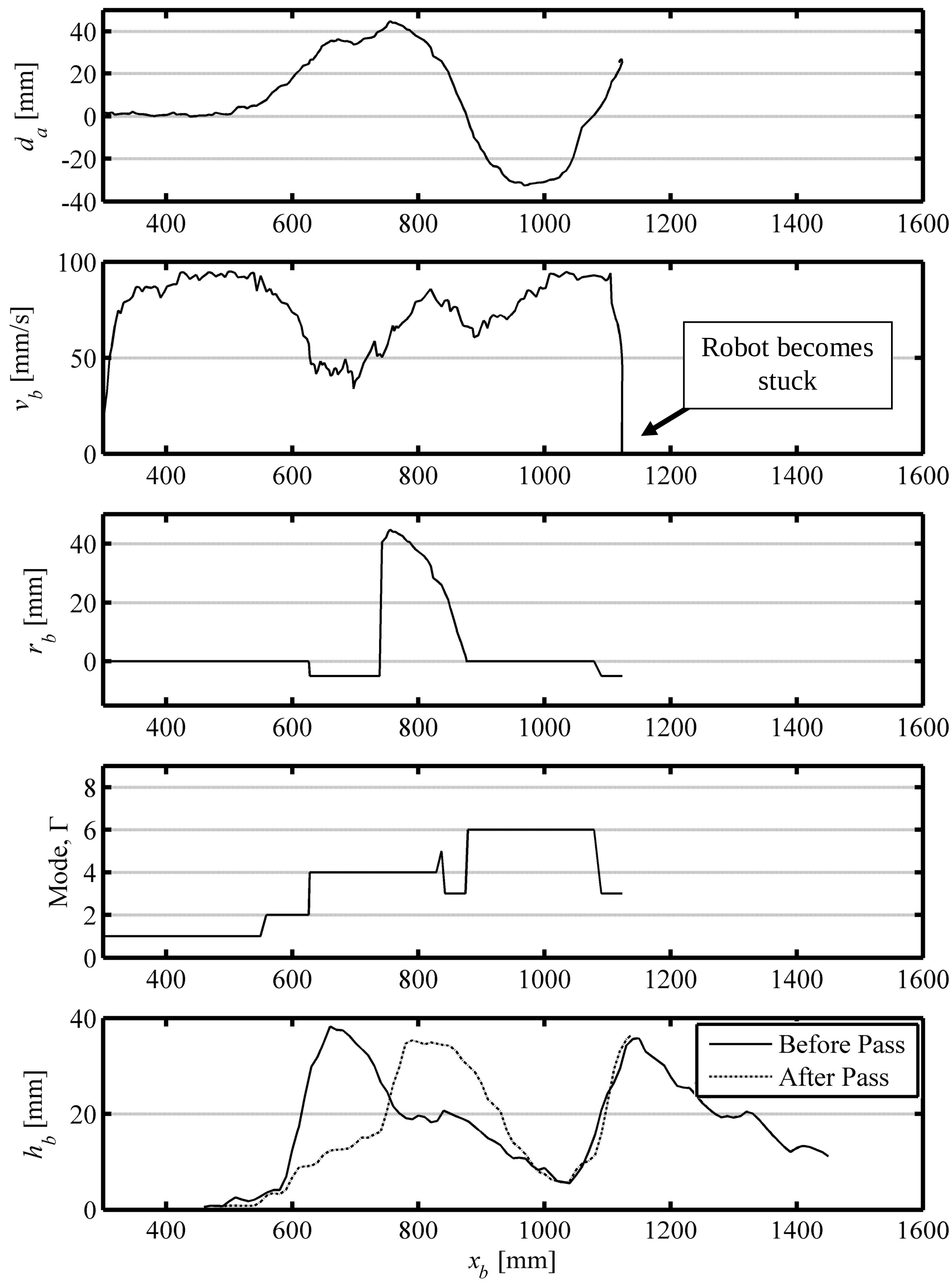

Fig. 7.4 Another example of mode 6 activation experimental results using $K_{rb} = 1$, pass 2 showing the robot becoming stuck ($v_b = 0$).

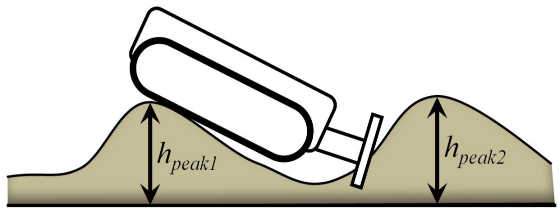

Fig. 7.5 Illustration of the robot becoming stuck between material profile peaks due to activation of mode 6.

As K_{rb} decreases, the height of the local mound decreases and the likelihood of mode 6 becoming active decreases. For example, Fig. 7.6 shows experimental results using K_{rb} = 0.25 where h_{peak} and $|d_a|_{\max}$ are significantly smaller. Another example of experimental results using K_{rb} = 0.25 in Fig. 7.7 shows that mode 6 is not activated at all.

The mean values $\bar{h}_{peak}$, $\overline{|d_a|_{max}}$ and $\overline{\Delta t_6}$ of the experimental results are tabulated in Table 7.3, along with the number of passes that the robot became stuck during the second pass, $n_{6,stuck}$, and the number of passes where mode 6 was did not become active, $n_{6,avoid}$. The mean values do not include the passes where the robot became stuck, nor when mode 6 was avoided. The results in Table 7.3 show that as K_{rb} decreases, $\bar{h}_{peak}$, $\overline{|d_a|_{max}}$ and $\overline{\Delta t_6}$ decrease. The results with $\mathrm{K_{rb}}$ = 0.25 compared with K_{rb} = 1 show improvements of 30%, 55% and 13% in $\bar{h}_{peak}$, $\overline{|d_a|_{max}}$ and $\overline{\Delta t_6}$, respectively. Furthermore, with K_{rb} = 0.25, mode 6 activation was avoided in 40% of the passes and did not become stuck in any passes.

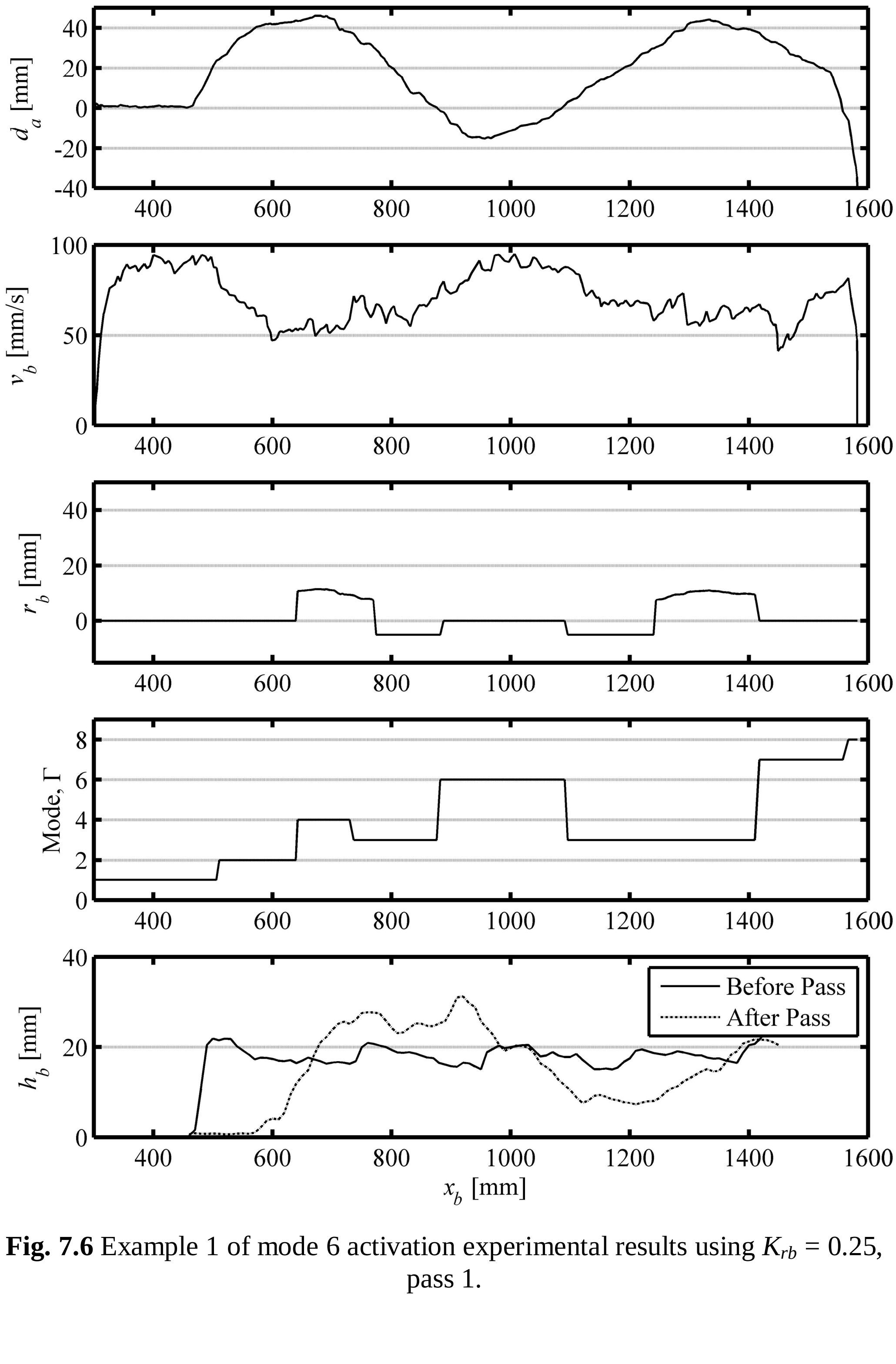

Fig. 7.6 Example 1 of mode 6 activation experimental results using K_{rb} = 0.25, pass 1.

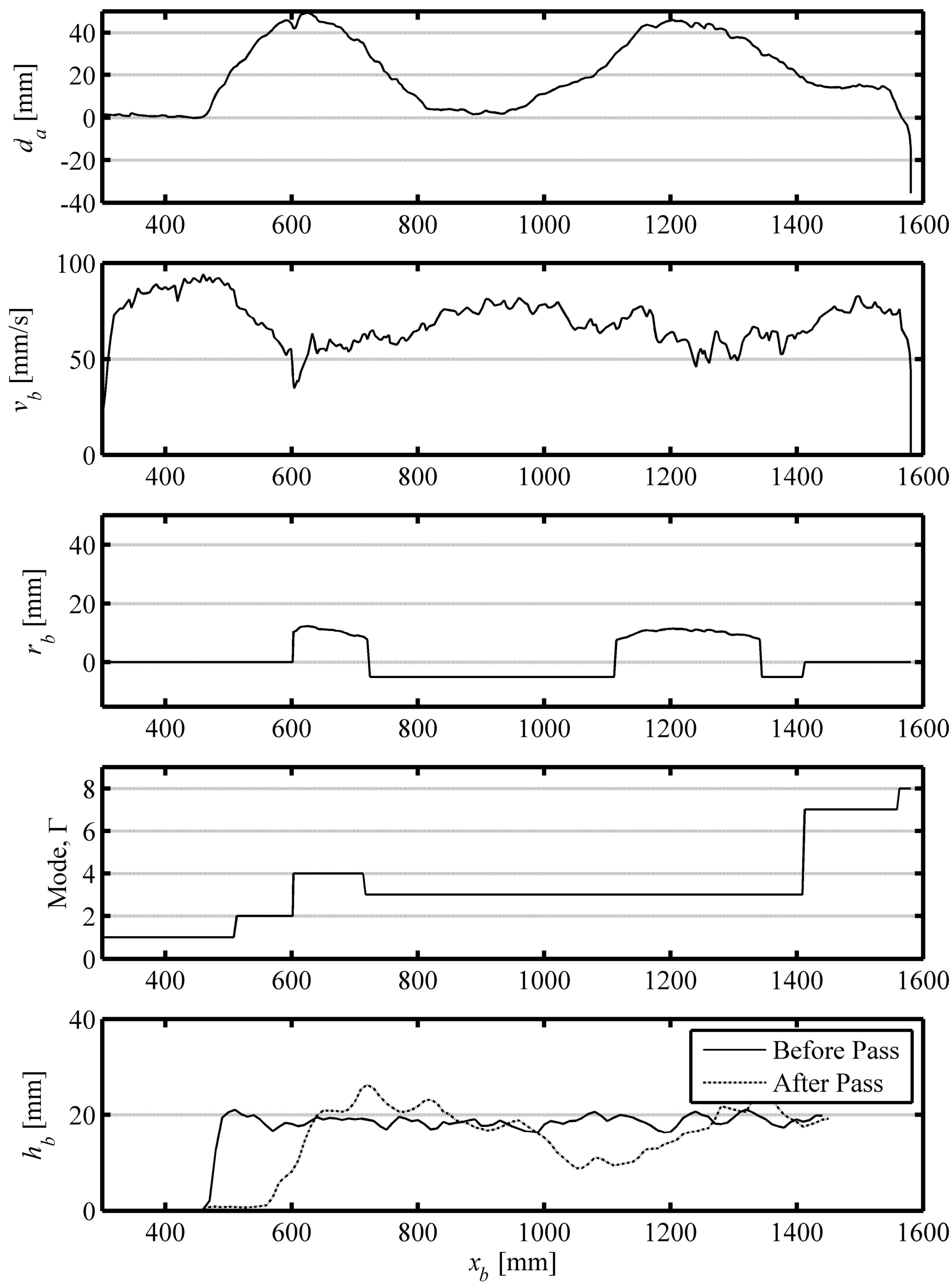

Fig. 7.7 Example 2 of mode 6 activation experimental results using K_{rb} = 0.25, pass 1 showing no mode 6 activation.

7.3.2 Blade Control for Mode Γ = 6 Recovery

The experimental investigation of mode 6 activation and avoidance was extended to include the development of a method for selecting the blade constraint parameter K_{rb} in conjunction with a mode 6 recovery blade control algorithm. Recovery from mode 6 can be achieved more quickly by positioning the blade downward to penetrate down into the underlying material surface with the following blade position control law:

$$r_b = d_a - h_{thres1} \tag{7.19}$$

This allows material to resume accumulating on the blade during mode 6 until the point when $d_a > 0$ which transitions the system out of mode 6. The amount of 'negative accumulation' is a function of the height of the local mound and hence a function of the raised blade position when the local mound is formed. Therefore, the allowable maximum blade position, $r_{b,max}$, should be a function of the minimum blade position, $r_{b,min}$, so that the mode 6 recovery control downward blade position penetrates sufficiently into the underlying material. The principle of the mode 6 recovery control law is illustrated in Fig. 7.8.

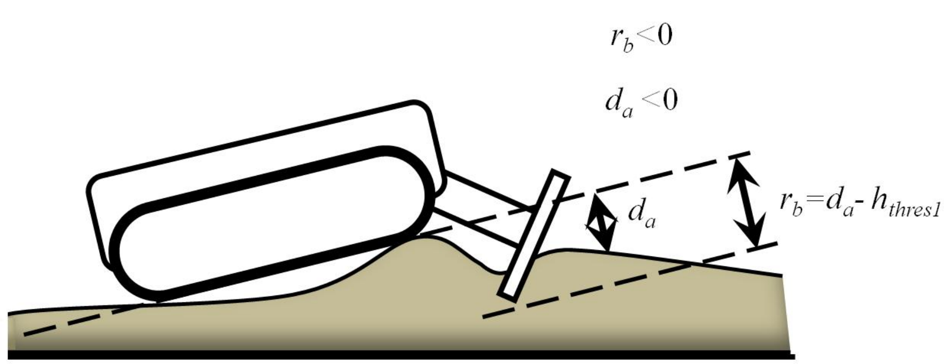

Fig. 7.8 Illustration of mode 6 recovery blade control law.

With the blade constrained by $r_b < K_{rb} \cdot d_a$ to avoid mode 6 activation, the value of K_{rb} limits $r_{b,max}$ with respect to the maximum material accumulation, $d_{a,max}$, which limits the maximum height of a potential local mound $h_{local,max}$. Thus it is desirable to minimize h_{local} to minimize the effects of mode 6, should it become active. For the mode 6 recovery blade control law to be effective the blade must be able to be lowered to a position below the grade of the underlying surface (*i.e.* penetrate and dig into the material). The minimum physically constrained blade position, $r_{b,min}$, can limit the effectiveness of the mode 6 recovery control law. For example, if h_{local} becomes too large and the magnitude of the 'negative accumulation' is greater than $r_{b,min}$ (*i.e.* $d_a < r_b$) then the blade cannot penetrate downward into the material. Therefore, the value of K_{rb} should be chosen such that if a transition to mode 6 occurs, the recovery control law is capable of positioning the blade below the grade of the underlying material at least to the depth of a single layer of stones (*i.e.* $r_b + h_{thres1} < d_a$). Thus the value of K_{rb} can be used to determine an allowable 'negative accumulation' and an allowable $h_{local,max}$ so that the recovery control law can be effective.

A method for determining an appropriate value of K_{rb} with respect to the minimum constrained blade position, $r_{b,min}$, and the maximum material accumulation, $d_{a,max}$, proceeds as follows. Assume for small distances and elevations, the following approximation holds:

$$h_{local} \approx r_b, \text{ for } r_b > 0 \tag{7.20}$$

Thus, an approximate allowable 'negative accumulation', $d_{a,6,min}$ during mode 6 is:

$$-d_{a,6,min} \approx h_{local,max} \approx r_{b,max} \tag{7.21}$$

For effective recovery control during mode 6, the blade position must satisfy:

$$r_b \le d_a - h_{thres1} \tag{7.22}$$

Using the minimum allowable material accumulation, $d_{a,6,min}$ in (7.22) gives:

$$r_b \le d_{a,6,min} - h_{thres1} \tag{7.23}$$

Substituting the minimum blade constraint $r_b = r_{b,min}$ into (7.23) gives:

$$r_{b,min} \le d_{a,6,min} - \mathrm{h}_{\mathrm{thres1}} \tag{7.24}$$

which can be re-written as:

$$-d_{a,6,min} \le -r_{b,min} - h_{thres1} \tag{7.25}$$

Substituting the approximation $-d_{a,6,min} \approx r_{b,max}$ into (7.25) gives:

$$r_{b,max} \le -r_{b,min} - h_{thres1} \tag{7.26}$$

Substituting $r_{b,max} = K_{rb} \cdot d_{a,max}$ into (7.26) gives:

$$K_{rb} \cdot d_{a,max} < -r_{b,min} - h_{thres1} \tag{7.27}$$

Solving (7.27) for K_{rb} gives:

$$K_{rb} \le \frac{-r_{b,min} - h_{thres1}}{d_{a,max}} \tag{7.28}$$

Using (7.28) with the values $d_{a,max}$ = 55 mm, $r_{b,min}$ = –15 mm and h_{thres1} = 5 mm, the maximum blade constraint proportionality coefficient is calculated to be $K_{rb,max}$ = 0.18.

A set of five two-pass experimental trials were performed similar to those presented in Section 7.3.1, except that K_{rb} was made equal to $K_{rb,max}$ and the mode 6 recovery blade control law, Eq. (7.19), was initiated when a transition to mode 6 occurred. The mode 6 activation combined with the recovery control law algorithm is summarized in Table 7.2. Note that only Eq. (7.18) with $K_{rb} = K_{rb,max}$, and lines 13 and 14 of this algorithm, are applied during normal operation of the bulldozer.

Table 7.2 Mode 6 activation combined with recovery control law algorithm.

1. INITIALIZE $\Gamma = 0$
2. ACTIVATE $\Gamma = 1$
3. $S_{rb} = 0$
4. **WHILE** $\Gamma > 2 \wedge \Gamma \neq 7$
5.   **IF** $\Gamma \neq 6$
6.   **IF** $S_{rb} = 0 \wedge d_a \leq 0.8 \cdot d_{a,max}$
7. $r_b = -h_{thres1}$
8.   **ELSEIF** $S_{rb} = 0 \wedge d_a > 0.8 \cdot d_{a,max}$
9. $S_{rb} = 1$
10.   **ELSE**
11. $r_b = K_{rb,max} d_a$
12.   **ENDIF**
13.   **ELSEIF** $\Gamma = 6$
14. $r_b = d_a - h_{thres1}$
15. $S_{rb} = 0$
16.   **ENDIF**
17. **ENDWHILE**

The mean value $\overline{h}_{peak}$, $\overline{|d_a|}_{max}$ and $\overline{\Delta t_6}$ of the experimental results are tabulated in Table 7.3, along with the number of passes that the robot became stuck during the second pass, $n_{6,stuck}$, and the number of passes where mode 6 was did not become active, $n_{6,avoid}$. The mean values do not include the passes where the robot became stuck, nor when mode 6 was avoided.

Table 7.3 Average performance measures of experimental results for mode 6 activation and recovery control investigations.

Experimental Algorithm	$\overline{h}_{peak}$ (mm)	$\overline{\lvert d_a \rvert}_{max}$ (mm)	$\overline{\Delta t_6}$ (s)	$n_{6,stuck}$	$n_{6,avoid}$
Mode 6 Activation, K_{rb} = 1	39	-29	2.4	5	0
Mode 6 Activation, K_{rb} = 0.5	33	-23	2.9	0	2
Mode 6 Activation, K_{rb} = 0.25	27	-13	2.1	0	4
Mode 6 Activation and Recovery Control, K_{rb} = 0.18	27	-10	1.6	0	3

An example of experimental results with the combined mode 6 activation and recovery control law algorithm is shown in Fig. 7.9. This example shows that with $r_b < K_{rb,\max} \cdot d_a$, h_{peak} was small with a smaller slope, which caused a more gradual climb by the robot, leading to a smaller 'negative accumulation' during mode 6. Subsequently, the recovery period to transitioning out of mode 6 was much smaller. The distance covered during the recovery period was approximately 100 mm which corresponds to the length of the blade arm, which is the distance that the robot must travel for the front of the tracks to reach the blade location.

From Table 7.3, the results with K_{rb} = 0.18 and recovery control compared with K_{rb} = 1 without recovery control show improvements of 30%, 65% and 33% in $\overline{h}_{peak}$, $\overline{\lvert d_a \rvert}_{max}$ and $\overline{\Delta t_6}$, respectively. Furthermore, with K_{rb} = 0.18 and recovery control, mode 6 activation was avoided in 30% of the passes and did not become stuck in any passes.

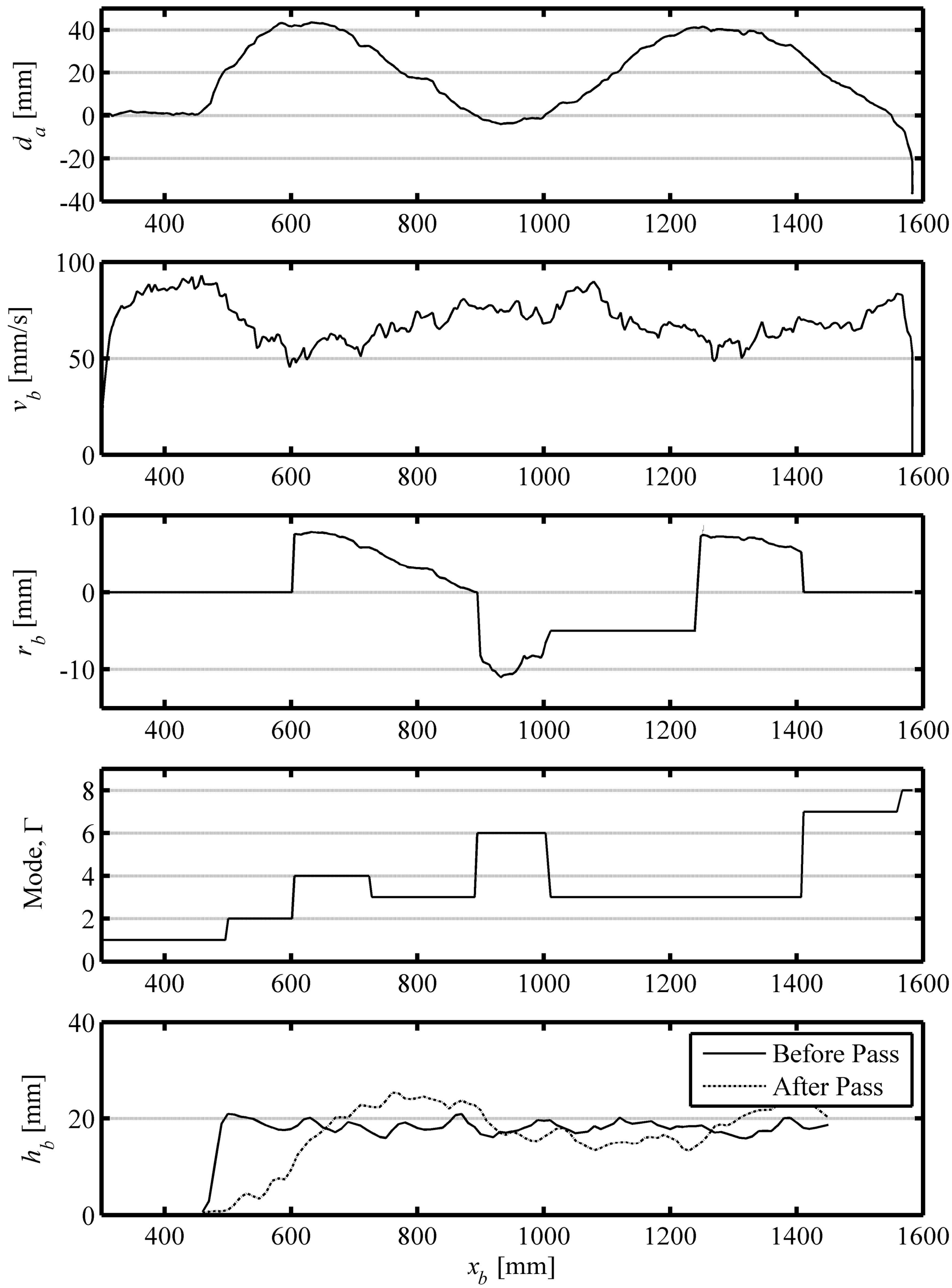

Fig. 7.9 Example of mode 6 activation and recovery blade control experimental results using K_{rb} = 0.18.

7.4 Conclusions

Optimal blade position control laws were designed for modes Γ = 2-5 and 7 with the objective of maximizing the material removal rate. The discrete-time one-step ahead prediction formulations of the d_a and v_b equations from Chapter 3 were used. The control objective was focused on enhancing productivity by maximizing the material removal rate.

The conditions that cause the robot to transition into mode 6 were investigated experimentally. It was found that avoidance of mode 6 can be accomplished with an appropriate state dependent blade constraint imposed in modes Γ = 2-5 and 7. The results of this investigation formed the basis for the development of a blade control law to a transition out of mode 6 if it occurs.

The next chapter presents an analysis of the stability and performance of the deterministic closed loop dynamics.

Chapter 8

Deterministic Performance and Stability Analysis

8.1 Introduction

This chapter presents a theoretical analysis of the performance and stability of the deterministic open-loop and closed-loop dynamics. To allow investigation of the underlying deterministic dynamics, the effects of the d_a and v_b process disturbances, defined in Eq. (6.1), were neglected. Also, the blade position constraints $r_{b,min} < r_b < r_{b,max}$ were neglected. For convenience, the condensed discrete-time deterministic open-loop d_a and v_b are reproduced as follows:

$$\hat{d}_{a,k+1} = d_{a,k} + C_{11,\Gamma} \cdot v_{b,k} \cdot d_{a,k} + C_{12,\Gamma} \cdot v_{b,k} \cdot r_{b,k} + v_{b,k} \cdot H_{\Gamma,k} \text{ and} \tag{8.1}$$

$$\hat{v}_{b,k+1} = C_{tr} + C_{21,\Gamma} \cdot d_{a,k} + C_{22,\Gamma} \cdot v_{b,k} + C_{23,\Gamma} \cdot r_{b,k} \tag{8.2}$$

The deterministic optimal control law equations are reproduced as follows:

$$r^*_{b,k,3} = -\frac{C_{12,3} \cdot v_{b,k} \cdot \left(C_{tr} + C_{21,3} \cdot d_{a,k} + C_{22,3} \cdot v_{b,k}\right) + C_{23,3} \cdot \left(d_{a,k} + C_{11,3} \cdot d_{a,k} \cdot v_{b,k} + H_{3,k} \cdot v_{b,k}\right)}{2 \cdot \left(C_{12,3} \cdot C_{23,3} \cdot v_{b,k} - \mathrm{R}_3\right)} \tag{8.3}$$

and

$$r^*_{b,k,\Gamma} = -\frac{C_{tr} + C_{21,\Gamma} \cdot d_{a,k} + C_{22,\Gamma} \cdot v_{b,k}}{2 \cdot \left(C_{23,\Gamma} + \mathrm{R}_\Gamma\right)} \text{, for } \Gamma = 2, 4, 5 \text{ and } 7 \tag{8.4}$$

Performance analysis of the open-loop dynamics includes identifying the conditions whereby the robot could stall (*e.g.* forward velocity is reduced to zero) according to the dynamic equations. Similarly, closed-loop stall conditions were also determined in addition to a more general analysis of the deterministic closed-loop performance with respect to control law tuning. Furthermore, stability analysis in the context of the robotic bulldozing operation involved showing that the closed-loop trajectories of d_a and v_b converge to their steady state optimal values.

8.2 Open-Loop Stall Conditions

Open-loop stall conditions can exist whereby the steady state robot speed diminishes to zero, *i.e.* $v_b = 0$. A set of open-loop steady state stall conditions were found using Eq. (8.2) and setting $\hat{v}_{b,k+1} = v_{b,k} = 0$ resulting in:

$$C_{tr} + C_{21,\Gamma} \cdot d_{a,k} + C_{23,\Gamma} \cdot r_{b,k} = 0 \tag{8.5}$$

Solving Eq. (8.5) for $d_{a,k} = d_{a,\Gamma,stall}$ gives the open-loop stall material accumulation:

$$d_{a,\Gamma,stall} = -\frac{C_{23,\Gamma} \cdot r_{b,k} + C_{tr}}{C_{21,\Gamma}} \tag{8.6}$$

Alternatively, solving Eq. (8.6) for $r_{b,k} = r_{b,\Gamma,stall}$ gives the open-loop stall blade position reference:

$$r_{b,\Gamma,stall} = -\frac{C_{tr} + C_{21,\Gamma} \cdot d_{a,k}}{C_{23,\Gamma}} \tag{8.7}$$

The stall condition equations Eq. (8.6) and Eq. (8.7) show that while there is coupling between the d_a and v_b state trajectories, either d_a or r_b can cause stall independently with sufficiently large magnitudes.

The open-loop system d_a and v_b trajectories are important when considering stall conditions. The conditions where v_b is decreasing, *i.e.* $v_{b,k+1} - v_{b,k} < 0$, are found using Eq. (8.2) as follows:

$$C_{tr} + C_{21,\Gamma} \cdot d_{a,k} + \left(C_{22,\Gamma} - 1\right) \cdot v_{b,k} + C_{23,\Gamma} \cdot r_{b,k} < 0 \tag{8.8}$$

Solving Eq. (8.8) for $r_{b,k} = r_{b,\Gamma,v-}$ gives:

$$r_{b,\Gamma,v-} < -\frac{C_{tr} + C_{21,\Gamma} \cdot d_{a,k} + \left(C_{22,\Gamma} - 1\right) \cdot v_{b,k}}{C_{23,\Gamma}} \tag{8.9}$$

The conditions where d_a is increasing, *i.e.* $d_{a,k+1} - d_{a,k} > 0$, are found using Eq. (8.1) as follows:

$$C_{11,\Gamma} \cdot v_{b,k} \cdot d_{a,k} + C_{12,\Gamma} \cdot v_{b,k} \cdot r_{b,k} + v_{b,k} \cdot H_{\Gamma,k} > 0 \tag{8.10}$$

Solving Eq. (8.10) for $r_{b,k} = r_{b,d+}$ (Note: $C_{12} < 0$) gives:

$$r_{b,\Gamma,d+} < -\frac{C_{11,\Gamma} \cdot d_{a,k} + H_{\Gamma,k}}{C_{12,\Gamma}} \tag{8.11}$$

Eq. (8.11) shows that the direction of change in the d_a dynamics is strongly influenced by the sign of $H_{\Gamma,k}$, which is an uncontrollable external input. For a constant r_b, the dynamics of d_a either increase uncontrollably toward the stall condition $d_{a,stall}$ or decrease toward zero. In any case, the natural system constraint $d_{a,max}$ is a limiting factor regarding whether stall will occur on not. Conversely, according to Eq. (8.9) if stall occurs, recovery of robot velocity can be achieved with any blade position $r_{b,k} \geq r_{b,\Gamma,v-}$.

A worst case blade position stall condition, $r_{b,\Gamma,stall,min}$, can be calculated for which any $r_b > r_{b,\Gamma,stall,min}$ will allow v_b to increase when $d_a = d_{a,max}$ and $v_b = 0$. Using eq. (8.7) and substituting $d_{a,k} = d_{a,max}$ gives:

$$r_{b,\Gamma,stall,min} = -\frac{C_{21,\Gamma} \cdot d_{a,max} + C_{tr}}{C_{23,\Gamma}} \tag{8.12}$$

If the magnitude of the worst case blade position stall condition is greater than the minimum blade constraint, *i.e.* $\left|r_{b,\Gamma,stall,min}\right| > r\left|_{b,min}\right|$, then open-loop stall cannot occur.

The values of minimum open-loop blade position to avoid stall, $r_{b,\Gamma,stall,min}$, were calculated for each mode using the estimated dynamic equation parameters in Table 5.6 and $d_{a,max}$ = 55 mm. These $r_{b,min,stall}$ values are tabulated in Table 8.1. Since $r_{b,\Gamma,stall,min} > r_{b,min}$ for Γ = 2 and 4, open loop stall can occur for these modes.

Table 8.1 Calculated $r_{b,\Gamma,stall,min}$ values for modes 2-5 and 7.

	Mode, Γ				
	2	3	4	5	7
$r_{b,\Gamma,stall,min}$ (mm)	-5	-29	-5	-16	-16

8.3 Closed-Loop Dynamic Equations

Setting $r_{b,k} = r^*_{b,k,\Gamma}$ and substituting the optimal blade control equations Eq. (8.3) and Eq. (8.4) into the open-loop prediction equations Eq. (8.1) and Eq. (8.2) , gives the closed-loop dynamic equations for $d^{cl}_{a,k+1,\Gamma}$ and $v^{cl}_{b,k+1,\Gamma}$ for each mode. The resulting mode 3 closed-loop dynamic equations are:

$$d^{cl}_{a,k+1,3} = d_{a,k} + v_{b,k} \cdot H_{\Gamma,k} \cdots \\ + \frac{\left(C_{12,3} \cdot C_{23,3} \cdot d_{a,k} \cdot v_{b,k} + C^2_{12,3} \cdot C_{21,3} \cdot d_{a,k} \cdot v^2_{b,k} + C^2_{12,3} \cdot C_{tr} \cdot v^2_{b,k} + C^2_{12,3} \cdot C_{22,3} \cdot v^3_{b,k} + C_{12,3} \cdot C_{23,3} \cdot v^2_{b,k} \cdot H_{3,k}\right)}{2 \cdot \left(R_3 - C_{12,3} \cdot C_{23,3} \cdot v_{b,k}\right)} \quad (8.13)$$

and

$$v^{d}_{b,k+1,3} = C_{21,3} \cdot d_{a,k} + C_{22,3} \cdot v_{b,k} + C_{tr} \cdots$$
$$+ \frac{\left(C_{23,3}^{2} \cdot d_{a,k} + C_{23,3}^{2} \cdot v_{b,k} \cdot H_{3,k} + \left(C_{23,3}^{2} \cdot C_{11,3} + C_{23,3} \cdot C_{12,3} \cdot C_{21,3}\right) \cdot d_{a,k} \cdot v_{b,k} + C_{23,3} \cdot C_{12,3} \cdot C_{tr} \cdot v_{b,k} + C_{23,3} \cdot C_{12,3} \cdot C_{22,3} \cdot v_{b,k}^{2}\right)}{2 \cdot \left(R_{3} - C_{12,3} \cdot C_{23,3} \cdot v_{b,k}\right)} \quad (8.14)$$

The resulting closed-loop dynamic equations for modes 2, 4, 5 and 7 are:

$$d^{cl}_{a,k+1,\Gamma} = d_{a,k} + C_{11,\Gamma} \cdot d_{a,k} \cdot v_{b,k} + v_{b,k} \cdot H_{\Gamma,k} - \frac{C_{12,\Gamma}}{2 \cdot \left(C_{23,\Gamma} + \mathrm{R}_{\Gamma}\right)} \cdot C_{tr} \cdot v_{b,k} + C_{21,\Gamma} \cdot d_{a,k} \cdot v_{b,k} + C_{22,\Gamma} \cdot v_{b,k}^{2} \quad (8.15)$$

and

$$v^{cl}_{b,k+1,\Gamma} = C_{21,\Gamma} \cdot d_{a,k} + C_{22,\Gamma} \cdot v_{b,k} + C_{tr} - \frac{C_{23,\Gamma} \cdot \left(C_{tr} + C_{21,\Gamma} \cdot d_{a,k} + C_{22,\Gamma} \cdot v_{b,k}\right)}{2 \cdot \left(C_{23,\Gamma} + \mathrm{R}_{\Gamma}\right)} \quad (8.16)$$

The closed-loop steady-state equations for each mode may be found using Eqs. (8.13)-(8.16) by setting $d^{cl}_{a,k,\Gamma} = d^{cl}_{a,k+1,\Gamma} = d_{a,ss,\Gamma}$ and $v^{cl}_{b,k,\Gamma} = v^{cl}_{b,k+1,\Gamma} = v_{b,ss,\Gamma}$ then solving for $d_{a,ss,\Gamma}$ and $v_{b,ss,\Gamma}$. The resulting mode 3 steady-state d_a and v_b equations are:

$$v_{b,ss,3} = \left(\frac{\left(4 \cdot C_{12,3} \cdot C_{21,3} \cdot C_{23,3} \cdot C_{tr} + C_{23,3}^{2} \cdot \left(C_{22,3}^{2} - 2 \cdot C_{22,3} + 1\right)\right)}{4 \cdot C_{12,3}^{2} \cdot C_{21,3}^{2}} - \frac{C_{23,3}^{2}}{C_{12,3}^{2} \cdot C_{21,3}} \cdot H_{3} - \frac{2}{C_{12,3}^{2}} \cdot H_{3} \cdot \mathrm{R}_{3} \right)^{1/2} \cdots$$
$$+ \frac{C_{23,3} \cdot \left(C_{22,3} - 1\right)}{2 \cdot C_{12,3} \cdot C_{21,3}} \quad (8.17)$$

and

$$d_{a,ss,3} = \frac{\left(-C_{22,3} \cdot C_{12,3}^{2} \cdot v_{b,ss,3}^{2} - C_{tr} \cdot C_{12,3}^{2} \cdot v_{b,ss,3} + C_{23,3} \cdot C_{12,3} \cdot H_{3} \cdot v_{b,ss,3} - 2 \cdot H_{3} \cdot \mathrm{R}_{3}\right)}{\left(C_{12,3} \cdot C_{23,3} + 2 \cdot C_{11,\Gamma} \cdot \mathrm{R}_{3} + \left(C_{12,3}^{2} \cdot C_{21,3} - C_{12,3} \cdot C_{11,3} \cdot C_{23,3}\right) \cdot v_{b,ss,3}\right)} \quad (8.18)$$

The resulting steady-state d_a and v_b equations for modes 2, 4 and 5 are:

$$v_{b,ss,\Gamma} = \frac{\left(-C_{11,\Gamma} \cdot C_{23,\Gamma} \cdot C_{tr} + C_{23,\Gamma} \cdot C_{21,\Gamma} \cdot H_{\Gamma} - 2 \cdot C_{11,\Gamma} \cdot C_{tr} \cdot \mathrm{R}_{\Gamma} + 2 \cdot C_{21,\Gamma} \cdot H_{\Gamma} \cdot \mathrm{R}_{\Gamma}\right)}{\left(C_{12,\Gamma} \cdot C_{21,\Gamma} - C_{11,\Gamma} \cdot C_{23,\Gamma} \cdot \left(2 + C_{22,\Gamma}\right) + 2 \cdot C_{11,\Gamma} \cdot \left(C_{22,\Gamma} - 1\right) \cdot \mathrm{R}_{\Gamma}\right)} \quad (8.19)$$

and

$$d_{a,ss,\Gamma} = \frac{\left(C_{12,\Gamma} \cdot C_{tr} - 2 \cdot C_{23,\Gamma} \cdot H_{\Gamma} - 2 \cdot H_{\Gamma} \cdot \mathrm{R}_{\Gamma} + C_{12,\Gamma} \cdot C_{22,\Gamma} \cdot v_{b,ss,\Gamma}\right)}{2 \cdot \left(C_{11,\Gamma} \cdot C_{23,\Gamma} - C_{12,\Gamma} \cdot C_{21,\Gamma} + C_{11,\Gamma} \cdot \mathrm{R}_{\Gamma}\right)} \quad (8.20)$$

The steady-state d_a and v_b equations for mode 7 are a special case. Recall from Chapter 3 that mode 7 is defined by the robot near the edge of the task space and pushing material into the removal space. Thus, in mode 7, d_a tends to decrease until the robot reaches the edge where d_a must become zero (or negative due to the removal space being below the grade of the floor). The mode 7 parameters estimated in Chapter 5 support this tendency. The mode 7 parameters of the d_a dynamic equation Eq. (3.14) are $C_{da3,7}$ = -17.6 mm^{-1} and $C_{da4,7}$ = 3.2 mm^{-1}. These parameters form terms with h_b and $h_{\delta r}$, respectively, which tend to have values of similar magnitude. Since $C_{da3,7}$ is negative and its magnitude is much larger than $C_{da4,7}$, the d_a dynamics will almost always be negative. The steady state d_a and v_b equations for the mode 7 were derived by setting $d_{a,k,7}^{cl} = d_{a,k+1,7}^{cl} = d_{a,ss,7} = 0$ and $v_{b,k,7}^{cl} = v_{b,k+1,7}^{cl} = v_{b,ss,7}$ then solving for $v_{b,ss,7}$, resulting in:

$$v_{b,ss,7} = \frac{C_{tr} \cdot \left(C_{23,7} + 2 \cdot \mathrm{R}_7\right)}{2 \cdot C_{23,7} - C_{22,7} \cdot C_{23,7} + 2 \cdot \left(1 - C_{22,7}\right) \cdot \mathrm{R}_7} \quad (8.21)$$

An example of the simulated deterministic closed-loop dynamics switching between multiple modes is shown in Fig. 8.1. These plots show that d_a and v_b converge to their optimum steady-state equilibrium values, and that the steady-state optima depend on both H_Γ and Γ.

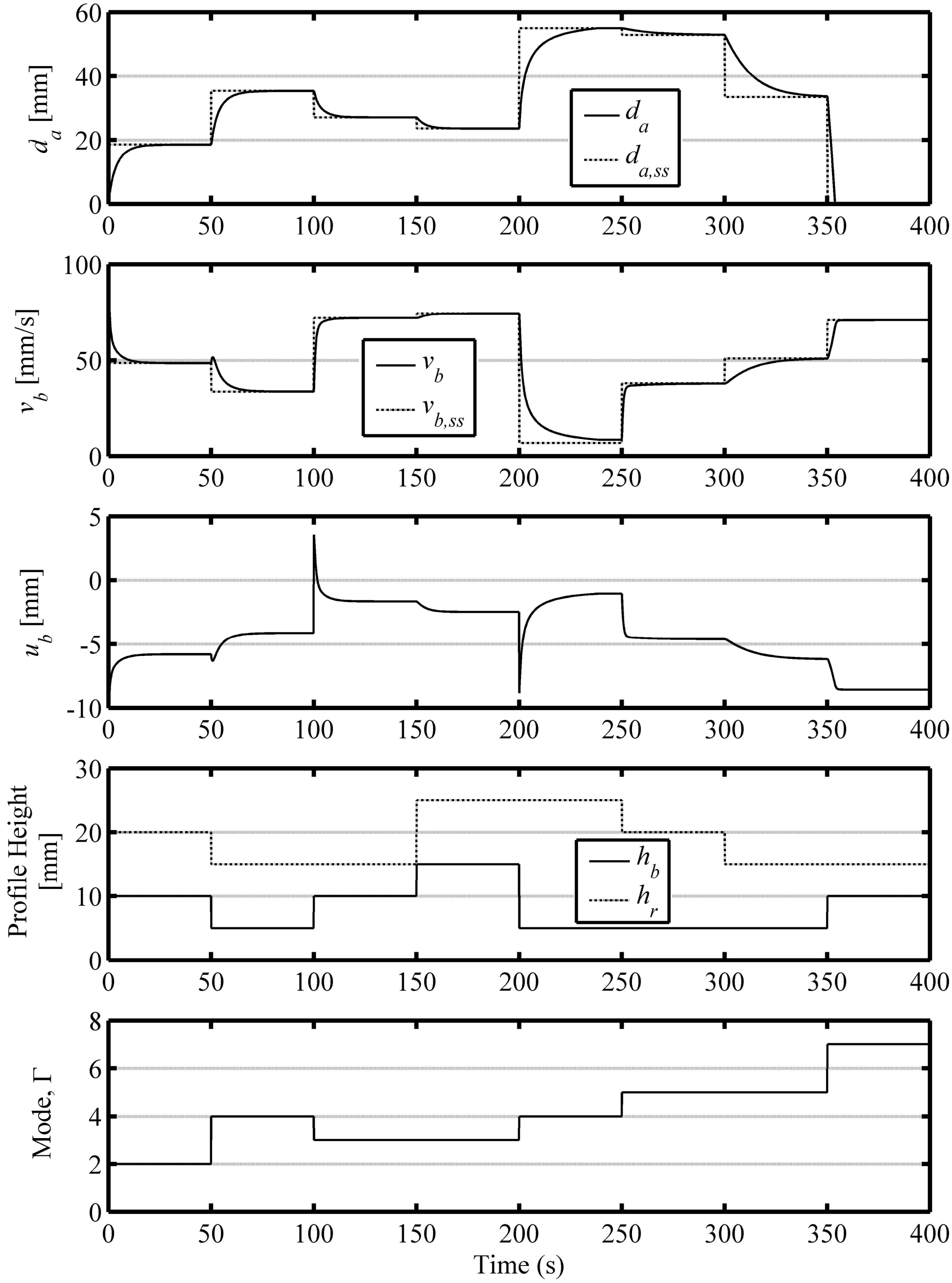

Fig. 8.1 Simulation of deterministic bulldozing dynamics with mode transitions.

Values of $d_{a,ss,\Gamma}$ and $v_{b,ss,\Gamma}$ were calculated over a range of H_Γ values and a range of R_Γ values for modes Γ = 2-5 and 7 using Eqs. (8.17)-(8.20). The values of H_Γ were determined experimentally. They were calculated using Eq. (7.1) with the measured values of h_a, h_b, $h_{r,l}$ and $h_{r,r}$ from the mode-segmented system identification data sets described in Chapter 5. The range of H_Γ values used for the calculations of $d_{a,ss,\Gamma}$ and $v_{b,ss,\Gamma}$ includes the minimum, $H_{\Gamma,min}$, the mean $\bar{H}_\Gamma$ and the maximum, $H_{\Gamma,max}$. The $H_{\Gamma,min}$, $\bar{H}_\Gamma$ and $H_{\Gamma,max}$ values from the experimental data sets for modes Γ = 2-5 and 7 are tabulated in Table 8.2.

Table 8.2 Experimental values of $H_{\Gamma,min}$, $\bar{H}_\Gamma$ and $H_{\Gamma,max}$ for modes 2-5 and 7.

	Mode, Γ				
	2	3	4	5	7
$H_{\Gamma,min}$ (s)	0.006	-0.0026	0.012	0.0044	-0.0077
$\bar{H}_\Gamma$ (s)	-0.005	-0.0096	0.0083	0	-0.029
$H_{\Gamma,max}$ (s)	0.0177	0.0029	0.017	0.0076	0

The steady state blade position, $r_{b,ss,\Gamma}$ was calculated over the ranges of H_Γ and R_Γ for modes Γ = 2-5 and 7 using Eq. (8.3) and Eq. (8.4), and substituting the values of $d_{a,ss,\Gamma}$ and $v_{b,ss,\Gamma}$ for $d_{a,k}$ and $v_{b,k}$ respectively. The deterministic steady state material removal rate was calculated using $Q_{ss,\Gamma} = d_{a,ss,\Gamma} \cdot v_{b,ss,\Gamma} \cdot w_b$, with the experimental robot blade width w_b = 200 mm.

Plots of deterministic $d_{a,ss,\Gamma}$ values for modes Γ = 2-5 are shown in Fig. 8.2. Since $d_{a,ss,7}$ = 0, mode 7 was not included in Fig. 8.2. Recall from Chapter 3 and Chapter 5 that the d_a dynamics of modes 2, 4 and 5 are independent of blade position, which is indicated by parameter $C_{da5,\Gamma}$ = 0 in Eq. (3.14) and parameter $C_{12,\Gamma}$ = 0 in Eq. (8.1). Therefore, for these modes 2, 4 and 5, $d_{a,ss,\Gamma}$ is a function of H_Γ only.

Plots of deterministic $v_{b,ss,\Gamma}$ values for modes Γ = 2-5 and 7 are shown in Fig. 8.3. For modes 2, 4 and 5 $v_{b,ss,\Gamma}$ becomes larger as H_Γ decreases and becomes larger as R_Γ increases. For mode 3, $v_{b,ss,3}$ tends to become larger as H_3 decreases but the relationship with R_3 depends on H_3. For mode 7, $v_{b,ss,7}$ is independent of H_7 and is a function of R_7.

Plots of deterministic $r_{b,ss,\Gamma}$ values modes Γ = 2-5 and 7 are shown in Fig. 8.4. For mode 3, the results indicate that the equilibrium steady state blade position balances is a function of H_3 only. For modes 2, 4, 5 and 7 the steady state blade position increases as R increases and H increases. The effect of a larger magnitude of downward blade position resulting in a smaller $v_{b,ss,\Gamma}$ for modes 2, 4, 5 and 7 is apparent in Fig. 8.3. As discussed in Chapter 3, as the blade pushes down further, the increased resistance due to friction causes the velocity to decrease.

Plots of deterministic $Q_{ss,\Gamma}$ for modes Γ = 2-5 are shown in Fig. 8.5. Since $Q_{ss,7}$ = 0, mode 7 was not included in Fig. 8.5. For modes 2, 4 and 5, $Q_{ss,\Gamma}$ clearly increases as

R_Γ increases. Conversely, for mode 3, $Q_{ss,3}$ clearly decreases as R_3 increases. From these results, the best choice for blade control law tuning to maximize the material removal rate is to select $R_3 = 0$ for mode 3 and $R_\Gamma > 10$ for modes $\Gamma = 2, 4, 5$ and 7. However, this analysis neglects state disturbances and blade position constraints. It also assumes constant H_Γ, neglecting the dynamic response to H_Γ as it changes with respect to the material profile conditions. Therefore, when implemented experimentally, these extreme tuning values may not be appropriate. The next chapter addresses the inclusion of state disturbances, blade position constraints and a stochastic model of H_Γ.

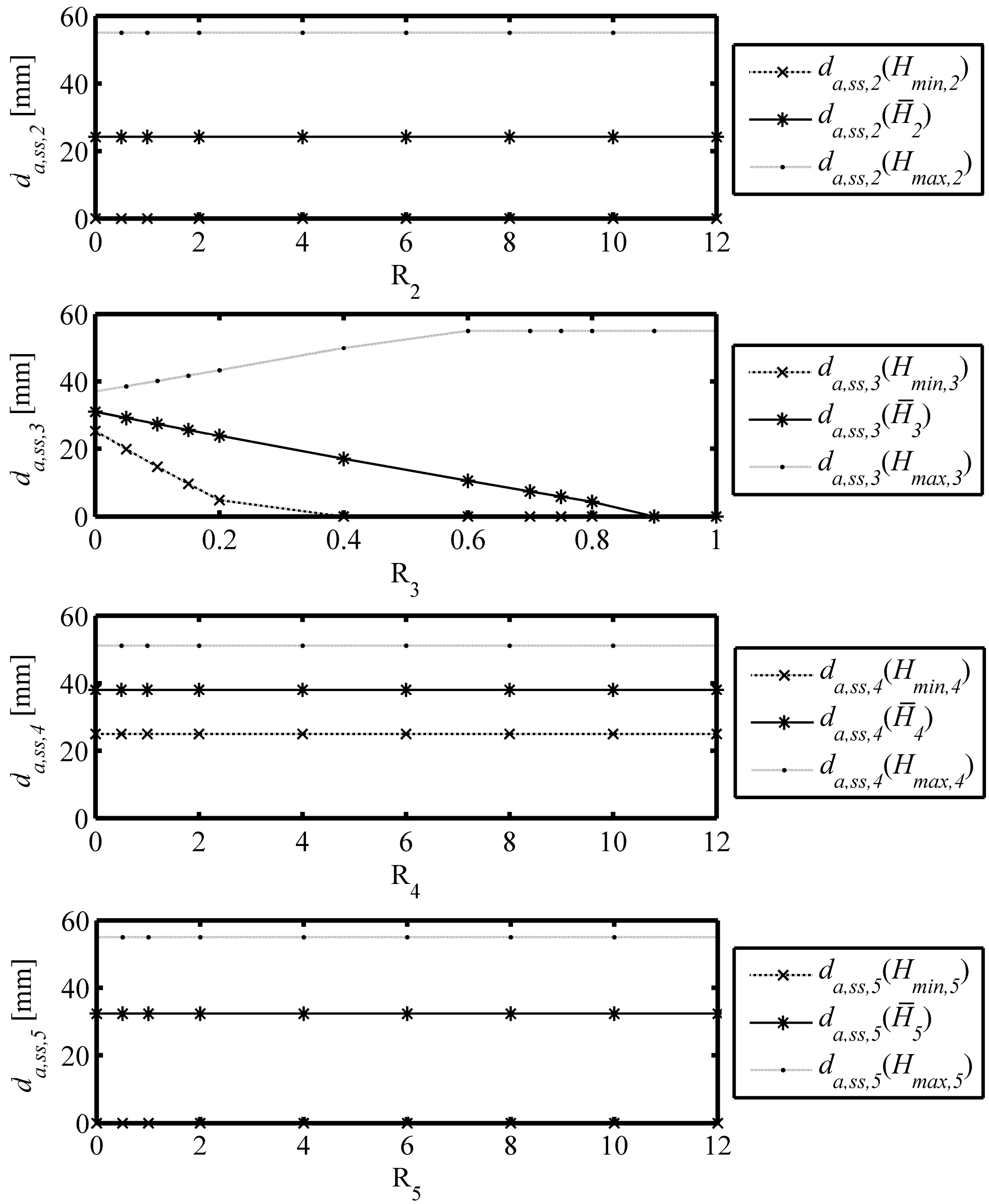

Fig. 8.2 Calculated deterministic $d_{a,ss,\Gamma}$ values for Γ = 2-5 and 7.

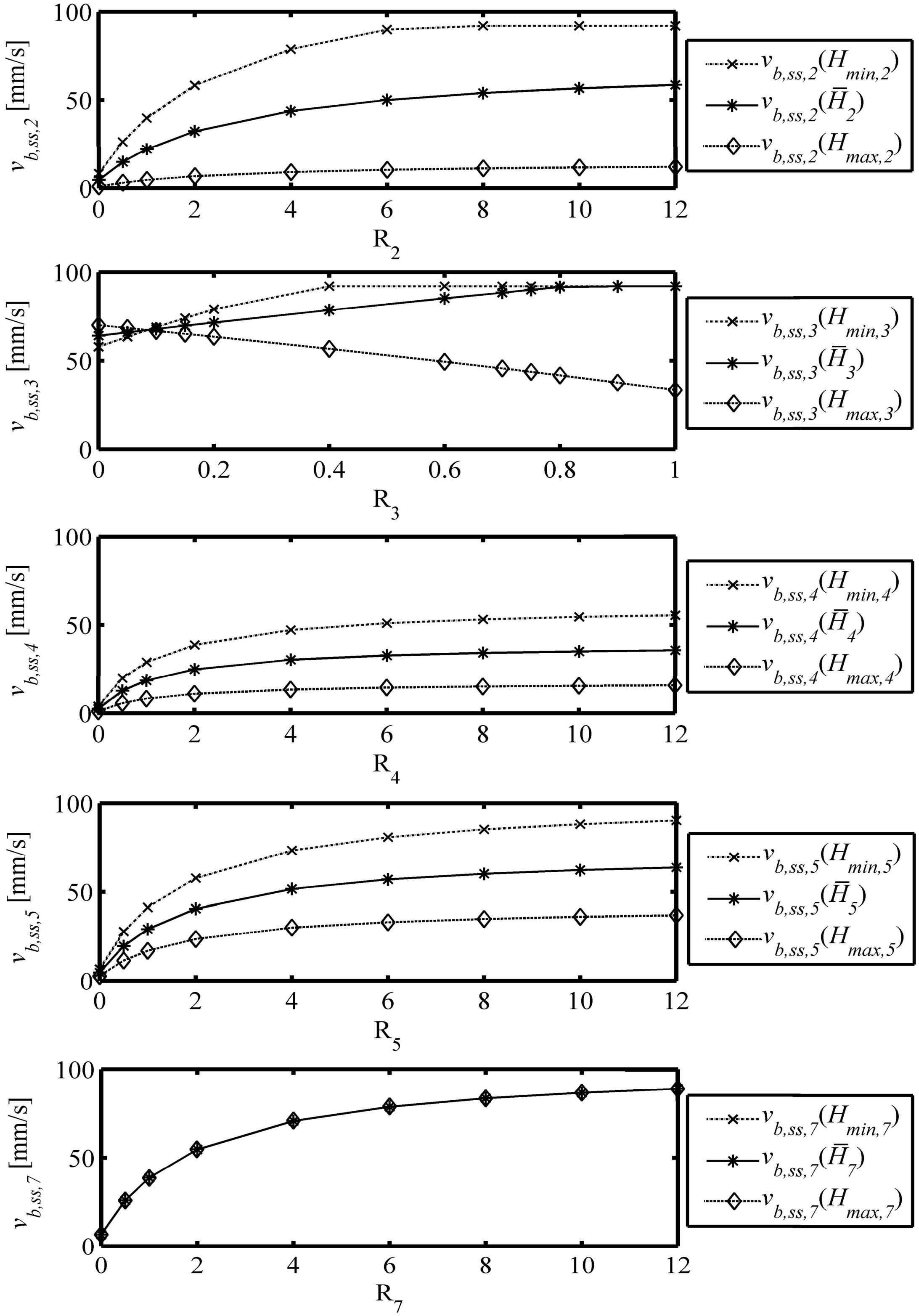

Fig. 8.3 Calculated deterministic $v_{b,ss,\Gamma}$ values for Γ = 2-5 and 7.

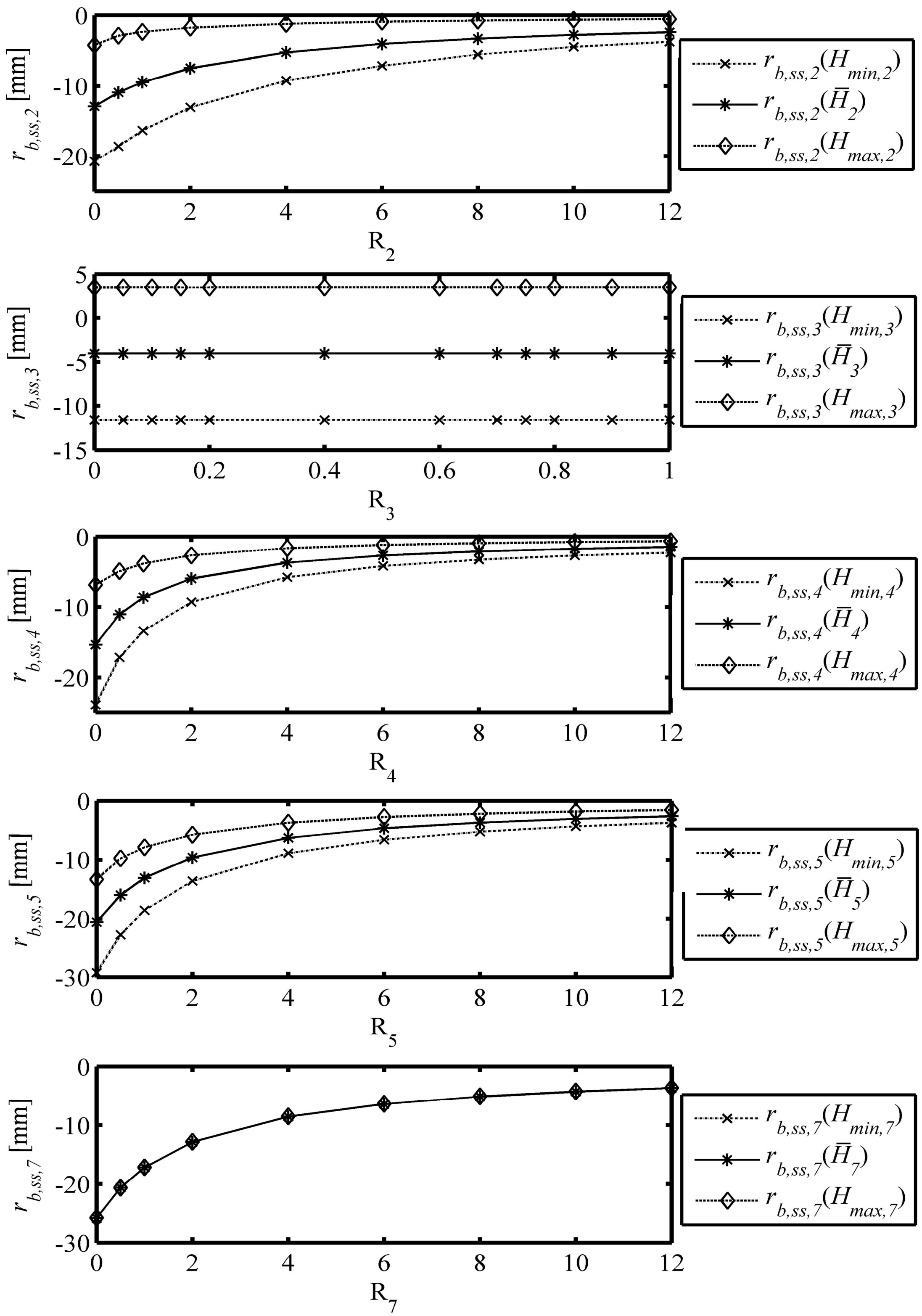

Fig. 8.4 Calculated deterministic $r_{b,ss,\Gamma}$ values for Γ = 2-5 and 7.

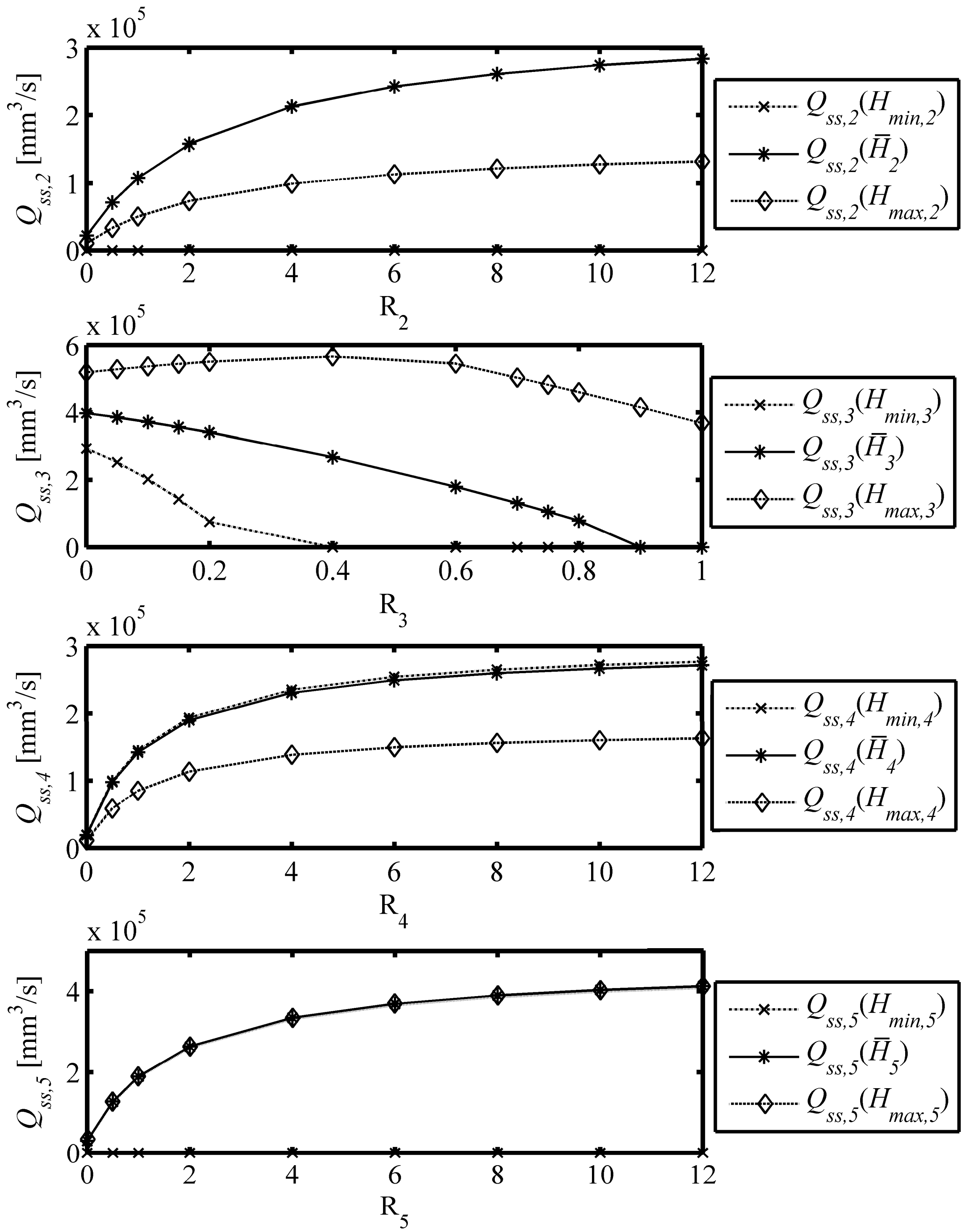

Fig. 8.5 Calculated deterministic $Q_{ss,\Gamma}$ values for Γ = 2-5 and 7.

8.4 Closed-Loop Stall Conditions

Similar to the open-loop stall conditions discussed previously, closed-loop stall conditions can exist whereby the robot speed diminishes to zero. A set of closed-loop stall conditions were found using the steady state robot velocity equations and setting $v_{b,ss,\Gamma} = 0$.

For mode Γ = 3, using Eq. (8.17), setting $v_{b,ss,3} = 0$ and solving for $H_3 = H_{3,cl,stall}$ results in the closed-loop stall H condition:

$$H_{3,cl,stall} = \frac{C_{23,3} \cdot C_{12,3} \cdot C_{tr}}{\left(C_{23,3}^2 + 2 \cdot C_{21,3} \cdot R_3\right)} \tag{8.22}$$

and alternatively, solving for $R_3 = R_{3,stall}$ results in the closed-loop stall control law tuning condition:

$$R_{3,stall} = \frac{C_{23,3} \cdot C_{12,3} \cdot C_{tr}}{2 \cdot C_{21,3} \cdot H_3} - \frac{C_{23,3}^2}{2 \cdot C_{21,3}} \tag{8.23}$$

For modes Γ = 2, 4 and 5, using Eq. (8.19), setting $v_{b,ss,\Gamma} = 0$ and solving for $H_\Gamma = H_{\Gamma,cl,stall}$ results in:

$$H_{\Gamma,cl,stall} = \frac{C_{11,\Gamma} \cdot C_{tr}}{C_{21,\Gamma}} \tag{8.24}$$

and alternatively, solving for $R_\Gamma = R_{\Gamma,stall}$ results in:

$$R_{\Gamma,cl,stall} = -\frac{C_{23,\Gamma}}{2} \tag{8.25}$$

For mode Γ = 7, using Eq. (8.21), setting $v_{b,ss,7} = 0$ and solving for $R_7 = R_{7,stall}$ results in two solutions:

$$\mathrm{R}_{7,stall,1} = -\frac{C_{23,7}}{2} \tag{8.26}$$

and

$$\mathrm{R}_{7,stall,2} = \frac{-2 \cdot C_{23,7} + C_{22,7} \cdot C_{23,7}}{2 \cdot \left(1 - C_{22,7}\right)} \tag{8.27}$$

Note Eq. (8.21) is independent of H_7.

A set of closed-loop $d_{a,ss,\Gamma,stall}$ stall conditions were found using the steady state material accumulation equations and setting $v_{b,ss,\Gamma} = 0$. The condition $d_{a,ss,\Gamma,stall} > d_{a,max}$ is an indication that stall will not occur as a result of d_a.

For mode Γ = 3, using Eq. (8.18), setting $v_{b,ss,3} = 0$ and solving for $d_{a,ss,3} = d_{a,ss,3,stall}$ results in:

$$d_{a,ss,3,stall} = \frac{-2 \cdot H_3 \cdot R_3}{C_{12,3} \cdot C_{23,3} + 2 \cdot C_{11,\Gamma} \cdot R_3} \tag{8.28}$$

Substituting eq. (8.22) into (8.28) for $H_3 = H_{ss,3,stall}$ gives:

$$d_{a,ss,3,stall} = \frac{-2 \cdot C_{23,3} \cdot C_{12,3} \cdot C_{tr} \cdot \mathrm{R}_3}{\left(C_{12,3} \cdot C_{23,3} + 2 \cdot C_{11,\Gamma} \cdot \mathrm{R}_3\right) \cdot \left(C_{23,3}^2 + 2 \cdot C_{21,3} \cdot \mathrm{R}_3\right)} \tag{8.29}$$

For modes Γ = 2, 4 and 5 using Eq. (8.20), setting $v_{b,ss,\Gamma} = 0$ and solving for $d_{a,ss,\Gamma} = d_{a,ss,\Gamma,stall}$ results in:

$$d_{a,ss,\Gamma,stall} = \frac{C_{12,\Gamma} \cdot C_{tr} - 2 \cdot \left(C_{23,\Gamma} + R_{\Gamma}\right) \cdot H_{\Gamma}}{2 \cdot \left(C_{11,\Gamma} \cdot C_{23,\Gamma} - C_{12,\Gamma} \cdot C_{21,\Gamma} + C_{11,\Gamma} \cdot R_{\Gamma}\right)} \tag{8.30}$$

Substituting eq. (8.24) into (8.30) for $H_{\Gamma} = H_{ss,\Gamma,stall}$ gives:

$$d_{a,ss,\Gamma,stall} = \frac{-C_{12,\Gamma} \cdot C_{tr} + 2 \cdot C_{11,\Gamma} \cdot C_{tr} \cdot \left(C_{23,\Gamma} + R_{\Gamma}\right)}{2 \cdot C_{21,\Gamma}^{2} \cdot C_{12,\Gamma} - 2 \cdot C_{11,\Gamma} \cdot C_{21,\Gamma} \cdot \left(C_{23,\Gamma} + R_{\Gamma}\right)} \tag{8.31}$$

Another closed loop stall condition to consider is the worst case closed-loop blade position, $r_{b,stall,\Gamma,min}^{cl}$, which is the minimum blade position reference that the control law will provide for the worst stall case of $d_a = d_{a,max}$ and $v_b = 0$. If the worst case closed-loop blade position is greater than the worst case open-loop blade position stall condition, *i.e.* $r_{b,\Gamma,stall,min}^{cl} > r_{b,\Gamma,stall,min}$, then closed-loop stall will not occur.

For mode 3, using eq. (8.3), substituting $d_{a,k} = d_{a,max}$ and $v_{b,k} = 0$ then solving for $r_{b,k,3}^{*} = r_{b,3,stall,min}^{cl}$ gives:

$$r_{b,3,stall,min}^{cl} = \frac{C_{23,3} \cdot d_{a,max}}{2 \cdot R_{3}} \tag{8.32}$$

Since $R_3 > 0$ and $C_{23,3} > 0$, then $r_{b,3,stall,min}^{cl} > 0$. Considering the open-loop stall blade position in Eq. (8.12), $C_{21,3} > 0$ and $C_{tr} > 0$, then $r_{b,\Gamma,stall,min} < 0$. Therefore, since $r_{b,3,stall,min}^{cl} > r_{b,3,stall,min}$, closed loop stall cannot occur for any value of R_3.

For modes Γ = 2, 4, 5 and 7, using eq. (8.4), substituting $d_{a,k} = d_{a,max}$ and $v_{b,k} = 0$ then solving for $r_{b,k,\Gamma}^{*} = r_{b,\Gamma,stall,min}^{cl}$ gives:

$$r^{cl}_{b,\Gamma,stall,min} = \frac{-\left(C_{tr} + C_{21,\Gamma} \cdot d_{a,max}\right)}{2 \cdot \left(C_{23,\Gamma} + R_{\Gamma}\right)} \tag{8.33}$$

The largest magnitude of $r^{cl}_{b,\Gamma,stall,min}$ for Γ = 2, 4, 5 and 7 is for $R_{\Gamma} = 0$, thus this represents the worst case of blade control law tuning.

For all modes, Γ = 2-5 and 7, the values of $R_{\Gamma,stall}$, $d_{a,ss,\Gamma,stall}$ and $r^{cl}_{b,stall,\Gamma,min}$ were calculated using the estimated dynamic equation parameters in Table 5.6, $d_{a,max}$ = 55 mm and a worst case value of $R_{\Gamma} = 0$ for Γ = 2, 4, 5 and 7, and a worst case value of $R_3 = 1$. These calculated values are tabulated in Table 8.3. For all modes, Γ = 2-5 and 7, the conditions hold for $R_{\Gamma,stall} < 0$, $d_{a,ss,\Gamma,stall} < d_{a,max}$ and $r^{cl}_{b,stall,\Gamma,min} > r_{b,stall,\Gamma,min}$, therefore, closed loop stall will not occur for any control law tuning value $R_{\Gamma,stall} \geq 0$.

Table 8.3 Calculated values of $R_{\Gamma,stall}$, $d_{a,ss,\Gamma,stall}$ and $r^{cl}_{b,stall,\Gamma,min}$ for Γ = 2-5 and 7.

	Mode, Γ				
	2	3	4	5	7
$R_{\Gamma,stall}$	-0.18	N/A	-0.082	-0.11	-0.13, -2
$d_{a,ss,\Gamma,stall}$ (mm)	79	108	62	110	N/A
$r^{cl}_{b,stall,\Gamma,min}$ (mm)	-3	N/A	-2	-8	-8

8.5 Lyapunov Stability Analysis

Simulation results, such as those shown in Fig. 8.1, support the conclusion that the closed-loop system is stable. Lyapunov’s second method was used to more rigorously analyze the stability of the deterministic elements of the nonlinear discrete-time closed-loop system. The vector of controlled states is $\mathbf{x}_k = \left[d_{a,k,\Gamma}^{cl} \quad v_{b,k,\Gamma}^{cl} \right]^{\mathrm{T}}$. The deterministic system is globally asymptotically stable, if there exists a Lyapunov function $V\left(\mathbf{x}\right)$ with the following properties:

1. $V\left(\mathbf{x}_{eq}\right) = 0$ where $\mathbf{x}_{eq} = \left[d_{a,ss,\Gamma} \quad v_{b,ss,\Gamma} \right]^{\mathrm{T}}$,
2. $V\left(\mathbf{x}_k\right) > 0 \ \ \forall \mathbf{x} \neq \mathbf{x}_{eq}$,
3. $\left|V\left(\mathbf{x}\right)\right| \to \infty \ \forall \left\|\mathbf{x}\right\| \to \infty$,
4. $\Delta V\left(\mathbf{x}_k\right) = V\left(\mathbf{x}_{k+1}\right) - V\left(\mathbf{x}_k\right) < 0 \ \ \forall \mathbf{x}_k \neq \mathbf{x}_{eq}$ and
5. $\Delta V\left(\mathbf{x}_{eq}\right) = 0$.

The following quadratic function was studied for each mode:

$$\begin{aligned} V_\Gamma\left(\mathbf{x}_k\right) &= \left[\mathbf{x}_k - \mathbf{x}_{eq}\right]^{\mathrm{T}} \begin{bmatrix} \alpha_{V,\Gamma} & 0 \\ 0 & 1 \end{bmatrix} \left[\mathbf{x}_k - \mathbf{x}_{eq}\right] \\ &= \alpha_{V,\Gamma} \cdot \left(d_{a,k,\Gamma}^{cl} - d_{a,ss,\Gamma}\right)^2 + \left(v_{b,k,\Gamma}^{cl} - v_{b,ss,\Gamma}\right)^2 \end{aligned} \tag{8.15}$$

This Lyapunov function candidate satisfies the first three stability conditions for any $\alpha_{V,\Gamma} > 0$. Conditions 4 and 5 will only be satisfied if a suitable value of the $\alpha_{V,\Gamma}$ can be found. Unfortunately, proving the fourth stability condition analytically was found to be intractable. For instance, using the Matlab Symbolic Toolbox, it was found that the resulting $\Delta V_\Gamma\left(\mathbf{x}_{eq}\right)$ analytical equation for $\Gamma = 3$ has 57814 irreducible terms. Therefore, a numerical solution was employed. For each dynamic mode, a minimum value of $\alpha_{V,\Gamma}$ was found numerically such that $\Delta V_\Gamma\left(\mathbf{x}_k\right) < 0$ for all values of $\mathbf{x}_k \neq \mathbf{x}_{eq}$ using a four dimensional exhaustive grid search over the operation ranges: d_a = [0, $d_{a,max}$] in increments of 1 mm, where $d_{a,max}$ = 55 mm; v_b = [0, $v_{b,max}$] in increments of 1 mm/s, where $v_{b,max}$ = 92 mm/s; H_Γ = [$H_{\Gamma,min}$ $H_{\Gamma,max}$] in increments of 0.0001 s; R_Γ = [0 12] in increments of 1 for Γ = 2, 4, 5 and 7; and R_3 = [0 1] in increments of 0.1 for Γ = 3. The searches terminated successfully, producing the $\alpha_{V,\Gamma}$ values tabulated in Table 8.4 for Γ = 2-5 and 7. Examples of $\Delta V_\Gamma(\mathbf{x}_k)$ calculated over the ranges of d_a and v_b, $H_\Gamma = \bar{H}_\Gamma$, $R_2 = R_4 = R_5 = R_6 = 4$ and $R_3 = 0.4$ for Γ = 2-5 and 7, are shown in Figs. 8.6-8.10.

Subject to the limitations of this numerical approach, these results support the conclusion that the optimal control laws provide locally asymptotic closed-loop stability for each mode. By extension, cycling between modes may occur. When a mode switch occurs, the exit conditions from the prior mode become the initial conditions of the next mode and the state trajectories will tend toward their equilibrium values for the next mode.

Table 8.4 Deterministic numerical Lyapunov stability $\alpha_{V,\Gamma}$ values for Γ = 2-5 and 7.

	Mode, Γ				
	2	3	4	5	7
$\alpha_{V,\Gamma}$	4.9	6.8	88.5	3.1	102.1

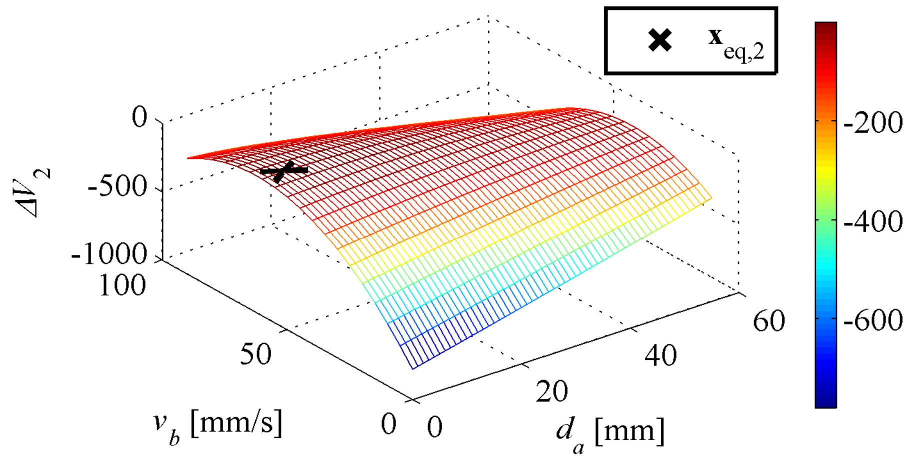

Fig. 8.6 Example of ΔV_2 calculated with $H_2 = \bar{H}_2$ and $R_2 = 4$.

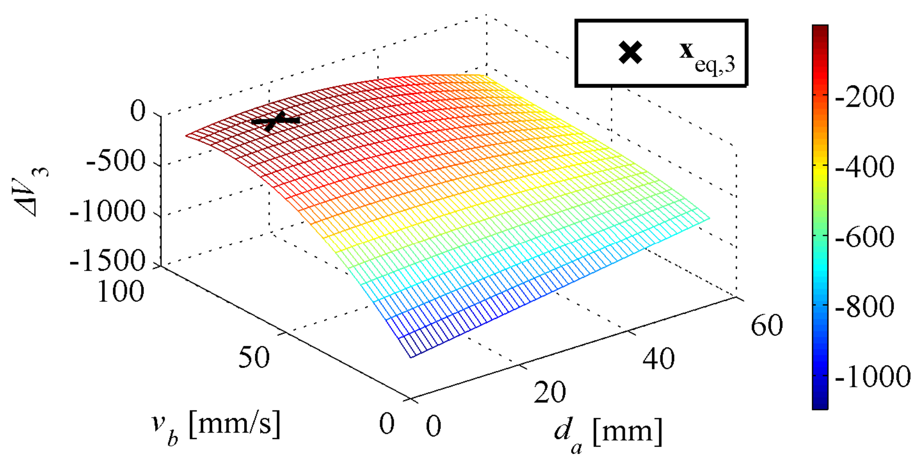

Fig. 8.7 Example of ΔV_3 calculated with $H_3 = \bar{H}_3$ and $R_3 = 0.4$.

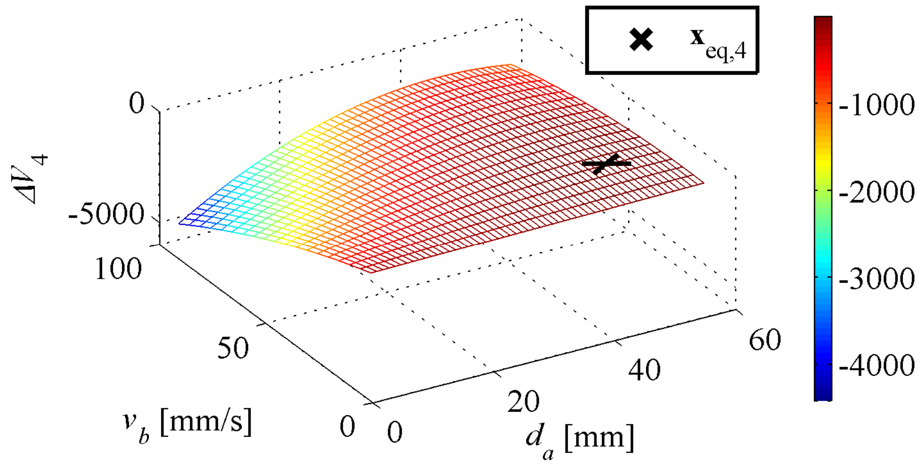

Fig. 8.8 Example of ΔV_4 calculated with $H_4 = \bar{H}_4$ and $R_4 = 4$.

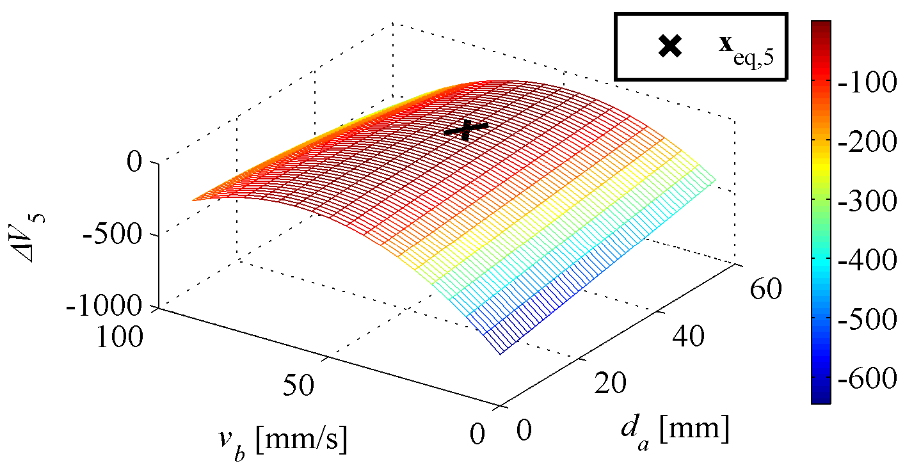

Fig. 8.9 Example of ΔV_5 calculated with $H_5 = \bar{H}_5$ and $R_5 = 4$.

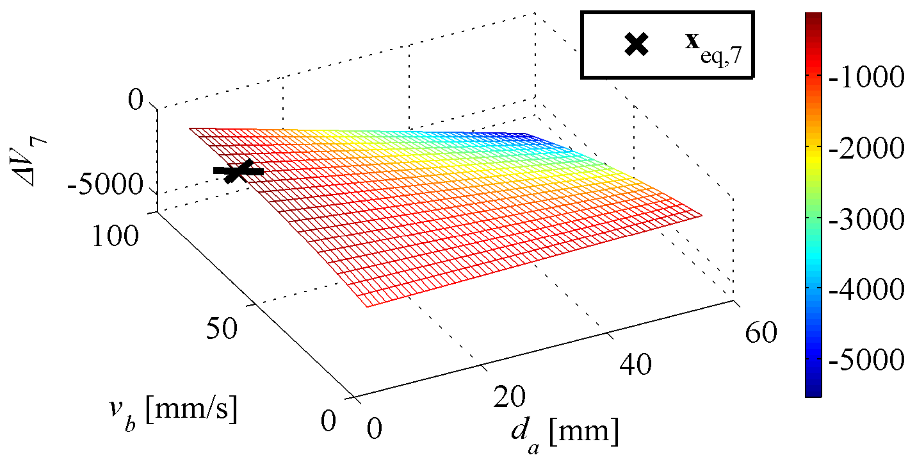

Fig. 8.10 Example of ΔV_7 calculated with $H_7 = \bar{H}_7$ and $R_7 = 4$.

8.6 Conclusions

Performance and stability were analyzed for the deterministic open-loop and closed-loop robot bulldozing process dynamics neglecting blade position constraints for modes Γ = 2, 4, 5 and 7. Open-loop and closed-loop stall conditions were identified whereby the robot velocity could diminish to zero. It was shown that for the experimental robot bulldozing system closed-loop stall cannot occur for any control law tuning value. A general analysis of the deterministic closed-loop performance was completed with respect to the experimental ranges of H_Γ and ranges of control law tuning R_Γ. From this analysis, it was shown that control law tuning maximizes the deterministic steady state material removal rate Q_{ss} with $R_3 = 0$ and $R_\Gamma > 10$ for modes Γ = 2, 4, 5 and 7. A numerical Lyapunov stability analysis showed that the deterministic closed-loop trajectories of d_a and v_b converge to their steady state optimal equilibrium values.

The next chapter addresses closed-loop performance and stability analysis of the stochastic robot bulldozing process dynamics incorporating the stochastic model of H_{Γ}, state disturbances and blade position constraints.

Chapter 9

Stochastic Performance and Stability Analysis

9.1 Introduction

This chapter presents a numerical analysis of the performance and stability of the stochastic closed-loop dynamics of modes Γ = 2-5 and 7. The effects of the zero mean stochastic residual process disturbances, $\hat{w}_{d,\Gamma}$ and $\hat{w}_{v,\Gamma}$, on the d_a and v_b dynamics were included. The EKF was not used in the stochastic closed-loop simulation analysis in this chapter[1]. The discrete-time one-step ahead prediction equations Eq. (7.2) and Eq. (7.3) were used to simulate the state dynamics with the residual process disturbances $\hat{w}_{d,\Gamma}$ and $\hat{w}_{v,\Gamma}$ included as in Eq.(6.23). The residual process disturbance standard deviations used for the stochastic simulation were from Table 6.3. The optimal control laws in Eq. (7.7) and Eq. (7.9) were used for simulation of closed-loop control. Also, the blade position constraints $r_{b,min} < r_b < r_{b,max}$ were included for all modes Γ = 2-5 and 7, where the state-dependent constraint $r_{b,max} = K_{rb} \cdot d_a$ with K_{rb} = 0.18 was determined in Chapter 7.

Monte Carlo simulation was used for performance and stability analysis of the stochastic, constrained, closed-loop, process dynamics. In addition to the inclusion of the

[1] Recall that the model parameters were obtained in Chapter 5 using low-pass filtered measurements. As shown in Chapter 6, the EKF provides similar smoothing behavior with less time delay than the low-pass filter. In the controller implementation, the EKF will be used rather than the low-pass filter. So a simulation without the EKF should provide a conservative estimate of the closed-loop dynamics.

state stochastic disturbances, a stochastic model of the H_Γ dynamics was included. The sets of stochastic simulation results included statistical distributions of process performance measures.

9.2 Stochastic Closed-loop Performance Analysis

9.2.1 Stochastic Model of the H_Γ Dynamics

The combined measured disturbances, H_Γ, were modeled as a random walk with a third-order autogressive (AR) model. A third-order model was found to be the lowest order for which the correlation function of the residuals was less than ±0.15 for lags up to 25. Higher-order models showed no improvement in the correlation function of the residuals. The AR models of the H_Γ dynamics for modes Γ = 2-5 and 7 take the form:

$$H_{\Gamma,k} = H_{k-1} + w_{H,\Gamma,k} \quad \text{and} \tag{9.1}$$

$$w_{H,\Gamma,k} = \eta_{H,\Gamma} + C_{H1,\Gamma} \cdot w_{H,k-1} + C_{H2,\Gamma} \cdot w_{H,k-2} + C_{H3,\Gamma} \cdot w_{H,k-3} \tag{9.2}$$

Where $C_{H1,\Gamma}$, $C_{H2,\Gamma}$ and $C_{H3,\Gamma}$ are the model coefficients, $w_{H,\Gamma,k}$ is the stochastic disturbance and $\eta_{H,\Gamma}$ is Gaussian zero mean random noise with standard deviation $\sigma_{\eta,H,\Gamma}$.

The AR model coefficients and noise standard deviation $\sigma_{\eta,H,\Gamma}$ were estimated using least squares regression on the differences between consecutive values of H_Γ for each sample within the mode-segmented set of experimental fitting data discussed in Chapter 5. The H_Γ values were calculated using Eq. (7.1) with the measured values of

h_a, h_b, $h_{r,l}$ and $h_{r,r}$. For instance, the AR model fitting data set of the differenced H_Γ values, ΔH_Γ, for modes Γ = 2-5 and 7 included:

$$\Delta H_\Gamma(i) = H_\Gamma(i) - H_\Gamma(i-1), \text{ for samples } i = 2, 3, \ldots, N_{s,\Gamma,total}^{fit} \tag{9.3}$$

where, $N_{s,\Gamma,total}^{fit}$ is the number of points in the segmented fitting data set per mode Γ. The least squares regression was implemented with the Matlab System Identification toolbox 'ar' function. The resulting AR model parameters and noise standard deviation $\sigma_{\eta,H,\Gamma}$ for modes Γ = 2-5 and 7 are tabulated in Table 9.1.

Table 9.1 Model parameters of the random walk H_Γ dynamics.

Mode, Γ	$C_{H1,\Gamma}$ (ms)	$C_{H2,\Gamma}$ (ms)	$C_{H3,\Gamma}$ (ms)	$\sigma_{\eta,H,\Gamma}$ (ms)
2	29	-93	-170	0.47
3	20	-180	-120	0.36
4	16	64	36	0.38
5	2.5	-83	-89	0.19
7	0.28	-32	-52	0.63

9.2.2 Monte Carlo Simulation

The Monte Carlo simulation was composed of two stages. In the first stage, a set of deterministic closed-loop simulations (*i.e.* disturbances set to zero) was completed for different values of R_Γ for each mode to determine the durations of the initial transients. Each set of deterministic closed-loop simulations included initial conditions exhaustively covering the full range of values [0, $d_{a,max}$], [0, $v_{b,max}$] and [$H_{\Gamma,min}$, $H_{\Gamma,max}$] with 28, 23 and 20 equal increments, respectively. The value of $d_{a,max}$ = 55 mm, the value of $v_{b,max}$ = 92 mm/s and the values of $H_{\Gamma,min}$, $H_{\Gamma,max}$ are from Table 8.2. Each simulation run was terminated when the changes in the d_a and v_b dynamics remained small over a period of time, *i.e.* $\Delta d_a < 0.001$ mm and $\Delta v_b < 0.001$ mm/s for a $10 \cdot T_s$ period. The settling times, $t_{set,da}$ and $t_{set,vb}$, were determined as the time when the d_a and v_b trajectories remained within 1% of their final steady state values. Plots of the deterministic settling times as a function of control law tuning R_Γ for each mode are shown in Fig. 9.1. These results show that the closed-loop response time increases exponentially as R_Γ decreases for Γ = 2, 4, 5 and 7. Conversely, the closed-loop response time increases more proportionately as R_3 increases.

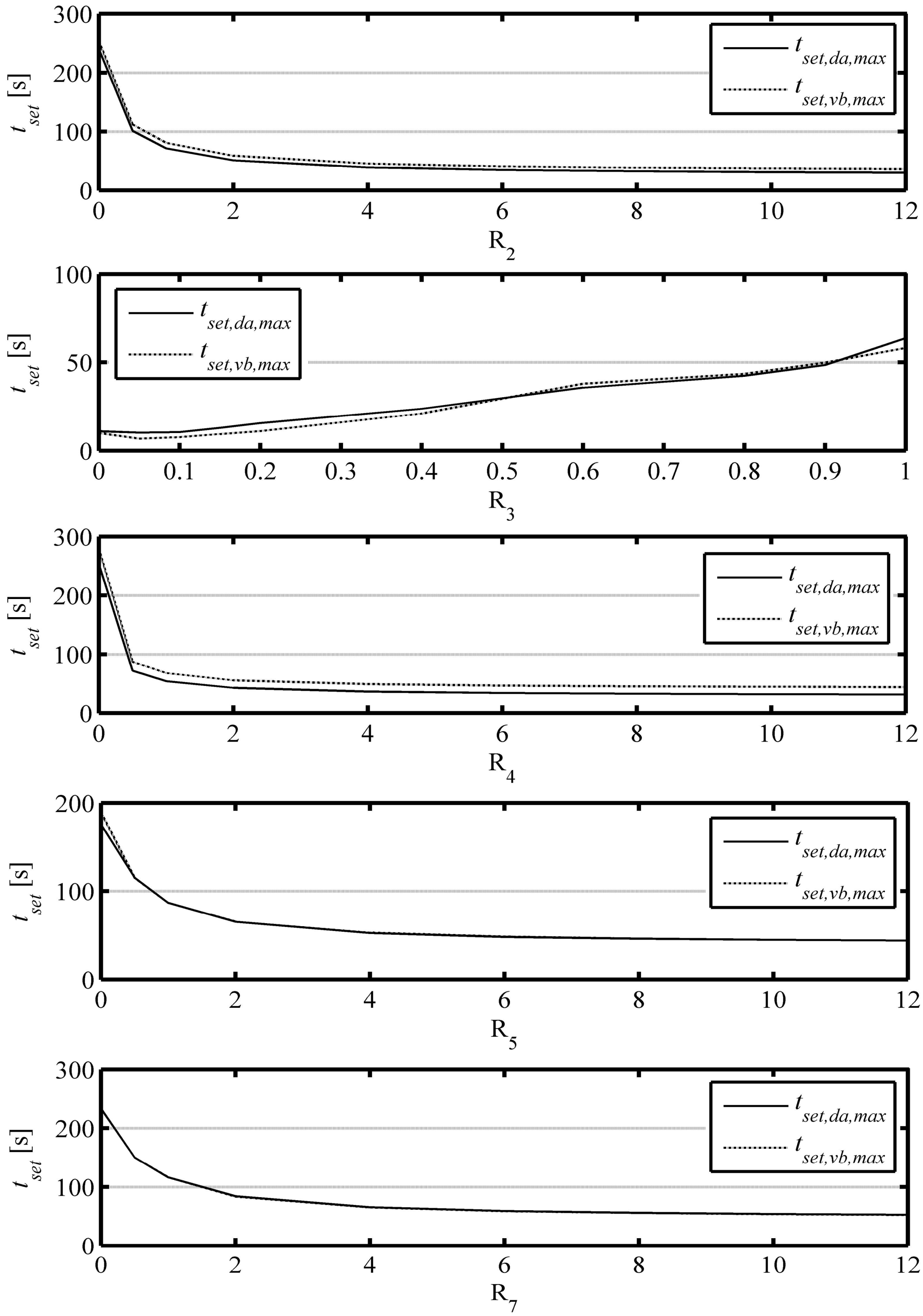

Fig. 9.1 Deterministic settling times for Γ = 2-5 and 7.

In the second stage of the Monte Carlo simulation, a set of single-mode stochastic closed-loop simulation runs were completed for the same R_Γ ranges as the first stage. The disturbances $w_{d,\Gamma}$ and $w_{v,\Gamma}$ were included as zero-mean white noise sequences, with variances determined in Chapter 6. The disturbances $w_{H,\Gamma}$ were included as the third-order AR models discussed in the previous section. For each run the mean values of d_a, denoted $\bar{d}_{a,run}$, of v_b, denoted $\bar{v}_{b,run}$, of Q, denoted $\bar{Q}_{run}$ and the absolute value of the blade position reference $|r_b|$, denoted, $\overline{|r_{b,run}|}$ were recorded. Each run was begun with initial conditions for d_a, v_b and H_Γ randomly chosen from uniform distributions with the ranges [0, $d_{a,max}$], [0, $v_{b,max}$] and [$H_{\Gamma,min}$ $H_{\Gamma,max}$]. H_Γ was simulated as a random walk process. To allow the decay of the transient due to the initial conditions to complete, the duration of each run, N_r, was five times the maximum settling time for the R_Γ value, *i.e.* $N_r = 5 \cdot \max(t_{set,da}(R_\Gamma), {}_{set,vb}(R_\Gamma))$. Examples of a single stochastic closed-loop simulation of modes Γ = 2-5 and 7 are shown in Figs. 9.2 - 9.6, respectively. These examples show that the closed-loop stochastic the d_a and v_b trajectories follow steady state optimal values $d_{a,ss}$ and $v_{b,ss}$ as they change over time as a function of H_Γ.

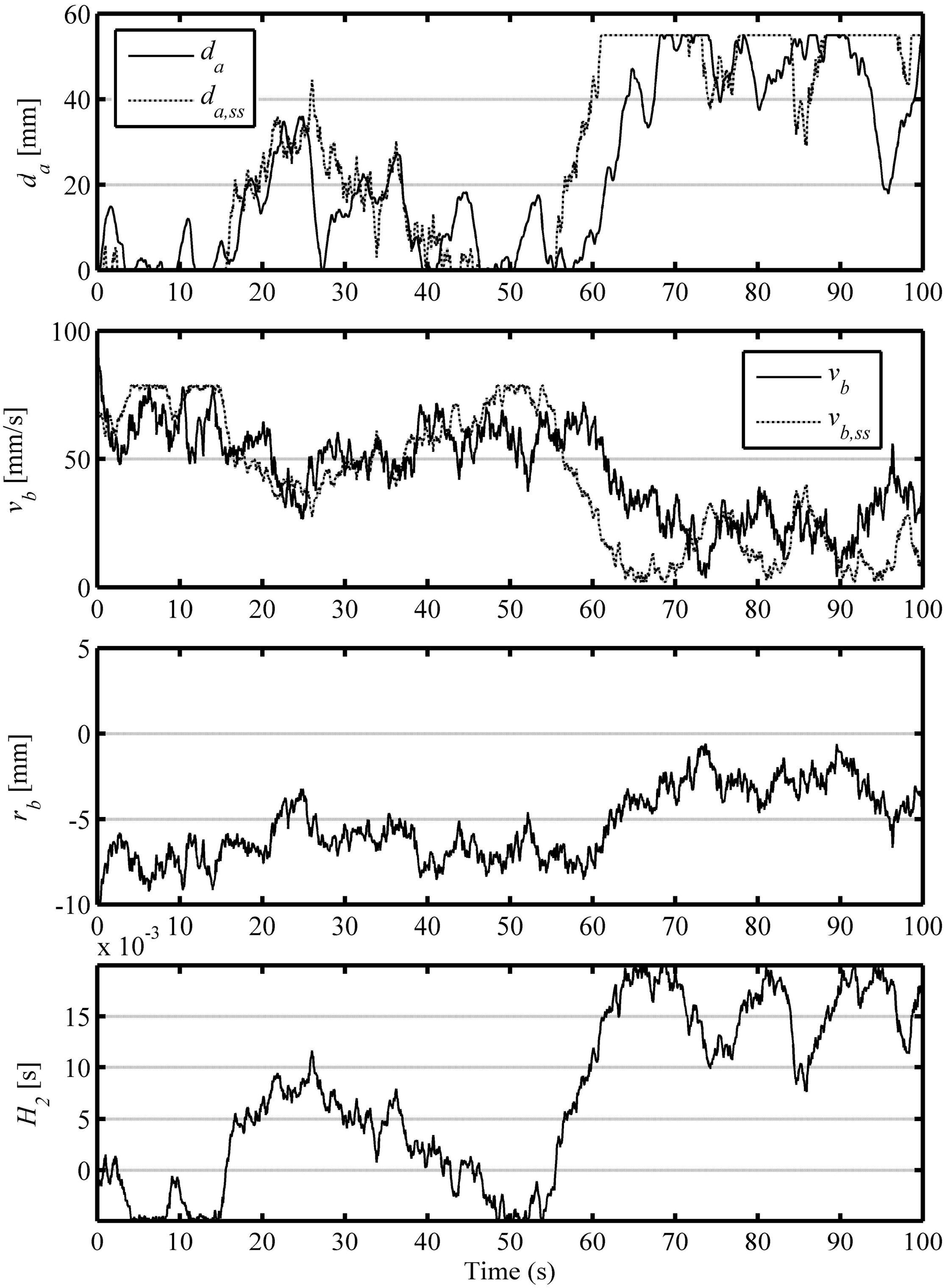

Fig. 9.2 Example of simulated stochastic closed-loop dynamics of mode $\Gamma = 2$.

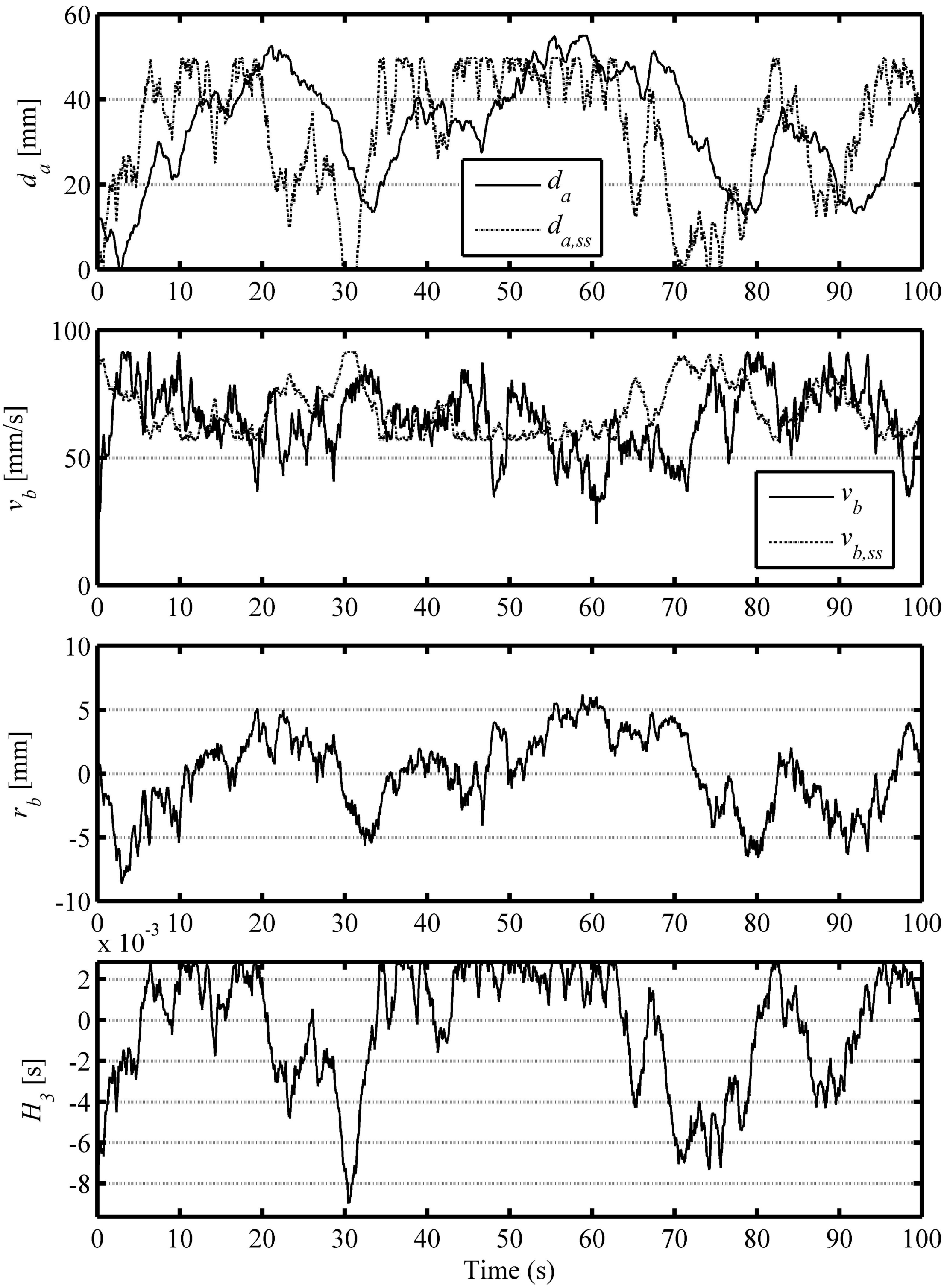

Fig. 9.3 Example of simulated stochastic closed-loop dynamics of mode $\Gamma = 3$.

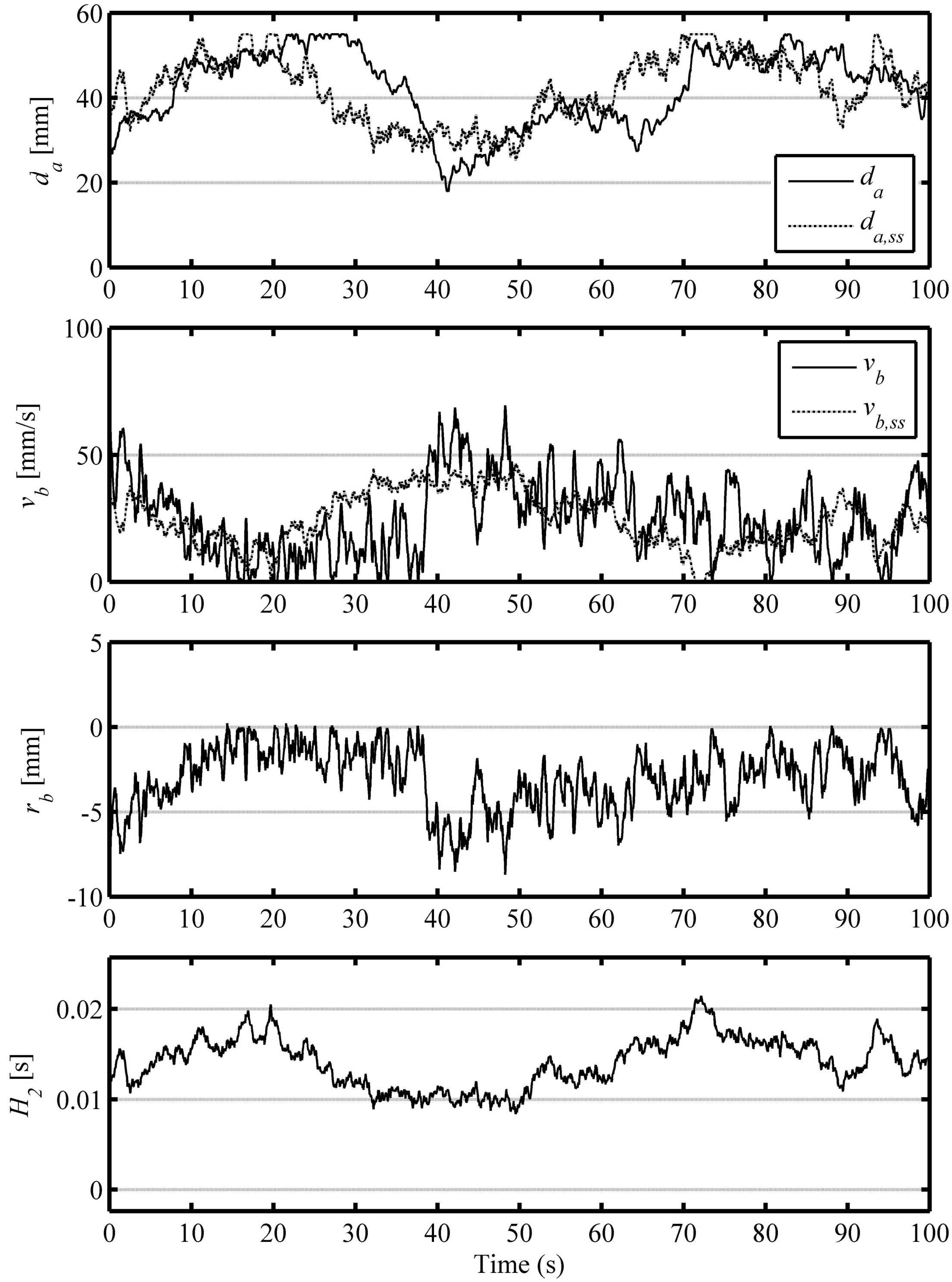

Fig. 9.4 Example of simulated stochastic closed-loop dynamics of mode $\Gamma = 4$.

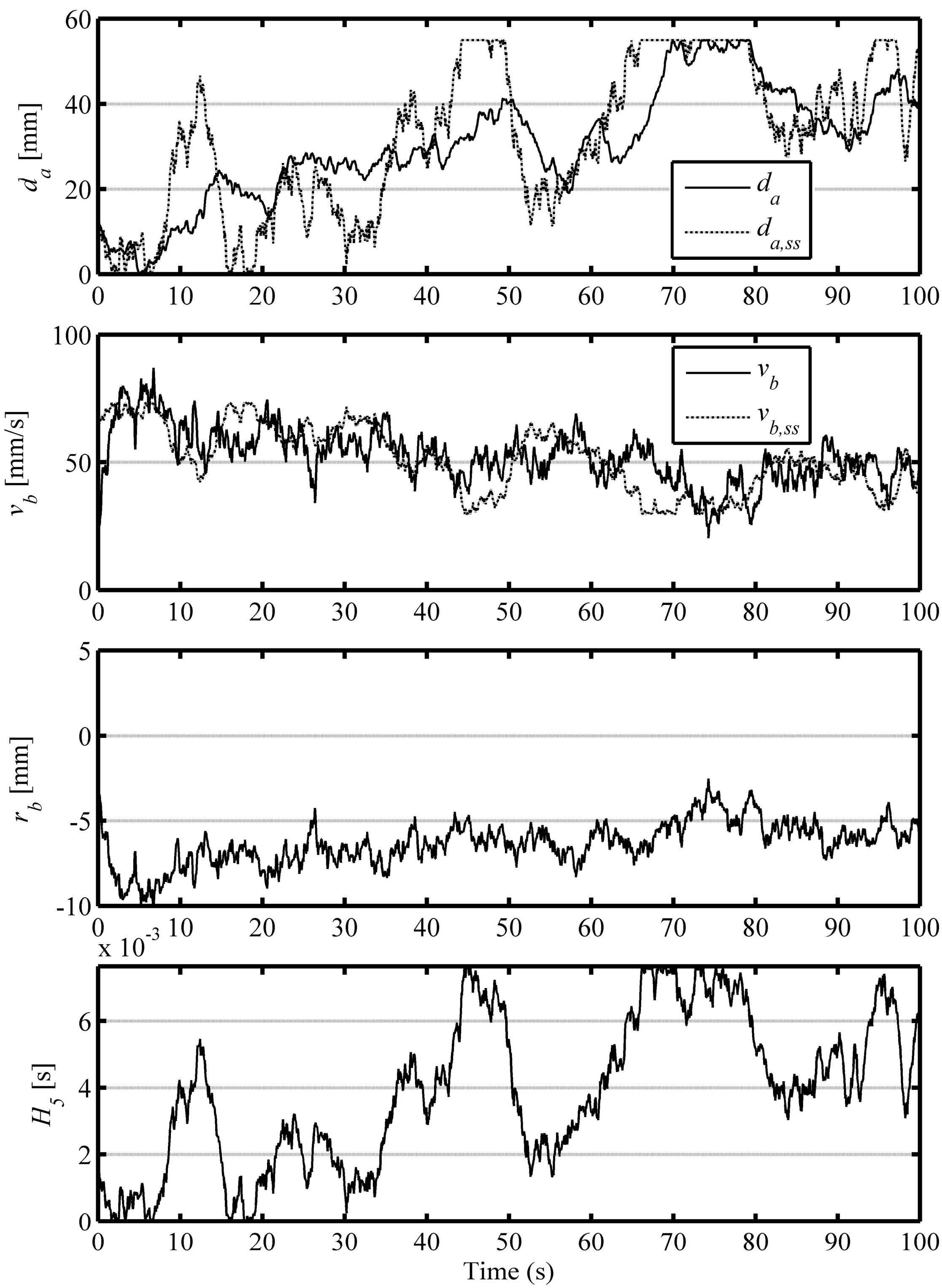

Fig. 9.5 Example of simulated stochastic closed-loop dynamics of mode $\Gamma = 5$.

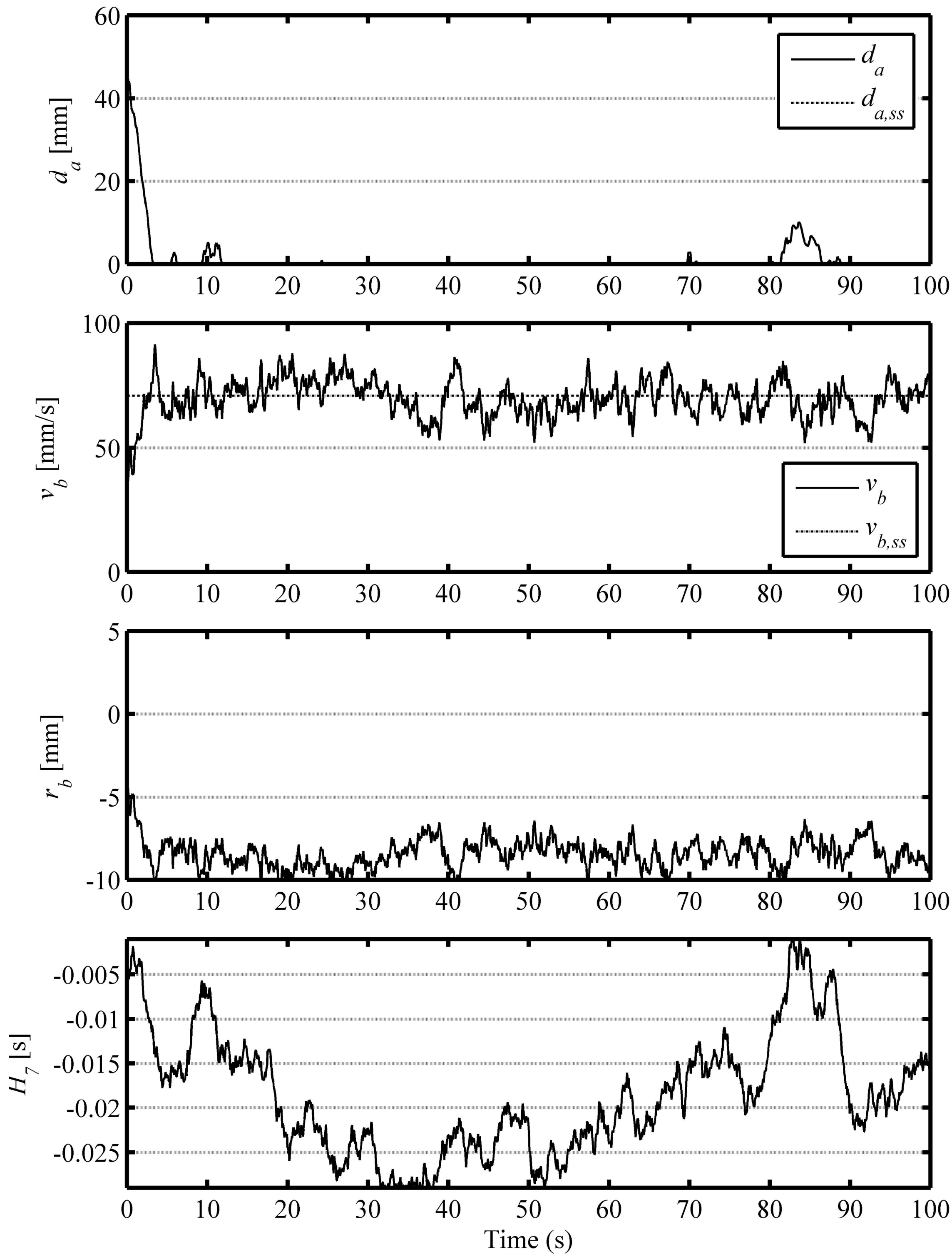

Fig. 9.6 Example of simulated stochastic closed-loop dynamics of mode $\Gamma = 7$.

The number of simulation runs was found using the sequential approach from Asmussen and Glynn (2007). Specifically, for each of the modes, a minimum set of 1000 simulation runs were performed per R_{Γ}. The mean values of $\bar{d}_{a,run}$, $\bar{v}_{b,run}$, $\bar{Q}_{run}$ and $\overline{|r_{b,run}|}$ over the set of simulations were denoted $\bar{d}_{a,set}$, $\bar{v}_{b,set}$, $\bar{Q}_{set}$ and $\overline{|r_b|}_{set}$, respectively. The minimum values of $\bar{d}_{a,run}$, $\bar{v}_{b,run}$, $\bar{Q}_{run}$ and $\overline{|r_{b,run}|}$ over the set of simulations were denoted $d_{a,set,min}$, $v_{b,set,min}$, $Q_{set,min}$ and $|r_b|_{set,min}$, respectively. The maximum values of $\bar{d}_{a,run}$, $\bar{v}_{b,run}$, $\bar{Q}_{run}$ and $\overline{|r_{b,run}|}$ over the set of simulations were denoted $d_{a,set,max}$, $v_{b,set,max}$, $Q_{set,max}$ and $|r_b|_{set,max}$, respectively. Each set of simulation runs was terminated when the 99% confidence intervals about $\bar{d}_{a,set}$ and $\bar{v}_{b,set}$ were less than 1mm and 1 mm/s, respectively.

Plots of $d_{a,set,min}$, $\bar{d}_{a,set}$ and $d_{a,set,max}$ for Γ = 2-5 and 7 are shown in Fig. 9.7. These results confirm that d_a is independent of r_b for modes Γ = 2, 4, 5 and 7, which was shown with the deterministic $d_{a,ss,\Gamma}$ values in Fig. 8.2.

Plots of $v_{b,set,min}$, $\bar{v}_{b,set}$ and $v_{b,set,max}$ for Γ = 2-5 and 7 are shown in Fig. 9.8. Plots of $|r_b|_{set,min}$, $\overline{|r_b|}_{set}$ and $|r_b|_{set,max}$ for Γ = 2-5 and 7 are shown in Fig. 9.10. The results shown in Fig 9.8 and 9.10 confirm the effect of a larger magnitude of downward blade position resulting in a smaller v_b for modes 2, 4, 5 and 7, which was shown with the deterministic $v_{b,ss,\Gamma}$ results in Chapter 8. Furthermore, that for all modes Γ = 2-5 and 7 the average magnitude of the blade position increases as R decreases, indicating more aggressive tuning of the blade position control law.

Plots of $Q_{set,min}$, $\bar{Q}_{set}$ and $Q_{set,max}$ for Γ = 2-5 and 7 are shown in Fig. 9.9. These results agree with the deterministic $Q_{ss,\Gamma}$ results presented in Chapter 8. For modes 2, 4 and 5, Q clearly increases as R_{Γ} increases. Conversely, for mode 3, Q clearly decreases as R_3 increases. From these results, the best choice for blade control law tuning to maximize the material removal rate is to select $\mathrm{R}_3 = 0$ for mode 3 and $\mathrm{R}_{\Gamma} \geq 10$ for modes Γ = 2 and 5, and $\mathrm{R}_{\Gamma} \geq 8$ for modes Γ = 4 and 7.

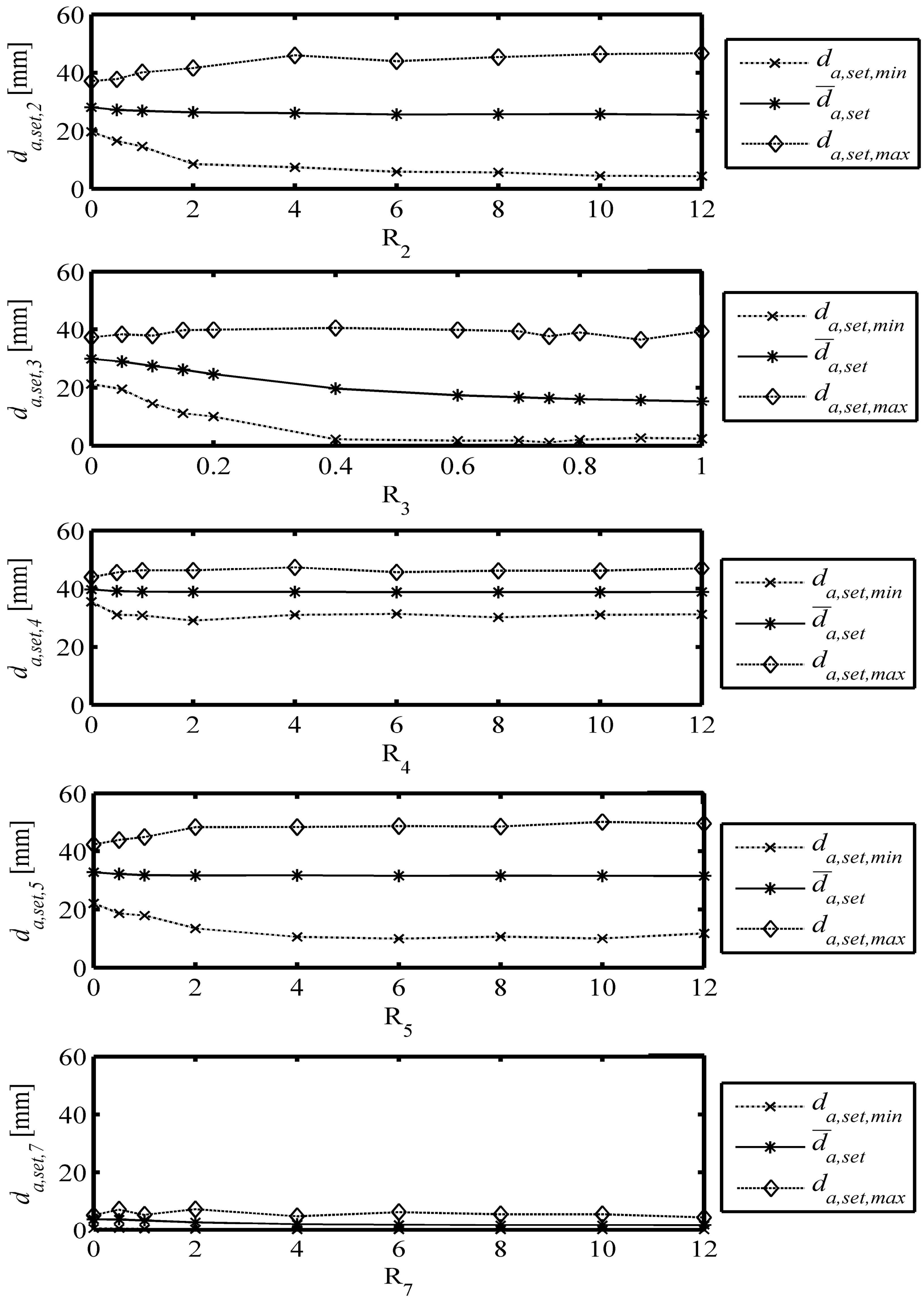

Fig. 9.7 Stochastic simulation $d_{a,set}$ results for Γ = 2-5 and 7.

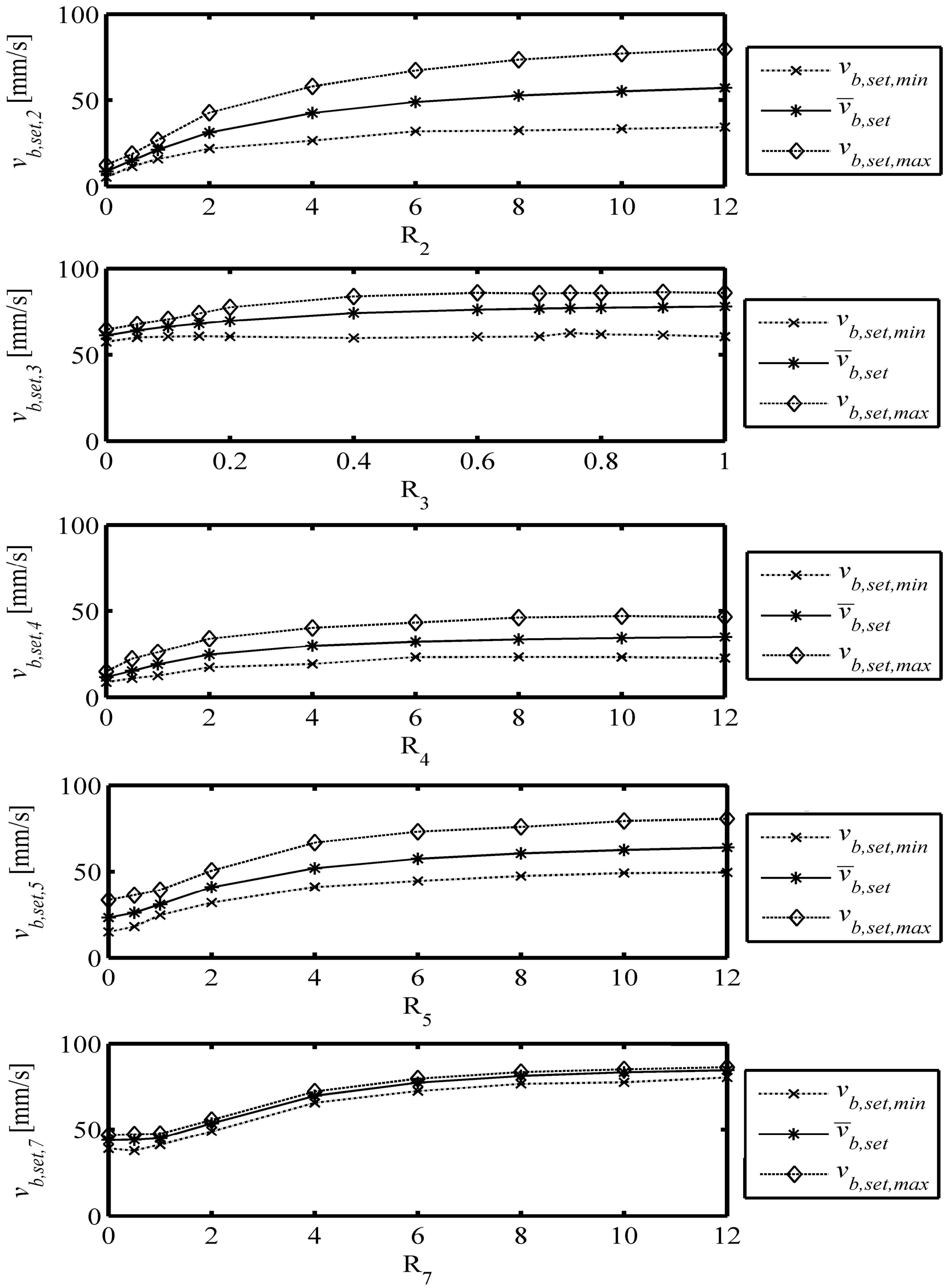

Fig. 9.8 Stochastic simulation $v_{b,set}$ results for Γ = 2-5 and 7.

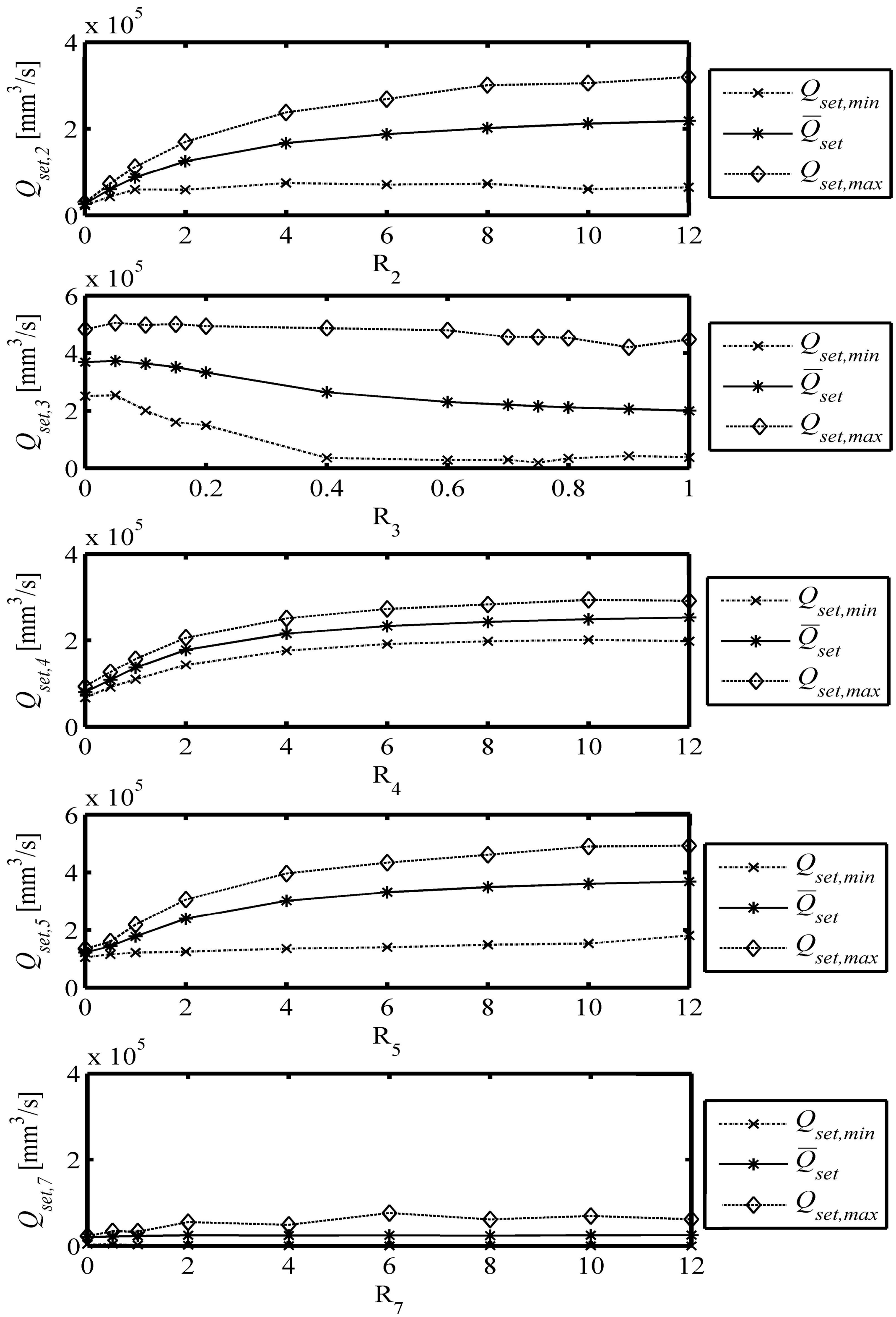

Fig. 9.9 Stochastic simulation Q_{set} results for Γ = 2-5 and 7.

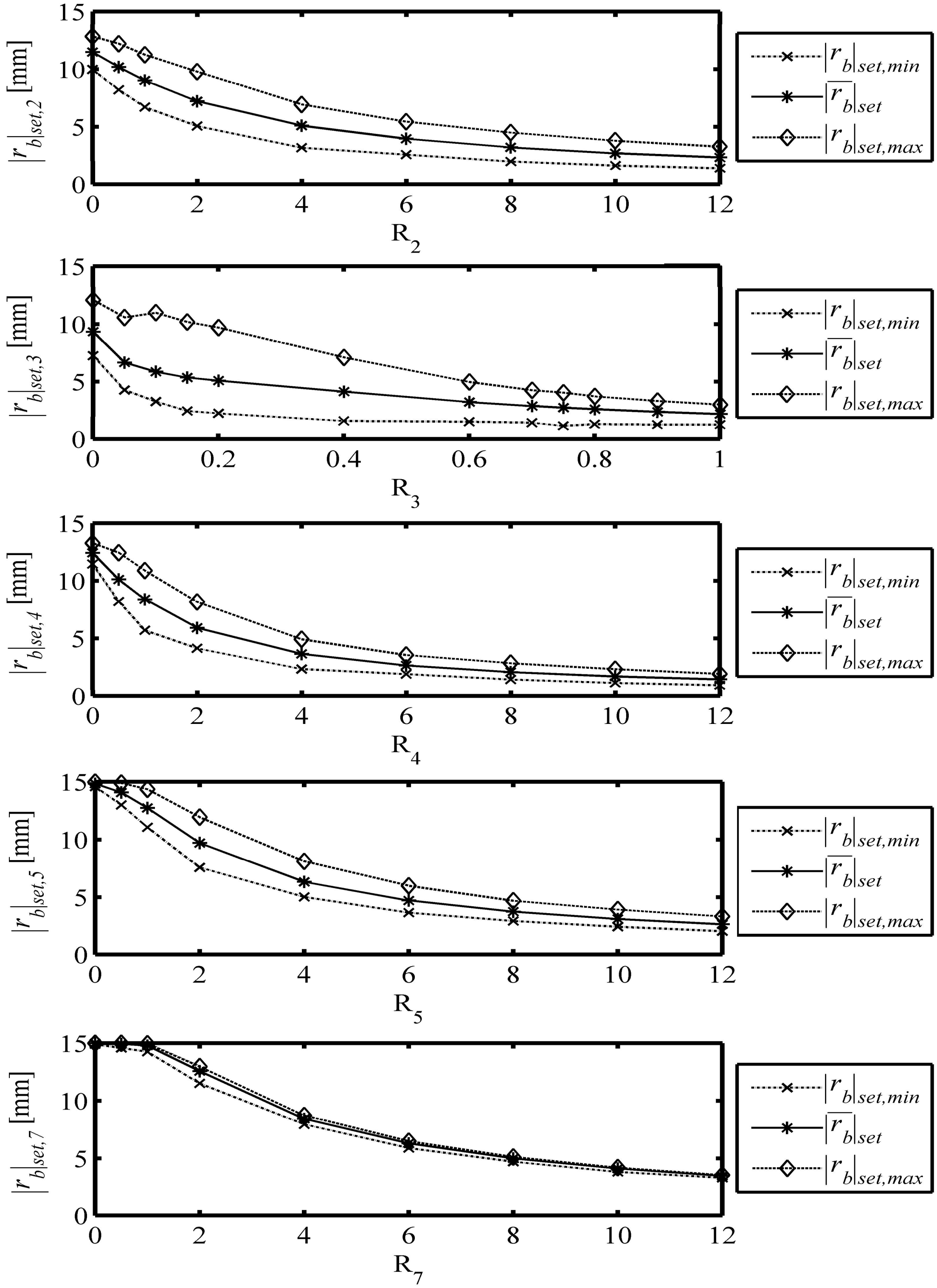

Fig. 9.10 Stochastic simulation $|r_b|_{set}$ results for Γ = 2-5 and 7.

9.3 Stochastic Stability Analysis

Of the many definitions of stochastic stability that exist, the definition of Lyapunov stable in the m^{th} mean from Kozin (1969), reformulated for discrete-time, was selected as being the most appropriate for this system. Accordingly, the equilibrium solution $\mathbf{x}_{eq}$ is Lyapunov stable in the m^{th} mean if given $\varepsilon_{m,\Gamma} > 0$, there exists $\delta_m > 0$ such that $\left\|\mathbf{x}_0\right\|_m < \delta_m$ implies:

$$E\left\{\sup_{0\le k\le N_r}\left\|\mathbf{x}_k - \mathbf{x}_{eq}\right\|_m^m\right\} < \varepsilon_{m,\Gamma} \tag{9.4}$$

or equivalently:

$$E\left\{\sup_{0\le k\le N_r}\left|d_{a,k,\Gamma}^{cl} - d_{a,ss,\Gamma}\right|^m + \left|v_{b,k,\Gamma}^{cl} - v_{b,ss,\Gamma}\right|^m\right\} < \varepsilon_{m,\Gamma} \tag{9.5}$$

where $E\{\bullet\}$ is the expected value, and sup indicates the supremum. An analysis of the stochastic simulation results using Eq. (9.5) concluded that $\mathbf{x}_{\text{eq}}$ is Lyapunov stable in the mean and mean squared (*i.e.* for m = 1 and m = 2). To consider the worst case, δ_m was calculated from the maximum values of the state variables, *i.e.* $\delta_m = \left\|\begin{bmatrix} d_{a,\max} & v_{b,\max}\end{bmatrix}^{\mathrm{T}}\right\|_m$. The values of $\varepsilon_{m,\Gamma}$ were calculated over all of the Monte Carlo simulation runs for each mode. The ratio $\varepsilon_{m,\Gamma}/\delta_m^m$ is a useful dimensionless metric for quantifying the solutions to Eq. (9.5). The computed $\varepsilon_{m,\Gamma}/\delta_m^m$ values with m = 1 and m = 2 for modes Γ = 2-5 and 7 are tabulated in Table 9.1. These results indicate that the expected values of the stochastic closed-loop d_a and v_b trajectories remain bounded about their optimal equilibrium values.

Table 9.2 Results of stochastic Lyapunov stability analysis.

Mode, Γ	$\varepsilon_{m,\Gamma} / \delta_m^m$ $m = 1$	$\varepsilon_{m,\Gamma} / \delta_m^m$ $m = 2$
2	0.78	0.76
3	0.74	0.54
4	0.59	0.47
5	0.64	0.45
7	0.58	0.48

9.4 Conclusions

Monte Carlo simulation was used for performance and stability analysis of the stochastic, constrained closed-loop process dynamics. The sets of stochastic simulation results included statistical distributions of process performance measures. These results were found to be in agreement with the results of the deterministic closed-loop performance analysis in Chapter 8. The Monte Carlo simulation data also allowed a stochastic Lyapunov stability analysis to be performed. It was shown that the stochastic closed-loop trajectories are Lyapunov stable in the mean and mean squared, *i.e.* their expected values remain bounded about their optimal equilibrium states in the presence of system disturbances.

The next chapter describes a series of experiments with the optimal control laws implemented with the scaled-down robotic bulldozing system.

Chapter 10

Control Experiments

10.1 Introduction

This chapter presents a series of experiments with the optimal control laws implemented. Experiments were conducted with the experimental robotic bulldozing system. The control laws were implemented with various tuning values using the results from the stochastic closed-loop performance analysis in Chapter 9. As a comparison, the rule-based blade control algorithm presented in Chapter 5 was also implemented.

10.2 Optimal Control Law Tuning

As discussed in Chapter 9, the tuning parameter R_Γ of the optimal control laws strongly influences the magnitude of the blade position. A smaller R_Γ results in a larger magnitude of blade position (*e.g.*, the blade will tend to penetrate down more deeply into the underlying stones). A lower blade position will reduce the robot speed due to increased d_a and/or increased friction acting on the bottom of the blade, therefore a smaller R_Γ will produce a smaller $v_{b,ss}$. In the case of mode 3 a lower blade position will produce a larger steady-state material accumulation, $d_{a,ss}$. (Recall that for the other modes material accumulation is independent of blade position). Conversely, a larger R_Γ will tend to result in a larger $v_{b,ss}$ and smaller $d_{a,ss}$. Since the material removal rate depends on the product $d_a \cdot v_b$, R_Γ should be tuned to balance the opposing trends of d_a and v_b with mode 3. This and other trends were illustrated in the results of the Monte Carlo simulation shown in Fig. 9.7-9.10. The $\bar{Q}_{set}$ results for modes 2, 3, 4 and 5, and the $\bar{v}_{b,set}$ results for mode 7 were used to select the R_Γ values. Note, for mode 7, d_a always diminishes to zero, resulting in Q diminishing to zero, therefore, $\bar{v}_{b,set}$ was used for tuning. The R_Γ values corresponding to the largest $\bar{Q}_{set}$ or $\bar{v}_{b,set}$ are the best choices for satisfying the bulldozing task objective of maximizing the material removal rate.

Although controller tuning involves selecting R_Γ that will result in the best expected $\bar{Q}_{set}$, overly aggressive and overly conservative values will effectively result in open-loop control. Overly conservative tuning will tend to result in the blade position remaining near its zero position regardless of the system state. Conversely, overly aggressive tuning will tend to result in the blade position remaining near $r_{b,min}$.

10.3 Experimental Procedure

Four distinct controller tuning schemes were created to demonstrate the significance of the R_Γ values on the closed-loop performance. A set of eight experimental trials were completed with each of the four schemes (subsequently referred to as Ctrl1 – Ctrl4) and the rule-based controller from Chapter 5 (subsequently referred to as Ctrl5). Each trial consisted of four passes. The initial material pile structure had a uniform nominal height of 20 mm and length of 1100 mm, covering to the edge of the task space.

The controller tuning values for each scheme are tabulated in Table 10.1. Ctrl1 combined aggressive tuning of R_3 with conservative tuning of the remaining values. Conservative values were used for all modes in Ctrl2, whereas all aggressive values are used in Ctrl4. Ctrl3 used intermediate values. Note that the state dependent maximum blade position constraint $r_b < 0.18 \cdot d_a$, described in Chapter 7, was implemented for all modes. Also, the mode 6 recovery control law described in Chapter 7, was implemented for all optimal control schemes Ctrl1-Ctrl4. The manually tuned rule-based controller parameters were: T1 = 0.1 s, T2 = 0.5 s, $d_{a,thres}$ = 35 mm, $v_{b,thres}$ = 50 mm/s and Δr_b = 1 mm.

Table 10.1 Optimal control tuning schemes.

	Control Law Gains				
Control Scheme	R_2	R_3	R_4	R_5	R_7
Ctrl1	10	0.1	8	10	8
Ctrl2	10	0.8	8	10	8
Ctrl3	4	0.4	3	4	4
Ctrl4	1	0.1	1	1	1

An example of a result with Ctrl1 is shown in Fig. 10.1.

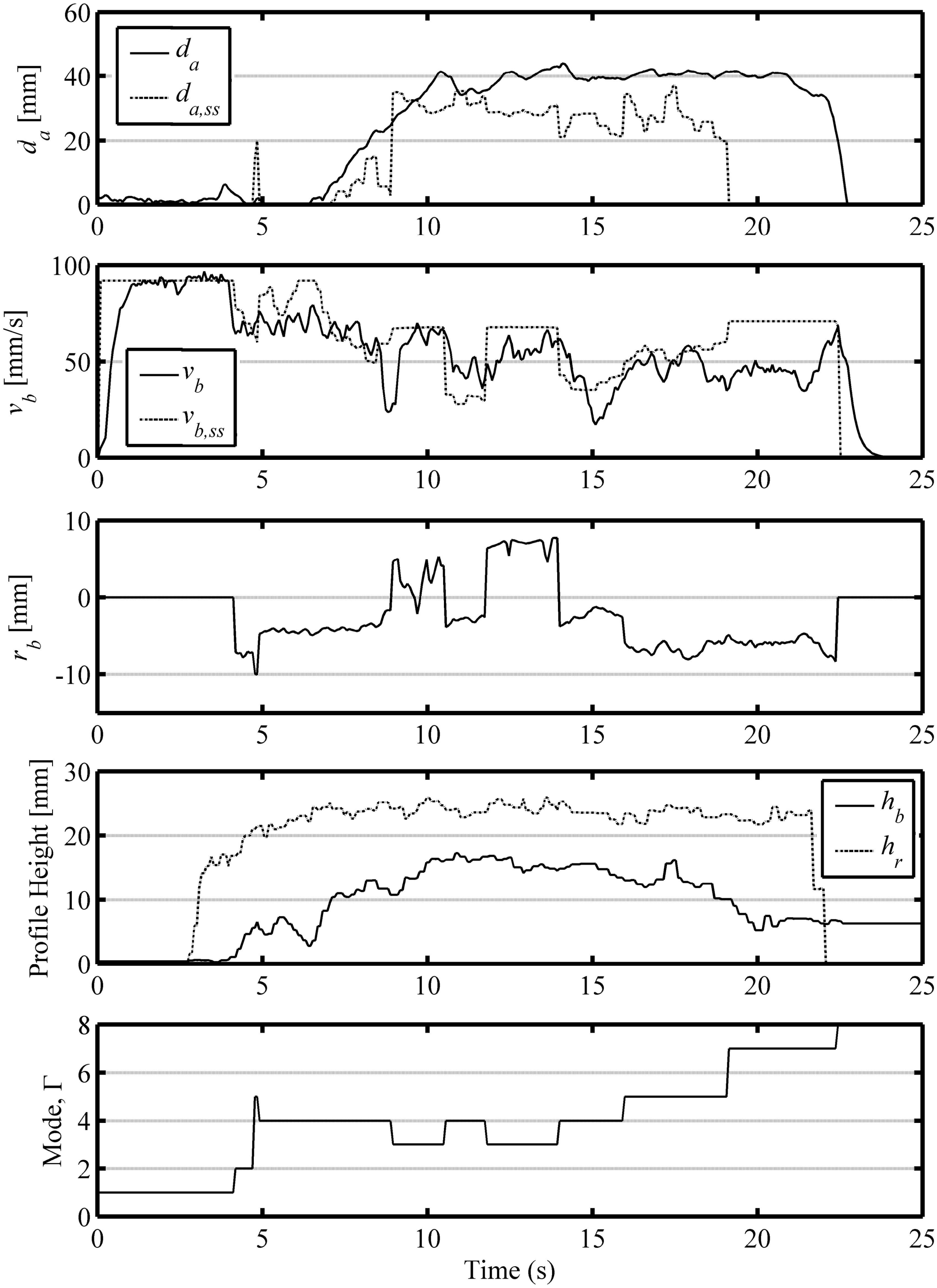

Fig. 10.1 Example of an experimental result with tuning scheme Ctrl1, pass 3.

10.4 Experimental Results Analysis Methodology

The following metrics were calculated to evaluate the performance of the control algorithms: $\bar{d}_{a,pass}$, the average material accumulation over one pass; $\bar{d}_{a,pass,\Gamma}$, the average material accumulation of mode Γ over one pass; $\bar{v}_{b,pass}$ the average robot speed over one pass; $\bar{v}_{b,pass,\Gamma}$ the average robot speed of mode Γ over one pass; $\bar{Q}_{pass}$, the average material removal rate over one pass; $\bar{Q}_{pass,\Gamma}$, the average material removal rate of mode Γ over one pass; $\overline{|r_b|}_{pass}$, the average absolute blade position over one pass; $\overline{|r_b|}_{pass,\Gamma}$, the average absolute blade position of mode Γ over one pass; $\bar{d}_{a,trial}$, the $\bar{d}_{a,pass}$ values averaged over the trials; $\bar{v}_{b,trial}$ the $\bar{v}_{b,pass}$ values averaged over the trials; $\bar{Q}_{trial}$, the $\bar{Q}_{pass}$ values averaged over the trials; and $\overline{|r_b|}_{trial}$ the $\overline{|r_b|}_{pass}$ values averaged over the trials.

To account for the variation in the system variable measurements due to measurement noise, process noise or disturbance, and the inherent uncertainty associated with the overall task environment (*i.e.* composition and distribution of material) a statistical approach was used to analyze the optimal control experimental results. The standard one-way analysis of variance (ANOVA) of the selected performance metrics was used to compare the performance of the different controllers. ANOVA is an appropriate methodology for testing the equality of several means, as in Montgomery (2001).

In general, ANOVA involves the comparison of *a* treatments or different levels of a single factor. In this case of experimental results of robotic bulldozing with different tuning schemes, each tuning scheme is considered a different treatment. The observed response from each of the a treatments is a random variable. There are n_i observations made under the ith treatment. A model to describe the observations from an experiment can be written as:

$$y_{ij} = \mu_i + \varepsilon_{ij} \quad \begin{cases} i = 1, 2, \dots, a \\ j = 1, 2, \dots, n_i \end{cases} \tag{10.1}$$

Where y_{ij} is the ij^{th} observation, μ_i is the mean of the i^{th} factor level or treatment and ε_{ij} is a random error component that incorporates all other sources of variability in the experiment including measurement noise, process noise or disturbance, and any source of uncontrolled factors. It is assumed that ε_{ij} is normally distributed with zero mean and variance σ^2.

The objective of a one-way ANOVA investigation is to test an appropriate hypothesis about the treatment means of one factor. The calculations are summarized as follows:

$$y_{i,total} = \sum_{j=1}^{n_i} y_{ij} \tag{10.2}$$

$$\bar{y}_{i,total} = \frac{y_{i,total}}{n_i} \text{ for } i = 1, 2, \dots, a \tag{10.3}$$

$$y_{total} = \sum_{i=1}^{a} \sum_{j=1}^{n_i} y_{ij} \qquad \text{and} \tag{10.4}$$

$$\bar{y}_{total} = \frac{y_{total}}{N} \text{ for } N = \sum_{i=1}^{a} n_i \tag{10.5}$$

Where $y_{i,total}$ is the sum of all observations under treatment i, $\bar{y}_{i,total}$ is the average of all observations under treatment i, y_{total} is the sum of all observations, $\bar{y}_{total}$ is the average of all observations, n_i is the number of observations under treatment i, and N is the total number of observations.

A measure of overall variability in the data is the total sum of squares, calculated with:

$$SS_{Total} = \sum_{i=1}^{a}\sum_{j=1}^{n_i} y_{ij}^2 - \frac{y_{total}^2}{N} \tag{10.6}$$

The sum of squares due to treatments (or between treatments) is calculated with:

$$SS_{Treatments} = \sum_{i=1}^{a} \frac{y_{i,total}^2}{n_i} - \frac{y_{total}^2}{N} \tag{10.7}$$

The sum of squares due to error (or within treatments) is calculated with:

$$SS_E = SS_{Total} - SS_{Treatments} \quad \text{and} \tag{10.8}$$

The mean squares, which is an estimates σ^2, is calculated with:

$$MS_E = \frac{SS_E}{N-a} \tag{10.9}$$

For comparing all pairs of a treatment means with the null hypothesis H_0: $\mu_i = \mu_j$ for all $i \neq j$, Tukey's test can be used, as in Montgomery (2001). This test states that two means are significantly different with percent confidence level $100 \cdot (1-\alpha)$ if the absolute value of their sample differences exceeds a value T_α calculated as follows:

$$T_\alpha = \frac{q_\alpha(\alpha, df)}{\sqrt{2}} \sqrt{MS_E \cdot \left(\frac{1}{n_i} + \frac{1}{n_j}\right)} \tag{10.10}$$

Where $q_\alpha(\alpha,df)$ is the studentized range statistic which values may be found in studentized range distribution tables, $df = N - a$ is the number of degrees of freedom associated with the MS_E and the sample sizes of compared treatment means i and j, are n_i and n_j, respectively.

Equivalently, a set of 100·(1- α) percent confidence intervals for all pairs of means can be constructed as:

$$\bar{y}_{i,total} - \bar{y}_{j,total} - T_\alpha \le \mu_i - \mu_j \le \bar{y}_{i,total} - \bar{y}_{j,total} + T_\alpha \text{ for } i \ne j \quad (10.11)$$

An aggregate comparison interval about the mean of the k^{th} treatment is calculated from the confidence intervals for $k = 1, 2, \ldots, a$ as follows:

$$w_{C.I.,k} = \frac{q_\alpha(\alpha, df)}{\sqrt{2}} \left(\frac{(a-1)\cdot \sum_{\substack{i=1,\\ i\ne j}}^{a} \sum_{j=1}^{a} \sqrt{MS_E \cdot \left(\frac{1}{n_i} + \frac{1}{n_j}\right)} + \sum_{\substack{i=1,\\ i\ne k}}^{a} \sqrt{MS_E \cdot \left(\frac{1}{n_i} + \frac{1}{n_k}\right)}}{(a-1)\cdot(a-2)} \right) \quad (10.12)$$

This provides a consolidated comparison interval for all pairs such that any two means are significantly different if their comparison intervals no not overlap.

10.5 Experimental Results

The mean values of the experimental performance metrics with 95% confidence intervals, $w_{95\%}$, calculated for the number of treatments a = 5 (*i.e.* the number of control schemes to compare) are shown for each mode in Fig. 10.2 and for each pass in Fig. 10.3. For the per mode ANOVA results in Fig. 10.2, the number of observations for each mode are not necessarily the same because some modes may not become active during a pass.

The numbers of per mode observations for each control scheme are tabulated in Table 10.2. For the per pass ANOVA results in Fig. 10.3, the number of observations is the same for all comparisons, where a = 5, $n_i = n_j = n_k$ = 8 and $q_{0.05}$ = 2.85.

Table 10.2 Number of per mode observations of the experimental performance metric.

Mode, Γ	Control Scheme	Number of observations, n
2	Ctrl1	32
	Ctrl2	32
	Ctrl3	32
	Ctrl4	32
	Ctrl5	32
3	Ctrl1	27
	Ctrl2	28
	Ctrl3	31
	Ctrl4	32
	Ctrl5	31
4	Ctrl1	32
	Ctrl2	32
	Ctrl3	32
	Ctrl4	32
	Ctrl5	32
5	Ctrl1	23
	Ctrl2	25
	Ctrl3	27
	Ctrl4	26
	Ctrl5	16
7	Ctrl1	32
	Ctrl2	32
	Ctrl3	32
	Ctrl4	32
	Ctrl5	32

Ctrl1 and Ctrl2 produced the largest $\bar{Q}_{trial}$ with minimal statistical difference between each other. This similarity was unexpected and will be discussed in the next paragraph. The intermediate tuning of Ctrl3 produced the expected mid-level performance. The aggressive tuning of Ctrl4 produced consistently poor $\bar{Q}_{trial}$ results. While $\bar{d}_{a,trial}$ remained fairly large, $\bar{v}_{b,trial}$ was consistently small. The performance of the rule-based controller was also poor, despite best efforts at tuning. The $\bar{v}_{b,trial}$ and $\overline{|r_b|}_{trial}$ results for modes 2, 4, 5 and 7 in Fig. 10.2 confirm the expected trend of large r_b resulting in smaller v_b. Similarly, the most aggressive tuning scheme Ctrl4 resulted in the largest $\overline{|r_b|}_{trial}$ and smallest $\bar{v}_{b,trial}$ results, as shown in Fig. 10.3.

The $\bar{d}_{a,trial}$ results in Fig 10.3 show that d_a remains relatively consistent from pass to pass regardless of control scheme. However, the $\bar{d}_{a,trial}$ results in Fig. 10.2 show significant differences in d_a for mode 3 and mode 5. This is an indication of the coupled behavior between modes from pass to pass. For example, with Ctrl1 and Ctrl 4, the mode 3 controller is aggressive and will remove a large amount of material in the first two passes. Consequently, when mode 5 becomes active in subsequent passes, there will be significantly less material in the task space resulting in smaller d_a.

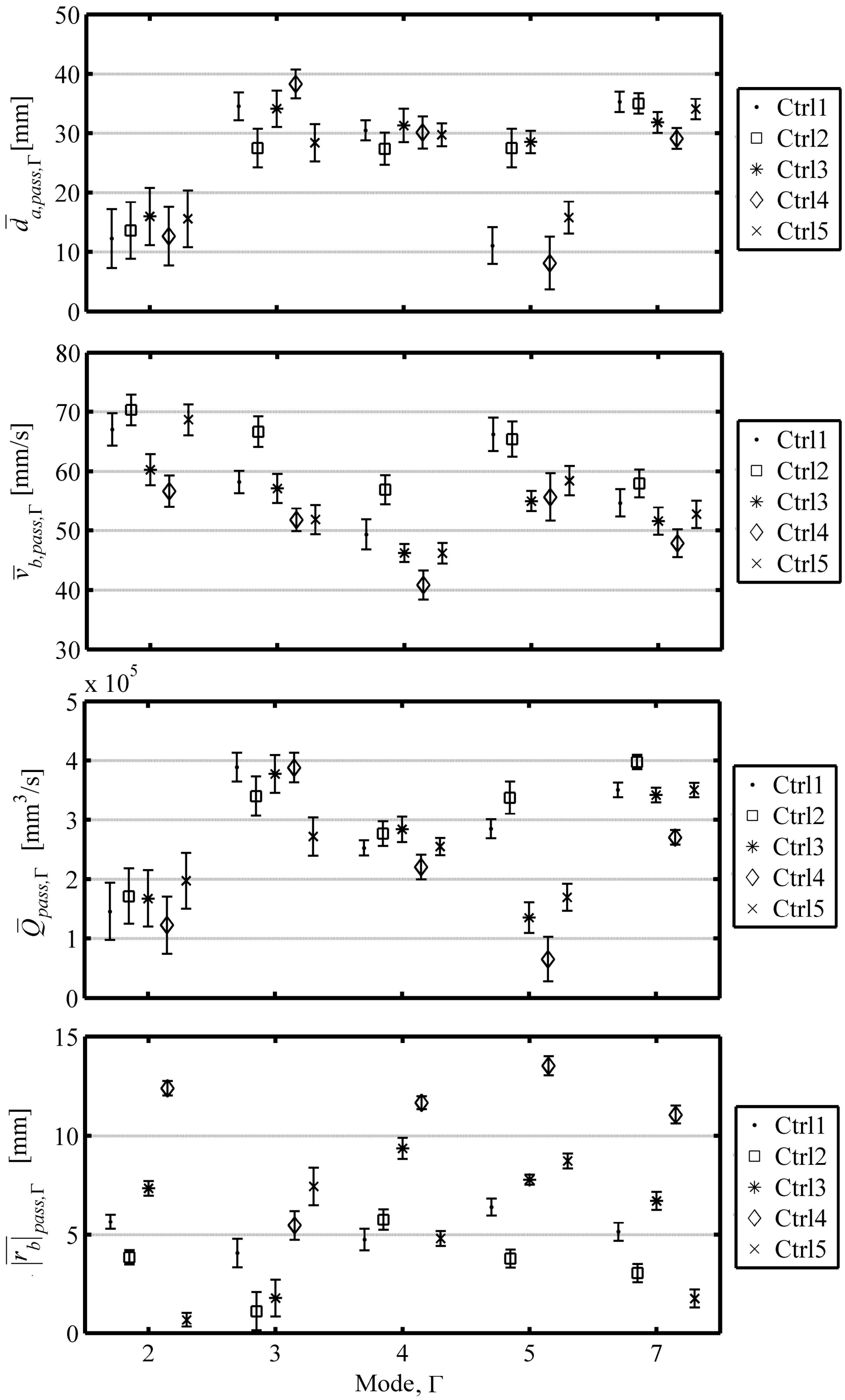

Fig. 10.2 Comparison of experimental results per mode.

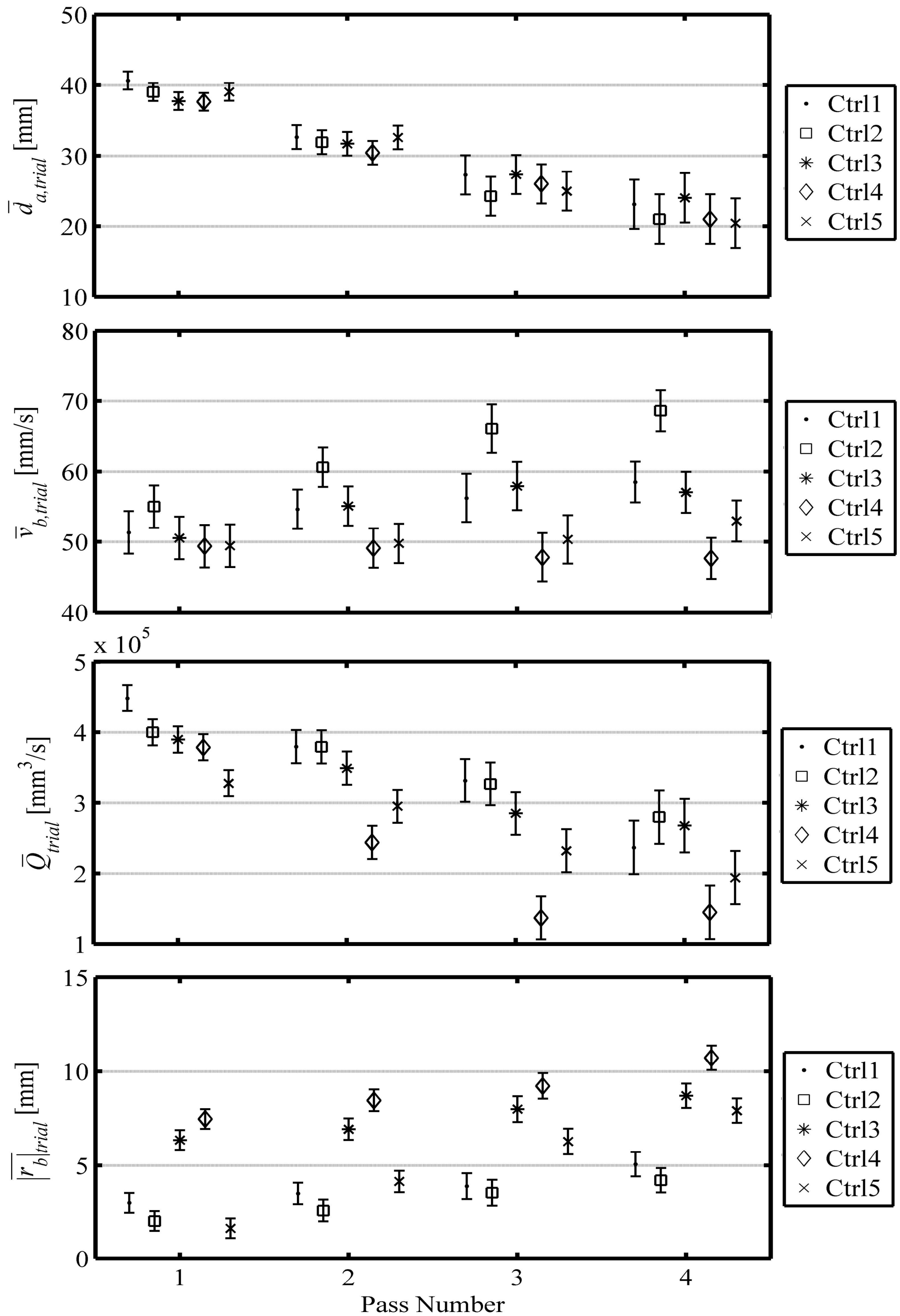

Fig. 10.3 Comparison of experimental results per pass.
(The ANOVA parameters for each pass were: a = 5, $n_i = n_j = n_k = 8$ and $q_{0.05} = 2.85$)

The similarity of Ctrl1 and Ctrl2 was due to the mode dependent process behavior that occurred during each pass. In the first and second passes modes 3 and 4 typically were predominant. In the third and fourth passes modes 5 and 4 were typically predominant. As per the mode transition conditions, a significant amount of accumulated material d_a must be maintained in mode 4 for a transition to mode 3 to occur. Therefore, the mode 3 controller was always initiated with a significantly large d_a. This large d_a was typically close to the optimal value. Then regardless of the R_3 tuning, a balance with v_b was achieved resulting in a large Q when mode 3 was active. This is apparent in Fig. 10.2 whereby for mode 3, if $\bar{d}_{a,trial}$ is relatively large, $\bar{v}_{b,trial}$ tends to be relatively small. Thus the performance tended to be insensitive to the tuning of R_3. In the $\Gamma \neq 3$ modes the most significant influence on $\bar{Q}_{trial}$ was v_b. In particular, aggressively tuned mode 4 or 5 controllers greatly reduced v_b, resulting in much smaller $\bar{Q}_{trial}$ values. The best optimal control tuning scheme Ctrl1 resulted in an average 37% larger $\bar{Q}_{trial}$ than the worst optimal control tuning scheme Ctrl4 and an average 33% larger $\bar{Q}_{trial}$ than the rule-based controller Ctrl5.

10.6 Conclusions

Experimental results with various optimal controller tuning values and a rule-based controller were presented to compare the performance of the different controllers. The results with the optimal control laws significantly increased the average material removal rate compared to the rule-based controller.

The next chapter concludes this thesis with a summary of research contributions and a discussion on recommendations for future work.

Chapter 11

Conclusions and Recommendations

11.1 Conclusions

The theoretical and experimental investigations presented in this thesis on modeling and control of a robotic bulldozing operation lead to the following conclusions:

1. Observations of a full scale bulldozing process formed the basis for the development of a theoretical nonlinear hybrid dynamic model in Chapter 3. A set of nine nonlinear dynamic system equations were developed that model the low-level bulldozing process. Ten discrete operation modes with 16 mode transition conditions were defined.
2. A system identification methodology was used in Chapter 4 for estimation of the dynamic equation parameters for modes 1-5 and 7 and model refinement. The refined model was validated and simulation results confirmed the expected model dynamic behaviour.
3. An extended Kalman filter (EKF) was designed in Chapter 6 and implemented on the experimental robot bulldozing system using the dynamic equations from Chapter 3 and the estimated parameters from Chapter 4. The performance of the Kalman filter is comparable with the performance of a 2nd order 1 Hz Butterworth lowpass filter. The main advantage of the Kalman filter is that less delay is introduced in the signal and tuning is more flexible with more meaningful parameters.

4. Analysis of the deterministic open-loop dynamics in Chapter 8 showed that steady state open-loop stall conditions exist for this experimental system but can be avoided with an appropriate minimum blade constraint. Further analysis of the deterministic closed loop dynamics using the control laws designed in Chapter 7 showed that closed-loop stall cannot occur for this experimental system. A numerical Lyapunov stability analysis showed that the deterministic closed-loop trajectories of d_a and v_b converge to their steady state optimal equilibrium values.
5. It was found experimentally in Chapter 7 that avoidance of mode 6 can be accomplished with an appropriate state dependent maximum blade constraint imposed in modes Γ = 2-5 and 7. The results of this investigation formed the basis for the development of a blade control law to transition out of mode 6 if it occurs.
6. Analysis of the stochastic closed loop dynamics in Chapter 9 showed agreement with the results of the deterministic closed-loop performance analysis in Chapter 8. Furthermore, a stochastic Lyapunov stability analysis showed that the expected values of the mean stochastic closed-loop trajectories remain bounded about their optimal equilibrium states.
7. Experimental results with various optimal controller tuning values and a rule-based controller were presented to compare the performance of the different controllers. The best optimal control tuning scheme Ctrl1 resulted in an

average 37% larger $\bar{Q}_{trial}$ than the worst optimal control tuning scheme Ctrl4 and an average 33% larger $\bar{Q}_{trial}$ than the rule-based controller Ctrl5.

11.2 Summary of Research Contributions

This thesis addressed the challenge of developing a novel approach to autonomous bulldozing operations. This included the following key research contributions:

1. Design of a reduced-scale robotic bulldozer and experimental environment.
2. A hybrid dynamic model of a robotic bulldozing process including a set of novel nonlinear dynamic equations to model the low-level dynamics.
3. Design of a rule-based closed-loop blade control algorithm.
4. A novel system identification and model validation framework for the robotic bulldozing process.
5. Design of model-based optimal control laws for the execution of the robotic bulldozing operation, including a deterministic and stochastic performance and stability analysis.
6. Design of an approach for avoidance and recovery control of a special-case operation mode.
7. Experimental validation of the robotic bulldozing model and control design.

Three refereed conference papers on work with the prototype full-scale bulldozer and mining application form the basis for introductory material regarding conceptual task analysis, control requirements and motivation for the development of the reduced scale experimental robotic bulldozing system, which are Olsen *et al.* (2006), Olsen *et al.* (2008a) and Olsen *et al.* (2008b). Another refereed conference paper, Olsen and Bone (2011), presents preliminary model development and system identification with the reduced-scale robotic bulldozing system. A journal paper, Olsen and Bone (2012a), was submitted on modeling and system identification. Another journal paper, Olsen and Bone (2012b), was submitted on the design of model-based optimal control laws and experimental implementation.

11.3 Recommendations for Future Work

Building on the results presented in this thesis, there are a number of interesting avenues for extending this research. An overview of some directions for future work follows.

The overall experimental system scope could be extended to include different types of material for dozing, *e.g.* different sizes and densities of stones and/or soil; different blade shapes and sizes; and different floor surface textures. Furthermore, a more intensive investigation on track-slip could be conducted including detailed modelling and design of a control approach for track-slip reduction.

The scope of the bulldozing process could be extended to include additional degrees of freedom beyond the current constraints with a single direction of motion, *e.g.* introducing steep slopes to climb and introducing multi-directional planar navigation throughout the task space. In addition to low-level control design, higher-level strategies could be developed involving multiple bulldozing robots.

Different control laws could be formulated with different objectives other than to maximize the material removal rate. For example, a related bulldozing task involves blade control to achieve desired terrain profile characteristics for construction site preparation. This may entail formulation of a blade position control law with respect to minimizing the error between the actual underlying material profile height and a desired material profile height.

Ultimately, full scale realization of the work presented in this thesis could be investigated. This includes experimental implementation of the system identification framework and the control laws with a full-scale robotic bulldozing system. The current vision-based localization system and the vision-based laser scanning system are not intended for use as part of a full-scale system, although similar technologies may be applicable. For full-scale above-ground vehicle localization, global positioning system (GPS) based methods are becoming well-established for real-time vehicle localization, for examples see Crane *et al.* (1995), Le *et al.* (1997) and Redmill *et al.* (2001). For underground applications, vehicle localization is a challenging area of active research, where various approaches have been investigated. These include artificial beacons and integrated systems combining inertial sensors, magnetometers, range finders and odometry. For examples see Scheding et al. (1999), Bakambu and Polotski (2007), Xiong *et al.* (2009) and Chi et al. (2012). Similarly, material profile measurement for automation of mining and construction operations continues to be an active area of investigation, for examples see Stentz et al. (1999) and Brooker et al. (2007).

References

Althoefer, K., Tan, C.P., Zweiri, Y.H. and Seneviratne, L.D. 2009. "Hybrid soil parameter measurement and estimation scheme for excavation automation". *IEEE Transactions on Instrumentation and Measurement*, **58**(10), pp. 3633-3641.

Asmussen, S. and Glynn, P.W. 2007. Stochastic Simulation: Algorithms and Analysis, Chapter III, pp. 68-95. Springer.

Bakambu, J.N. and Polotski, V. 2007. "Autonomous system for navigation and surveying in underground mines", Journal of Field Robotics, 24(10), 829-847.

Bernold L.E. 1993. "Motion and path control for robotic excavation", Journal of Aerospace Engineering, 6(1):1-18, January.

Bevly, D.M., Gerdes, J.C. and Parkinson, B.W. 2002. "A new yaw dynamic model for improved high speed control of a farm tractor". ASME Journal of Dynamics Systems, Measurement and Control, 124(4), pp.659-667.

Boyd, S. and Vandenberghe, L. 2004. Convex Optimization, Chapter 5. Cambridge University Press.

Bradley D. and Seward D. 1998. "The development, control and operation of an autonomous robotic excavator', Journal of Intelligent and Robotic Systems, 21(1):73–97.

Branicky, M.S., Borkar, V.S. and Mitter,S.K. 1998. "A unified framework for hybrid control: model and optimalcontrol theory". IEEE Transactions on Automatic Control, 43(1), pp. 31-45.

Brooker, G., Hennessey, R., Lobsey, C., Bishop, M. and Widzyk-Capehart, E. 2007. “Seeing through dust and water vapor: millimeter wave radar sensors for mining applications”, Journal of Field Robotics, 24(10), 527-557.

Bullock D.M. and Oppenheim I.J. 1992. “Object-oriented programming in robotics research for excavation”, Journal of Computing in Civil Engineering, 6(3):370-385, July.

Caihua Xiong, Donggui Han, Youlun Xiong 2009. "An integrated localization system for robots in underground environments", Industrial Robot, 36(3): 221 – 229.

Chi, H., Zhan, K. and Shi, B. 2012. “Automatic guidance of underground mining vehicles using laser sensors”, Tunnelling and Underground Space Technology, 27(1):142-148.

Crane, C.D., Armstrong, D.G. and Rankin, A.L. 1995. “Autonomous Navigation of Heavy Construction Equipment”, Computer-Aided Civil and Infrastructure Engineering, 10(5):357-370.

Finkel, D.E. 2004. “Direct – A Global Optimization Algorithm”. URL http://www4.ncsu.edu/~ctk/Finkel_Direct/.

Gartley, E. and Bevly, D.M. 2008. “Online estimation of implement dynamics for adaptive steering control of farm tractors”. IEEE/ASME Transactions on Mechatronics, 13(4), pp. 429-440.

Grune, L. and Pannek, J. 2001. Nonlinear Model Predictive Control Theory and Algorithms. Springer.

Ha Q.P., Nguyen Q.H, Rye D.C., and Durrant-Whyte H.F. 2000. "Impedance control of a hydraulically actuated robotic excavator", Automation in Construction, 9(5):421-435.

Homma, T., and Saltelli, A. 1996. ''Importance measures in global sensitivity analysis of nonlinear Models''. Reliability Engineering System Safety, 52(1), pp.1–17.

Ito, N. 1991. "Bulldozer Blade Control". Journal of Terramechanics, 28(1), pp. 65-71.

Koch, R.D. 2005., Method and system of controlling a work tool. United States Patent Application No. 20050132618 June.

Koivo, A.J, Thoma A., Kocaoglan E., and Andrade-Cetto J. 1996. "Modelling and control of excavator dynamics during digging operation", Journal of Aerospace Engineering, 9(1):10{18, January.

Kozin, F. 1969. "A survey of stability of stochastic systems". Automatica, 5(1), pp. 95-112.

Le, A.T., Rye, D.C. and Durrant-Whyte, H.F. 1997. "Estimation of track-soil interactions for autonomous tracked vehicles". In Proceedings of the IEEE Intl. Conf. on Robotics and Automation, Albuquerque, New Mexico, April, pp. 1388-1393.

Marshall, J.A., Murphy, P.F. and Daneshmend, L.K. 2008. "Toward autonomous excavation of fragmented rock: full-scale experiments", IEEE Transactions on Automation Science and Engineering, 5(3):562-566, July.

Matsushita, H. 1996. Load control unit for a bulldozer. United States Patent No. 5,564,507 October.

Montgomery, D.C. 2001. Design and Analysis of Experiments, 5th Edition, John Wiley & Sons, Inc., New York.

Murphy, P.F.R. 2005. Engineering Manager, Sandvik Mining and Construction, Burlington, Ontario, private communication.

Nakagami, A. 1997. Running slip control system for a bulldozer. United States Patent No. 5,699,248 December.

Nakagami, A. 1998. Ground leveling control system for a bulldozer. United States Patent No. 5,819,190 October.

Ohtsubo K. and Ward E.D. 1975. "A Nonlinear automatic feedback blade controller for improved bulldozer performance", SAE Preprints, no. 750819, 12 pages.

Olsen, S.G., Daneshmend, L.K., Hall, R.A. and Murphy, P.F.R. 2006. "Matching Machine Design to the Production Process: A Case Study in the Integrated Design of Mobile Equipment and Mining Methods", 3rd Canadian Design Engineering Network Conference, Toronto, June, 2006.

Olsen, S.G., Hall, R.A., Daneshmend, L.K. and Murphy, P.F.R. 2008a. "Integrated design of an XLP Dozer", 3rd South African Institute of Mining and Metallurgy International Platinum Conference, Sun City, ZA, October, 2008.

Olsen, S.G., Hall, R.A. and Bone, G.M. 2008b. "Evaluation and Development of Technologies for Bulldozer Automation", 17th International Symposium on Mine Planning and Equipment Selection, Beijing, October, 2008.

Olsen, S.G. and Bone, G.M. 2011. "Modelling of Robotic Bulldozing Operations for Autonomous Control," Proceedings of the 24th IEEE CCECE, Niagara Falls, Canada, May, 2011.

Olsen, S.G. and Bone, G.M. 2012a. "Development of a Hybrid Dynamic Model and Experimental Identification of Robotic Bulldozing", ASME Journal of Dynamic Systems, Measurements and Control, Submitted December 15, 2011, Revision Submitted June 8, 2012 (DS-11-1391).

Olsen, S.G. and Bone, G.M. 2012b. "Model-based Control of Three-DOF robotic Bulldozing", ASME Journal of Dynamic Systems, Measurements and Control, Submitted June 11, 2012 (DS-12-1185).

Parker, A.C. and Zhang, H. 2006. "Collective Robotic Site Preparation", Journal of Adaptive Behaviour, 14(1), 5-19.

Perttunen, C.D, Jones, D.R. and Stuckman, B.E. 1993. "Lipschitzian optimization without the lipschitz constant". Journal of Optimization Theory and Application, 79(1), October, pp. 157-181.

Qin, S.J. and Badgwell, T.A. 2000. "An overview of nonlinear model predictive control applications". In Nonlinear Predictive Control, pp. 369–392. Springer.

Qinsen, Y. and Shuren, S. 1994. "A Soil-tool Interaction Model for Bulldozer Blades", Journal of Terramechanics, Vol. 31, No. 2, pp. 55-65, 1994.

Salculdean S., Tafazoli S., Hashtrudi-Zaad, K., and Lawrence, P.D. 1997. "Evaluation of impedance control and teleoperation control of a teleoperated mini excavator", in

Proceedings of the 5th International Symposium on Experimental Robotics,ISER 97, Spain, pp. 187–198.

Scheding, S., Dissanayake, G., Nebot, E.M. and Durrant-Whyte, H.F. 1999. “An experiment in autonomous navigation of an underground mining vehicle”, IEEE Transaction on Robotics and Automation, 15(1): 85-95.

Stentz A., Bares J., Singh A., and Rowe P. 1999. “A robotic excavator for autonomous truck loading”, Autonomous Robots, 7(2):175-186.

Shi, X., Lever, P.J.A. and Wang F.-Y. 1996. “Fuzzy behavior integration and action fusion for robotic excavation” IEEE Transactions on Industrial Electronics, 43(3), pp. 395-402.

Redmill, K.A., Kitajima, T. and Ozguner, U. 2001. “DGPS/INS integrated positioning for control of automated vehicle”, Proceedings of IEEE Intelligent Transportation Systems Conference, Oakland, CA, USA, August 25-29, pp. 172-178.

Rodriguez-Fernandez, M. and Banga, J. R. 2010. “SensSB: a software toolbox for the development and sensitivity analysis of systems biology models”. Bioinformatics 26(13), pp. 1675-1676.

Simon, D. 2006. Optimal State Estimation: Kalman, H-Infinity, and Nonlinear Approaches, Wiley-Interscience.

Sobol, I.M. 2001. “Global sensitivity indices for nonlinear mathematical models and their Monte Carlo estimates”. Mathematics and Computers in Simulation, 55(1), pp. 271-280.

Takahashi, H., Hasegawa, M. and Nakano, E. 1999. "Analysis on the resistive forces acting on the bucket of a load-haul-dump machine and a wheel loader in the scooping task". Advanced Robotics, 13(2), pp. 97-114.

Terano T., Masui S. and Nagaya K. 1992. "Experimental Study of Fuzzy Control for Bulldozer". In Proceedings of the IEEE Region 10 Conference, Tencon 92, November 11-13, Melbourne, Australia, pp. 644-647.

Thangavelautham, J., El Samid, N.A., Grouchy, P., Earon, E., Fu, T., Nagrani, N. and D'Eleuterio, G.M.T. 2009. "Evolving multirobot excavation controllers and choice of platforms using an artificial neural tissue paradigm". In Proceedings of the IEEE Intl. Symposium on Computational Intelligence in Robotics and Automation, CIRA, pp. 258-265.

Vaha P.K. and Skibniewski M.J. 1993. "Cognitive force control of excavators", Journal of Aerospace Engineering, 6(2):159-166, April.

Wong, J.Y. 2001. Theory of Ground Vehicles, Third Edition, John Wiley and Sons.

Yamamoto 2001. Dozing device for bulldozer. United States Patent No. 6,181,999 January.

Appendix A

Details of the Experimental Robotic Bulldozing System

A.1 Introduction

This appendix documents the details of the sensors and process variable measurements of the robot bulldozer experimental system. These include robot location measurement, material accumulation measurement, blade position measurement, robot pitch measurement, task space material profile height measurement and calculation of the material profile process auxiliary variables. It also includes the details of the blade position controller and heading controller.

The primary fixed components that compose the task space environment include the line laser mounted on the stepper motor, the robot tracking camera, the laser scan camera and the elevated platform on which the robotic bulldozer pushed loose stones. A diagram showing the geometric locations of these components is shown in Fig. A.1.

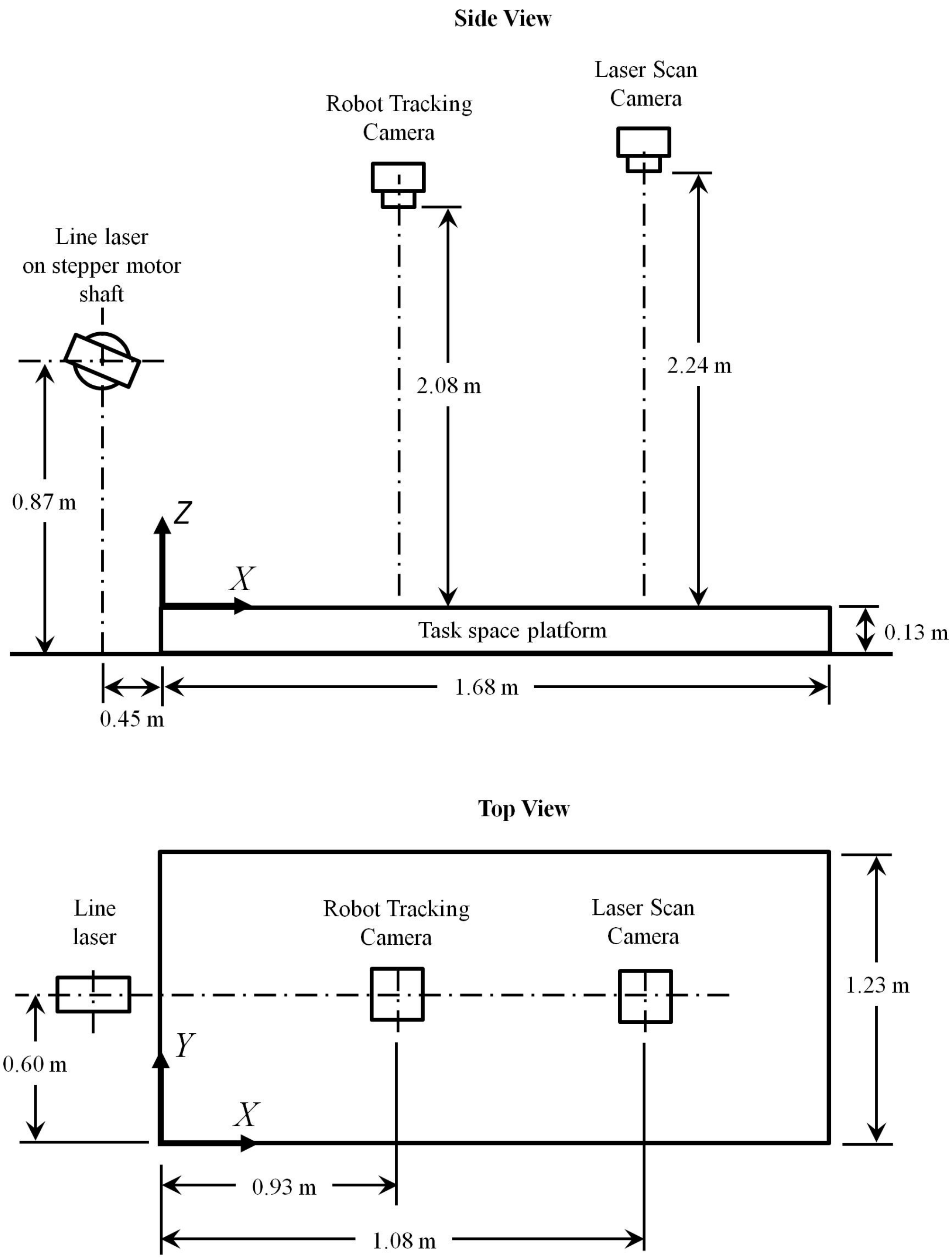

Fig. A.1 Locations of the task space components in the world coordinate frame (X-Y-Z).

A.2 Robot Location Measurement

A.2.1 Robot Localization Camera Calibration

The camera was calibrated with a chessboard pattern to determine camera position and pose with respect to the task space, and camera intrinsic parameters and distortion parameters. The estimated calibration parameters are used to compensate for lens distortion and calculate robot task space world coordinates in the vision localization system. The calibration pattern is composed of a 5x7 grid of alternating black and white squares. The size of each square is 209 mm along an edge. The average number of pixels along the edges of each square was 71 giving a resolution of 3 mm per pixel. The calibration pattern was positioned level and flat against the task space floor surface. The OpenCV software library was used for camera calibration. Specific OpenCV functions were used to find the corners of the calibration pattern, estimate camera parameters, undistort the image in addition to other image processing. An example image of the chessboard calibration pattern with detected corner points is shown in Fig. A.2.

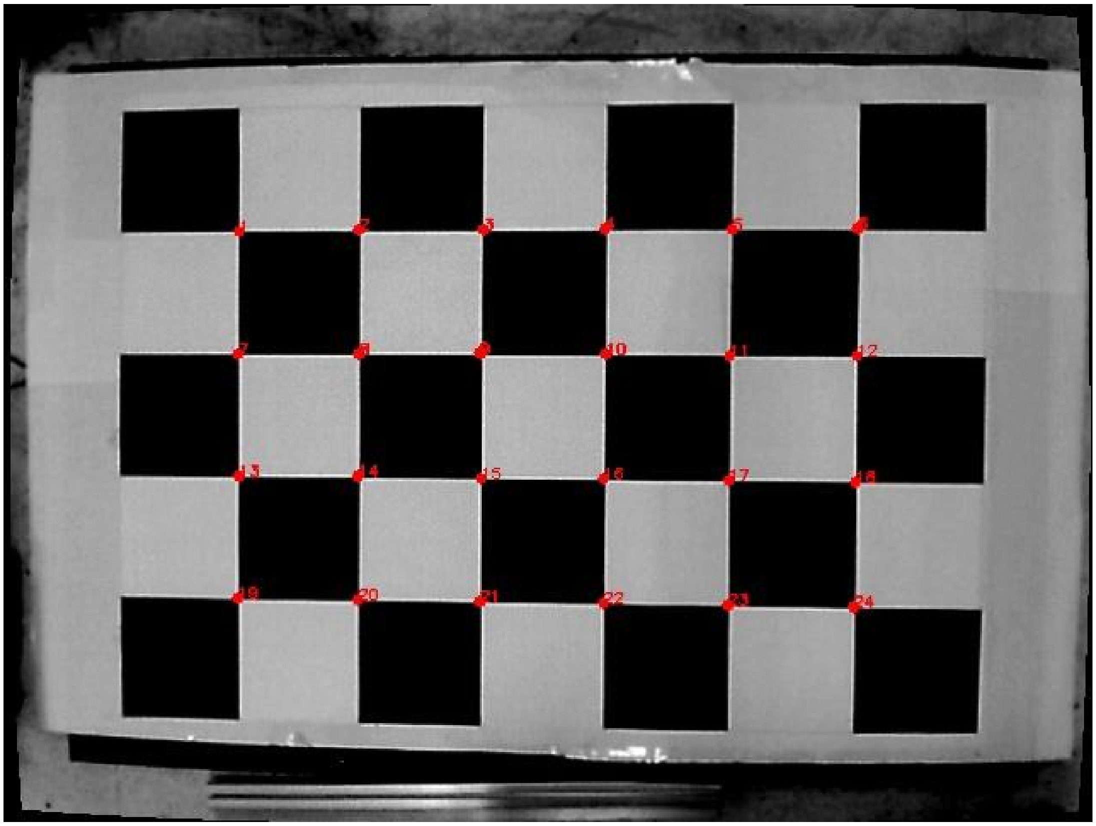

Fig. A.2 Camera calibration chessboard configuration.

The camera model used to calculate world coordinates from image pixel coordinates with lens distortion compensation is defined by the following equations:

$$\begin{bmatrix} x \\ y \\ z \end{bmatrix} = R \begin{bmatrix} X \\ Y \\ Z \end{bmatrix} + t \tag{A.1}$$

$$x' = x/z \tag{A.2}$$

$$y' = y/z \tag{A.3}$$

$$x'' = x'\left(1 + k_1 r^2 + k_2 r^4 + k_3 r^6\right) + 2 p_1 x' y' + p_2\left(r^2 + 2x'^2\right) \tag{A.4}$$

$$y'' = y'\left(1 + k_1 r^2 + k_2 r^4 + k_3 r^6\right) + p_1\left(r^2 + 2y'^2\right) + 2 p_2 x' y' \tag{A.5}$$

$$r^2 = x'^2 + y'^2 \tag{A.6}$$

$$u = f_x \cdot x'' + c_x \text{ and} \tag{A.7}$$

$$v = f_y \cdot y'' + c_y \tag{A.8}$$

where, (X, Y, Z) are the coordinates of a point in the world coordinate frame; (u, v) are the coordinates of the point projection in pixels; R is a rotation matrix describing the relative rotation of the camera with respect to the calibration pattern; t is a translation vector describing the relative translation of the camera with respect to the calibration pattern corner point #1 (*i.e.* corner point #1 defines the origin of the world coordinate frame); (c_x, c_y) is a principle point located at the image centre; f_x and f_y are the focal lengths; k_1, k_2 and k_3 are radial distortion coefficients; p_1 and p_2 are tangential distortion coefficients.

The values of the intrinsic parameters and distortion coefficients, estimated from the chessboard calibration pattern in the image, are tabulated in Table A.1.

Table A.1 Robot tracking camera calibration estimated intrinsic parameters and distortion coefficients.

c_x	c_y	f_x	f_y	k_1	k_2	k_3	p_1	p_2
320	240	817	817	-0.10	0.67	-0.0047	-0.0020	-0.10

The combined rotation-translation matrix [R|t] takes the form:

$$[R\,|\,t] = \begin{bmatrix} R_{11} & R_{12} & R_{13} & t_1 \\ R_{21} & R_{22} & R_{23} & t_2 \\ R_{31} & R_{32} & R_{33} & t_3 \end{bmatrix} \tag{A.9}$$

The estimated values of the rotation translation matrix elements are tabulated in Table A.2.

Table A.2 Robot tracking camera calibration estimated elements of the rotation translation matrix.

R_{11}	R_{12}	R_{13}	R_{21}	R_{22}	R_{23}	R_{31}	R_{32}	R_{33}	t_1 (mm)	t_2 (mm)	t_3 (mm)
1.0	-0.012	0.068	0.013	1.0	-0.012	-0.068	0.012	1.0	-530	-318	2373

For each of the calibration pattern corner points the error in the estimated world coordinates was calculated. The mean error in X was 1.6 mm with standard deviation 1.0 mm. The mean error in Y was 0.93 mm with standard deviation 0.75 mm.

A.2.2 Robot Localization Target Tracking

The basic robot target tracking algorithm is summarized as follows:

1. Acquire raw color image
2. Convert image to grey scale
3. Threshold the image to segment the bright pixels belonging to the target circles from the background.
4. Find all contours in the thresholded image.
5. Perform least squares ellipse fit on each contour that greater than the minimum expected number of points in the contours of the target circles appearing in the image.

To improve the execution time of image processing within the vision tracking program, a method of adaptive region of interest (ROI) around the robot target has been implemented. The image processing algorithm executes much faster and with less variability on the smaller ROI. For example, the vision tracking program begins by capturing a raw image of the entire task space, as shown in Fig. A.3. The initial ROI is set to just encompass the boundaries of the robot task space panel platform, as shown in Fig. A.4. After the centres of the two robot target circles are found, the size of the ROI is decreased to just encompass the robot target and the location of the centre ROI is set to

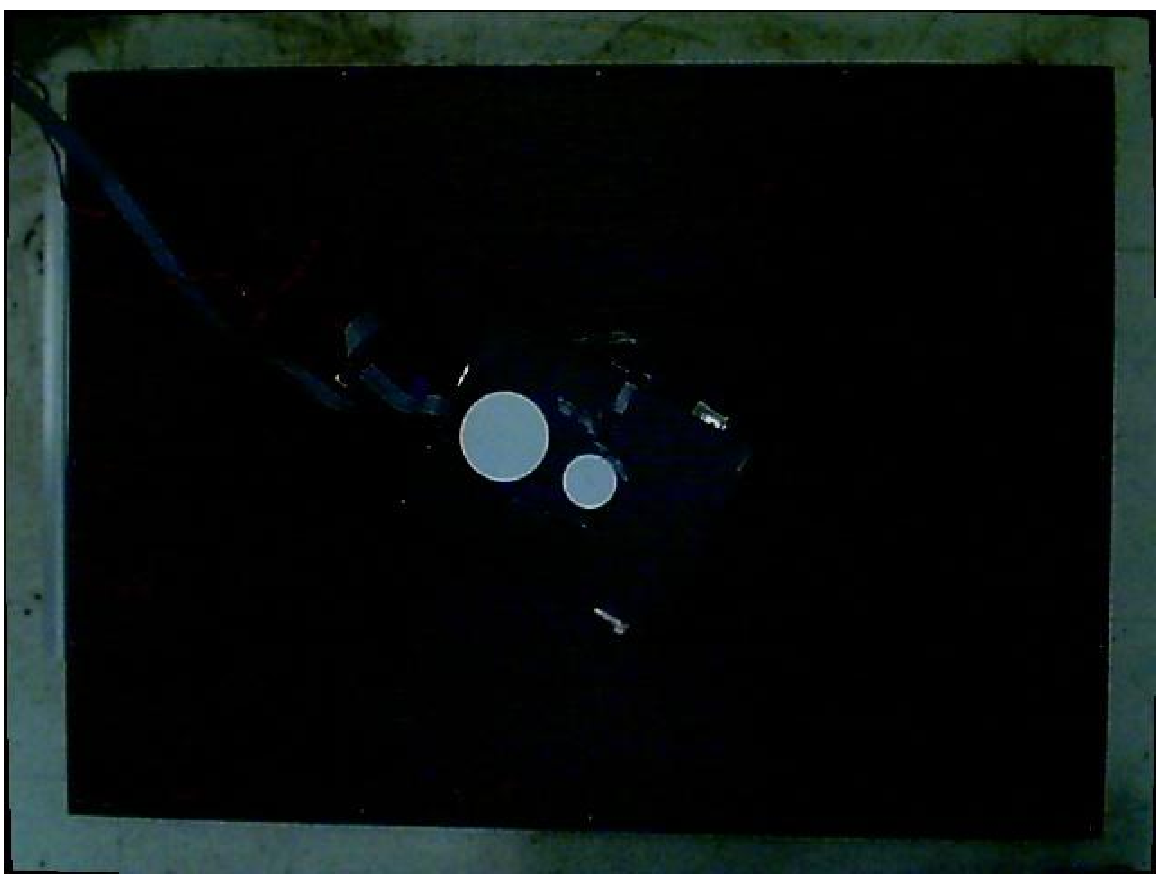

Fig. A.3 Vision tracking raw image of the task space with visible robot target circles.

the middle point between the two target circle centres, as shown in Fig. A.5. As the robot travels around the task space, the location of the image ROI follows the robot by shifting to the middle of the detected circle centres with each image capture update. The resulting target tracking within the task space image is shown in Fig. A.6 with the target circles highlighted and robot heading indicated by the arrow.

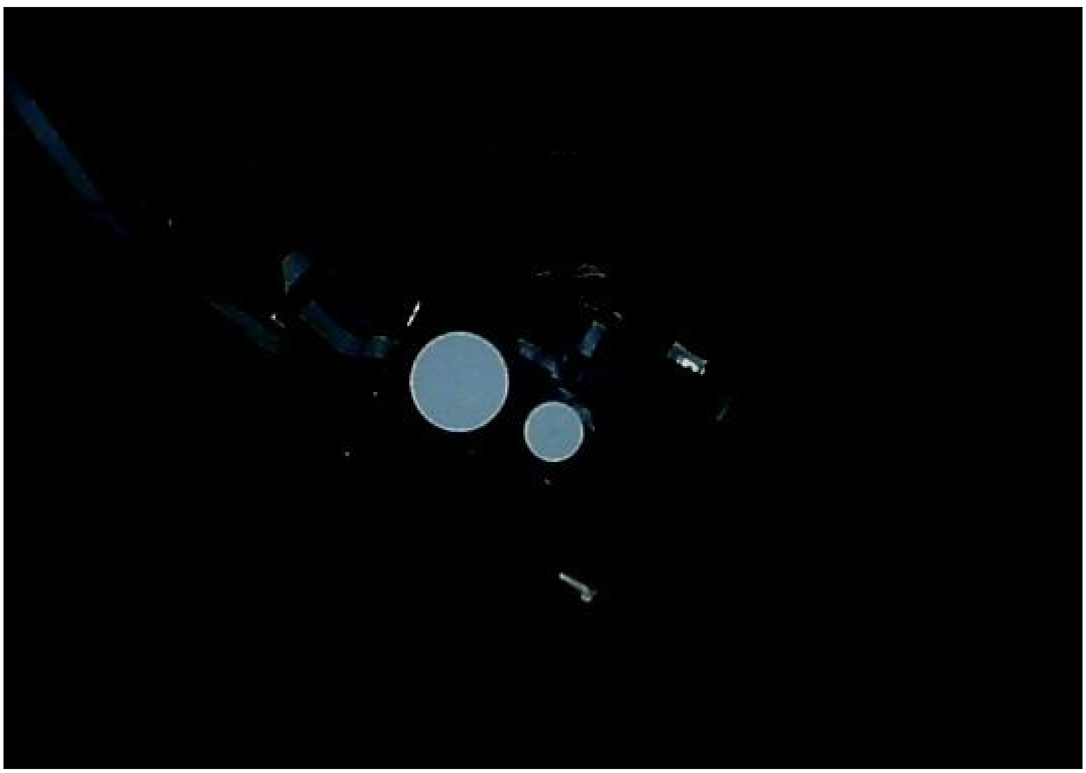

Fig. A.4 An example of the vision tracking image initial ROI.

Fig. A.5 An example of the vision tracking image reduced ROI.

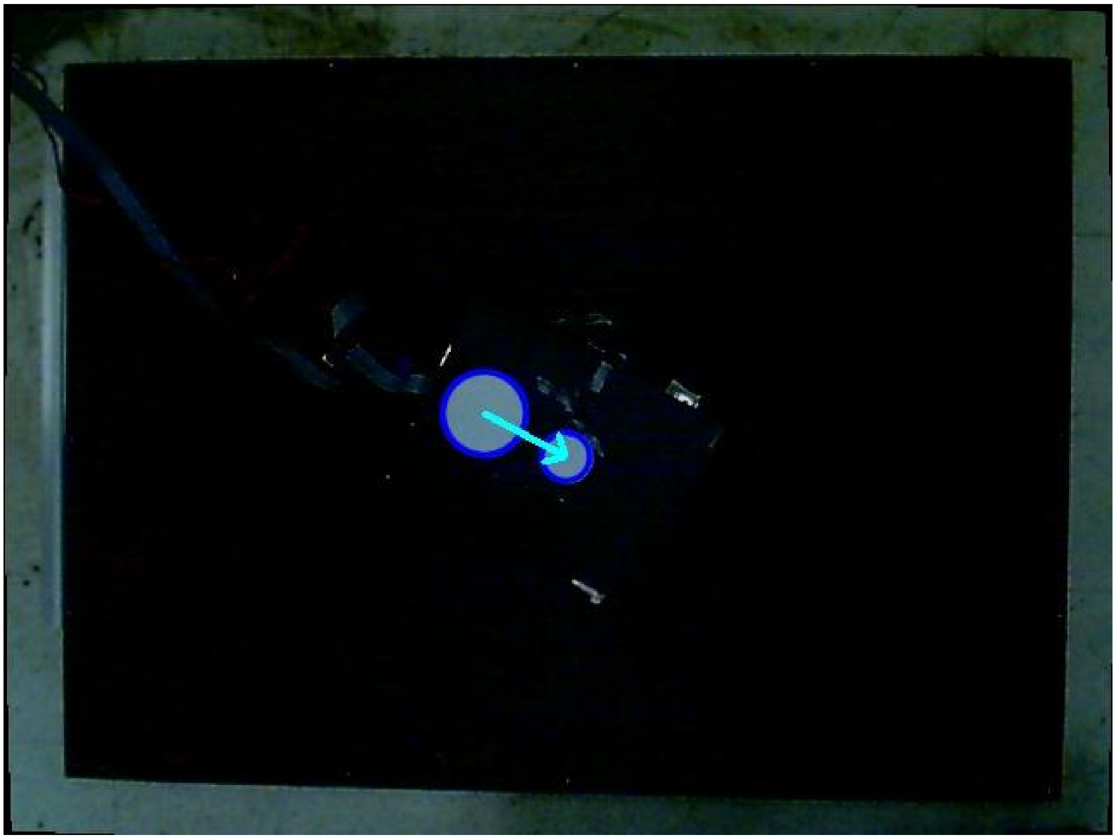

Fig. A.6 An example illustrating the result of the vision tracking.

The calculation of the world coordinates of the robot targets from the pixel coordinates required the elevation (*i.e. Z* coordinate) of the target above the floor surface, which was measured to be 190 mm when the tracks were on the floor. When the robot was engaged in task execution, elevation of the targets could change by a maximum of 30 mm. This was found to have a negligible effect on the localization measurements. The equations used to calculate the world coordinates (X, Y) of the target centres from undistorted pixel coordinates (*u'*, *v'*) are:

$$x' = \frac{\left(u' - c_x\right)}{f_x} \tag{A.10}$$

$$y' = \frac{\left(v' - c_y\right)}{f_y} \tag{A.11}$$

$$z = \frac{Z + R_{1,3} \cdot t_1 + R_{2,3} \cdot t_2 + R_{3,3} \cdot t_3}{R_{1,3} \cdot x' + R_{2,3} \cdot y' + R_{3,3}} \tag{A.12}$$

$$x = x' \cdot z \tag{A.13}$$

$$y = y' \cdot z \tag{A.14}$$

$$X = R_{1,1} \cdot \left(x - t_1\right) + R_{2,1} \cdot \left(y - t_2\right) + R_{3,1} \cdot \left(z - t_3\right) \text{ and} \tag{A.15}$$

$$Y = R_{1,2} \cdot \left(x - t_1\right) + R_{2,2} \cdot \left(y - t_2\right) + R_{3,2} \cdot \left(z - t_3\right) \tag{A.16}$$

The large target circle is positioned above the centre of the robot chassis and the small circle is positioned above the blade edge, as illustrated in Fig. 4.1. Thus, the X and Y coordinates of the robot centre, (x_c, y_c), are calculated from the centre coordinates of the large circle, and the X and Y coordinates of the robot blade, (x_b, y_b), are calculated from the centre coordinates of the small circle, using Eqs. (A.10)–(A.16). The robot heading, θ, is calculated from (x_c, y_c) and (x_b, y_b) using the equation:

$$\theta = \operatorname{atan2}\left(y_b - y_c, x_b - x_c\right) \tag{A.17}$$

The robot location in the task space calculated from image pixel coordinates was verified by comparing physical displacement measurements of (x_c, y_c) across the length and width of the task space with displacements calculated from the vision localization system. The robot was located at initial coordinates (x_{co}, y_{co}) and relocated to coordinates (x_{c1}, y_{c1}). Then the displacement between (x_{co}, y_{co}) and (x_{c1}, y_{c1}) was calculated. The results are shown in Table A.3. The average percent absolute error in estimated displacement is 2.3% with a standard deviation of 0.4%.

Table A.3 Robot vision localization experimental verification.

Position Coordinates (mm)				Displacement (mm)		Absolute Error (mm)	% Error
x_{co}	y_{co}	x_{c1}	y_{c1}	Calculated	Measured		
230	66	786	66	556	544	12	2.2
810	261	250	273	560	550	10	1.8
244	472	795	479	551	538	13	2.4
815	460	802	51	409	400	9	2.3
552	53	568	52	399	389	10	2.7
235	444	220	72	372	362	10	2.9
-68	188	638	162	706	685	21	3.1
-79	-110	618	396	861	845	16	1.9
1237	-141	5	532	1404	1375	29	2.1
-101	-113	1028	661	1369	1342	27	2.0

A.2.3 Summary of Robot Location Measurement Details

The robot location measurement details are summarized as follows:

- Equipment: Point Grey Research Scorpion Camera (640 x 480 pixels^2) with a Pentax zoom lens set to 12 mm focal length.
- Accuracy and precision in position coordinates at zero elevation:
    - X coordinate mean abs. error 1.6 mm with standard deviation 1.0 mm.
    - Y coordinate mean abs. error 0.93 mm with standard deviation 0.75 mm.

- Mean error in robot displacement: mean percent error 2.3%.
- Resolution: < 3 mm/pixel.

A.3 Robot Blade Material Accumulation Measurement

A.3.1 Material Accumulation Measurement Calibration

Five distance sensors, denoted S_1-S_5, were mounted on the front of the robot pointing downward perpendicular to the floor approximately 10 mm ahead of the blade. The sensor voltage signals were calibrated by measuring the varying height of a flat level surface located directly beneath the sensors, as illustrated in Fig. A.7. Plots of the range sensor calibration data with linear fits are shown in Fig. A.8.

The range sensor calibration functions used to calculate object height beneath each sensor, h_s, from sensor output voltage, V_s are:

$$h_{s1} = -89.7 \cdot V_{s1} + 155 \tag{A.18}$$

$$h_{s2} = -88.1 \cdot V_{s2} + 153 \tag{A.19}$$

$$h_{s3} = -89.4 \cdot V_{s3} + 155 \tag{A.20}$$

$$h_{s4} = -89.4 \cdot V_{s4} + 156 \text{, and} \tag{A.21}$$

$$h_{s5} = -89.6 \cdot V_{s5} + 158 \tag{A.22}$$

The results of the calibration are as follows. The mean height measurement absolute error of sensor S_1 is 0.4 mm with standard deviation 0.4 mm. The mean height measurement absolute error of sensor S_2 is 0.3 mm with standard deviation 0.3 mm. The mean height measurement absolute error of sensor S_3 is 0.2 mm with standard deviation

0.2 mm. The mean height measurement absolute error of sensor S_4 is 0.3 mm with standard deviation 0.3 mm. The mean height measurement absolute error of sensor S_5 is 0.2 mm with standard deviation 0.2 mm.

The material accumulation process variable, d_a,is calculated as the average of the height measurements beneath each range sensor, *i.e.* $d_a = (h_{s1} + h_{s2} + h_{s3} + h_{s4} + h_{s5})/5$.

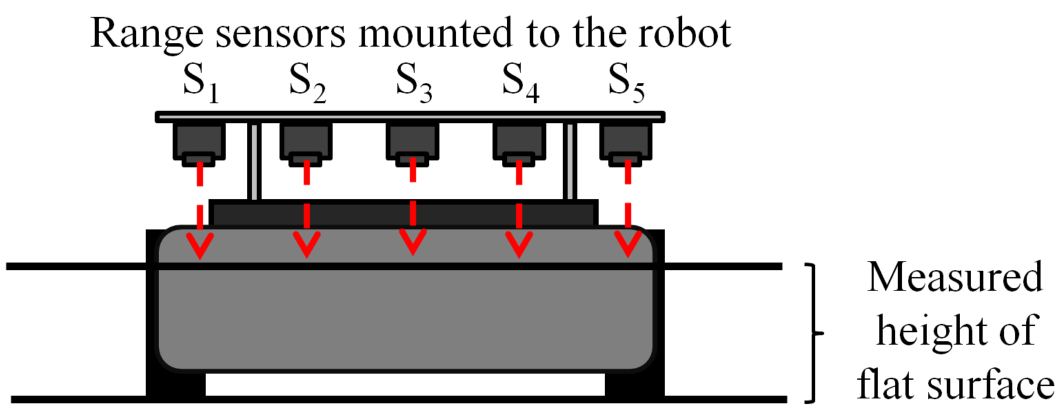

Fig. A.7 Illustration of material accumulation sensor calibration.

A.3.2 Summary of Material Accumulation Measurement Details

The material accumulation measurement details are summarized as follows:

- Equipment: Baumer Distance Sensor FADK 14I4470/S14 and National Instruments PCI-6251 16-bit data acquisition board.
- Mean errors in position coordinates at zero elevation:
    - S1 mean absolute error 0.4 mm with standard deviation 0.4 mm.
    - S2 mean absolute error 0.3 mm with standard deviation 0.3 mm.
    - S3 mean absolute error 0.2 mm with standard deviation 0.2 mm.
    - S4 mean absolute error 0.3 mm with standard deviation 0.3 mm.
    - S5 mean absolute error 0.2 mm with standard deviation 0.2 mm.

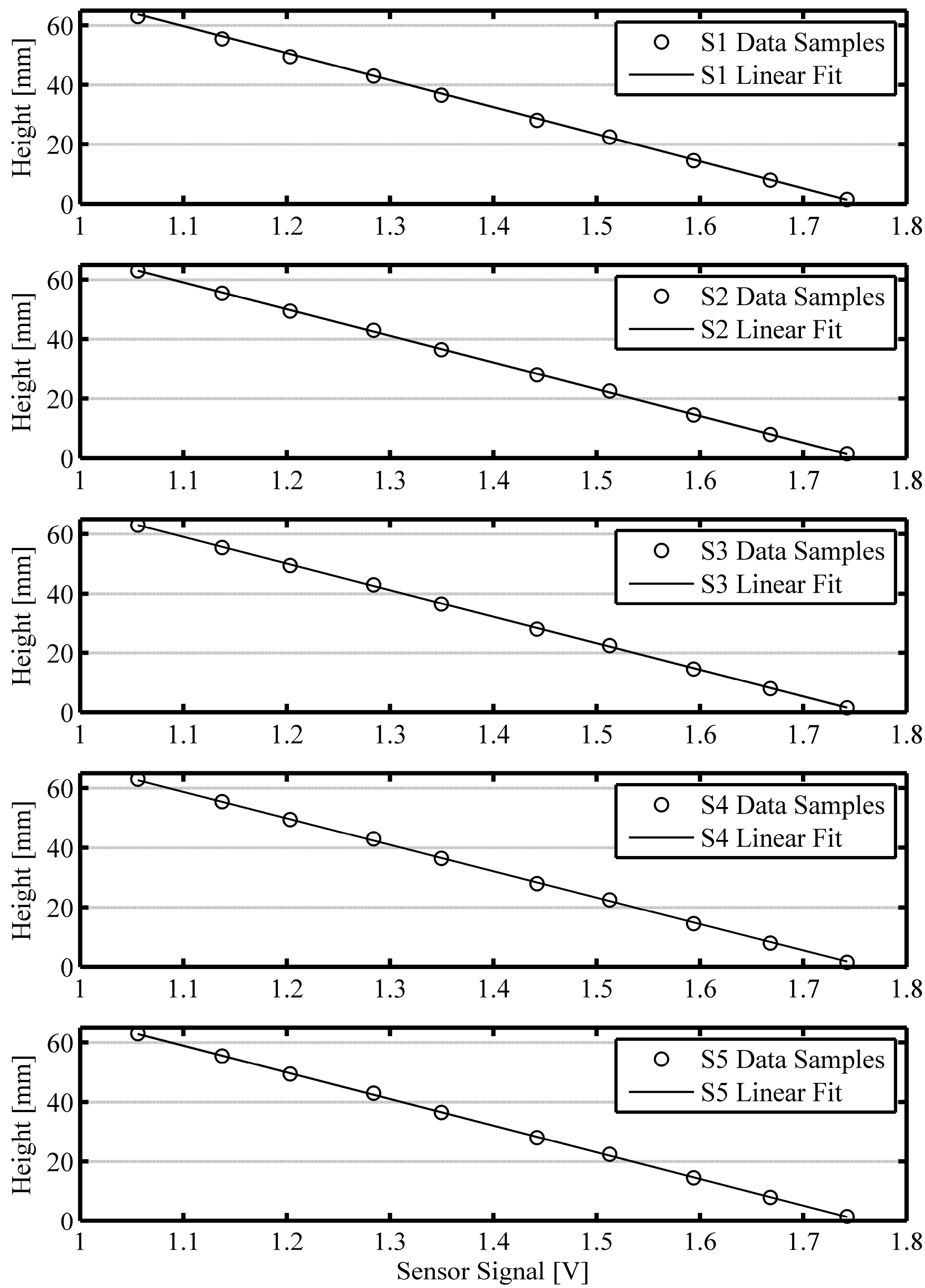

Fig. A.8 Range sensor calibration.

A.4 Robot Blade Position Measurement

A.4.1 Blade Position Measurement Calibration

To calibrate the blade position measurement, the blade was raised to various fixed positions. The height of the bottom edge of the blade was measured with respect to the floor and plotted against the corresponding blade motor encoder counts, as shown in Fig. A.9 with the corresponding linear fit calibration function. The theoretical resolution of the blade position measurement is 0.000772 mm per encoder count. From the calibration results, the mean blade position measurement absolute error is 1 mm with standard deviation 0.7 mm.

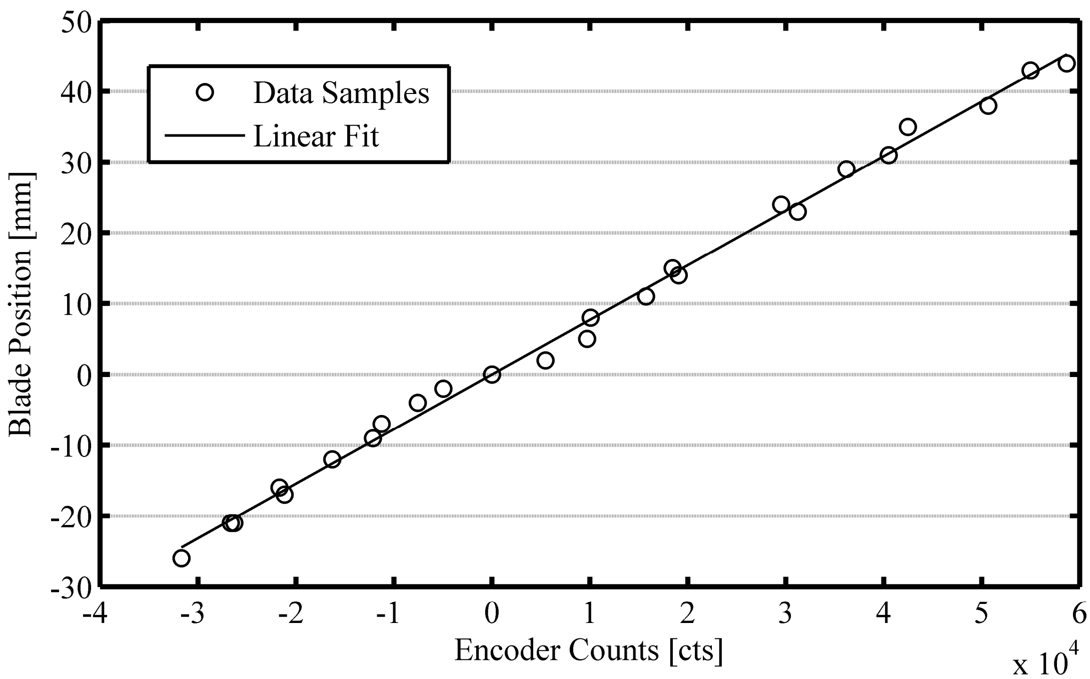

Fig. A.9 Blade position measurement calibration.

A.4.2 Summary of Blade Position Measurement Details

The blade position measurement details are summarized as follows:

- Equipment: Faulhaber HES164A quadrature encoder integrated with a 1524E006S123 motor and 15/5S141:1K832 gearhead
- Mean error: mean absolute error 1 mm with standard deviation 0.7 mm

A.5 Robot Pitch Measurement

A.5.1 Robot Pitch Measurement

The tilt sensor was mounted directly to the robot chassis aligned with its longitudinal and lateral axes. Accuracy and resolution values were taken from the data sheet. The sensitivity and voltage offset values from the data sheet were used to calculate pitch angle, ϕ, from the orientation sensor voltage, $V_{s,\phi}$,. The pitch angle is calculated with the equation:

$$\phi = \sin^{-1}\left(\frac{V_{s,\phi} - 2.5}{0.0349}\right) \tag{A.23}$$

A.5.2 Summary of Robot Pitch Measurement Details

The robot pitch measurement details are summarized as follows:

- Equipment: Crossbow Tilt Sensor CXTA02 and National Instruments PCI-6251 16-bit data acquisition board.
- Accuracy: 0.5 degrees.
- Resolution: 0.05 degrees.

A.6 Task Space Material Profile Height Measurement

A.6.1 Task Space Material Profile Measurement

A diagram of the material profile measurement system is illustrated in Fig. A.10. The laser position was fixed at height h_L above the reference surface. The laser was mounted perpendicularly to the shaft of the stepper motor allowing it to rotate and scan along the length of the task space. The laser beam reflects off of the measured surface at a distance d_B and reflects off of the reference surface at a distance $d_{B,ref}$. The difference between the distance of the beam reflected off of the measured surface and the reference surface in the camera image is *c'* with magnification *M*. The height of the measured surface, *a*, at position d_B is determined as a function of the relationship between these geometric variables as follows:

$$c = Mc' \tag{A.24}$$

$$d_{B,ref} - d_B = Mc' \frac{\cos\alpha}{\sin\beta} \text{ and} \tag{A.25}$$

$$a = Mc' \frac{\cos\alpha}{\sin\beta} \frac{h_L}{d_{B,ref}} \tag{A.26}$$

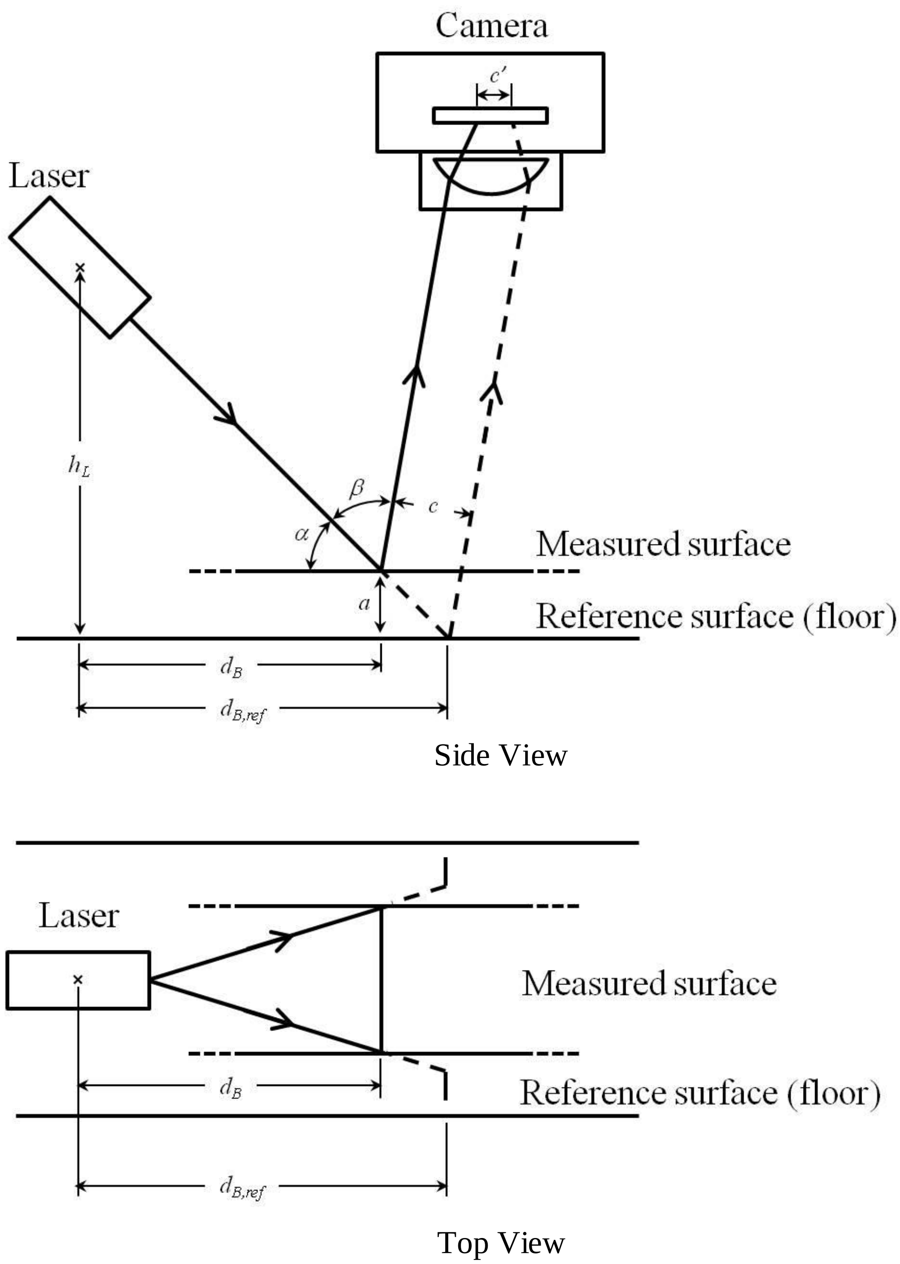

Fig. A.10 Diagram of the material profile measurement system.

A.6.2 Synchronization of the Stepper Motor and Camera

The stepper motor driver was set to microstep at a resolution of 32 microsteps per step (or 6400 steps per revolution). At this resolution the maximum longitudinal distance change of the laser beam projected on the task space is less than 7 mm (occurring at the farthest edge of the task space). The laser beam distance travelled in the task space is much smaller at the 'start' of the task space. To reduce the number of images saved while maintaining an acceptable change in beam travel per frame with a constant frame rate, images are saved after two motor microsteps for the first 60 frames (approximately 1/3 of the task space). A total of 275 images are saved over a total distance in the task space of 1200 mm giving an average beam travel resolution of 4.4 mm/frame. The motion of the stepper motor is synchronized with the camera to advance one microstep after a new frame is captured and saved. Communication between the stepper motor control computer and the image capture computer is achieved by sending discrete pulses from the camera.

A.6.3 Laser Scan Image Processing and Calibration

After the scanning process is complete each image is processed to identify the contour of the beam and calculate the height profile. The height profile is determined with respect to the reference segments of the beam (*i.e.* known region of the level floor surface). Prior to processing an image of the task space with no laser is saved. The image processing algorithm is described as follows:

1. Subtract 'laser off' image from 'laser on' image to produce the 'beam only' image
2. Threshold the 'beam only' image at a level of 15% to produce a binary image of the beam contour points.

3. For each row along the X-axis of each ‘beam only’ image the beam contour width is condensed to one pixel by taking the average of all pixel Y-values.
4. To handle the possible condition of two apparently distinct contours, if the difference between the largest and smallest Y-values is greater than 5 pixels (*e.g.* the maximum expected beam width) then either the largest Y-value or smallest Y-value is chosen depending which is closer to the mean value.
5. Fit a least squares line to the ‘tail’ points of the beam contour which are known to be at the zero elevation floor surface reference.
6. Calculate the difference between all contour points and the reference line, *i.e.* the c' term in Eq. (A.24).

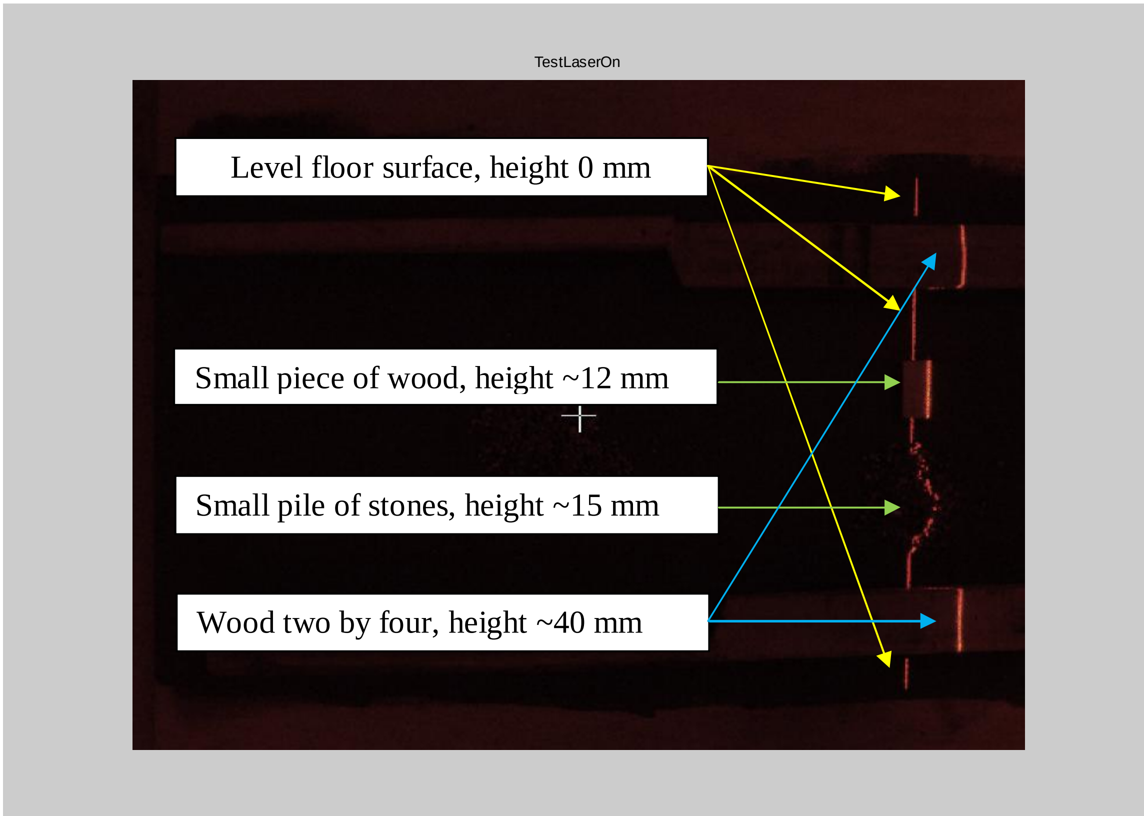

Fig. A.11 Example of a raw laser scan image with various objects of different heights in the task space.

An example of the result of the image processing algorithm is shown in Fig.A.11.

To calibrate the calculation of the height profile from each image using Eq. (A.25) the value of $d_{B,ref}$ and the ratio $\frac{\cos\alpha}{\sin\beta}$ were determined experimentally as functions of the Y-axis position of the reference line in the image. A plot of laser beam position, $d_{B,ref}$, measured in the task space with respect to the Y-axis laser beam position in the image is shown in Fig. A.12.

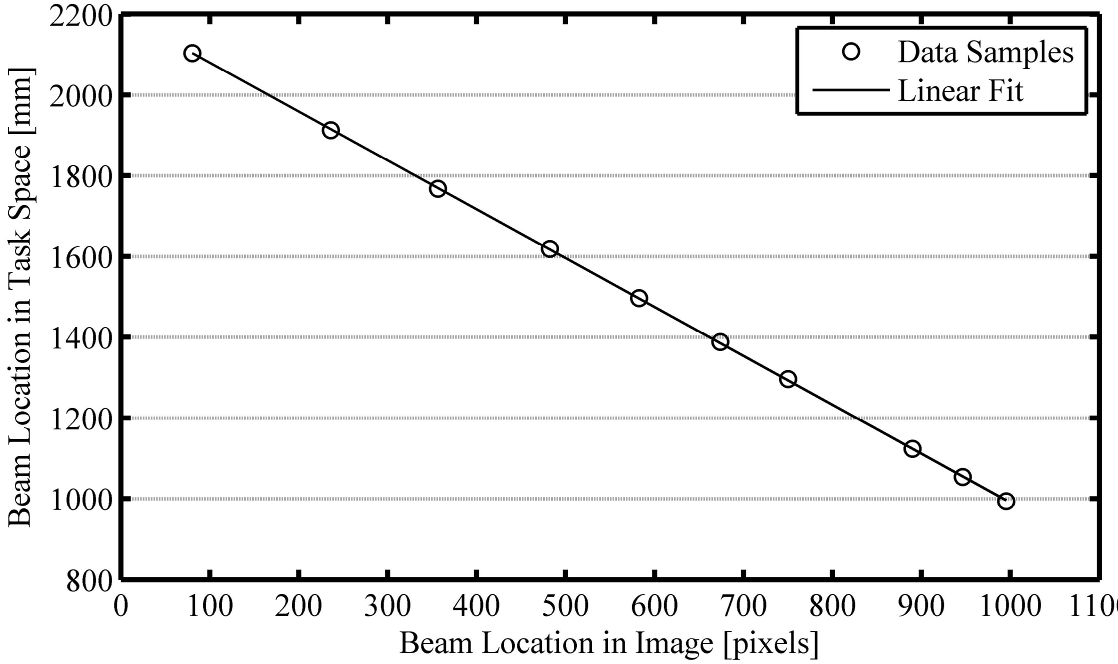

Fig. A.12 Calibration of the beam reference task space position with respect to image position.

To determine the ratio $\frac{\cos\alpha}{\sin\beta}$ as a function of Y-axis beam position, the height of an object in the task space was calculated at different positions in the task space with Eq. (A.26) using the calibrated function for $d_{B,ref}$ found previously and the ratio $\frac{\cos\alpha}{\sin\beta}$ set to unity. The ratio $\frac{\cos\alpha}{\sin\beta}$ as a function of beam reference position in the image is determined with the following equations:

$$h_{calc,uncalib} = Mc' \frac{h_L}{d_{B,ref}} \tag{A.27}$$

$$\frac{h_{measured} - h_{calc,uncalib}}{h_{measured}} = f\left(d_{B,ref}^{pix}\right) \tag{A.28}$$

$$h_{measured} = \frac{h_{calc,uncalib}}{1 - f\left(d_{B,ref}^{pix}\right)} \text{ and} \tag{A.29}$$

$$\frac{\cos\alpha}{\sin\beta} = \frac{1}{1 - f\left(d_{B,ref}^{pix}\right)} \tag{A.30}$$

where $h_{calc,uncalib}$ is the calculated height with $\frac{\cos\alpha}{\sin\beta} = 1$, $h_{measured}$ is the measured height and $f\left(d_{B,ref}^{pix}\right)$ is the linear fit function of percent error as a function of reference line distance in the image. A plot of percent height error as a function of beam reference position in the image is shown in Fig. A.13.

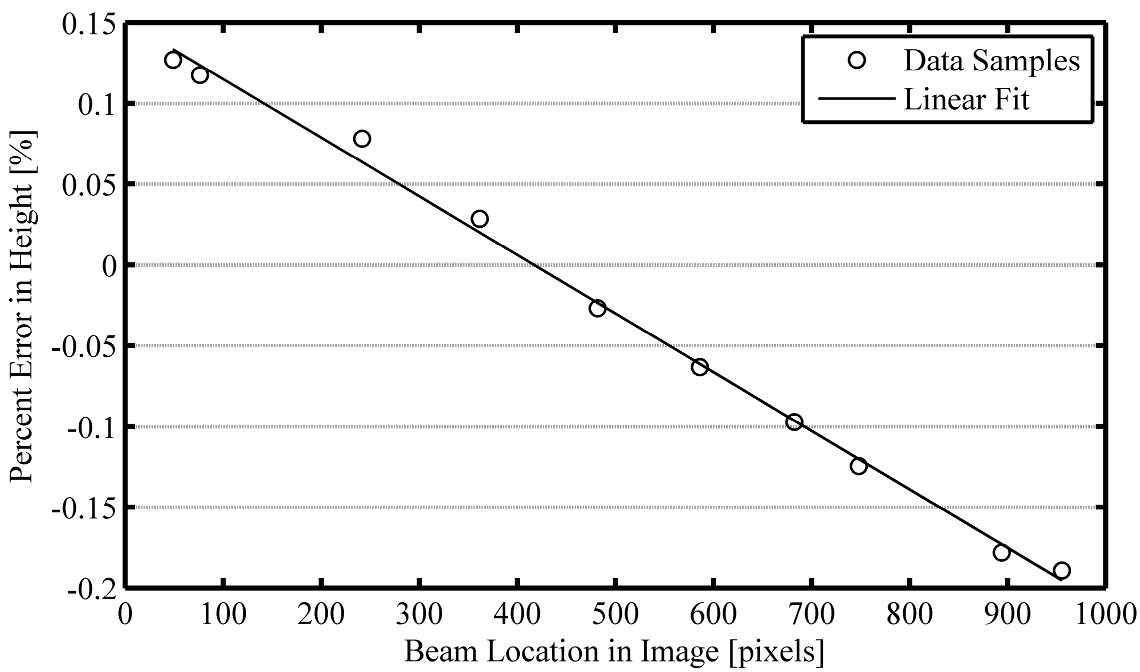

Fig. A.13 Calibration of ratio $\frac{\cos\alpha}{\sin\beta}$ with respect to beam reference position in the image.

A.6.4 Laser Scan Height Measurement Validation

The calibration of the height measurement system was verified with four straight metal beams of constant height placed in the task space. An example image with the laser stripe is shown in Fig. A.14. An example of the resulting height measurements of one ‘beam slice’ are shown in the Fig. A.15. The final calculated height contour over the task space is shown in Fig. A.16. The mean absolute error of the calculated height of each metal beam over the entire task space is 0.23 mm, 0.34 mm, 0.26 mm and 0.26 mm. Overall, the height measurement mean absolute error is 0.26 mm with standard deviation 0.24 mm.

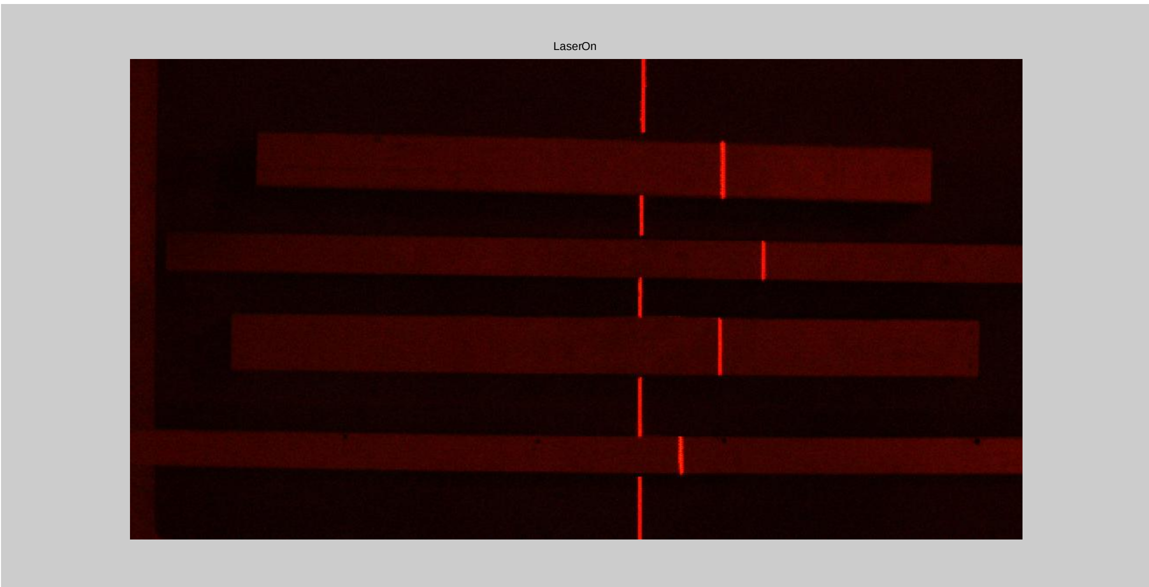

Fig. A.14 Laser scan height measurement verification example image with four straight metal beams with different heights.

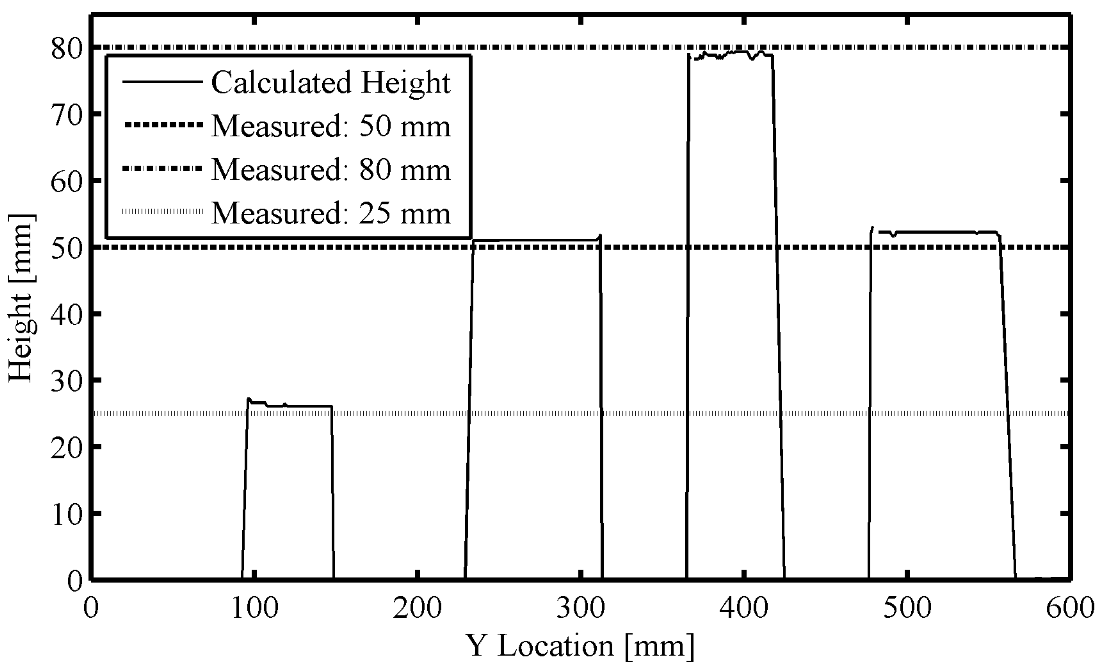

Fig. A.15 Laser scan height measurement verification example height calculation from a single image.

A.6.5 Summary of Task Space Material Profile Measurement Details

The task space material profile measurement details are summarized as follows:

- Equipment: Point Grey Research Dragonfly2 Camera (1024 x 768 pixels^2) with a 8.5 mm focal length lens and a red filter. Lasiris 635 nm, 5mW laser.
- Mean error: mean absolute error 0.26 mm with standard deviation 0.24 mm.
- Height Resolution: 2 mm to 7 mm.

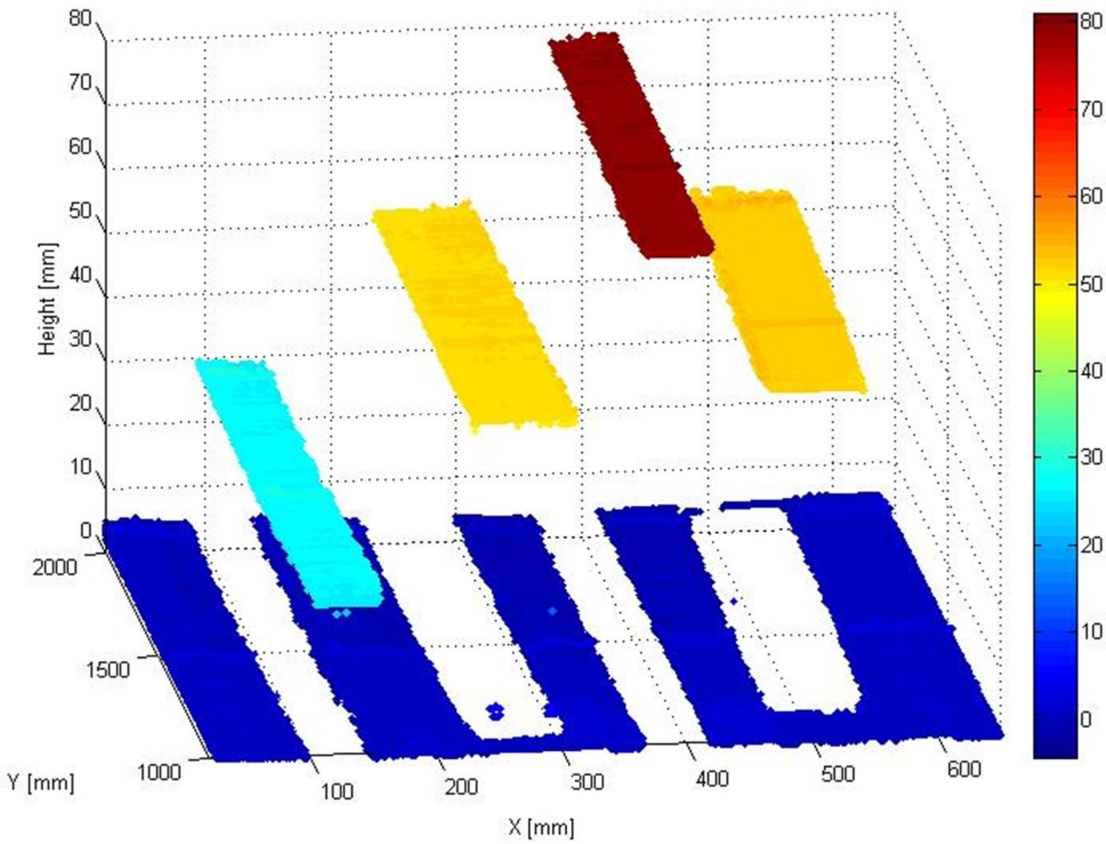

Fig. A.16 Laser scan height measurement verification calculated height over the entire task space.

A.7 Material Profile Process Auxiliary Variables

To calculate the process auxiliary variables h_b, $h_{r,l}$ and $h_{r,r}$, the locations of the edges of the blade $((x_{b,l},\ y_{b,l}),\ (x_{b,r},\ y_{b,r}))$ and the locations of the outer edges of the material ridges $((x_{rl},\ y_{rl}),\ (x_{r,r},\ y_{r,r}))$ were calculated from the measured location of the blade centre, x_b and the robot heading, θ. This is illustrated in Figure A.17.

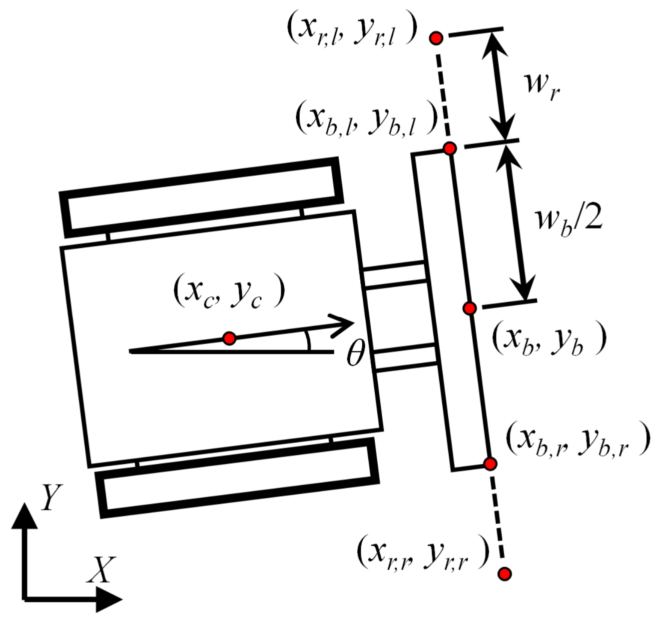

Fig. A.17 Diagram illustrating the robot location and process auxiliary variable locations coordinates.

The locations of the blade edges and outer ridge locations are calculated as follows:

$$x_{b,l} = x_b - \frac{w_b}{2}\cos\left(90^\circ - \theta\right) \tag{A.31}$$

$$y_{b,l} = y_b + \frac{w_b}{2}\sin\left(90^\circ - \theta\right) \tag{A.32}$$

$$x_{b,r} = x_b + \frac{w_b}{2}\cos\left(90^\circ - \theta\right) \tag{A.33}$$

$$y_{b,r} = y_b - \frac{w_b}{2}\sin\left(90^\circ - \theta\right) \tag{A.34}$$

$$x_{r,l} = x_b - \left(\frac{w_b}{2} + w_r\right)\cos\left(90^\circ - \theta\right) \tag{A.35}$$

$$y_{r,l} = y_b + \left(\frac{w_b}{2} + w_r\right)\sin\left(90^\circ - \theta\right) \tag{A.36}$$

$$x_{r,r} = x_b + \left(\frac{w_b}{2} + w_r\right)\cos\left(90^\circ - \theta\right) \text{ and} \tag{A.37}$$

$$y_{r,r} = y_b - \left(\frac{w_b}{2} + w_r\right)\sin\left(90^\circ - \theta\right) \tag{A.38}$$

where w_b is the width of the blade (200 mm) and w_r is the nominal ridge width (50 mm).

The process auxiliary variable h_b is calculated as the mean material profile height within a region along the width of the blade at each location x_b in the task space. This is summarized as follows:

$$h_b(x_b) = mean\left(h_{scan}\left(x, y\right)\right), \text{ for } x_b - \varepsilon \le x \le x_b + \varepsilon \wedge y_{b,r} \le y \le y_{b,l} \tag{A.39}$$

where, h_{scan}(x,y) is the set of all height measurement points in the task space at coordinates (x,y) and ε is a small distance equal to the nominal resolution of the laser scanning system (5 mm) to ensure that enough points are included in the calculation. Similarly, the process auxiliary variables $h_{r,l}$ and $h_{r,r}$ are calculated as the mean profile height within regions defined by the edges of the blade and the approximate width of the ridge. This is summarized as follows:

$$h_{r,l}(x_b) = mean\left(h_{scan}\left(x, y\right)\right), \text{ for } x_{b,l} - \varepsilon \le x \le x_{b,l} + \varepsilon \wedge y_{b,l} \le y \le y_{r,l} \text{ and} \tag{A.40}$$

$$h_{r,r}(x_b) = mean\left(h_{scan}\left(x, y\right)\right), \text{ for } x_{b,r} - \varepsilon \le x \le x_{b,r} + \varepsilon \wedge y_{r,r} \le y \le y_{b,r} \tag{A.41}$$

An example of a topological material profile scan with the robot path superimposed is shown in Fig. A.18.

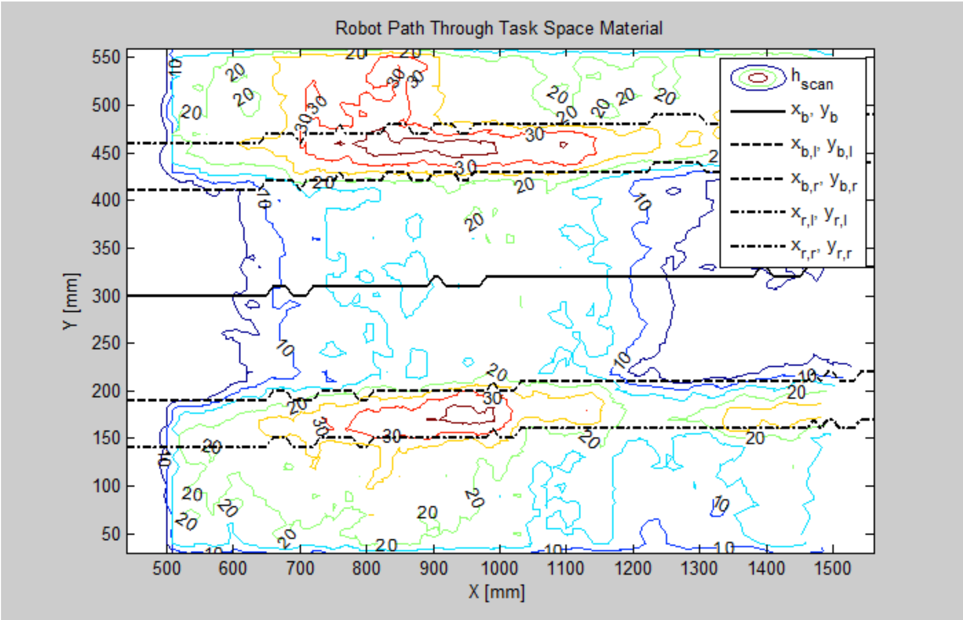

Fig. A.18 Example of material profile scan height measurements with the robot path superimposed.

A.8 Blade Position Control

Proportional-integral-derivative (PID) control was implemented for position control of the robotic bulldozer blade, however, after extensive effort at tuning it was found to be ineffective. It is believed that this was due to lack of robustness to the uncertainty in interaction forces between the blade and the environment. This motivated the use of a simplified sliding mode controller. The sliding mode controller takes the form:

$$u_b = V_{s,b} \cdot sign(s) \text{ and} \tag{A.42}$$

$$s = r_b - \zeta \tag{A.43}$$

where, u_b is the blade actuator control signal, $V_{s,b}$ is the voltage supply to the blade actuator, s is the sliding surface, r_b is the blade position reference, and ζ is the blade position. An example of blade position control with the simplified sliding mode controller is shown in Fig. A.19. This example shows an extreme case of blade positioning with step changes in large control increments. Typically, blade positioning is much smoother with smaller increments, and the position overshoots are negligible.

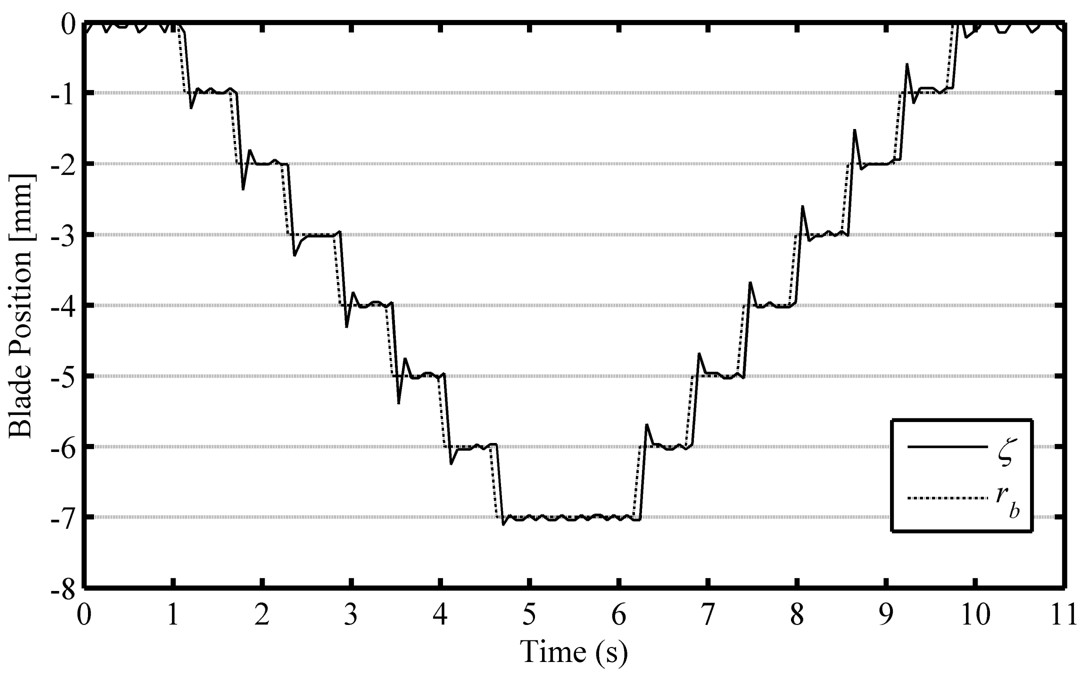

Fig. A.19 Example of blade position control with the simplified sliding mode controller.

A.9 Robot Heading Control

A differential steering proportional-integral (PI) heading controller was implemented on the robotic bulldozer to maintain straight forward motion along a straight path with a constant heading. The same constant nominal input is sent to each of the robot tracks. In response to heading error, the controller decreases the input to one track and increases the input to the other track by the same amount with respect to the heading error. The heading control algorithm is defined as follows:

$$u_\theta = K_{P,\theta} \cdot e_\theta + K_{I,\theta} \cdot \Sigma e_\theta \quad \text{(A.44)}$$

$$u_{t,l} = u_{t,nom} + u_\theta \text{ and} \quad \text{(A.45)}$$

$$u_{t,r} = u_{t,nom} - u_\theta \quad \text{(A.46)}$$

where, u_θ is the track control heading correction input; $K_{P,\theta}$ is the heading control proportional gain; $K_{I,\theta}$ is the heading control integral gain; $u_{t,nom}$ is the nominal constant track input; $u_{t,l}$ is the input voltage to the left track motor; $u_{t,r}$ is the input voltage to the right track motor; e_θ is the error between the desired constant heading, θ_d, and the measured heading, θ; and Σe_θ is the sum of the heading error. The manually tuned heading controller gains were $K_{P,\theta}$ = 7 %/deg and $K_{I,\theta}$ = 0.5 %/deg·s. The nominal constant track input, expressed as the percentage of the maximum supply voltage was $u_{t,nom}$ = 45%, where the maximum track motor supply voltage was 12 V. The heading controller was able to maintain a constant robot heading to within ± 1 degree. An example of robot heading with the controller maintaining a constant desired heading of θ_d = 0 degrees is shown in Fig. A.20.

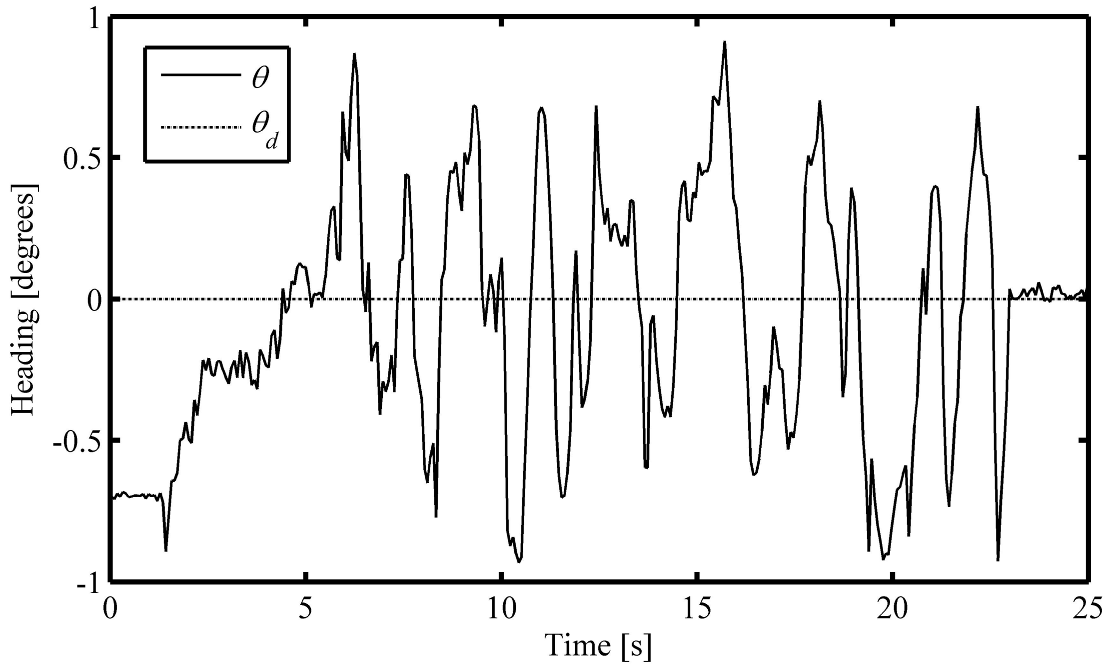

Fig. A.20 Example of robot heading controller maintaining θ_d = 0 degrees.